Doctoral Dissertation
Doctoral Program in Chemical Engineering (34^{th} cycle)

Infrared thermography for freeze-drying applications: from ice crystal size prediction to primary drying process monitoring and design space determination

Maitê Harguindeguy

* * * * * *

Supervisor
Prof. Davide Fissore

Doctoral Examination Committee:
Prof. Roberto Moscetti, Università della Tuscia
Prof. Geoff Smith, De Montfort University

Politecnico di Torino
2022

I hereby declare that, the contents and organization of this dissertation constitute my own original work and does not compromise in any way the rights of third parties, including those relating to the security of personal data.

. . . . . .

Maitê Harguindeguy
Turin, 2022

Summary

Freeze drying processes are crucial to the pharmaceutical industry because they can produce shelf-stable high-quality heat-sensitive medicines. Freeze-dried products make up 16% of the top-selling 100 pharmaceuticals and ensuring product quality is of most importance. In fact, the 2004 FDA Guidance for Industry states that product quality needs to be achieved by design and not by testing after production. Hence, optimal cycle design and thorough process monitoring are pivotal for high-quality drug manufacturing through freeze-drying processes.

Most temperature monitoring tools currently in use are invasive ones, i.e., they are in direct contact with the product. With a sensor in direct contact with the product, the product phase change dynamics is affected. During freezing, the first step of a freeze-drying process, the presence of the sensor will drive ice nucleation to happen earlier. If this happens, freezing will occur at a higher temperature for that particular vial, resulting in larger ice crystals than in other vials. This way, their monitoring may not represent well the batch. Additionally, Thermocouples (TC)s are destructive to the monitored sample as they are invasive sensors and sterility concerns arise. Within this scenario, non-invasive temperature monitoring tools become essential.

IR-based sensors can measure product temperature in a non-invasive way without presenting the drawbacks of commonly used tools. Of course, as a novel technology, they present their own drawbacks such as the field of view, low penetration and the need to pre-establish the object's emissivity prior to IR monitoring. Nonetheless, preliminary studies using IR thermography to monitor freeze-drying processes have shown encouraging results, and further studies regarding its application became imperative.

In this present research work, the application of infrared thermography to monitor freeze-drying batches is investigated. The prototype used in this research is placed inside the drying chamber on the same shelf as the monitored vials. This positioning allows monitoring the whole product's axial temperature profile. However, this placement inside the chamber makes it necessary first to evaluate if the sensor's presence can have an effect on batch dynamics. Hence, the starting point of the research was to evaluate this by performing tests with and without the IR camera inside the drying chamber. Thermocouple-based temperature profiles

from each batch were compared. It was found that the sensor's case can have a slight shielding effect when a long freezing duration is used or a slight irradiating effect if a short freezing duration is used. This effect is strictly related to the temperature of the camera case after freezing and was ruled as not relevant. Once the sensor's effect was deemed minimal, its accuracy had to be verified. Hence, IR-based thermal profiles were confronted with TC-based ones from the same batch. Different batch and vial sizes were tested, and the IR temperature measurements were always in good agreement with those of the thermocouples within their accuracy range ± 1 K.

Following the process steps in order, applying IR monitoring to the freezing step brought great insights into the freezing phenomena in vials. Since ice nucleation and crystal growth are exothermic phenomena, special attention was given to maxima temperature points and any evidence of heat release. IR thermography allowed the observation of the heat of nucleation affecting neighbouring vials. Additionally, tracking the axial T_{max} after nucleation could be an experimental inference of the freezing front temperature and position for vials being cooled in direct contact with the shelf. The correlation between larger temperature gradients during nucleation and freezing resulting in larger variability on the resulting cake pore sizes was confirmed in this study. Additionally, the *in-line* application of the IR-based freezing front data coupled to different mathematical models to estimate the resulting pore sizes was successfully validated using vacuum induced surfaced freezing (VISF). Three different freezing models were used, an empiric, a mechanistic and a supersaturation one. The first two, were not very well suited to predict the resulting pore sizes for the cake edges using the experimental data. The last was the more suited for the *in-line* application with IR-based experimental data.

Moving on to primary drying, batch representativity of IR-thermography had to be investigated. A series of tests with up to 157 vials were performed comparing thermocouple temperature measurements to IR-based ones. A hexagonal array was used to improve batch representativeness, and an assumption was made based on the observed results. The front-row vials that are more shielded in this array were regarded as representative of central vials, while the more exposed ones were regarded as representative of edge vials. This assumption worked well to represent the batch better. Additionally, since sublimation is an endothermic process, tracking the axial T_{min} during primary drying allowed the inference of the sublimation front temperature and position for vials being heated in direct contact with the shelf. This data yielded a more accurate estimation of the primary drying end-time and, thus, a new non-gravimetric K_v estimation method. Based on this, a new and more straightforward design space calculation protocol was developed and proved successful.

In sum, IR temperature monitoring applied to freeze-drying batches offers unique advantages for process assessment and design. IR-monitoring is a promising non-invasive tool to monitor freeze-drying processes.

Acknowledgements

First, I would like to acknowledge my academic adviser Dr. Davide Fissore, who was always available and able to give the fastest spot-on reviews, which were a blessing to move forward with the research work. This support was vital, and it made me feel confident that I could find academic advice and support whenever needed. So, thank you a lot.

I could not forget to thank the other professors from my group. Thank you Dr. Antonello Barresi for always working to make sure we had the necessary tools to develop our work. And thank you Dr. Roberto Pisano for helping me learn more through the work we developed together.

Then, of course, I was lucky to have colleagues who always helped with the everyday experimental work and made our routine more joyous. My office mates Serena Bobba, Elena Lietta, Domenico Colluci and Luigi Capozzi were very important. Then, of course, Merve Adali and Lorenzo Stratta, with whom I had the pleasure of conducting experimental work. Additionally, Esperanza Batuecas, Francesco Maniscalco, Carlos Gomez, Angelo Romano, Parnian Kianfar, Elahe Davar, Marco Bazzano, Mohsen Shia, Marco Sangermano, Luisa Baudino, Raffaele Aaron, Andrea Arsiccio, Claudia Udrescu, Daniela Velez and many others that will be always remembered.

Outside my university, I was lucky to have Dr. Aleksander Litdke revise some of my papers in addition to my adviser. He was always great in giving me meticulous advice besides general document structure ideas. Additionally, I would like to thank my dear friends Paulo Gonzaga and Gustavo Gomes. On more than one occasion, they helped me with specific topics or let me ramble about my ideas until they were better defined.

Finally, I would like to thank my parents, Eduardo Harguindeguy and Ana Carranza. My siblings, Ignacio and Jimena, and even my grandmas for *being there* for me. Sometimes love comes as a shared recipe, sometimes as a phone call. In any case, feeling loved by all of you was, is, and will always be of crucial importance to me.

Grazie mille a tutti!

Frozen Haiku

Ice crystals forming
defining the porous cake
Can IR predict it?

Contents

List of Tables

List of Figures

Part I

Prologue

Chapter 1

Introduction

This thesis research deals with the use of a non-invasive monitoring tool, an infrared camera, applied to the monitoring of freeze-drying (FD) processes. In this chapter, a brief introduction covering freeze-drying processes, its state of the art tools and techniques and current challenges is presented. This introduction serves to understand the thesis objectives, structure and discussed subjects in the following chapters.

1.1 Freeze-drying overview

The pharmaceutical industry has undertaken a profound renovation during the past years. Bioactive compounds have been gaining importance over chemically synthesised drugs [1]. Biopharmaceuticals offer several benefits, which can explain this shift. These benefits include: few side effects, highly effective and potent action, and the ability to treat previously untreatable diseases [2]. Furthermore, the Covid-19 pandemic highlighted the critical importance of having reliable ways to stabilize and store therapeutic products. The manufacturing process of pharmaceuticals must allow fast and affordable distribution of doses all around the world. Several of these active compounds are very unstable in solution, thus, stabilization through dehydration is often used.

Different drying technologies can be applied to pharmaceutical formulations depending on the characteristics of the active compounds. The objective is to remove the moisture without impairing the active ingredients, achieving a shelf-stable product with a reduced requirement for a cold supply chain. If the active compound is heat-resistant, high temperature drying processes may be used to achieve very stable products with low residual moisture content ($< 1\%$). Conventional air drying (using hot air at $\sim$330 to 380 K), spray drying (using hot air at $\sim$370 K), evaporation without atomization (using shelf temperature at $\sim$300 K) are some examples of such processes [3]. Withal, many active ingredients lose their drug

activity when processed under the high temperatures used in conventional drying processes [2]. Some drying technologies operate close to room temperature (∼290 - 300 K) but yield products with a sightly higher moisture content ($> 1\%$ and $< 3\%$) and diminished reconstitution when administering the product. Foam drying, microwave vacuum drying and supercritical fluid drying are examples of such drying processes [4]. Finally, the drying of pharmaceuticals can be achieved using sub-zero temperatures through freeze-drying processes and yielding final products with very low residual moisture ($< 1\%$) and great reconstitution properties.

Freeze-drying is a dehydration technique performed at low temperatures, which makes it suitable for heat-sensitive compounds [5]. It can increase the product's shelf life while maintaining its biological activity. It is a sophisticated drying process capable of producing shelf-stable products while preserving active compounds, and product characteristics [6]. This low-temperature drying technology is applied mainly to pharmaceutical products. In the food industry, freeze-drying applications have increased as nutritional and sensory characteristics become more valuable to the consumers. The freeze-drying equipment market had a value of 4.9 billion dollars in 2020 with a Compound Annual Growth Rate (CAGR) of 8.2% until 2025. In 2025, this market is expected to reach a 7.3 billion dollars in value. Estimates based on equipment uses found that roughly 34% of the FD market is destined to the food and packaging segment followed by pharmaceutical and biotechnology with 30%. Multiple key biologics will lose their patent in the following years, which is expected to provoke yet an increase in the freeze-drying market [1].

When it comes to product sales, pharmaceuticals hold a higher financial value. By 2024, global prescription drug sales are expected to reach 1.18 trillion US dollars, with biotech products reaching nearly a 50% share of the top 100 pharmaceutical products being sold [7]. These estimates show the economic relevance and growth projections for the freeze-drying industry.

The freezing drying process itself - also called lyophilization - is divided into three well-defined steps:

1. Freezing,
2. Primary drying,
3. Secondary drying.

Freeze-drying is based on the sublimation of the solvent, typically water, which occurs at temperature and pressure conditions below the triple point of the solvent. The essence of the process is depicted in Figure 1.1 where the path from liquid to the solid-state (frozen solvent, in this case, water) takes place to allow solvent removal through sublimation at low temperatures.

A schematic of a freeze-drying equipment is shown in Figure 1.2. The heating/cooling shelves are located in the drying chamber. The shelves usually have

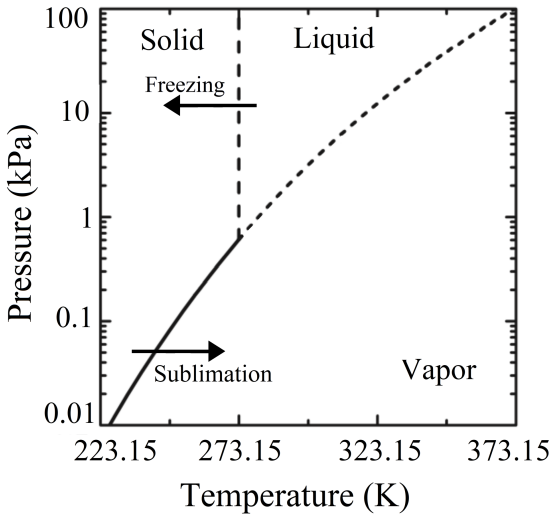

Figure 1.1: Water phase diagram evidencing the phase changes that take place in a lyophilization process. Adapted from [8]

a wide range of operating temperatures, typically from 210 K to 340 K. They are able to cool the product to freeze it and to supply heat to the product during primary drying. The vacuum pump will reduce the chamber pressure which will decrease the vapor pressure. This will drive sublimation of the frozen solvent. The sublimated solvent flows towards the condenser because of the pressure drop produced by the vacuum pump in that direction. The condenser is at a much lower temperature than the product, usually around 190 - 210 K, to be able to trap the sublimated solvent even at a very low pressure. If the Isolation valve (ISO valve) is closed, no vapor can flow from the drying chamber to the condenser. This is used in some applications, as it will be explained in Subsections 1.2.1 and 1.2.2. In the end of a freeze-drying cycle, the trapped solvent may be removed from the condenser once it melts and discarded [9].

In typical a industrial process, the pharmaceutical solution is prepared and inserted in vials, which are then loaded onto the freeze-dryer shelves [10]. Freezing is the first step of a freeze-drying process and it can be done in many ways. The most utilized method is shelf-ramp freezing, where the inner fluid of the shelves is cooled to remove heat from the product in the vials [11]. Once the product is frozen, primary drying can take place. The pressure of the chamber is reduced and heat is supplied to the frozen product, usually through the shelves, to promote sublimation of the frozen solvent. Afterward, the shelf temperature is further increased to facilitate the removal of the remaining solvent, linked to the product structure, in a step called secondary drying [10]. The dried product structure after freeze-drying is also called cake.

Although freeze-drying is usually done using trays as described above,

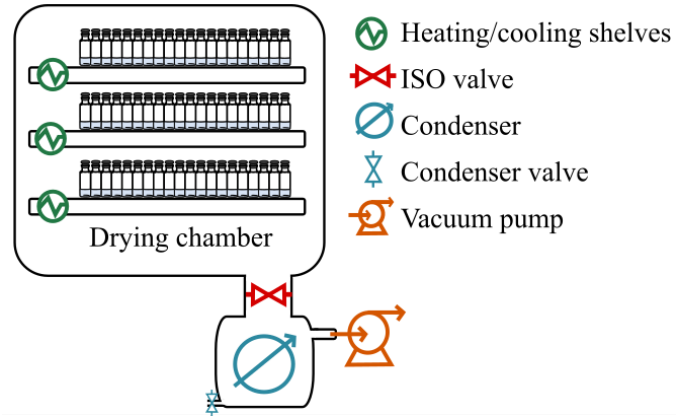

Figure 1.2: Simplified schematic of a freeze-drying equipment main parts (not to scale).

this process can be done through other methods or have modifications in one or more steps. Freezing can be done using liquid nitrogen in spray freeze-drying applications [12]. Also, using liquid nitrogen, a spin-freezing technique has been recently proposed as a way to increase product surface area and improve drying times [13]. Alternatively, freezing can be done using shelf ramp but introducing control methods such as annealing [14], Vacuum Induced Surface Freezing (VISF) [11], ice-fog technique [15] or ultrasonic vibrations [16] as it will be described in detail later in this work. Additionally, primary drying may be assisted by other methods such as ultrasonic waves [17] to increase the sublimation rate, although this is usually only applied to food products and not pharmaceutical solutions.

Freeze-drying also has its limitations. The physical state of a formulation, i.e., whether it has a crystalline or amorphous structure, is critical to determine its stability as a solid. Freeze-drying may not be feasible if the amorphous fraction of the cake structure is not able to stabilize the active compounds. On the other hand, crystalline solutes often are used to ensure a good cake structure. This structure is useful to ensure good reconstitution properties when administering the product. If the product lacks cake forming agents, the cake will collapse, potentially exposing the active compounds to degradation an impairing its drug reconstitution features.

Additionally, freeze-drying is an expensive and low-efficiency process in terms of capital cost and operating expenses. Consequently, it is crucial to develop processing conditions that maximize efficiency [18]. Lean manufacturing and continuous freeze-drying methods, such as spray freeze-drying or continuous vial freeze-drying [19], are expected to have a larger market share in the upcoming years because they may present a higher production efficiency. This is the case when a continuous process is capable of increasing the production rate per time, thus diluting the capital and operational costs in larger production outputs. Additionally, adequate process design according to the product's characteristics, optimization,

and control are required. Figure 1.3 shows an example of a typical freeze-dried solution in a vial from this research work.

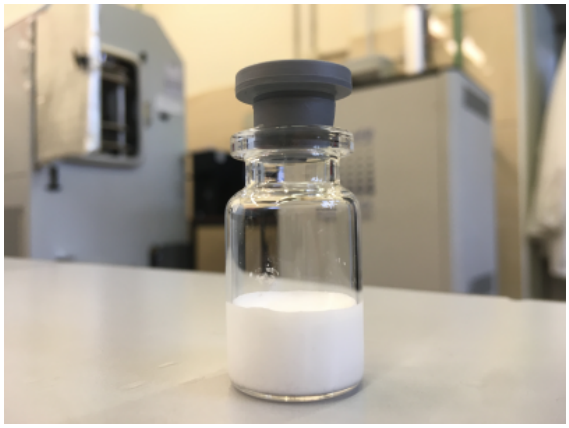

Figure 1.3: Freeze-dried product from this research.

Ensuring product quality is as crucial for lyophilized products as it is for pharmaceuticals in general. In the past, product quality was ensured through sampling and testing of the finished product, based on statistical quality control methods [20]. In 2004 the US Food and Drug Administration (FDA) issued the "Guidance for Industry Pocess Analytical Technology (PAT)" [21]. These guidelines prescribed that pharmaceutical processes must be designed to ensure product quality by design, and the products no longer need testing at the end of manufacturing. Thus, quality must be achieved by design, which must be built-in. To achieve *Quality by Design (QbD)*, suitable PAT tools must be used [22]. Hence, systems for designing, monitoring, and controlling a process must be implemented to guarantee product quality.

Representative process monitoring of a batch is a difficult task because the vials in a batch do not necessarily present homogeneous characteristics [23]. As it will be discussed in more detail in Subsection 1.2, the freezing process will define how the ice crystals will be formed, which in turn defines product cake. The cake structure will determine the drying duration and product temperature. Meanwhile, freezing is a highly stochastic phenomenon which increases the heterogeneity in a batch. Additionally, the vials are not subjected to the same heat exchange conditions during drying. Edge vials exchange heat through radiation with the drying chamber walls, while central vials are shielded from the sides by the neighboring vials [24]. All these factors increase batch heterogeneity and present significant challenges to both process monitoring and control.

Besides implementing the best current Good Manufacturing Practices (cGMP), some process parameters are essential to ensure product quality [25]. During freezing, temperature monitoring is important to determine the nucleation temperature in case controlled nucleation is used [14]. Additionally, it is important

to ensure the freezing of the solution. According to the formulation's characteristics, a temperature threshold value must not be surpassed during primary drying until all "free" solvent is removed. The frozen product structure may collapse if these threshold temperatures are reached [26]. Meanwhile, operating at the highest possible temperatures is desired because this will promote sublimation and make the process much faster. On top of that, process design must take into account the equipment's characteristics and limitations. If sublimation is extremely fast, choking may happen, jeopardizing pressure control during the process [27] leading to longer drying times. Hence, accurate product monitoring is vital for efficient and effective manufacturing.

1.2 Current trends in freeze-drying processes

Historically, much effort was put into researching and optimizing the primary drying step. The sublimation process is typically the longest one of the three stages and thus represents the more significant portion of operational costs in terms of energy, equipment use and personnel. An economic evaluation of the freeze-drying process found that the most expensive aspect of implementing freeze-drying in a facility is the initial capital cost of the equipment [28]. This perspective pushes forward initiatives to reduce the freeze-drying cycle duration. This reduction in duration intends to fit as many cycles as possible into a working year and extract as much value as possible to mitigate the substantial initial investment of new equipment. In the end, the ultimate goal of freeze-drying processes is to deliver high-quality products at affordable prices to the end consumer. This way, all efforts are always towards optimizing the freeze-drying cycles in terms of product quality and overall process costs. Some trending topics gained attention as they play a significant role in freeze-drying processes, whether for product quality or process costs. These trending topics are:

- the impacts of freezing on batch heterogeneity, the overall product quality, cake morphology, and on the sublimation rate during the primary drying step,
- robust monitoring systems for *in process* product quality assurance,
- fast and reliable process design methods and tools, i.e., determining the best operating conditions for a certain product to be produced and commercialized as fast as possible.

Regarding the impacts of freezing, many research articles explore freezing effects on lyophilized products [29–33]. The size and homogeneity of the resulting ice crystals will vary according to the heat exchange characteristics during freezing, the freezing rate, and nucleation temperature. Based on the ice crystal sizes formed, the porous structure of the product will be defined and hence influence the kinetics

of primary and secondary drying kinetics [14, 15] and even drug activity may be altered [34]. In summary, the freezing conditions directly affect the morphology and quality attributes of the final product. Thus, the freezing step needs to be studied further.

New technologies for the continuous production of lyophilized products [2, 19], new personalized drugs [35] and new dosage forms [36], plus the new strict requirements on product quality and standardization [37] drive the need for process design and monitoring. Modern pharmaceutical manufacturing is moving in the direction of assuring a robust QbD, PAT, Performance, Quality and Safety (PQS), and Real Time Release Testing (RTRT) to guarantee the quality of final products. In this perspective, monitoring tools are more important than ever. Most monitoring systems are capable of giving only localized product information or a mean parameter. Each monitoring system offers its advantages and disadvantages. The first type offers detailed information, but that is the only representative of a single vial or batch position. In contrast, the second offers average information regarding the whole batch but cannot offer in-depth information considering the batch heterogeneity. Thus, for monitoring robustness, the use of combined motoring systems is recommended.

Besides ensuring quality through adequate product monitoring, the process design should guarantee the targeted product quality standards. For this to be done, the Design Space (design space (DS)) has to be delimited. The DS is simply the set of freeze-drying operating conditions that will result in a product following the required quality parameters. There are different methods in place to determine the DS. However, many are still quite laborious, and new, faster methodologies should be developed. These observed trends that are pertinent to the development of the present research thesis are further discussed in Subsection 1.2.2.

1.2.1 Freezing impacts on process and product quality

In recent years, the freezing step has been studied in detail. This new research focus is due to the major influence of the freezing process on the product structure [14, 32, 38] and on the drug residual activity [34, 39].

The freezing process first involves the cooling of the solution to promote the formation of the first ice nuclei, called nucleation and subsequently the ice crystal growth. Although freezing may be thermodynamically favoured when the solution reaches its freezing point, the ice nucleation process is stochastic and does not take place immediately. Instead, the solution is cooled below its freezing equilibrium temperature and enters a meta-stable supercooled state. The greater the supercooling degree, i.e., temperature degrees below the actual equilibrium freezing temperature, the greater the probability of nucleation taking place. During the formation of the first nuclei, part of the solution freezes instantly, releasing energy and increasing the system's temperature to its equilibrium temperature [40].

This first nucleation event is called primary nucleation and is the highly

stochastic one. Practically, this nucleation is heterogeneous because the formulation has different ingredients and the solution is in contact with the glass wall of the vial, thus, the first nuclei generally initiate close to the surface of the system. After this first nucleation event, secondary nucleation may happen, producing more casts for ice crystals to grow. Secondary nucleation is the birth of new crystals in the presence of parent crystals of the same substance. However, the inference of this phenomenon's kinetics is complicated to be described [41]. Its kinetics is complex because it is affected by the creation of new frozen surfaces over time. Additionally, it usually has a modest impact on the final ice crystals formed since it strongly depends on the primary nucleation event, thus it is often ignored in the literature [16, 42–44]. The size increase of the ice crystals being formed is called crystal growth. Figure 1.4 shows a schematic of the freezing process observed in vials with pharmaceutical solutions. While nucleation at lower temperatures results in more ice nuclei than at higher temperatures, the molecular diffusion is also affected by the temperature of the solution. Lower temperatures are associated with lower rate of movement. This molecular movement is required for the ice crystal growth.

The ice crystals formed during freezing are the casts of the porous structure of freeze-dried products. The number and size of the ice crystals depend strongly on the temperature at which nucleation takes place. When nucleation occurs at low temperatures, a vast number of small nuclei form. On the other hand, when using higher temperatures, fewer nuclei are obtained [14]. From the nuclei cast, the ice crystals begin to grow at a specific rate and cause freeze concentration of the solution, producing crystalline or amorphous solids, or mixtures of them. There is limited space in terms of "freezable" water in the solution for the ice crystals to be formed. This way, when low nucleation temperatures are used, resulting in many ice crystals, the final crystals formed are many but smaller in size. On the other hand, fewer nuclei are formed when higher nucleation temperatures are used, growing and creating larger ice crystals.

The way the ice crystals are cast deeply influences product quality, batch homogeneity, and drying kinetics during primary drying. Below, a more detailed description of the impacts of freezing in freeze-drying processes is provided, from increasing scale order:

Drug activity From a drug activity perspective, forming an ice−water interface is a critical destabilization factor for proteins. The ice surface formed affects protein folding in an intricate process that the use of cryo−protectants may offset. As a general rule, protein stability is improved when interactions with different surfaces, such as the ice crystal ones, are avoided. Using low cooling rates and a high nucleation temperatures is associated with larger ice crystals and, therefore, smaller ice-freeze concentrate surface area. This smaller interface area, in turn, should minimize the ice-induced denaturation of proteins. In line with these considerations, a correlation has often been

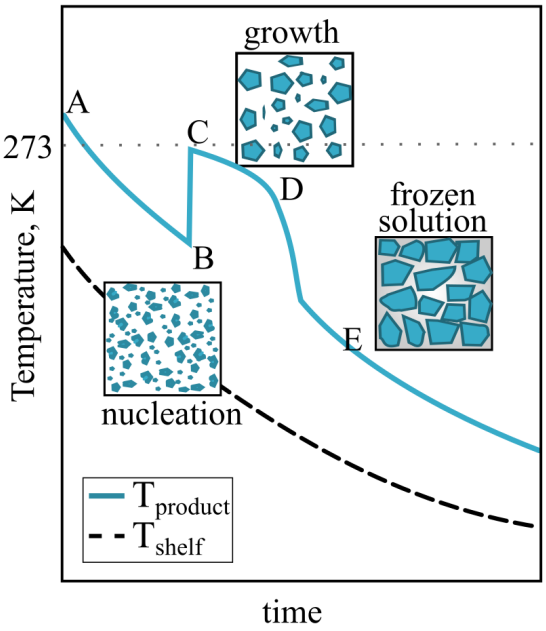

Figure 1.4: Schematic graph showing the events of ice nucleation (B-C) and crystal growth (C-D) until the liquid solution (A) is frozen (E).

observed between cooling rate and protein stability, with higher recovery at lower cooling rates [45, 46].

Product morphology The ice crystals morphology provide an initial template for the porosity of the dried cake. This happens because, once the ice is removed, the ice crystals leave behind the product's porous structure. Smaller crystals will create a fine porous structure with a large surface area for solubilization. Larger ice crystals, in turn, will leave large pores and consequently a smaller surface area of dried product − air. Additionally, in some circumstances, such as high filling height or other conditions that cause a high temperate gradient in the product during nucleation, intra−vial variability will be enhanced.

Sublimation rate during primary drying As the ice crystals formed sublimate during primary drying, they leave behind the porous structure of the dried cake. Hence, the ice formed has a profound influence on the primary drying stage from an operational perspective. When the freeze-drying process is carried out using vials on a heating shelf, sublimation occurs from the top of the product cake towards the bottom. Thus, the resistance to the vapor mass transport imposed by the dried cake (R_p) correlates with the distribution of the pores' size, sculpted by the ice crystals. In turn, the R_p affects the primary drying phase in terms of duration and maximum temperature reached by the product [47, 48]. Small pores will pose more resistance to the vapor flow while

larger ones will pose less resistance. Suppose the resulting porous matrix offers too much resistance to the vapor flow. In that case, the vapor pressure at the ice interface increases in order to allow sublimation to continue. As a consequence of this increased vapor pressure, there is an associated increase in the product temperature. This temperature increase could jeopardize product quality and drug activity. Thus, larger pores and a smaller dried cake surface area are better suited to the primary drying sublimation process.

Water-removal during secondary drying The desorption rate is correlated to the thickness of the wall of the interstitial matrix and its surface area. Hence, conversely to primary drying, a larger surface area improves secondary drying performance since the main mechanism of water removal in the secondary drying phase is the desorption from the solid matrix. [49].

Batch homogeneity Most batch heterogeneity is connected to the stochastic nature of nucleation. In cGMP conditions, supercooling may range up to 30 K or more [48, 50]. Freezing affects the vial-to-vial variability in the product structure, which affects the sublimation rate, the final residual moisture, and the drug activity.

Nucleation is a highly stochastic phenomenon, thus, the solution in each vial nucleates at different times during the freezing stage. Because freezing is many times performed by cooling the shelves using a constant cooling rate, each vial nucleates at a different temperature. This way, much of product variability in a batch comes from having the product nucleate at different temperatures. While the cooling rate can easily be controlled and adjusted, the nucleation temperature is an uncertain variable. Several strategies have been developed to address this problem by implementing controlled freezing techniques. These techniques have gained popularity in the freeze-drying field recently aiming to improve batch homogeneity and overall product quality [51]. Thus, the freezing phenomena and its impacts product morphology must be further studied.

Commonly employed freezing methods

Shelf-ramp based methods

The most common freezing method employed industrially is the shelf-ramped freezing method. When using this method alone, nucleation is spontaneous, thus stochastic, leading to batch heterogeneity. For this method, the filled vials are placed onto the freeze-dryer shelves, and then the shelf temperature is decreased linearly with time. Cooling rates typically range from 0.1 K/min up to 5 K/min, depending on the capacity of the freeze-dryer. The time for complete solidification generally depends on the filling volume but usually ranges from 2 to 5 hours [52].

A modification of this method is the two-step freezing which achieves a more homogeneous supercooling across the total filling volume of the vial. In this technique, the vials are cooled until a supercooling plateau temperature (between 263 and 268 K) and held for a period from 30 minutes to several hours. After this holding period, the shelf temperature is decreased for further freezing, and a relatively homogeneous ice formation is observed. The ice crystal growth occurs speedily when shelf-ramp freezing is used. Thus, when this technique is used, the ice nucleation cannot directly be controlled and is therefore quite random [53].

Annealing

Besides the above-listed modifications, the introduction of an annealing step was also studied by different authors [54, 55]. The objective of this technique is to improve the cake morphology and batch homogeneity. A hold step above the glass transition temperature is added during the freezing stage to perform annealing. This enhances molecular mobility and larger ice crystals are formed at the expense of smaller ones, a phenomenon referred to as Ostwald ripening [15]. Thus, annealing minimizes the differences in pore size and drying rate caused by different degrees of super-cooling. This extra step reduces inter-vial heterogeneity and increases drying rates. A proposed method increases product temperature 10 – 20 K above glass transition temperature after the final freezing shelf temperature is reached for products containing crystalline and amorphous excipients. This holding temperature should still be well below eutectic melting temperature and held for several hours [50].

Pre-cooled shelves

Another shelf-based method is based on the use of pre-cooled shelves. In this case, the vials are placed on a shelf that has already been cooled to the desired value for shelf temperature - typically around 233 K. This achieves higher nucleation temperatures (263 K) compared to the conventional shelf-ramped freezing (259 K) [14, 38] although they present widely distributed nucleation temperatures [14].

Gap freezing

In gap freezing, vials are placed and cooled in a stainless tray, with a particular gap from the shelf. This gap significantly eliminates conductive heat transfer from the shelf to the vial bottom. This modification makes the freezing process slower but may improve intra-vial homogeneity. This freezing approach reduces the lyophilization cycle time by promoting a nearly isothermal freezing [56]. In this present thesis, a modification of this technique is used and investigated in the form of suspended vial configuration, called OFF-shelf configuration in Chapters 5 and 6.

Quench freezing

For quench freezing, samples are first cooled and equilibrated at a temperature below the equilibrium freezing temperature, e.g. at 268 K, and kept for several minutes. Then, the temperature of cryogenic liquid nitrogen is rapidly decreased to 195 K in a couple of minutes. This results in a fast temperature drop in the vials to 263 K followed by uniform ice nucleation [52]. Quench freezing is characterized by a fast cooling and fast freezing. The former tends to stabilize metastable states by retaining greater quantities of unfrozen water. The later tends to promote a finer subdivision of the ice. It has also been reported that quench freezing results in a directional freezing [57] although there are no literature reports on temperature quench freezing used in lyophilization [52].

Spin freezing

Spin-freezing consists of rotating the vials with the solution around their longitudinal axis while, at the same time, immersing them in a cryogenic fluid or a dry ice bath. The product is spread around the vial wall, forming a 1-5 mm thick cylindrical shell [13]. The main advantage of this method is the sublimation rate increase during primary drying due to the higher surface area formed compared to traditionally frozen products. However, there is little flexibility in the freezing protocol and poor control of the freezing process.

Methods to induce ice nucleation

Several requirements should be ideally fulfilled when inducing ice nucleation for freeze-drying processes. The first is the success of nucleation, which refers to the ability to induce ice nucleation in supercooled solutions. Robustness and controllability are essential too. Ice nucleation should ideally be done in a reproducible and controllable way, and nucleation should take place in all vials at the *same* time. Additionally, ice nucleation should occur instantaneously to ensure homogeneity in product temperature during nucleation. The method must be scalable to allow its use in the research and development level and industrial production set-ups. An ideal method should ensure a target product temperature before ice nucleation to manipulate the T_n and not just a specific time after cooling begins. Finally, product quality must not negatively affected by the method of choice. Last but not least, sterility and aseptic conditions must be maintained throughout the nucleation process [52].

Pressure change based methods

Some freezing methods induce nucleation at the desired temperature by subjecting the solution to a pressure change. A relative pressure lowering can induce nucleation while holding the vials with the solution at a desired T_n. In the VISF technique, vials are cooled and held at a desired T_n, and then chamber pressure

is reduced. This pressure reduction causes the water on the solution surface to evaporate, causing a dramatic cooling of the product surface. This dramatic cooling induces nucleation of the solution's top surface, which then induces nucleation in the rest of the vial at the set T_n and consequent freezing [11, 53]. This method is further explored and investigated in Chapters 5 and 6.

A similar technique is called high-pressure shift or depressurization freezing. It induces nucleation instantaneously through pressure reduction. This pressure drop is applied to vials already cooled to the desired nucleation temperature held at an initially elevated pressure. The concept is the same as in VISF, but subjecting the solution to a less dramatic pressure drop [48, 57]. Their advantage is that they do not require any modification of the freeze-drying equipment to be implemented, as long as the equipment has an ISO valve, i.e., a valve between the condenser and the drying chamber (as shown in Figure 1.2. The disadvantage is that if done for too long, it can cause the cake to float by suction in the vial, and the vacuum can cause a inelegant cake appearance due to boiling, especially for high fill volumes. This was previously reported [53, 58] and it is the case for a few reasons. First, high fill volumes will result in a large temperature gradient. This gradient results in less viscous solutions (smaller frozen fraction) after nucleation than when lower fill volumes are used because not all the solution nucleated satisfactorily. Meanwhile, nucleation is not induced in all vials at the same time. The vials that already nucleated are subjected to a very low pressure while the partially frozen cake is not well formed. This causes bubbling of the unfrozen, less viscous, part of the solution, resulting in very inelegant frozen cakes.

Ice cast introduction based methods

The easiest and most intuitive procedure to induce ice nucleation of supercooled solutions is by introducing ice crystals as seeds. This introduction can be done after holding the product at the desired T_n. Nitrogen gas, at marginally raised pressure, is carried through copper coils submersed in liquid nitrogen, chilling the gas stream to temperatures lower than 233 K. Subsequently, the gas enters the chamber, cooling the present water vapor and turning it into ice crystals. This gas enters the chamber at a slightly higher pressure, allowing the ice crystals to pass into the pre-cooled vials, inducing ice nucleation. The primary issue with this technique is the possibility of introducing external particles into the solutions through the ice fog formed, thus cGMP may be compromised [15]. To avoid this and improve nucleation homogeneity throughout the batch, modifications of this technique using sterile water vapor and liquid nitrogen have been proposed, but require more elaborated equipment and controls [52, 59].

In a more direct method, ice crystals are created from a condensed frost created on the internal surface of a condenser compartment. This compartment is separate from the product chamber and connected by a vapor port and may be used to induce nucleation. In this technique, ice crystals are injected into cold vials

as nucleating seeds. Still, it can be expensive and less effective at an industrial scale and it still needs more research to be conducted [60].

Reverberation-based methods

Finally, some methods induce nucleation by forcing the supercooled solution to nucleate by an external disturbance. Ultrasound-powered freezing is a promising technique that induces instant nucleation by applying ultrasound power after vials are cooled to the desired nucleation temperature. Thus, the T_n can be chosen to be the most suitable for the product. However, the intense vibration creates particulate matter and thus inserts a sterility concern. Additionally, it is not easy to scale up and optimize the process using this technique [57, 61].

In the electrofreezing technique, nucleation is induced by applying electric pulses after cooling the vials to the desired nucleation temperature. This technique was developed after observing that applying electric pulses to solutions increased their nucleation temperature [62].

In summary, there are many different freezing methods and modifications to attempt to control the freezing process of pharmaceutical solutions, each presenting its advantages and disadvantages. The best approach will depend on the product requirements, available equipment, and budgetary matters.

Ice crystal prediction models for pharmaceutical solutions

Modeling the freezing process may be used to better understand it from a mathematical perspective. Many research articles deal with the definition of mathematical models to estimate the size of the crystals formed at the end of a solidification process. A fundamental model is the one presented by Bald [44] in which the crystal size is considered to be proportional to the rate of temperature change in the system. Other proposed models assume the velocity of the solidification front and the temperature gradient in the frozen fraction of the product as driving factors to determine the size of the crystals formed. This concept was successfully applied to model the solidification of metal samples at low rates [63], the solidification of metal alloys at high rates [64] the freezing of apples [65], the freezing of starch gels [66] and of gelatin [67].

In an attempt to describe the freezing of pharmaceutical solutions according to the freezing conditions, Nakagawa et al. [31] presented an empirical model based on the solidification front rate and the temperature gradient as determining factors. It was successfully applied to predict the resulting pore sizes of frozen pharmaceutical solutions. Later, Arsiccio et al. proposed a new model, more physically grounded but also reliant on the solidification front rate and the temperature gradient parameters for ice crystal size estimation [43].

Phase-field models to describe the growth of ice crystals and the dynamics of freeze concentration were also proposed in the literature. These models take into

account the field approximation of solute concentration and the underlying heat, mass, and momentum transport phenomena [68, 69]

Colucci et al. [29] presented a mechanistic model using supersaturation as the driving force for ice nucleation and crystal growth. Vuist et al. also proposed a model for ice growth, taking into account the inclusion behavior of sucrose and proteins. Vuist's approach was aimed at freeze concentration applications but may also be applied to freezing in freeze-drying processes [70]. Freezing models can predict temperature profiles during freezing and the resulting ice crystal sizes. Then mathematical descriptions of the drying phase of freeze-drying can be combined with the results of freezing models. With this information, a broad characterization of the lyophilization process may be outlined for process design [71]. Nonetheless, all these models are based on heat and mass transfer assumptions, not from direct experimental observation. Further investigation is needed regarding the in-line application of these models based on real-time data to determine the best operating conditions to achieve QbD.

1.2.2 Monitoring tools for freeze-drying processes

The main goal of freeze-drying processes is to achieve the desired residual moisture in the final product. Additionally, the solvent removal rate should be optimized to maximize plant productivity in order to reduce the cost of the product. It is thus necessary to identify the primary drying stage's end point and the freeze-drying process's end point to ensure the desired final moisture content. It is required to understand when the ice sublimation is completed because product temperature is further increased in the secondary drying stage. If this temperature increase is premature, cake collapse from ice melting may occur. Thus, monitoring tools and methodologies are needed. Different types of sensors to monitor the freeze-drying process are available and have been described in the literature [72, 73].

In most industrial applications, the pharmaceutical solutions are placed inside vials loaded onto the freeze-drying shelves. After the freezing step, they receive heat for sublimation from the shelf. Under these conditions, the sublimation process is mainly unidirectional, i.e., a sublimation interface is formed during drying, moving from the top of the product cake to the bottom. Water removal in freeze-drying is different from conventional drying techniques, in which the product matrix is much less rigid since no freezing is done. Figure 1.5 schematically shows the differences between the water removal step during freeze-drying primary and secondary drying steps and conventional drying. During sublimation, the heat supplied to the product is mainly used for phase-change; thus, the product temperature remains constant. When the frozen water is removed, the heat supplied is used as sensible heat, increasing the product temperature.

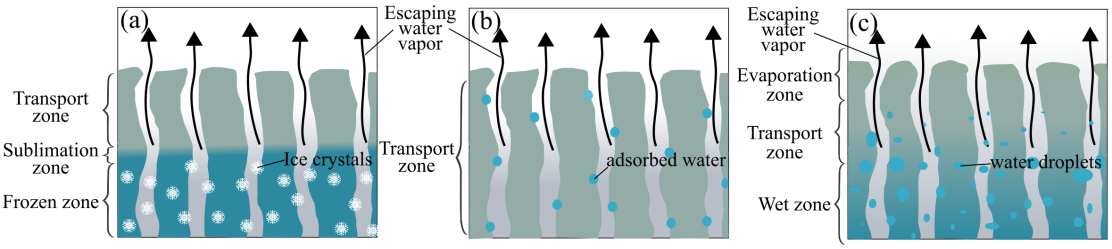

Figure 1.5: Schematic of the water-removal process in (a) the primary drying step (b) and the secondary drying step of a freeze-drying process and (c) during conventional drying.

Direct product temperature measurement

Product temperature can be readily monitored through a temperature-sensing device. Probes such as thermocouples or Resistance Thermal Detectors (RTD)s inserted into the vial, in contact with the product, are the most widely used. However, other types of instruments have been recently proposed. Thermocouples are the most common temperature assessment tool used in lab-scale applications. RTDs are extensively used in industrial-scale freeze-dryers because they can be sterilized and are durable [74]. Other methods such as Temperature Remote Interrogation Systems (TEMPRIS), Optical Fiber Sensor (OFS), and Thin-film thermocouples (TFTC) have been studied and proposed. The TEMPRIS systems do not require wire connections to be used; they are passive transponders that receive energy from an electromagnetic field [75]. However, the probe itself is huge relative to the vial size. Vials typically have diameters from 1.6 cm to 3 cm while thermocouples have diameters ranging from 0.02 to 0.6 cm. Thus, its insertion inside the vial for temperature measurement may alter the fill volume. Altering the fill volume increases proportion of the surface area subjected to radiation relative to the solution volume. Hence, heat-exchange in these vials will be different than in non-monitored vials, negatively affecting batch representativeness. The OFS were found to present higher sensitivity and faster response compared to TCs [76]. The TFTCs could be placed along the vial wall in an array. The array of thin-film thermocouples could measure the product's temperature profile and could also measure the position of the interface of sublimation within the array's resolution [77].

For invasive sensors such as thermocouples, TEMPRIS and RTDs, adequate representation of the product can be compromised. Invasive sensors are destructive because they damage the product cake and the sensor insertion may bring contamination issues to the monitored vial. Thus, monitored vials are typically discarded. Besides being destructive, the sensor's presence inside the vial affects product dynamics [78]. Moreover, it is often impossible to ensure product monitoring until primary drying is over as, many times, the thermocouple-based

profiles rise before the endpoint is reached [79]. There is an important point to take into consideration regarding the size of the sensing tip. Smaller sensors are usually easily placed inside the vial, thus having fewer issues of malpositioning. However, they offer only a local measurement of the temperature that may not represent the process. Larger sensors, on the other hand, better represent the thermal profile of the vial, but present challenges regarding their proper placement inside the vial [72].

The temperature measurement can also be used to determine the end of primary drying. During sublimation, the heat being supplied to promote sublimation is being used as latent heat for the phase change from solid to vapor. When the frozen solvent is removed, the heat being supplied is used as sensible heat, and the product temperature rises. This way, in theory, the product temperature profile should present a rise when sublimation is over, indication the end of primary drying. However, in practice this is not so straightforward. For invasive sensors, cake breakage and sensor bad positioning (not in the point with the last fraction of ice) result in temperature profiles rising before all ice is removed. Thus, typical invasive temperature monitoring profiles exhibit a rise in their profiles slightly before sublimation is actually over [79].

Meanwhile, the proposed non-invasive sensors have their own set of limitations. The TFTC, for instance, are as laborious to be placed in the vials as thermocouples. Additionally, this type of sensor is in direct contact with the vial, shielding a large surface area of the vial. This surface covering, of course, affects heat radiation effects on that vial and thus compromise batch representativeness.

Heat flux methods

Besides direct product temperature measurement tools, the heat flux can be used to monitor the lyophilization process and to determine the end of the primary drying [72]. Heat flux sensors can measure thermal events during freezing and product temperature during primary drying if the vial thermal conductivity is known [80]. Heat flux sensors are simple devices that can measure heat flux in discrete locations. They are composed of a thin-film differential thermopile that yields an electrical signal proportional to the total heat applied to the sensor's surface. When heat passes through the sensor, the sensor generates a voltage signal. This voltage signal is proportional to the heat passing through the sensor. A thermopile is an set of fifty to sixty thermocouples affixed in series inside a thin foil placed and connected directly to the freeze-dryer shelves. The vials are loaded over the thermopile, which thickness is only a few tenths of a millimeter. The signal is proportional to the heat flow per unit area, to the temperature difference and to the number of junctions in the thermopiles.

The measurement accuracy of heat flux sensors is optimized by proper installation and adequate coupling of the sensor to the materials surrounding it, paying attention to any prevailing thermal conditions on the system such as

convection currents [76]. Heat flux sensors could be used to monitor a lyophilization cycle by defining the drying time and were able to identify the nucleation event and end of crystal growth [80, 81]

An example of PAT based on this technology is the Accuflux^{TM} (Millrock Technology Inc., Kingston, NY, USA). This PAT measures the temperature difference between the two sides of the plate, i.e., the the top surface of the shelf and the side in contact with the vial. It is present in the MicroFD equipment, which is better discussed in Chapter 8, although the heat flux sensor was not used in this thesis research.

Methods based on the chamber gas composition

In freeze-drying processes, the sublimation flux and the chamber pressure control tool influence the gas composition in the chamber. During primary drying, the gas is mainly made of of water (or other solvents); however, when sublimation slows down, other gases predominate. Thus, direct monitoring of the gas composition in the chamber allows the detection of the endpoint of primary drying.

The ratio between the thermal conductivity and capacitance gauges signals ($\frac{Pi}{Ba}$) can be used to determine a representative value for primary drying duration. The Pirani (Pi) gauge determines the pressure based on the thermal conductivity through the gas of the system being monitored. Higher pressure systems will have greater frequency of collisions between the molecules, with a higher thermal conductivity, while at lower pressures, thermal energy will not be conducted efficiently. As a consequence, the gas composition and pressure will affect this measurement and this effect is used to help determine the end of sublimation. In the case of freeze-drying, the solvent vapor in the chamber's atmosphere causes an overestimation of the measured pressure by the thermal conductivity gauge. This happens because water vapor has a higher conductivity than dry air and nitrogen gas. The measurement by this sensor only becomes correct when the water vapor is removed from the chamber by the end primary drying. This way, the Pi signal profile exhibits a decreasing trend as the drying process is near to being completed (see Figure 1.6). The onset and the offset of this declining profile interval can be used to define the variability range of the drying time [26]. The capacitance gauge (Baratron, Ba) reads a *true* pressure value. It measures the pressure based on the state of its sensor membrane that is affected by the pressure of the measured system, but not by the gas composition. The Pi or $\frac{Pi}{Ba}$ method is broadly used to determine the end of primary drying, although it presents wide variability ranges between the onset and offset times. Nevertheless, this variation is technically correct since drying conditions, and thus the required time for drying to be completed across the batch, are non-uniform [23]. The batch presents heterogeneous drying conditions. A big contribution factor is the difference in heat exchange between edge and central vials. Edge vials are more exposed and thus subjected to increased radiation effects and

receive more heat during primary drying than central vials, which are shielded by the edge ones.

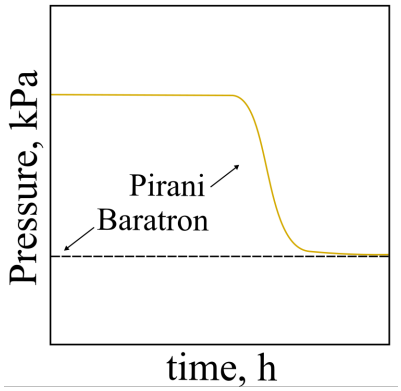

Figure 1.6: Illustrative example of the *Pi* and *Ba* signals during primary drying of a freeze-drying batch.

A dew point sensor is able measure the relative humidity, i.e., measures the water vapor content of air and, thus, the gas composition in the chamber. One type of dew point sensor exploits the capacity variation of a thin film of aluminum oxide caused by changes in the humidity. Another type is the chilled mirror hygrometers. They detect the dew point by cooling a reflective condensation surface until water begins to condense. The condensed fine water droplets are detected optically. Its sensitivity could detect less than 1% of vials in the batch having residual ice. The end time of primary drying measured by this sensor is typically significantly longer than the one found based on temperature measurement tools. These differences are related to the batch size, and being greatly affected by it [72].

Tuneable Diode Laser (TDLAS) is a widespread tool to determine primary drying endpoint [26]. Using the TDLAS is one of the proposed methods to measure the vapor flow rate generated through sublimation during primary drying. Installing the TDLAS sensor directly in the duct connecting the drying chamber and condenser was proposed in the literature [82]. The TDLAS emits a beam of diode laser radiation which, at a specified wavelength, is partially absorbed by water molecules. The amount of absorbed light then determines the number of water molecules per unit volume at the wavelength-specific water absorption. This way, this type of sensor can accurately estimate the mass flow rate of vapor through the duct. This information over time can then be used to estimate the mass of water removed through sublimation. With this information, the residual water content can be determined [83].

The cold plasma ionization device has a high sensitivity and it is also widely used [26]. It is based on inductively coupled plasma/optical emission spectroscopy. It creates cold plasma in a quartz tube under vacuum by radio frequency and the

light emitted by the plasma is specifically related to the gas present in the plasma. This way, a measure of the humidity can be obtained in real-time by assessing the optical spectrum. Some limitations of this method include the uncertainty on the final point determination, calibration issues, and dependence of the response on the probe location [84].

Pressure rise test methods

The Pressure Rise Test (PRT)s are a category of methods that have been proposed for the monitoring of primary and secondary drying dynamics. In the PRT, a step-change in the input is realized by creating a sudden change in the position (open/closed) of the ISO valve placed on the duct connecting the drying and condenser chambers. This ISO valve shift corresponds to a step-change in outflow, i.e., the vapor flow rate evacuated from the drying chamber. The drying chamber is isolated from the condenser, thus, no solvent vapor flows out of the drying chamber, increasing its pressure. The increase in pressure after the closure of the ISO valve is correlated to the vapor flow rate and, more specifically, to the speed of sublimation or desorption depending if the PRT is performed during primary or secondary drying.

The PRT approach estimates different process parameters by finding the best fit between the experimental pressure rise measured during the test and the predicted pressure increase based on mathematical models. It has been used with different algorithms which vary in complexity to make it more accurate, reliable, or straightforward to implement. To list some of them are the Pressure Rise Analysis (PRA) [85], the Manometric Temperature Measurement (MTM) [86], Dynamic Parameters Estimation Method (DPE) [5] and its more practical version DPE+ [87]. The PRT method requires some previous knowledge about the product and can be laborious to be practically implemented. Besides, they are indirect methods, and unforeseen process changes such as issues with chocked flow may affect the readings.

Near Infrared spectroscopy

Near Infrared Spectroscopy (NIR) monitoring is a non-invasive monitoring tool that has a deep penetration into the product (around 5 mm for 6% sucrose cakes) [88]. NIR wavelength absorptions are related to the chemical composition of the liquids being measured [89]. Correlating the correct wavelength peaks to the corresponding compound of interest, the concentration of the targeted compound can be determined employing NIR spectroscopy. NIR can be used to determine the end of primary drying and secondary drying by targeting water molecules. NIR spectroscopy has been proposed as a PAT tool for non-invasive in-line process monitoring of a freeze-drying process [90]. It may have some limitations during

the beginning of the drying process, being only capable of determining the residual moisture in the samples after a large portion of ice has already sublimated. Thus, it is better suited for monitoring the end of primary drying and the secondary drying step. Additionally, to effectively monitor the product the sensor probe needs to have sight of the monitored vial, only being suited for edge vials.

Infrared thermography

IR thermography was proposed as a monitoring tool [91] and even validated in proof of concept tests applied to freeze-drying processes [92, 93]. However, further investigation on practical applications for larger batches and additional studies are still needed to be able to implement this monitoring tool in industrial applications. This monitoring tool is described in detail and discussed in Part II because it is at the core the research presented in this thesis.

1.2.3 Design space determination methods

The Design Space is a critical element of QbD. The Design Space is the set of freeze-dryer operating conditions used for a particular product and batch configuration that will result in a final product with the expected quality standards, defined by design. The DS for primary drying needs to take into account the product temperature constraints for elegance and process costs. Additionally, it must establish the space beyond which the critical quality attributes are not maintained. Independent of the chosen approach, the objective is to gain an understanding of the process parameters on drug product quality from which to develop appropriate control strategy [94].

The optimization of the primary drying step is the industry focus, targeting product quality and reduction of process costs. On the one hand, progressing into secondary drying before all ice is removed would result in product melt back. This early progression would damage product quality. On the other hand, holding the product for too long in the primary drying stage after all ice has been already removed will result in unnecessary processing costs. The optimum point that ensures complete drying avoiding unnecessary processing time is the ultimate goal when calculating the DS for a product.

Because the process design space delimits a safe zone for the operating conditions, it helps discern if process deviations (like unexpected shelf temperature rise, change in the pressure) pose a real risk to product integrity. The product quality will not be affected if operating parameters are maintained within the specified design space. Thus, the DS significantly minimizes the number of process deviations that need to be handled due to variations in shelf temperature and chamber pressure from the set point during the process.

To obtain the K_v parameter, typically, gravimetric tests are performed.

These tests are performed based on weighting the vials before and after a truncated primary drying session to measure the mass of sublimated water. The energy to sublimate this mass of sublimated water is then computed based on the temperature profile of the product and the heating shelf [95]. With this information, the K_v can be obtained based on different heat and mass exchange models, as better explained in Section 7.2.1.

The mechanistic approach depends on the K_v and R_p parameter determination and to ensure a efficient process, the sublimation flux (J_w) should be optimized. Using the K_v and the product thermal profile, J_w and the resistance to the vapor flux (R_p) are determined. Because of the need for these parameters, the design space determination for a formulation may be a laborious task, even when using a mechanistic approach. Alternatively, K_v determination methods based on the heat flux or PRT may be used instead of gravimetric tests. However, they offer values that represent a batch, which typically has a non-negligible heterogeneity [81, 87]. This way, the design space based on these methods may fail to ensure product quality of edge vials, for instance, or may result in recommendations for excessively long drying times. Tools and new methodologies are welcomed to be investigated to reduce process development and optimization times.

Chapter 2

Scope of this thesis

In this work, the use of an infrared camera as a minimally invasive monitoring tool applied freeze-drying processes is further explored, verified, and validated. Several experiments testing the use of different batch sizes, batch configurations, and vial dimensions are investigated. Focus is given to the freezing, and primary drying stages deemed the most critical ones in terms of impact on product quality, process duration, and costs.

2.1 Research roadmap

To achieve the research aims, a detailed investigation roadmap was established (Figure 2.1), performed, and adjusted along the way, according to the results and observations found.

The following research objectives were set for this work:

I Sensor validation:

- Verify that the IR thermal profiles are accurate enough to be used to monitor freeze-drying batches.
- Determine if the presence of the IR camera inside the drying chamber affects batch dynamics.

II Monitoring the freezing stage:

- Further explore the freezing stage using IR monitoring since it is a non-invasive tool and could bring new insights from monitoring without interfering with the process kinetics.
- Test the applicability of the IR camera to monitor the whole axial temperature profile of vials subjected to VISF during freezing

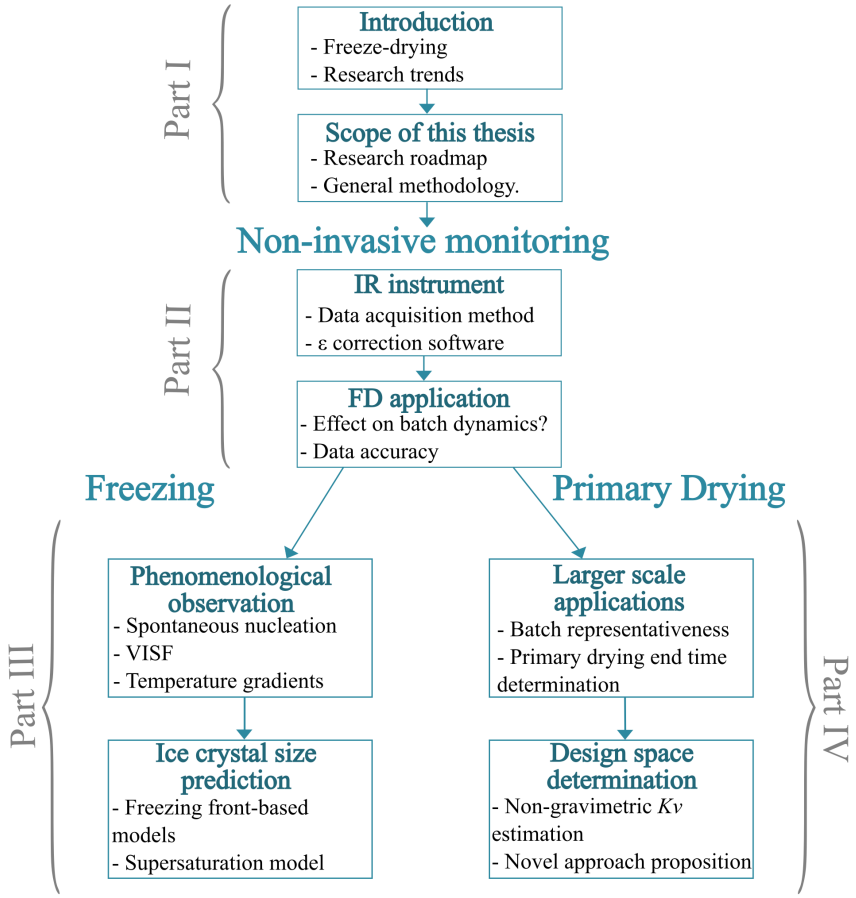

Figure 2.1: Flow of the topics covered in this thesis following a logical order for presenting and discussing them.

- Test the applicability of the IR camera to monitor and track the maximum axial temperature position of vials subjected to VISF during freezing.
- Determine if the IR camera was capable of discerning differences in the temperature gradients during freezing between suspended vials and vials placed directly on the chamber shelf.
- Test if the temperature profiles measured provide enough data to estimate the resulting cake structures using different freezing models.

III Monitoring the primary drying stage:

- Determine if infrared monitoring can be applied to batch freeze-drying processes with adequate batch representativeness despite its field o view limitation;
- Test the applicability of the IR camera to determine primary drying

duration through monitoring and tracking the minimum axial temperature position of vials during primary drying.

- Demonstrate the use of the IR sensor as an innovative tool for design space determination.

2.2 Relevance of research

Infrared monitoring is a powerful tool that has been under-explored for freezing-drying applications. An IR sensor such as the one used in this thorough investigation can provide a large amount of thermal data about the batch in real-time. This data, in turn, can help better understand heat transfer dynamics in detail. This better understanding is essential for freeze-drying performed on shelves because there is much inter-vial heterogeneity in heat and mass transfer. At the same time, quality must be assured for all vials, while the operating parameters must be set to ensure maximum efficiency. On the other hand, with the rise of continuous processes, temperature assessment will become a challenge since most temperature monitoring tools require direct contact with the product. This aspect will be a challenge for spray freeze-drying applications, for instance. Also, for continuous vial processes, IR monitoring may be the most practical temperature assessment tool available. Therefore, IR thermal monitoring must be further explored and pave the way for its application in industrial processes and even in future continuous applications.

During this academic work, the following original papers were published in peer-reviewed international journals directly related to this thesis research:

1. Harguindeguy M, Fissore D. Micro Freeze-Dryer and Infrared-Based PAT: Novel Tools for Primary Drying Design Space Determination of Freeze-Drying Processes. Pharm Research. 2021;38: 707-719. doi:10.1007/s11095-021-03021-x.

2. Harguindeguy M, Fissore D. Temperature/end point monitoring and modelling of a batch freeze-drying process using an infrared camera. Eur J Pharm Biopharm. 2021;158(January): 113-122. doi:10.1016/j.ejpb.2020.10.023.

3. Fissore D, Harguindeguy M, Ramirez DV, Thompson TN. Development of freeze-drying cycles for pharmaceutical products using a micro freeze-dryer. J Pharm Sci. 2020;109(1): 797-806. doi:10.1016/j.xphs.2019.10.053.

4. Harguindeguy M, Stratta L, Fissore D, Pisano R. Investigation of the Freezing Phenomenon in Vials Using an Infrared Camera. Pharmaceutics. 2021;13(1664): 1–22. doi: 10.3390/pharmaceutics13101664.

Additionally, other research articles were published in international peer-reviewed journals regarding initial experimental and theoretical work, getting acquainted, and exploring freeze-drying techniques monitored through infrared thermography.

1. Bobba S, Harguindeguy M, Colucci D, Fissore D. Diffuse interface model of the freeze-drying process of individually frozen products. Dry Technol. 2020;38(5-6): 758-774. doi:10.1080/07373937.2019.1710711.

2. Harguindeguy M, Fissore D. On the effects of freeze-drying processes on the nutritional properties of foodstuff: a review. Dry Technol. 2020;38(July): 846-868. doi:10.1080/07373937.2019.1599905.

3. Harguindeguy M, Bobba S, Colucci D, Fissore D. Effect of vacuum freeze-drying on the antioxidant properties of eggplants (Solanum melongena L.). Dry Technol. 2020;39(January): 3-18. doi:10.1080/07373937.2019.1699834.

2.3 General methodology

As explained above, the main objectives of this thesis are related to the verification, validation, and testing of a novel monitoring tool. Thus, in general, the experimental methodology is usually centered on comparing the results obtained using the IR sensor to other well-established tools or methods. The validation is usually done based on a direct comparison of experimental results or through the results obtained using *in silico* models.

In Chapter 4 the IR sensor accuracy and possible effects in batch dynamics are evaluated using average thermocouple measurements as a reference method. From this point on, the IR-based profiles are regarded as adequate for the proposed studies. In Chapter 5, these IR-based profiles are used to investigate the freezing phenomenon. Subsequently, in Chapter 6 these profiles are coupled with mathematical models to predict the ice crystal sizes. In Chapter 7 thermocouple measurements are seen again in comparison to IR-based ones. However, at this time, this is done to evaluate the batch representativeness of acIR measurements. the thermal profiles of edge vials and central vials in a batch are evaluated separately. Finally, in Chapter 8 all relevant thermal profiles are again IR-based, used to propose a novel methodology for design space determination. The final chapter contains the conclusions reached in this thesis work.

The experiments described in detail in the following chapters share many of the equipment, materials and general methods. Thus, a detailed description of them is given in Appendixes A, B and C and will be only briefly referenced in the main manuscript.

Part II

Towards the use of infrared thermography to monitor freeze-drying processes

Chapter 3

IR thermography

3.1 Historical grounding

Thermal imaging technology evolved in giant steps with intervals of hundreds of years. The first one was the discovery of infrared radiation in the early 1800s by Sir William Hershel while studying the sun's radiation [96, 97]. Then, in the 1900's Max Planck quantitatively described the laws of thermal radiation. The first infrared-detecting cameras were developed only after 50 years from this [97]. At first, these cameras were extremely bulky apparatus used by the military. Around the 1970s, smaller, more portable systems started to be available. These systems consisted of single photons detection systems cooled by liquid nitrogen [97]. They used a single detector and were also called infrared scanning radiometers. The two-dimensionality of the image was achieved by rotating or oscillating mirrors and refractive elements, such as prisms (see Figure 3.1). These elements optomechanically scanned the whole field of view, whether vertical or horizontal directions [96]. At this point, commercial applications of such systems were already possible despite the bulkiness.

Towards the end of the twentieth century, micro-system technologies had tremendous progress. This success allowed the development of the first uncooled microbolometer cameras in the 1990s. This new generation of infrared cameras granted reliable measuring systems. With that, only in the 2000s was the last giant step taken. Currently, infrared imaging is affordable to a vast public and is primarily utilized for industry, health, military, and space applications [98]. Also, infrared thermography has been applied for condition monitoring, i.e., monitoring a condition parameter in machinery to identify a significant change, usually for predictive maintenance. This was implemented in diverse fields, such as civil engineering, nuclear, aerospace, electronic engineering, food processing, to cite a few [99]. As for today, mass production of infrared detectors leads to reduced-price cameras, which may even become high-end consumer products for anyone interested [97].

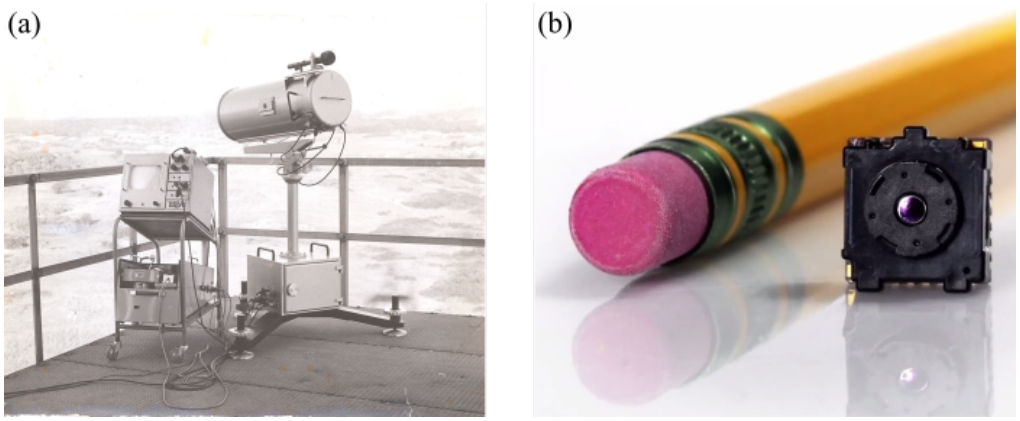

Figure 3.1: Old and new infrared cameras. (a) *TNO thermal imager* from 1960 and (b) current *Lepton WIR Micro Thermal Camera* module. *image sources: Museum Waalsdorp and www.flir.it, in order.*

Nowadays, two types of thermal imaging cameras are used. The high-performance cooled photon-counting cameras are the first type. The lower-cost uncooled cameras, based on microbolometers, are the second type. Most cooled cameras currently on the market use a sensor made from indium antimonide (InSb). These cameras work by counting energy photons in a specific frequency band, typically the mid-wave infrared band of about 3-5 μm. The photons hitting the pixels are converted into electrons which are accumulated in an integrating capacitor. Opening or closing the capacitor operates as a pixel shutter [100].

Uncooled thermal imaging cameras are cheaper, smaller, lighter. Additionally, they require less power than cooled infrared cameras. Uncooled thermal sensors have their pixels constituted of a material whose resistance changes markedly with temperature. The most frequently used materials for this application are Vanadium oxide (VOx) or Amorphous silicon (a-Si). The thermal energy is focused on the pixel while the pixel physically heats or cools. Because the pixel resistance varies with temperature, its value can be measured and redefined based on the subject's temperature through a calibration process. Furthermore, pixels have a finite mass, thus, they have a thermal time constant. The time constants found for modern microbolometer-based thermal imaging cameras are usually between 8-12 ms. However, they typically need five time constants to reach steady-state and generate a reliable thermal image [100]. The IR sensor used in this present thesis is an uncooled VOx microbolometer as it will be described in more detail in Subsection 3.3.1.

3.2 Practical applications of IR thermography

Conventional temperature assessment techniques usually use standard transducers (e.g., thermocouples, resistance temperature detectors (RTDs), amongst others). Each transducer is capable of yielding either the temperature at a single point or a space-averaged one. Hence, in spatial resolution terms, these types of sensors have to be regarded as zero-dimensional [96]. This constraint may make measurements meaningless if the temperature or the heat flux fields exhibit high spatial variations. On the other hand, infrared cameras constitute a two-dimensional temperature transducer since they allow accurate temperature measurements even with spatial gradients.

IR cameras are beneficial for specific applications. For instance, if the target object presents a hazard to direct contact with thermocouples like carrying electricity. If the object is too small to make contact with a physical sensor or too fragile, the sensor cannot be placed on it. Additionally, if the target is moving [101]. Regarding the errors and uncertainties of IR thermal imaging, temperature measurement errors depend mainly on components associated with the object's emissivity, ε_{obj}. The second significant contributor was found to be the ambient temperature surrounding the object, T_{amb}. On the other hand, factors such as relative humidity ω, the camera-to-object distance d and the atmospheric temperature T_{atm} do not contribute significantly to the total error [102]

Since the IR camera provides a two-dimensional thermal map, it allows a more straightforward error evaluation due to radiation and tangential conduction. Furthermore, the camera is non-invasive; hence it does not disturb the process. Another advantage is that it allows one to get rid of thermocouple or RTD wires and the associated conduction errors that may occur with them [96]. As such, IR thermography can be effectively applied to a more extensive array of processes and offer many advantages over conventional thermal assessment tools. Alternatively, the coupled use of sensors can also provide a robust solution for process monitoring.

3.2.1 Previous industrial applications of IR

IR thermal imaging has been applied for multiple purposes in different areas. An important use is for condition monitoring [99] and it is extensively used for evaluating machines [103] and electronic components [104]. It also has many applications in medicine practices [105]. It has been studied for early-stage diagnosis of diabetic foot [106] and to detect and prevent muscle injuries [107]. IR has also been applied in thermo-fluid dynamics studies [96] and to droplet transport during spray applications using atomizing spray nozzles [108].

In agricultural applications, it has been used to determine best irrigation practices [109] and to assess seed vigor [110]. Additionally, it has been used to measure the exotherm temperatures during freezing jojoba branches [111]. In another

study, it was used to visualize the freezing process of wheat plants [112]. A perhaps surprising recent application of IR was to evaluate dog's responses to certain smells and determine which ones were pleasant and which ones were unpleasant for the canines [113].

In the Food industry

In the food industry, IR has been used to monitor and control the process in diverse ways. Many of these applications regard food safety aspects since IR thermography can offer an additional tool to detect foreign bodies [114]. For instance, IR can be used to detect adulterant substances in food, such as in fruit, chocolate, and nut production lines [115]. It was proposed as well in biscuit manufacturing, where it was able to spot even tiny physical contaminants [116]. It was also proposed to detect seal contamination in heat-sealed food products [117].

Regarding food quality, IR offers many advantages as well [118]. Infrared monitoring was successfully applied to evaluate the quality of meat products [119]. It has also been used in extra-virgin olive oil quality evaluations to detect adulteration in this product [120]. IR thermography was applied to monitor the product's surface temperature during pulsed ultraviolet light microbial inactivation. The monitoring was done in a tandem application together with a thermocouple to assess the inner product temperature [121]. IR allowed a better understanding of heat transfer mechanisms during freezing of fruit juices [122]. Finally, a noteworthy application was the infrared monitoring use for the determination of moisture content in foods [123].

During processing, it was applied to monitor the freezing process of raw potatoes [124]. Later, it was also applied during thawing to evaluate and compare different thawing methods applied to starch-based sauces, such as water immersion batch and microwave-assisted [125]. Furthermore, it was used to assess temperature differences between beef patties being cooked with and without thawing [126]. For drying applications, it was used to control citrus surface drying to avoid overheating, which causes loss of sensory characteristics [127]. And finally, for freeze-drying applications, it was used to monitor poultry breasts [128], raspberries [129], bananas [130], lettuce stem slices [131], eggplants [132] and gelatin model solutions [133].

In the Pharmaceutical industry

Infrared thermal imaging was studied in the pharmaceutical industry for different applications. It was proposed as a new approach to measuring in-line ribbon relative density since this is a crucial quality attribute during roll compaction. Roll compaction is an agglomeration technique for specific unstable Active Pharmaceutical Ingredients (APIs), and it determines final granule porosity and product's size distribution [134]. Another study investigated the coating process using a nozzle with

ultrasonic fluid atomization through IR thermography. They were able to describe better the drying kinetics [135] using IR thermography. Infrared thermography was applied for thermal characterization of pharmacological compounds, specifically to determine the melting temperature of model compounds. They found IR to be promising for high-capacity thermal analysis in the pharmaceutical development process [136]. Finally, Infrared was applied to the drying of pharmaceuticals by microwave vacuum drying to experimentally map and quantitatively evaluate the heat distribution, which allowed the detection of the warmest regions to be used as critical control points to avoid overheating [137].

Freeze-drying of Pharmaceuticals

The first published application of infrared monitoring to freeze-drying processes of pharmaceuticals was made by Emteborg et al. in 2014 [91]. In that research, the infrared camera was placed outside the drying chamber, having a field of view of the whole batch from above. This approach has some advantages. First, the camera can monitor many vials, whether they are in the edge or the middle of the batch. Second, the product itself is being directly observed, and not the external wall. Finally, having the sensor outside the drying chamber, Cleaning in Place (CIP) and Sterilization in Place (SIP) routines can be executed. On the other hand, it also presents severe limitations.

The IR sensor monitoring the product from above can only see the temperature changes of the top layer of the product. This positioning significantly compromises product monitoring, especially for vials being cooled and heated up through the chamber shelves. For vial FD using this classical configuration, there are strong vertical temperature gradients [138]. During freezing, heat is removed from the bottom, and the freezing front moves from bottom to top [16]. Thus, monitoring just the top of the vial may be a big miss-representation of what is happening in terms of heat exchange and mass transfer. During primary drying, these gradients vary in magnitude according to the vial position within the batch [138]. Again, monitoring just the top layer may represent significant differences concerning the product temperature.

Van Bockstal et al. [139] proposed the use of an infrared camera for temperature monitoring of vials during freeze-drying using the spin freezing process. In that application, the camera was placed outside the chamber and monitored the vial axially through a germanium glass with a 90°angle. After the corrections regarding the germanium transmittance and the heat transfer between the external vial glass wall and the product inside, IR was undoubtedly a valuable tool for that application. However, the one-dimensional approximations for heat and mass exchange in this process are arguable. It is in fact a vial in contact with the shelf, exposed to an IR heater, exhibiting a thin product cake. This particular setup conferrers a large relative surface area exposed to radiation effects on the external

vial side. Additionally, it renders a large surface area in the inner vial side, free to sublimate. This processing technique may be great to have a faster drying process. However, in that case, the sublimation interface is not one-dimensional, and the horizontal (or azimuthal) temperature gradients are probably not homogeneous. The camera in such an application measures the vial's glass temperature in contact with the product. The whole temperature measurement, in this case, depends on the product being in thermal equilibrium with the glass. In the end, the IR thermal measurement was probably representative of the product temperature since the product layer was thin.

Since vertical temperate gradients are much more expressive than azimuthal ones for vials exchanging heat directly with the shelf [138], infrared temperature monitoring perpendicular to the vial wall is preferred. Thus, the placement of the camera in both previously described cases [91, 139] leaves room for improvement. To this end, Lietta et al. [92] proposed a new IR thermography sensor that can be placed inside the freeze-drying chamber. That study was done on a small batch of vials. It was in an initial proof of concept stage to verify if the sensor could provide temperature measurement with acceptable accuracy for processing monitoring.

The same sensor was then used in freeze-drying studies applied to food products. In this case, to eggplants. One initial study used the IR-based data to monitor the product temperature throughout freezing, primary drying, and secondary drying [121]. This thermal data was used to develop a diffuse interface model for individually frozen products [132].

Colucci et al. then proposed the use of this sensor coupled with multivariate statistical techniques for statistical process control to exploit the large amount of thermal data provided by IR thermography. Two algorithms, one based on Principal Component Analysis and the other on Partial Least Square Regression, were developed and compared. They could account for the heterogeneity of the batch and aim to reduce the off-specification products [140].

Following up, a new PAT was developed and tested for *on-line* process monitoring of a vacuum freeze-drying process based on image analysis. The IR sensor obtains thermal images of the process in progress and performs Multivariate Image Analysis (MIA) to extract the relevant data. The MIA-based PAT system can detect on-line undesired events occurring during the freeze-drying process [93, 141]. Subsequently, the image analysis algorithm was improved using an object detector network based on a Faster Region Convolutional Neural Network (FRCNN) and a Kernelized Correlation Filter (KCF) tracker. They were combined with monitoring the freeze-drying process of products in glass vials and identifying the product inside the vials through the images automatically. In their study, the localization of the vials was accurate enough to measure the average temperature with an acceptable error [42].

Then, that same infrared sensor was applied to the freezing stage coupled with mathematical modeling to estimate the ice crystal size distribution at the

end of the freezing stage. That study focused on vial freeze-drying processes using spontaneous nucleation and shelf-ramp freezing. The system was found effective for monitoring the freezing stage [142]. Following up on freezing applications, a new mathematical model for the freezing process in vials was proposed in an entirely simulated environment. The heat and mass exchange simulations were then validated based on the collected IR thermal data [29].

3.3 Infrared monitoring in this study

In this present study, the same sensor used by Lietta et al. [92] and Colucci et al. in 2019 [143] is used. The IR camera is also placed inside the drying chamber, allowing a direct temperature measurement of the targeted object, positioned perpendicularly to the vial wall. This configuration enables monitoring the complete axial profile of the vial, offering better product monitoring throughout freeze-drying processes. In those previous studies, although the applicability of the sensor was explored, priority was given to the sensor's survival and operation under the harsh operating conditions inside the chamber. Further investigation was necessary regarding the sensor's accuracy, batch representativeness, and whether the placement of the sensor inside the chamber could affect batch dynamics. Additionally, changes in the software used to extract the thermal data were done, and additional corrections were made. All these contents will be explained in detail in the sections ahead.

3.3.1 IR System's design

A few points needed to be taken into consideration since the IR sensor used in this study is placed inside the drying chamber. The drying chamber is characterized by harsh temperature, gas composition (moisture), and pressure conditions. Any electronics piece placed inside a freeze-drying chamber should be carefully designed. The sensor should never be cooled below its threshold temperature by design. Any contact with moisture should be avoided, and the case protecting the sensor must resist pressure changes and gradients. Furthermore, temperature measurement accuracy should be comparable with thermocouples, i.e., $\pm$ 1 K. Ideally, data must be accessible in real-time and safely stored. Meanwhile, low temperatures near 213-223 K are typically reached during the freezing stage. Additionally, the gas composition of the chamber during freezing is $\sim$100% water. During primary drying, chamber pressures around 5 Pa (or even less) are commonly used.

The final infrared system design was established by [143]. The total dimensions of the resulting sensor are 200 x 172 x 178 mm (L x D x H), weighing approximately 2 kg. All components of the IR system are mounted into a polyacetal

copolymer (Ertacetal®C natural) case, a thermally insulating, food-grade, plastic material (see Figure 3.2).

Into this case the following elements were assembled, as shown in Figure 3.3:

1. an infrared camera (FLIR Systems model A35);
2. an RGB camera HDTV 720p
3. a cold LED that provides the 0.5 lux required for the RGB camera to work properly
4. a microprocessor for the administration of the hardware and software of the sensor;
5. a WiFi communication antenna
6. a status LED, that signals when the sensor is running and
7. two valves designed to flush the inside of the case with an inert gas before being operated and resist to high-pressure gradients.

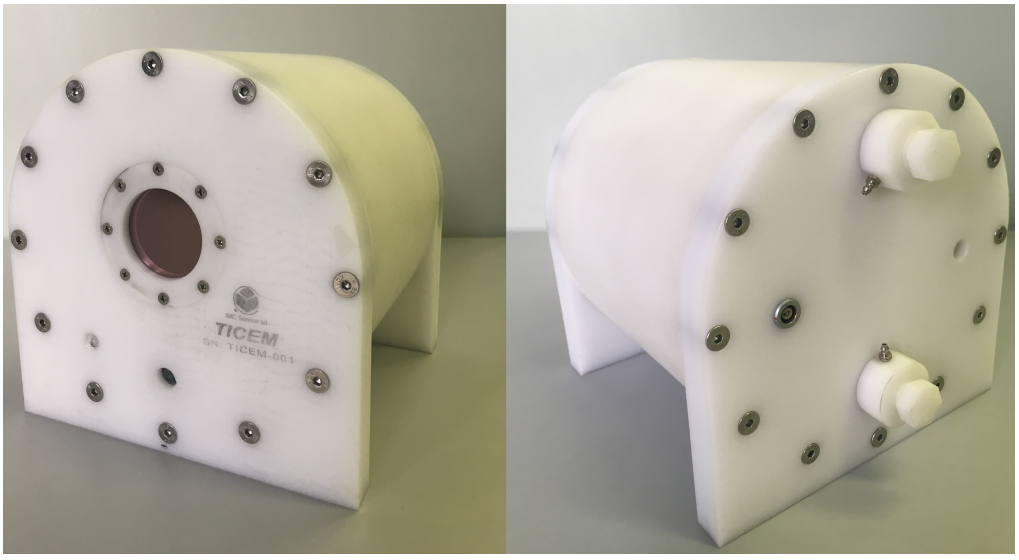

Figure 3.2: Final prototype of the IR system used from different angles, (a) front and (b) back.

More details about the system's characteristics can be found in Appendix C. The RBG camera was added to the design as a complementary device to the IR thermography because the glass vials are opaque to the IR radiation while

transparent to the visible radiation. The RGB sensor was used in this study only as a support tool to ensure data extraction from the right points, corresponding to the product in the vials.

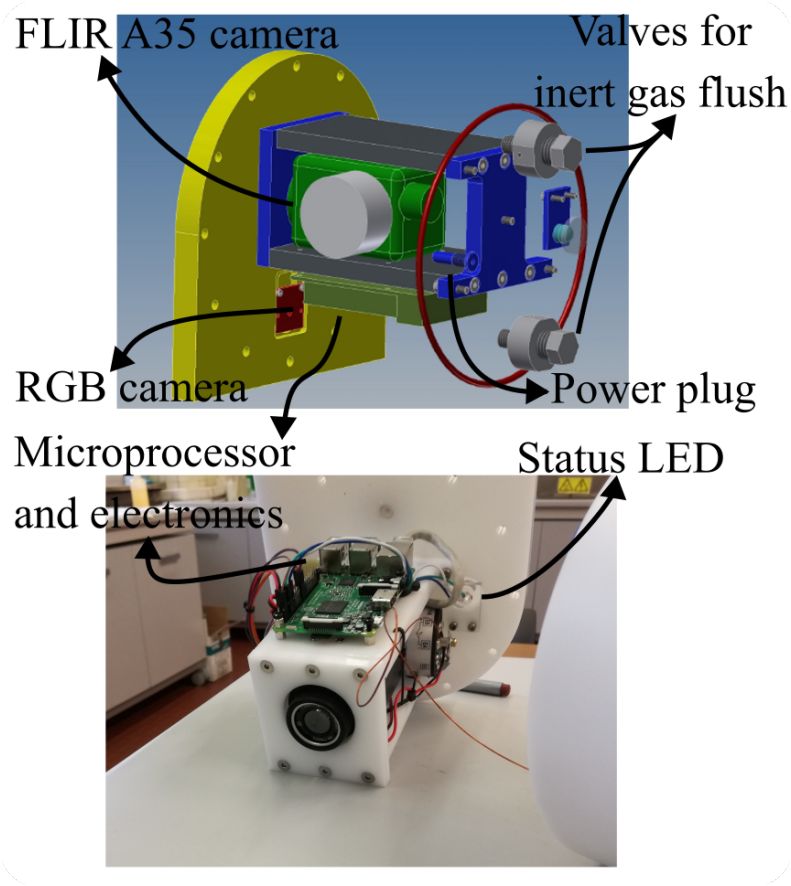

Figure 3.3: Details of the sensor's design evidencing system parts.

The only requirement is to have a power cable inside the freeze-drying chamber. To this end, a circular twin-pin connector (FGG.0T.302.CLAC50Z, Farnell Italia S.r.l.) was chosen to guarantee IP68 protection under harsh freeze-drying conditions. The actual energy consumption of the camera is lower than 3 A, while a 12 V and 10 A electrical supply is required. The precision is nearly ± 2 K, and it becomes less reliable for temperatures below 233 K. Other system characteristics can be seen in Table C.1 in detail.

Initially, it was advised to flush the polyacetal enclosure with nitrogen to remove any moisture from the inside of the IR's system before a freeze-drying cycle. However, this procedure was proven only necessary in some specific cases, such as after a gravimetric test or if the lab conditions favor a remarkably high relative humidity. Gravimetric tests are critical for this because the freeze-drying cycle is typically stopped and exposed to the outside environment while the sensor's case is

still icy. This way, much condensation may form in the sensor. Many times after a gravimetric test, the sensor would be left inside the chamber and brought to room temperature to attenuate condensation events.

3.3.2 Built-in software

The system was designed with a built-in software management tool easily accessible through any computer with a WiFi antenna. The software can be reached using any internet browser with an intuitive interface for easy navigation through the system's IP. As it can be observed in Figure 3.2, the IR camera is behind a germanium glass window. Germanium is primarily transparent to infrared radiation, having a very high transmittance from 0.825 to 0.85 based on the vial temperate being between from 235 K to 249 K [139]. For practicality, a constant value of 0.88 was considered and implemented in the built-in software

As with any electronic device, the infrared camera detects the signal of interest with its sensing part, that varies according to the type of camera. The parameter measured from this sensor is converted first into an electric signal, and then into the desired measured parameter, in this case, temperature. What the IR sensors capture is the thermal energy being emitted by its target object (Q_{obj}). However, the energy being emitted by the target has other contributions besides its own. As shown in Equation 3.4, these contributions are the energy emitted by the atmosphere (Q_{atm}) and the parasitic radiation emitted from the environment (Q_{ref}), which combined give the total energy received by the sensor (Q_{tot}).

$$Q_{tot} = Q_{obj} + Q_{atm} + Q_{ref} \tag{3.1}$$

More details can be found elsewhere [143]. What is important to point out is that this parasitic radiation can be regarded as equivalent to the radiation emitted by a fictitious body having temperature T_{ref}. The T_{ref} is called reflected apparent temperature, and its correct estimation has a substantial impact on the temperature readings of the targeted object.

The total radiation emitted from an object (W_{obj}) having emissivity ε_{obj} and temperature T_{obj} can be written following the Stefan–Boltzmann equation:

$$W_{obj} = \varepsilon_{obj}.\sigma_B.T_{obj}^4 \tag{3.2}$$

where ε_{obj} is the emissivity of the object and σ_B is the Stefan–Boltzmann constant.

Because only the fraction of energy that is not absorbed by the atmosphere effectively reaches the sensor, the first contribution to Q_{tot} can be written as:

$$Q_{obj} = \tau_a.\varepsilon_{obj}.\sigma_B.T_{obj}^4 \tag{3.3}$$

where τ_a is the atmosphere's transmittance.

The object's temperature (T_{obj}) is defined in Equation 3.4, accounting for the atmospheric and the reflected energy contributions [144]. For this, the emissivity of the object (ε_{obj}), the atmosphere's transmittance (τ_a), the temperature of the atmosphere (T_{atm}) and the reflected apparent temperature (T_{ref}) must be known.

$$T_{obj} = \sqrt[4]{\frac{Q_{tot} - \tau_a(1-\varepsilon_{obj}).\sigma_B T_{ref}^4}{\tau_a \varepsilon_{obj} \sigma_B}} \tag{3.4}$$

Under the typical conditions of a freeze-drying cycle, the τ_a was found to be close to 1, making the Q_{atm} contribution negligible. The temperature deviations caused by this factor were in the order of 0.01 K. The IR sensor's built-in software allows setting a spot to acquire the T_{ref} from a *pure reflector* to account for the parasitic radiation emitted to correct the temperature measurements in-line.

According to ISO 18434-1 guideline, Part 1, Annex A.1, a perfect reflector consists of a wrinkled sheet of aluminum foil [103]. The surface of aluminum has a low emissivity value ranging from 0.04 to 0.09 [101] and has the ability to reflect 95% of the infrared rays which strike it. Since aluminum foil has such a low mass to air ratio, very little conduction can take place, particularly when only 5% of the rays are absorbed. Additionally, it.

This sheet was placed on the freeze-dryer door inner side to have its "apparent temperature" measured throughout the process. Details of the *pure reflector* placement as view through the IR camera can be seen in Fig. 3.4.

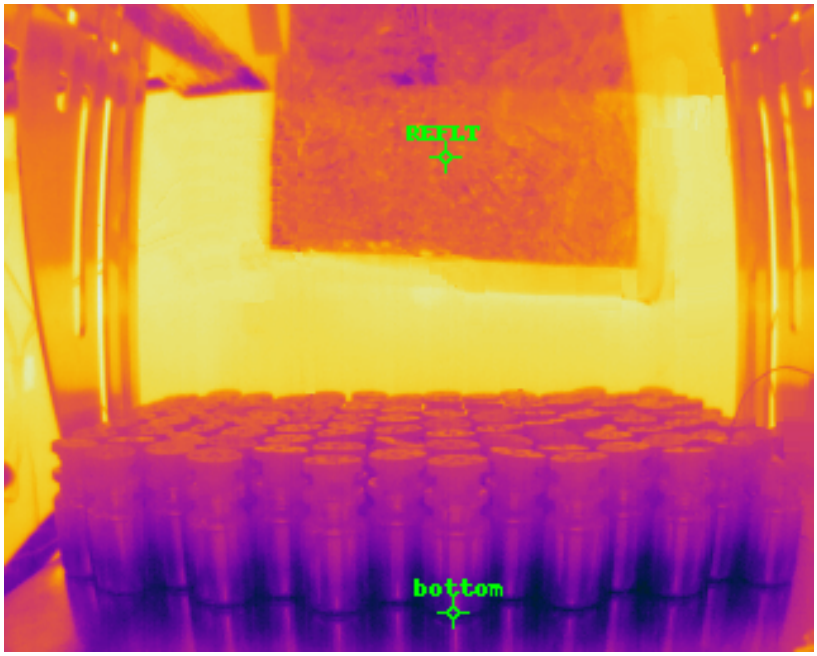

Figure 3.4: Pure reflector as seen by the IR camera on a random batch.

After placing the IR camera inside the chamber (Figure 3.5), a recording session must be started to register the infrared thermal data. The fastest data acquisition rate is one frame every 10 seconds (0.1 fps). This most rapid frame rate was used only for in-depth studies regarding the freezing step. Still, one frame per minute is typically enough to monitor a freeze-drying process.

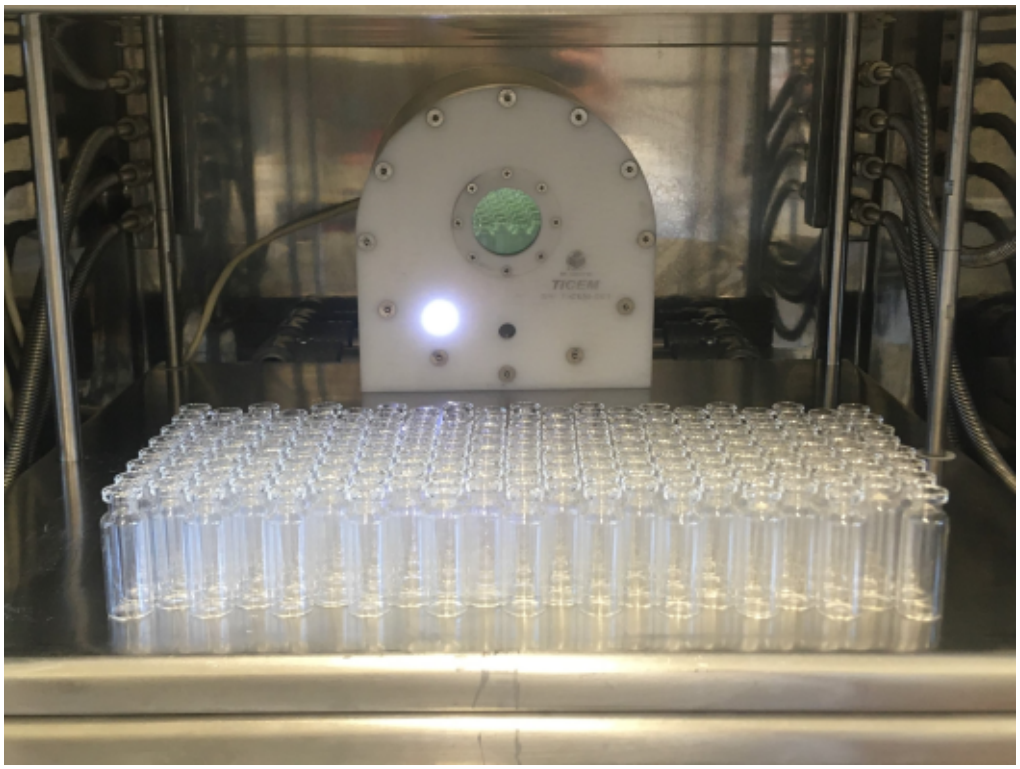

Figure 3.5: Example of camera placement inside the LyoBeta freeze-dryer.

The system's interface *as is* allows in-line monitoring of product temperature. However, the current software version only allows one constant emissivity value, defined at the beginning of each session. This issue is that the emissivity of materials may change with significant temperature changes. Luckily, if this is relevant, it can be corrected in the data post-processing step as it will be better described ahead.

Once the process is over, all collected data can be saved for post-processing. The thermal data are stored as a numeric matrix. Each cell represents the temperature measurement of a given pixel based on the setup emissivity of that session and the corrected reflected temperature.

3.3.3 Post-processing

All data post-processing was done using MATLAB R2019b. Based on the image analysis code initially developed by Colucci [143], a self-made code was developed. Substantial changes were made to the script, which will be explained ahead. One general change mentioned beforehand was removing all Savitzky–Golay filters (through a built-in MATLAB function) initially used in the source code.

Data acquisition

The data extraction during post-processing was based on vertical acquisition lines as illustrated in Figure 3.6. This approach is founded on the assumption that the main temperature gradients present in vials subjected to a conventional freeze-drying process are vertical, as they exchange heat mainly with the shelf through the vial bottom [138].

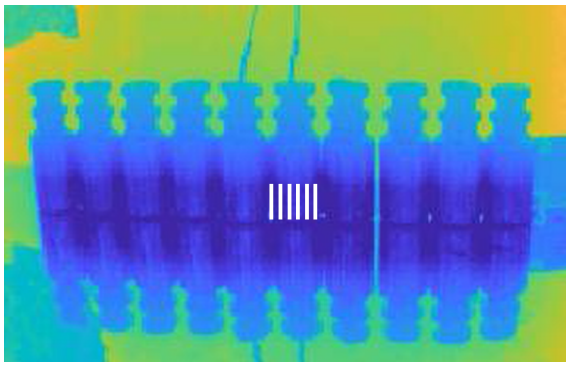

Figure 3.6: Representation of six acquisition lines used to obtain the vial's average parameters listed in Figure 3.7 and Figure 3.8. The batch average values were obtained from the vial's average values, always using six acquisition lines per vial.

Infrared thermography is very sensitive and may present data noise. Having multiple data points representing the target object and averaging their temperature reading reduces the data noise considerably. The number of acquisition lines used is among the changes made in the code. In previous applications, three vertical acquisition lines were used per vial. In this present study, six acquisition lines were used per vial. The choice for an even number was intentional to avoid extra noise caused by additional reflections on the center-line (vertically) of the vial.

The IR sensor was placed inside the drying chamber for all tests, 25 cm away from the monitored vials and on the same shelf. The sensor was aligned with the shelf center-line against the back wall. This way, each pixel of thermal data acquired corresponded to roughly 1.25 mm x 1.25 mm of product cake inside the vial. The distance of the camera away from the vial may be relevant for the temperature measurement during freezing because the atmosphere's transmittance

(τ_a) may affect the readings. During primary drying, because of the extremely low pressure used, τ_a's contribution is less substantial.

Depending on the fill volume used in each test, the cake height naturally varied. Thus, the number of pixels in each acquisition line changed depending on the test aiming to cover the whole cake height. The number of pixels used varied between 8 and 12 pixels for cake heights of 10 and 15 mm, respectively, resulting in roughly 1 pixel per 1.25 mm of cake. This is better described in Figure 3.7 and Figure 3.8.

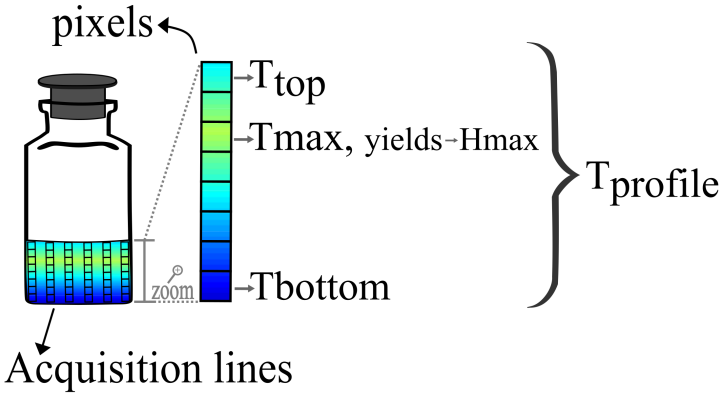

Figure 3.7: Representation of the acquisition lines, pixels, and relevant variables extracted from the thermal data during an arbitrary moment during the freezing stage.

The data acquisition approach was slightly different for freezing and primary drying because they have different variables of interest. Since freezing is an exothermic process, the data acquisition focuses on the maximum temperature profiles during freezing. If the thermal gradients are great enough with respect to the cameras sensitivity (0.05 K) during freezing, the freezing front may be detected by tracking the maximum temperature (T_{max}) position (H_{max}). Meanwhile, because sublimation is an endothermic process, the data acquisition for this stage focuses on the minimum temperate profiles during primary drying. Again, if the thermal gradients are great enough during sublimation, the sublimation interface may be detected by tracking the maximum temperature (T_{min}) position (H_{min}).The thermal gradients are minimal during secondary drying, and no crucial data could be acquired, only the average product temperature.

Another change made to the code was the order of the data acquisition and post-processing steps. In its previous version, the algorithm was the following:

1. Each vial had three vertical extraction lines, having as many pixels as necessary to cover the cake height;

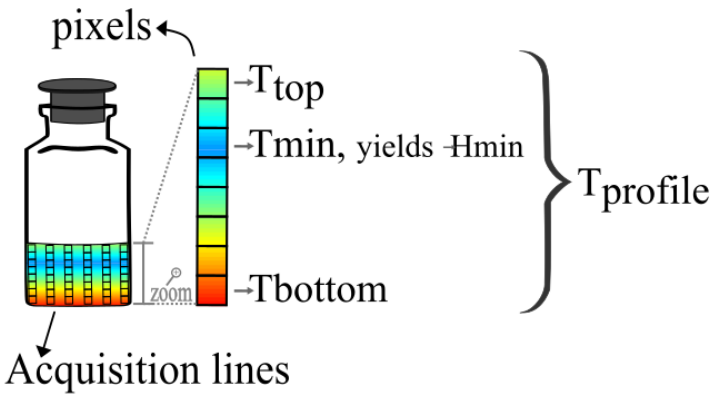

Figure 3.8: Representation of the acquisition lines, pixels, and relevant variables extracted from the thermal data during an arbitrary moment during the primary drying stage.

2. each line was then filtered with a Savitzky–Golay filter;
3. these three lines were then averaged to obtain the vial's average axial temperature profile (T_{prof});
4. the approximate derivative of the vial's T_{prof} was obtained using the *diff* built-in MATLAB function;
5. a Savitzky–Golay filter was applied to the resulting approximate derivative of the vial's T_{prof};
6. the H_{min} was detected as the point where this filtered approximate derivative of the profile crossed zero (analogously performed for the H_{max});
7. the temperature of the vial's T_{prof} at the H_{min} detected pixel was defined as the T_{min} (analogously performed for the T_{max}).

In the current post-processing code, the data acquisition order is as follows:

1. Each vial had six vertical extraction lines, having as many pixels as necessary to cover the cake height;
2. each line had the position of the pixel with the minimum temperature (H_{min}) detected using the *minimum* MATLAB function (analogously performed for the H_{max} with the *maximum* MATLAB function);
3. the temperature at the H_{min} was defined as the line's T_{min} (analogously performed for T_{max});

4. the vial's H_{min} position and temperature was obtained by averaging the H_{min} and T_{min} of the six acquisition lines of a vial (analogously performed for the H_{max} and T_{max});

5. The vial's average axial profile (T_{prof}) was obtained by averaging the six lines of each vial.

These changes permitted a *cleaner* data extraction algorithm, more faithful to the sensor's observations.

Data Processing

An IR camera is an image-based sensor and, as such, it measures the temperature based on what it *sees*. Furthermore, differently from the NIR sensor which has a 5 mm penetration, the IR camera does not have a deep penetration and it monitors just the surface of the targeted object. In this study's case, the outer surface of the vials glass is what is being effectively monitored by the camera. The vial walls typically has a 1 ± 0.04 mm thickness. Van Bockstal et al. [139] proposed a 1D model to account for the temperature gradient between the product inside the vial and the external glass wall. This model was developed to measure the product temperature behind the vial glass in a more accurate way. However, the vial wall is thin and an equilibrium between the product and the wall is reached in a relatively short time. Thus, the adjusted values tend to be very close to the surface temperature. In fact, a maximum difference of 0.2 K was found under similar conditions used in this study [143]. Because this is smaller than the accuracy of the IR sensor, this correction was not applied and the IR-based temperature measurements were regarded as representative of the samples inside the vials. Additionally, as it will be discussed further in Section 5.2, the radial gradients in the vials used can be assumed to be negligible compared to the vertical gradients using the tested vial configurations.

In simplified terms, the IR sensor is a non-contact device that detects radiated infrared energy and converts it into an electronic signal. This signal is then processed to produce a thermal image. Virtually all ordinary (baryonic) matter above zero Kelvin emits thermal radiation and absorbs some electromagnetic radiation. An idealized non-reflective, opaque body, which would absorb all incident electromagnetic radiation, is called a blackbody. Such a body, at thermal equilibrium, emits thermal radiation with a characteristic wavelength frequency distribution that depends on its temperature. A blackbody, by definition, has an emissivity of 1, and it emits as much or more thermal radiative energy as any other object at the same temperature. Ordinary objects do not express this idealized behavior. Typically, their characteristic emissivity is described as a ratio of the energy radiated from their surface, compared to a blackbody. Thus, ranging from 0 to 1 [97].

The object's emissivity depends on many parameters, such as the type of material, the structure of the object's surface, the viewing angle between the camera and the object, and object's temperature. Under the investigated conditions, the former three parameters were *always* the same as they correspond to the vial, made of glass, using similar batch configurations. However, the object's temperature may have a relevant effect on the emissivity change of the material being studied. In many applications, a constant emissivity value can be used for the regarded temperature range (233 K - 303 K). However, special care should be taken when the monitored process includes phase changes. More specifically, when wide temperature ranges are studied and phase change is present, the emissivity can significantly change, which in turn could lead to errors in the measured values [97, 102]. In our case, the glass on the vial is being monitored, which does not change phases. However, the monitored process presents a wide range of temperatures. Since the built-in software of the sensor used in this study requires a single emissivity value for a given data acquisition session, this emissivity value had to be corrected in the post-processing. Thus, a fixed emissivity value of 0.91 was used when monitoring the batches. However, this emissivity value was later adjusted using different emissivity values, according to the estimated vial temperature range.

To adjust the measured values using the constant emissivity, a correction was made using the emissivity values according to the temperature range of the glass vial as listed in Table 3.1.

Temperature range, K	emissivity
233 - 240	0.980
240 - 253	0.955
253 - 263	0.935
263 - 273	0.915

Table 3.1: Emissivity values for glass vials according to the temperature range [142].

A graph showing a measured profile and its adjusted profile using the emissivities listed in Table 3.1 can be seen in Figure 3.9.

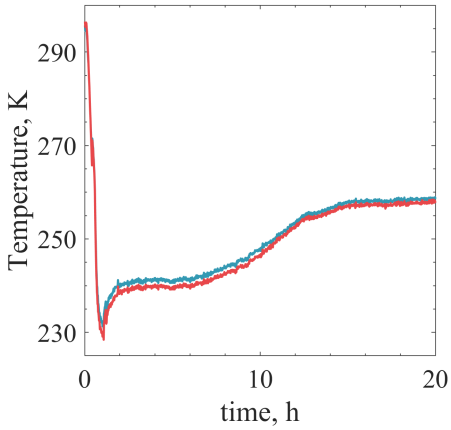

Figure 3.9: T_{bottom} acquired (red) and corrected (blue) IR thermal profile.

The test presented in Figure 3.9 as an example is from a random freeze-drying batch of 5% mannitol. To do these corrections, first, the total radiation (Q_{tot}) received by the sensor was calculated using Equation 3.4. The Q_{tot} was estimated based on the previously discussed assumptions regarding Q_{ref} and Q_{atm}. Then, the T_{obj} was corrected using the emissivity values according to the estimated vial's temperature range.

Chapter 4

IR application in a freeze-drying batch: proof of concept

4.1 Experimental investigation: How accurate is the IR sensor? Does it affect batch dynamics?

Any temperature measurement, reasoning, and conclusions using the present sensor and code would be void without preliminary studies. Since this sensor is placed inside the drying chamber, understanding if the sensor's presence affects the process is in hand. Additionally, the accuracy of the acquired data should be verified[1].

This way, the study objectives that will be discussed in this chapter are:

i. Assess if the presence of the infrared camera inside the drying chamber affects batch dynamics of larger batch sizes in any substantial way;

ii. Ascertain the accuracy of the temperature measurements acquired by the infrared camera using thermocouples as a reference tool.

4.1.1 Materials and methods

More specific details regarding the equipment and instruments model in given in Appendix A.

All experiments in this section were conducted using a REVO freeze-dryer. Three vial sizes were used, 20R, 6R and 4R, each being filled respectively with 10% w/w sucrose, 5% w/w sucrose and 5% w/w mannitol solutions. The 4R vials have the

[1]Part of the results presented in this Chapter have been previously published in [145].

largest surface area relative to the vial volume. This larger proportional surface area means that heat radiation effects from the chamber walls to the vial during primary drying become more pronounced for this vial size. Hence, temperature control may be more challenging for 4R vials, particularly for edge vials because the may heat up more than other vials. Sucrose is an amorphous solute and, as such, presents cake collapse if the product temperature surpasses its glass transition temperature before the ice fraction is removed [146]. This way, a crystalline solute, mannitol, was chosen to be used for the 4R vial size to avoid collapse issues. Mannitol formulations usually have a more stable cake structure, resulting in elegant final products with no observable shrinkage. Still, mannitol systems may present different polymorphs together with an amorphous phase [147]. A 10% crystalline mannitol formulation presenting α-mannitol and β-mannitol polymorphs, with the former as the most abundant one [148].

The fill volumes and vials used were as listed in Table 4.1.

Vial size	Fill volume, mL	Cake height, mm	Solution	Batch size
20R	5.0	12	10 % sucrose	30 (12 edge)
6R	3.0	11	5% sucrose	105 (39 edge)
4R	1.5	10	5% mannitol	157 (52 edge)

Table 4.1: Solutions, fill volume, cake height and batch size used for each vial size.

The batches were directly loaded onto a cooling/heating shelf of the freeze-dryer and arranged in a hexagonal array without any tray sides.

Heat-exchange modeling

All calculations to determine the global heat transfer coefficient (K_v) and the cake resistance to vapor flow (R_p) were based on a uni-dimensional heat and mass exchange approach [149].

Assuming the heat flux (J_q) to be proportional to the temperature gradient between the shelf (T_{shelf}) and the vial bottom (T_{bottom}), it leads to Equation 4.1. K_v is the overall heat transfer coefficient associated with the vials used, chamber pressure, and overall batch configuration.

$$J_q = K_v(T_{shelf} - T_{bottom}) \tag{4.1}$$

Assuming that the water vapor mass flow (J_w) is proportional to the difference between the ice partial pressure in the sublimation interface ($p_{w,i}$) and the water partial pressure in the drying chamber ($p_{w,c}$), J_w can be calculated using

Equation 4.2. The proportionality parameter R_p is resistance to vapor flow imposed by the solid fraction of the product cake.

$$J_w = \frac{1}{R_p}(p_{w,i} - p_{w,c}) \tag{4.2}$$

Equation 4.3, adapted from the Augustus Equation [145], can be used to calculate $p_{w,i}$:

$$p_{w,i} = e^{\frac{28.935-6150}{T_i}} \tag{4.3}$$

T_i is the temperature at the ice sublimation interface. Sometimes it is approximated to T_{bottom} if the cake is not very thick and the temperature gradient is small. While $p_{w,c}$ can be approximated to the chamber pressure, as the composition of the chamber is close to 100% water vapor. Finally, the energy balance at the sublimation interface is given by Equation 4.4 in which ΔH_s is the heat of sublimation [5]:

$$J_q = \Delta H_s J_w \tag{4.4}$$

A typical method for K_v estimation is performing a gravimetric test, as described in Fissore et al. [150]. To perform such a test, vials being studied are filled with water (or with the desired solution) and subsequently weighted and loaded into the freeze-dryer. First, freezing is carried out and and then primary drying is initiated by reducing the chamber pressure and increasing the shelf temperature according to the desired settings. However, after a few hours, primary drying is interrupted before sublimation is complete by restoring the chamber pressure to the atmospheric value. Then, the weight of each vial is measured again to compute the mass change (Δm) after this truncated session. The total heat received (Q) by the product during this session is assumed to be used for phase change from ice to vapor. This way, the mass-energy balance can be described as in Equations 4.5 and 4.6:

$$Q = \Delta m \Delta H_s \tag{4.5}$$

$$Q = K_v A_v \int_0^{t_d} (T_{shelf} - T_{bottom})\, \mathrm{d}t \tag{4.6}$$

where A_v is the vial bottom area, and t_d is the duration of the sublimation step.

The global heat exchange coefficient, K_v, may also be obtained at the end of a full primary drying cycle, if the end-time can be accurately determined. If sublimation can be assumed to be complete, Δm will correspond to the initial water content of each vial (m_0). This way, by setting t_d to the duration of the primary drying stage, Equation 4.6 may be used to obtain K_v.

Combining Equations 4.1, 4.2 and 4.3 we have:

$$R_p = \frac{\left[\Delta H_s \left(e^{\frac{28.935-6150}{T_i}} - p_{w,c}\right)\right]}{K_v(T_{shelf} - T_{bottom})} \tag{4.7}$$

This way, the R_p profile can be calculated using the product temperature profile during primary drying, if the K_v is known.

R_p has a dependence on the dried cake thickness (L_{dried}), which can be estimated through numerical integration of the water mass flux using Equation 4.2. Since in the very beginning of drying L_{dried} is zero, so should be the resistance to vapor flow at that point. As L_{dried} increases, a thicker cake layer will pose an increasing resistance to vapor flow. Cake micro collapses often happen, affecting the dried cake porous structure and resulting in regions with larger pores. These micro collapses create larger channels for the vapor to flow, preventing a further dramatic increase in the resistance to the vapor flow. This way, micro collapses render an asymptotic behavior to the R_p profile after the first ascending interval trend.

To properly account for this dependence between R_p and L_{dried}, the equation below (Equation 4.8) can be used [151].

$$R_p = R_{(p,0)} + \frac{A_{rp} L_{dried}}{1 + B_{rp} L_{dried}} \tag{4.8}$$

In this model, $R_{(p,0)}$, A_{rp} and B_{rp} are fitted to the experimental data based on the R_p and L_{dried} values calculated using Equations 4.2 and 4.3. A_{rp} is the linear term of this fit, representing the increase in the resistance as drying progresses while B_{rp} represent the decrease in the resistance, cause by the micro collapses. In practice, $R_{(p,0)}$ should be 0 at time zero, because there is no cake to pose resistance to vapor flow. Hence, Equation 4.8 can be simplified by removing the $R_{(p,0)}$ term.

Experimental conditions

The same operating conditions were used for all tests, i.e., the same cooling ramp and duration during freezing and the same chamber pressure and shelf temperature during primary drying. This was done to reduce the number of

independent variables across the tests and enable direct comparisons between them. Thus, only the vial size, batch size, and solution varied between the tests. The presence or absence of the IR sensor inside the chamber in each batch depended on the experimental design. Nonetheless, all batches had at least two thermocouples placed in edge vials and 2 in central vials for reference temperature monitoring.

Freezing was done for a total of two hours, with a one hour freezing ramp from 293 K to 233 K (1 K/min) and then one hour hold at 233 K. Primary drying was done using 253 K shelf temperature setting and 8 Pa chamber pressure. The $\frac{Pi}{Ba}$ offset time was used to determine and compare the primary drying duration between tests. More details about the $\frac{Pi}{Ba}$ method can be found in Appendix B. For the gravimetric tests, which were used to compare the mass change and the K_v values, different durations were used according to the vial size tested. Nonetheless, care was taken to ensure the same primary drying duration for each given vial size to ensure the validity of direct comparisons between tests. This was important mostly because of the mass change comparison, which would change if the drying sessions had different durations. Additionally, the dynamics of sublimation may not be constant during drying and this could result in differences in the resulting K_v values. This way, the gravimetric durations used were: 180 minutes for the 20R vials, 260 minutes for the 6R and, 250 minutes for the 4R vial sizes. One extra freezing test was done with a one hour freezing ramp from 293 K to 233 K (1 K/min) and then five-hour-hold at 233 K, resulting in six hours, as explained in the following Subsection.

i. Camera's effect

Because the infrared camera is placed inside the drying chamber, an evaluation regarding its potential effects on batch dynamics was conducted. Having the camera placed inside the chamber could affect batch dynamics, because it could affect in the heat radiation from the walls to the vials or present other unforeseen interferences such as affecting the pressure signals or releasing heat from the electronic panel of the camera.

To this end, gravimetric and complete freeze-drying tests were carried out. Each test was done with and without the IR camera inside the chamber to be compared. All temperature comparisons to evaluate the camera's effect in the drying chamber were based solely on TC's as the reference method. Central and edge vial temperature profiles are confronted. Edge vials are the vials in the border of the hexagonal array of a batch, having five or less neighboring vials. Central vials are vials with at least six neighboring vials.

This way, the gravimetric tests with and without the camera for a given vial size were compared in terms of: mass change in the vials, temperature profiles and global heat transfer coefficient (K_v). The complete tests with and without

the camera were compared in terms of their temperature profiles and the batch duration.

The exposure of vials to heat radiation from the walls and shelves during primary drying will vary according to the vial position in a batch [152]. Additionally, the temperature difference between the radiating surfaces and the vial will influence the radiation contribution. If the walls are relatively cooler, they will contribute less to the heat radiated to the vials.

As mentioned, the thermal camera was placed against the chamber's back wall. With this placement, the vials were being shielded from part of the back-wall radiation while they were exposed radiating effects from the camera case itself. The relative temperature profile of the camera and the wall during a batch will determine if the camera has a radiating or shielding effect over the vials. Because of this relation, an extra gravimetric experiment was done for six hours. This approach aimed to briefly explore if the freezing duration impacts the infrared sensor's influence during a batch. Longer freezing durations can result in significantly lower temperatures for the chamber walls and sensor outer case. This additional testing of two different freezing durations helps understand whether observed shielding of radiating effects were, in fact, a result of the sensor presence inside the chamber or simply due to typical wall radiating effects (or an interaction of both). With this in mind, TCs were placed on the back wall surface and on the outer case of the IR camera to evaluate their temperature.

The primary drying duration of batches with and without the infrared camera inside the chamber were compared. To this end, the $\frac{Pi}{Ba}$ method was used to determine the primary drying duration, as described in Appendix B.

ii. Sensor's Accuracy

To verify the sensor's accuracy, the IR extracted temperatures were compared with the TC-based temperatures. More specifically, the average bottom temperatures obtained with each type of sensor were compared. The average temperature gradient from edge to center measured using thermocouples in a $20x30cm$ 6R batch was roughly 0.08 K per centimeter. Additionally, IR-based and TC-based K_v and R_p values were evaluated, after being calculated as described in Subsection 4.1.1. These comparisons were helpful because the calculation of these parameters incorporates the mass change and temperature measurements, which can propagate accuracy issues becoming evident in the resulting variables. The proper and accurate estimation of these parameters by the infrared camera is critical to validate its application for temperature monitoring and process design and optimization.

Statistical analysis

Comparisons were always made confronting the values from two groups at a time. For example, for tests evaluating the camera's effect, the mass change for all vials in a test with the IR camera present was confronted to the mass change obtained in a test without the IR camera. For this type of comparison, a t-test would be recommended if the distribution of values within each group follows a normal distribution. Thus, the analyzed values (mass change and K_v values) were first tested using a Q-Q plot to verify if they followed a normal distribution. Because they seemed to follow a normal distribution, they were then confronted using a Student's t-test [153]. The t-tests done were two-tailed, two-sample t-tests assuming an unknown variance and considering a 95% confidence interval.

4.1.2 Results and discussion

i. Camera's effect

Some shielding effects on the vials placed immediately in front of the camera were reported by Lietta et al. [92]. However, that study was carried out using a small batch with 30 glass vials (ISO 8362-10R) in a rectangular array of 10 x 3 vials. In this present work, larger batches (with up to 157 vials) in a hexagonal array, 25 cm away from the IR camera were used. This larger vial number attempts to approach a real-scale process. Additionally, the impact of the camera may change with its size.

The first evaluations were gravimetric tests carried out with and without the sensor. Mass change, temperature profiles, and global heat exchange coefficient, K_v, were compared between these tests. Additionally, the mass change of the first-row vials, the ones facing the IR sensor, was closely inspected. The mass change values for the tests are shown in Figure 4.1.

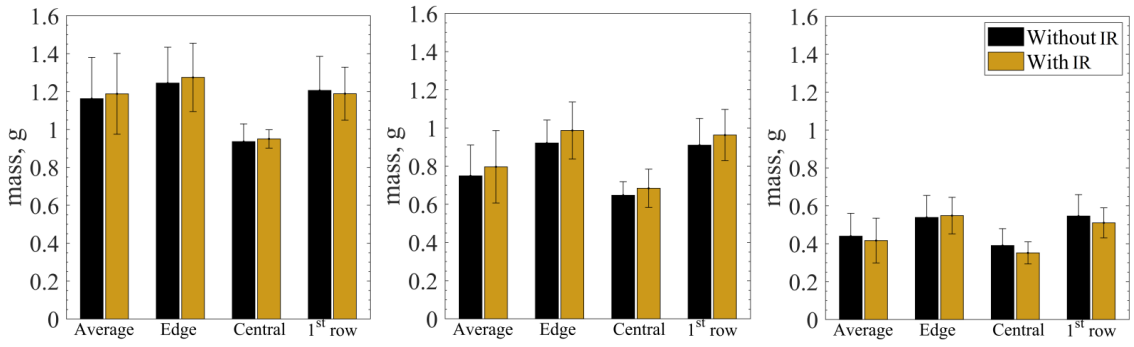

(a) 20R, 10% sucrose (b) 6R, 5% sucrose (c) 4R, 5% mannitol

Figure 4.1: Mass change for tests without and with the IR camera inside the drying chamber using the 2-hour freezing protocol.

From the results in Figure 4.1, it can be observed that they were almost unaffected by presence of the sensor. No significant difference ($p>0.05$) was found between the mean mass change of the batch and the mass change for the first row for all vials tested, 20R, 6R, and 4R.

An extra experiment using the 6R vials was performed to evaluate the camera's effect under different freezing conditions. This test compared the results from gravimetric tests using a 6-hour freezing duration with the results from a 2-hour duration. In this long-freezing experiment some shielding effect was observed from the resulting mass changes (Figure 4.2), a different result than the one obtained for the 2-hour freezing tests. Comparing the average or central mass change values, no substantial difference can be observed. However, using the 2-hour freezing, the mass change for edge vials was 2.5% greater than the mass change observed in the control test, i.e. without the camera. For the 6-hour freezing test, a 7.1% decrease was observed instead, compared to the control test. For the first-row vials, this difference was a ∼5% increase in the mass change using the 2-hour freezing (0.9627 g) while using a 6-hour freezing represented a ∼5% decrease in the resulting mass change (0.8592 g).

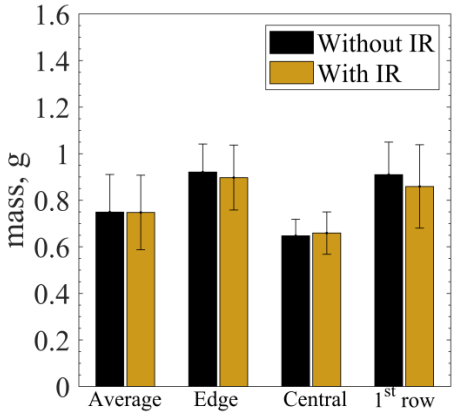

Figure 4.2: Mass change for test without and with the IR camera inside the drying chamber using the 6-hour freezing protocol for 6R vials with 5% sucrose solution.

To further investigate this behavior change, the back wall and the camera's outer case temperatures were monitored during the short and the prolonged freezing tests. At the end of prolonged freezing, the case's front temperature was 237.6 K while the back wall temperature was 261.1 K. At the end of the gravimetric test undertaken after the freezing step, their temperatures were 264.6 K and 275.6 K, respectively. This way, there was roughly a 10 K difference between the sensor case and the back wall throughout the whole test. On the other hand, at the end of the short freezing stage, the temperatures for the sensor and back-wall were 268.6 K and 272.8 K, whereas, at the end of the gravimetric test, they were 269.9 K and 267.9 K. Thus, a much smaller difference was observed between the camera and the

back wall temperature using the 2-hour freezing protocol.

It was unsurprising that the sensor reached a lower temperature than the back wall for the prolonged freezing tests as the sensor is in direct contact with the shelf, exchanging heat through conduction. The walls are not temperature-controlled in this freeze-dryer unit. When this difference between the sensor and wall temperature was modest (for short freezing), shielding effects seemed minimal. However, when this difference was pronounced enough, the cooler sensor seemed to have a shielding effect. Thus, the sensor's temperature was relatively lower when prolonged freezing was used compared to when short freezing was used. Under these conditions, the sensor can play a shielding role during the first hours of primary drying. However, this shielding effect is insignificant when short freezing durations are used.

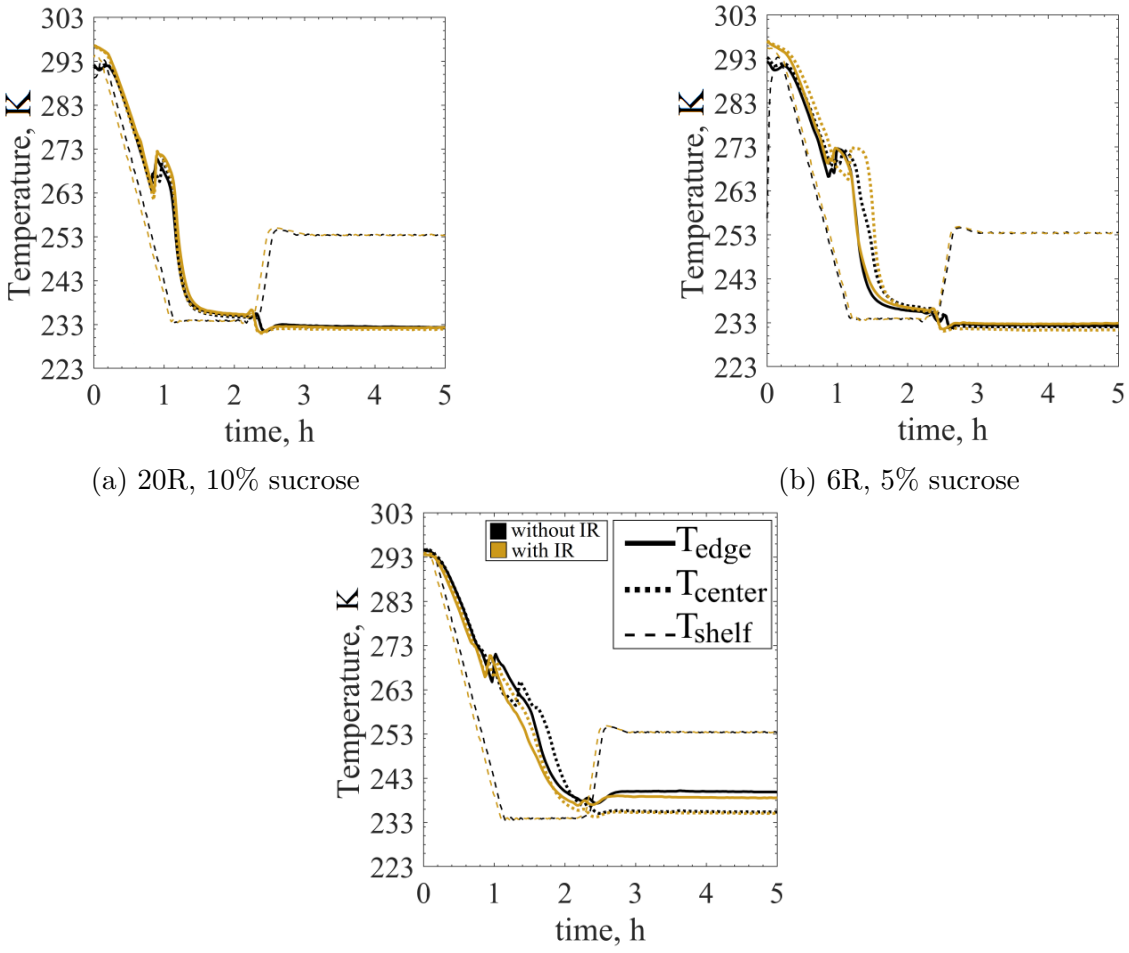

(a) 20R, 10% sucrose

(b) 6R, 5% sucrose

(c) 4R, 5% mannitol

Figure 4.3: TC-based temperature profiles for tests with and without the IR camera placed inside the chamber.

The temperature measurements during the gravimetric tests with and without the camera are shown in Figure 4.3. The 20R vials presented virtually the same temperature profiles for tests with and without the camera. The same is observed for the the 6R vials. However, for the 4R test results, while the temperature profiles seem very similar, the edge temperature profile in the test without the sensor seems slightly higher. This higher temperature was seen on the first row, edge, and overall mass change for this test, which was slightly higher than the values for the test with the camera. These profiles indicate that there was a small shielding effect from the camera for these tests.

Once mass change and temperature profile were evaluated, the resulting variable calculated from these observations, K_v, was also confronted. The mean K_v results are displayed in Figure 4.4.

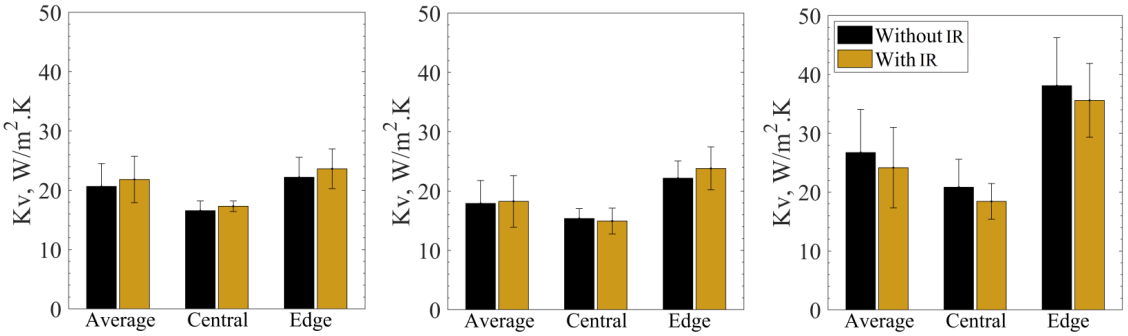

(a) 20R, 10% sucrose (b) 6R, 5% sucrose (c) 4R, 5% mannitol

Figure 4.4: Mean TC-based K_v values for tests without and with the IR camera inside the chamber.

As expected, since only small differences were observed in mass change and temperature profile, the K_v values calculated were very similar in both cases, with and without the camera inside the chamber. Average, central and edge K_v values showed no statistical difference ($p>0.05$) for 6R and 20R (Figure 4.4). However, the average and central K_v values for 4R presented a significant difference ($p<0.05$), with no significant difference for edge vials ($p = 0.48$). The precision of all used instruments was the same for all tests while the 4R vials had a smaller fill volume and a larger batch size. Hence, it makes sense that small errors derived from precision limitations would have a relatively bigger impact on the 4R measurements, resulting in more variations within and between tests. All K_v values presented in this chapter are thermocouple-based. The K_v values for the test without the thermal camera were more heterogeneous than the values in the test with it. However, checking in detail, the K_v standard deviation was derived from the mass change standard deviation, which was approximately the same for both tests.

It was necessary to investigate the distribution of K_v across the vials taking into account the typical non-uniform K_v distribution in a batch. A map with each

vial K_v is shown in Figure 4.5.

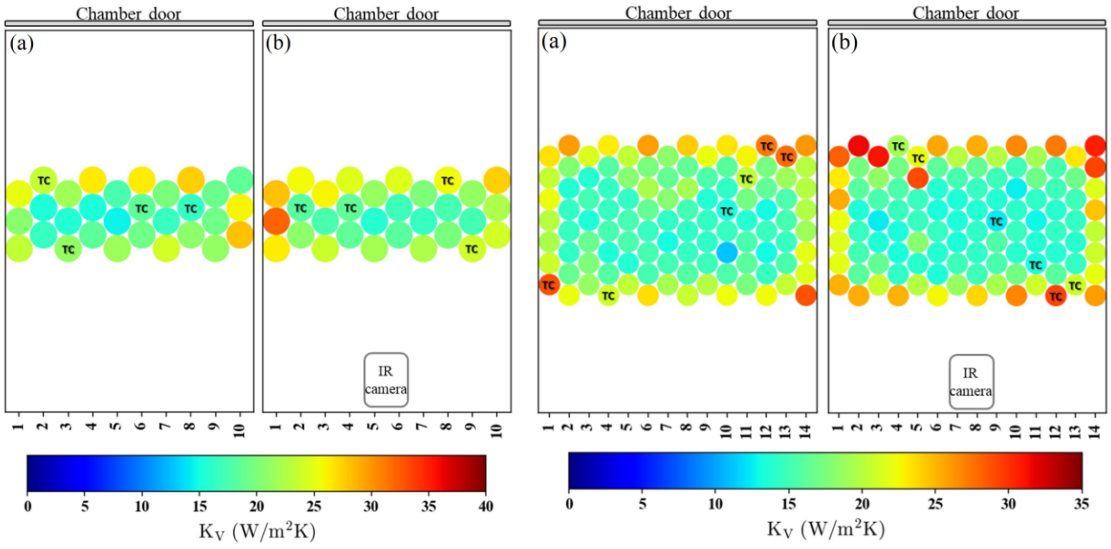

(a) 20R, 10% sucrose

(b) 6R, 5% sucrose

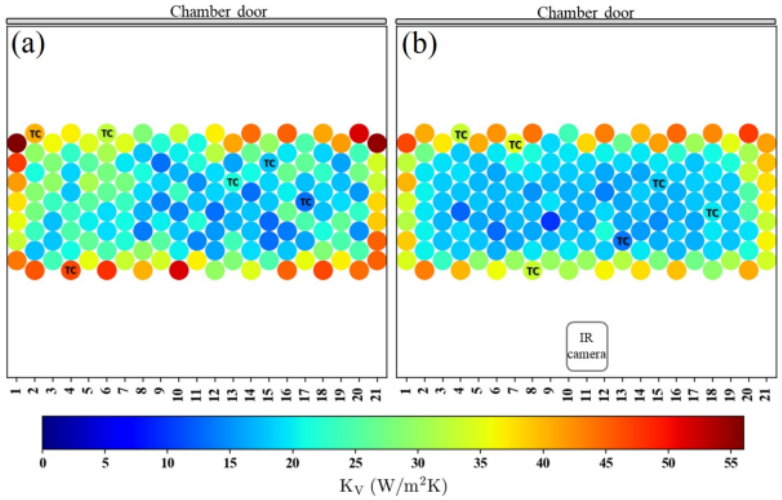

(c) 4R, 5% mannitol

Figure 4.5: TC-based K_v map for tests with (b) and without (a) the IR camera placed inside the drying chamber.

It is interesting to observe in all graphs of Figure 4.5 the more exposed edge vials using the hexagonal array (having 3 neighboring vials) present considerably higher K_v values than the less exposed edge vials (having 5 neighboring vials). This makes sense because the later are slightly more shielded by the larger number of neighboring vials. Additionally, evaluating the mass change for 4R batch after the gravimetric test with the sensor, the less exposed vials did not present a statistically significant difference from the central vials. The mass average change for central

vials was 0.37 $\pm 0.13g$ and the one for the less exposed ones was 0.45 $\pm 0.16g$. The p-value doing a Two-sample unequal variance T-test was 0.056. For edge vials, the mass change was 0.54 $\pm 0.18g$.

For the 4R tests, the initial standard deviations for the initial mass were 0.0784 and 0.0973 g before the gravimetric test. After the gravimetric test, the standard deviations of the final mass were equal to 0.1180 and 0.1206 g for the tests with and without the sensor, respectively. Since they were similar in all cases, this was considered to not affect the comparisons in any relevant way. Thus, under the tested conditions, the camera's presence does not significantly affect mass changes or temperature profiles in all tests, which is reflected in the K_v maps for 6R and 20R vials (Figure 4.5).

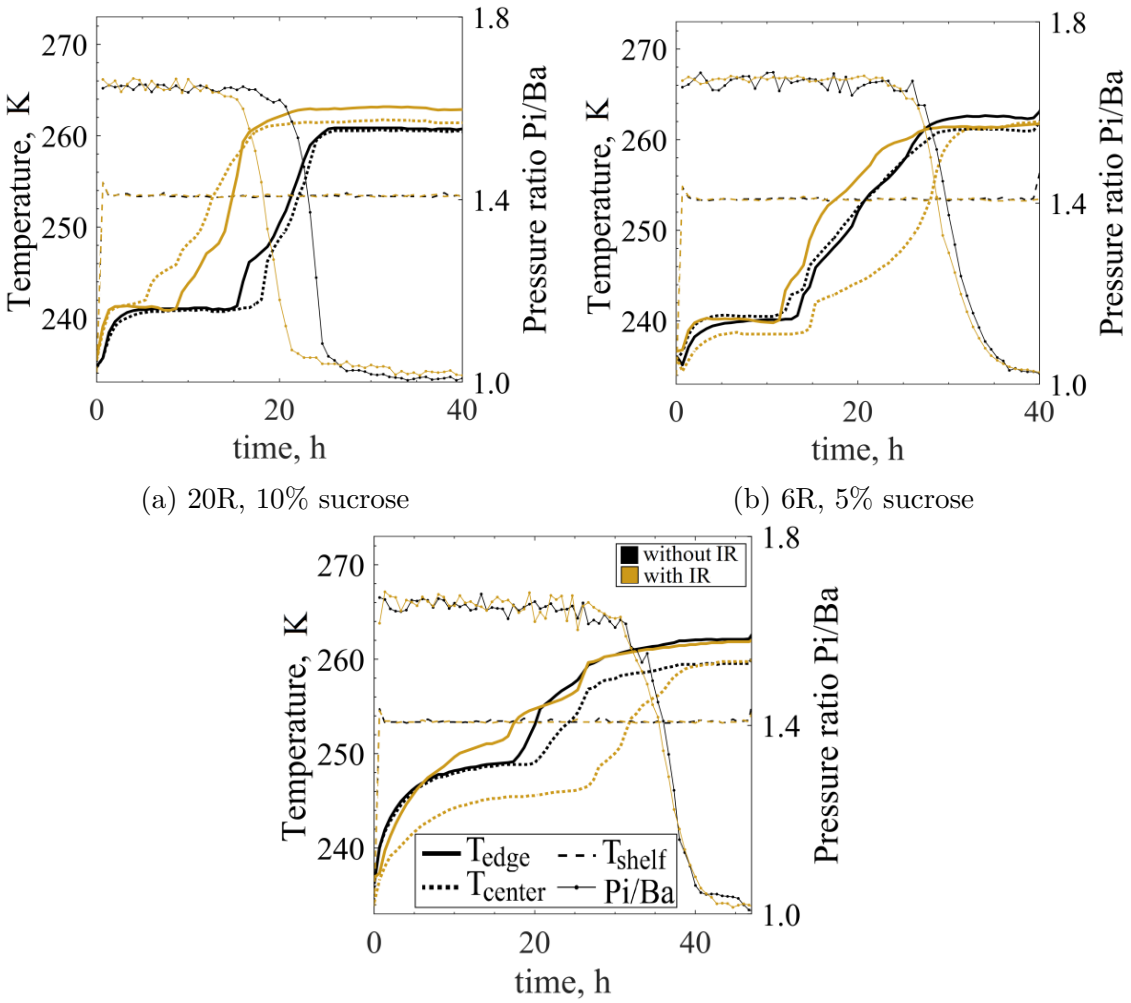

(a) 20R, 10% sucrose

(b) 6R, 5% sucrose

(c) 4R, 5% mannitol

Figure 4.6: TC temperature profiles for tests without and with the IR camera inside the chamber.

Finally, the last aspect to be analyzed was if the sensor's presence affects a complete freeze-drying cycle and its duration. Figure 4.6 shows several signals measured during primary drying, with and without the sensor in the drying chamber. As identified through the pressure ratio and temperature profiles, the camera does not seem to affect the batch duration. This lack of effect was also observed for the 6R vial batch. However, for the 20R batch, possible radiating effect were observed. The batch duration with the camera inside the chamber was approximately three hours shorter than for the test without the camera. Additionally, the temperature profiles were slightly higher, in the order of 1-2 K. This was not consistent with the previous results based on the gravimetric tests. Thus, these tests with the 20R vials were repeated because they presented a different result from what was previously observed for the 4R and 6R vials. Yet, the repeated tests yielded the same results. A possible explanation is that using shorter freezing the sensor had a slight heat radiating effect that was more pronounced after a couple hours of primary drying, whereas the gravimetric test was truncated before that. This later radiating effect was more noticeable in the 20R batch since this was a small batch with 73% edge vials, thus, more subjected to this radiation effects.

ii. Sensor's Accuracy

The accuracy of the sensor for monitoring the product temperature profile was evaluated using thermocouples as a reference tool. Figure 4.8 displays the IR-based average bottom temperature measured per vial for the 20R and 6R vial sizes. The profiles presented in Figure 4.8 evidence the temperature of more exposed edge vials (having 3 or less neighboring vials) and less exposed ones (having 5 neighboring vials) as shown in Figure 4.7.

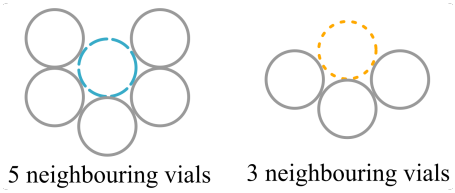

Figure 4.7: More shielded edge vials with five neighbouring vials and more exposed ones, with three neighbouring vials.

The IR-based temperature profiles for the 4R vials are can be seen in Figure 7.4 because they are also pertinent to the discussion presented in Chapter 7. Nonetheless, they present the same behavior observed here in Figure 4.8.

It is noteworthy the temperature accuracy is influenced by the angle between the object of interest and the IR camera. This angle effect means that vials away camera direct field of view, i.e., towards side edges, may present lower accuracy in the temperature measurements. Because the camera was centered relative to

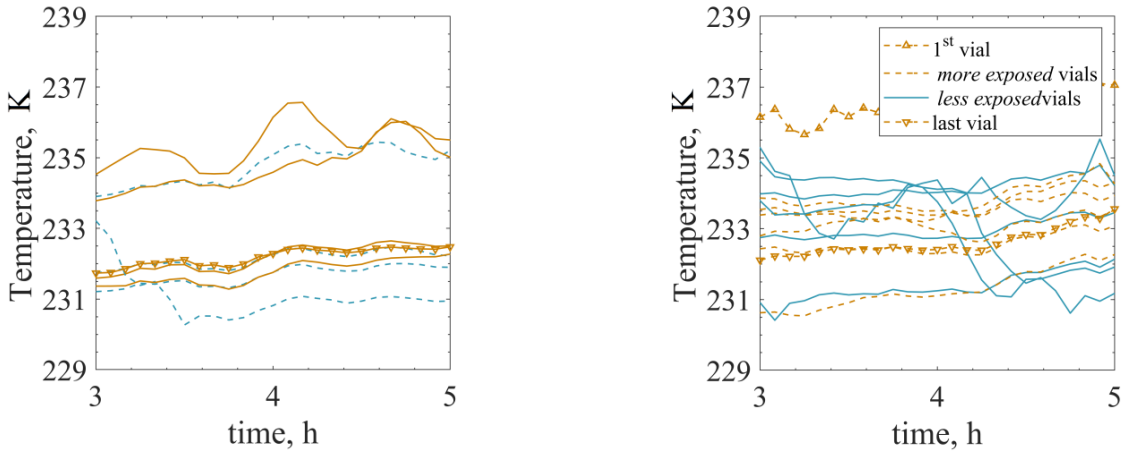

(a) 20R, 10% sucrose

(b) 6R, 5% sucrose

Figure 4.8: IR temperature profiles per vial for an arbitrary interval during the middle of primary drying. The first vial is the leftmost one and the last vial, the rightmost one from the camera's perspective. These profiles are discussed again in Chapter 7 where the 4R profiles are listed in Figure 7.4.

the shelf and the vials, angle effect should equally affect the vials towards the left and right. In Figure 4.8, the 1^{st} vial (leftmost vial) seems to present the highest temperature profiles for all batches. Apart from the inaccuracy issues that affect the less centered vials, there is another possible explanation for this behavior. From the K_v map in Figure 4.5 it can be inferred that the left side tends to be marginally warmer than the right side of the chamber. A possible explanation for that is that the electric panels of the freeze-dryer used were on the left, relatively to the camera's field of view. In any case, these results show another great advantage of infrared thermography: it easily allows exploring the heat distribution inside the equipment, enabling improved process control and design.

IR imaging provides a complete and detailed portrait of the temperature per vial in the first row. The first point to be noted is the wide range of thermal profiles according to the vial measured. Secondly, the consistently lower temperature measured for the less exposed vials (with five neighboring vials) than, the more exposed ones (with four neighboring vials) is quite interesting. This aspect is present because of the hexagonal array used and, it is further investigated in Chapter 7.

For the 6R vials, a difference up to 6 K is observed for the more exposed vial's profiles and a difference up to 5 K is observed for the less exposed ones using an hexagonal array. Although the profiles presented in Figure 4.8 present a wide distribution, the average values are practical for comparison with thermocouple measurements. Figure 4.9 presents the average thermocouple-based T_{bottom} compared to the IR-based profiles from the same batch.

The IR sensor used in this study has a reliable accuracy until around 233

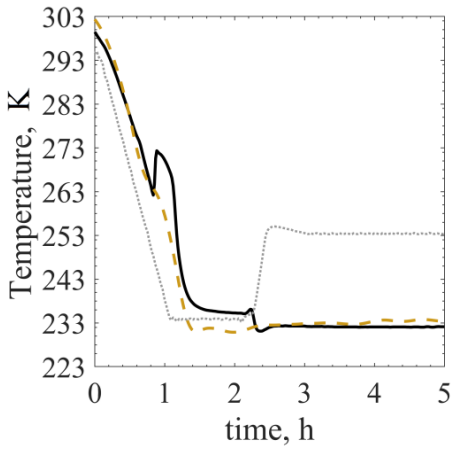

(a) 20R, 10% sucrose

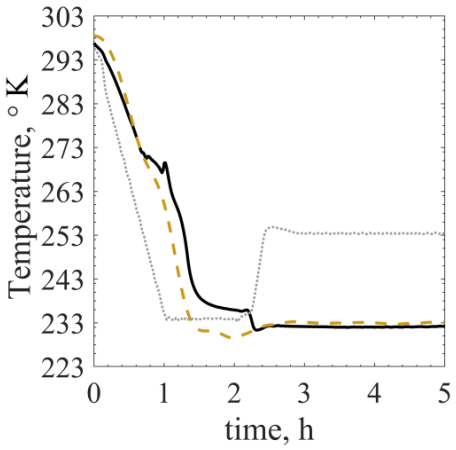

(b) 6R, 5% sucrose

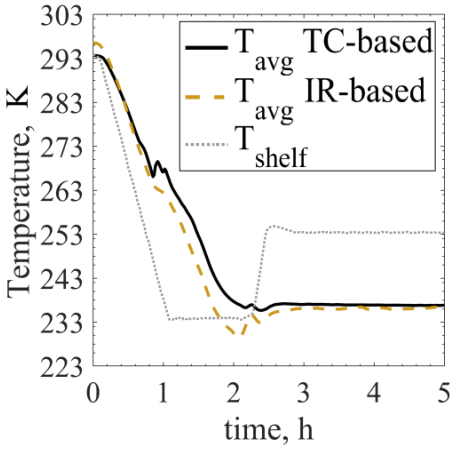

(c) 4R, 5% mannitol

Figure 4.9: TC-based average temperature profiles confronted to the average IR-based ones.

K. In the lowest point of freezing, it can be observed that part of its accuracy is lost. The IR sensor recorded marginally lower temperatures in the lower temperature section stretch with up to a 9 K difference compared to the thermocouple values observed in all tests. Nevertheless, the average thermal profiles were very close to the thermocouple ones during primary drying. The sections presenting less agreement show discrepancies of up to 3 K during the first hour of primary drying. Still, after that, it was within the thermocouple uncertainty range (± 1 K) for 4R vials. For 6R and 20R, the temperature profiles were within the ± 1 K uncertainty range most of the time.

The temperature profile accuracy will be evidenced on the K_v accuracy. For all tested vial sizes, the IR-based K_v values were very similar to the thermocouple-based ones (Figure 4.10). The differences observed were all below 2.2%.

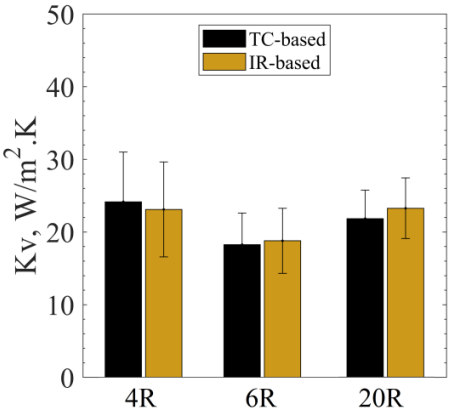

Figure 4.10: Average K_v values calculated based on the IR thermal profiles and on the TC ones.

Finally, the R_p profiles calculated using the IR-based temperature measurements were compared to the TC-based R_p. The R_p calculation used was based on the ice vapor pressure, which involves an exponential of the temperature measurements (Equation 4.3). This exponential which may magnify even the most negligible temperature measurement differences. The R_p profiles were calculated using the temperature data from the complete tests (Figure 4.6). The time interval for the R_p plot is the primary drying duration defined by the onset point of the $\frac{Pi}{Ba}$ signal.

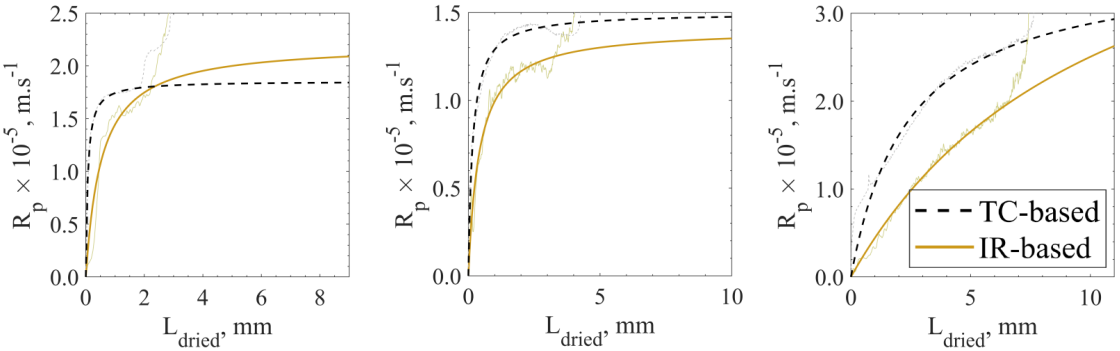

(a) R_p 20R, 10% sucrose (b) R_p 6R, 5% sucrose (c) R_p 4R, 5% mannitol

Figure 4.11: TC-based R_p profiles confronted to the average IR-based ones. The bolder lines are the fitted curves using Equation 4.8, the lighter lines are the R_p calculated with the raw data using Equation 4.7.

Each resulting R_p curve was calculated based on the average temperature profile using the thermocouples or the infrared camera measurements. This calculation was based on a simplified model (Equation 4.7), hence, it was a good approximation at the beginning of drying but not as much after a couple hours.

Thus, the R_p profile was approximated by curve fitting using Equation 4.8 to address the whole cake profile. Both resulting R_p profiles (Figures 4.11a and 4.11b) present similar values. Additionally, these observed results are within the expected range, based on values found in the literature for 5% sucrose [154]. Thus, verifying the applicability of the IR thermal imaging for estimating the R_p profiles during a freeze-drying process. For 4R vials (Figure 4.11c), again, the R_p trend based on either temperature sensor resulted in comparable R_p profiles that can be successfully used for cycle design. These R_p values for 5% mannitol were also within the range found in the literature for this solution [149].

4.2 Conclusions

This chapter evaluated potential effects of the infrared camera on batch dynamics due to the placement of the sensor inside the drying chamber. Additionally, the accuracy of this infrared camera to monitor larger scale freeze-drying batches was assessed. The camera's effect on larger batches, containing from 30 to 157 vials, was minimal and can be neglected under the tested conditions. Regarding the camera's accuracy, the temperature measurements were often within a ± 2 K range relative to the thermocouple measurements during primary drying. Furthermore, the infrared camera is a non-invasive monitoring tool and as such, it does not interfere with product and it is not destructive to the monitored samples. The use of an infrared sensor removes the need for placing the thermocouples in the monitored vials of a freeze-drying batch. Additionally, the heat and mass exchange parameters needed for primary drying design space calculation, K_v and R_p, were estimated with reasonable accuracy using the IR-based temperature profiles

Part III

Infrared thermography applied to the freezing stage

Chapter 5

The freezing phenomenon

5.1 Introduction

When water is frozen into ice, a complex interplay of events takes place. Most substances become denser as they are cooled, and they are denser in the frozen state than in the liquid state. However, when water is cooled below 277.15 K, it begins to expand. Because of this expansion, water becomes less dense than liquid water when it freezes. This density change is why ice floats [40].

Ice crystals may have several different structures (Figure 5.1). No other known substance presents such a variety of conformations [155]. The equilibrium line between liquid water and ice Ih has a negative slope. This slope shape is due to lower density of the solid phase compared to the liquid one. This behavior is different from most substances and different from the higher pressure ice phases. Although there are eleven crystalline forms of ice, only the hexagonal form (Ih) is found naturally on earth, manifested, for example, in six cornered snowflakes. At lower temperatures and pressures above 2 kbar, many other less common ice structures may exist [40].

Figure 5.2 shows the time-temperature relationship for freezing of pure water ($ABCDE$) and aqueous solutions ($AB'C'D'E'$). This figure serves as a brief review of the physicochemical events that occur during a freezing process. The first thermal event is called supercooling (also called undercooling), i.e., cooling the solution below its equilibrium freezing point T_f (B or B') [40]. Water cooled below its equilibrium temperature can remain in the liquid state for hours before the phase transition into ice. This undercooling (or supercooling) represents a metastable water state. When solutions are below the freezing equilibrium temperature, the formation of ice is thermodynamically favored.

Nucleation, is a process of random generation of small formations of the new, thermodynamically stable phase (nucleus) that have the ability for irreversible overgrowth to macroscopic sizes. However, to allow the firsts ice nuclei to form, an energy barrier has to be surpassed by the system. This energy barrier depends on

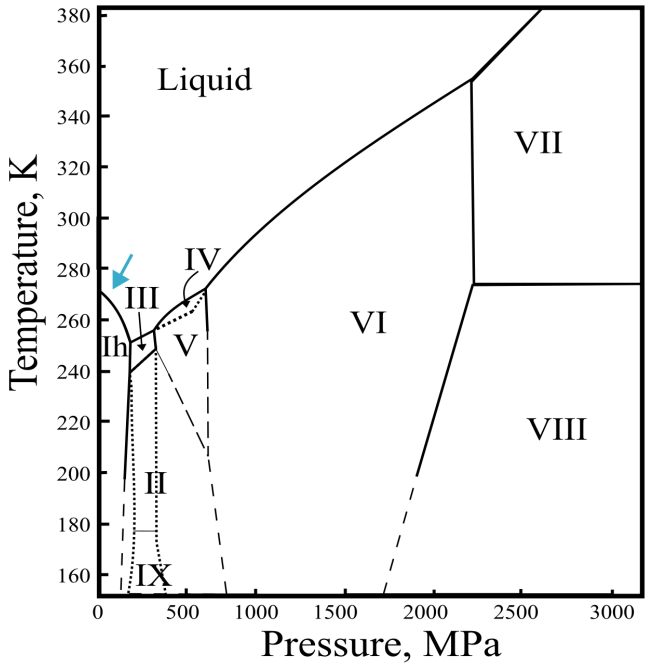

Figure 5.1: Ice-water phase diagram. The phase diagram of ice shows the conditions of stability for the ice phases. The arrow points out the Ih form [155].

the supercooling degree, i.e., the system's temperature below the freezing point [156]. The probability of such occurrence depends on the driving force for nucleation, which is the chemical potential differential between the thermodynamically stable phase (nuclei) and the metastable parent phase (supercooled solution) [157]. Moreover, the supercooling degree defines the critical nuclei dimension according to the system's conditions [156]. Forming an ice-water interface having ice nuclei below this critical value would require more energy than the one available in the solution.

After the formation of the first nuclei (B or B'), an event called nucleation, part of the solution freezes releasing energy. The energy released is enough to increase the solution's temperature to its equilibrium freezing temperature, T_f (C or C'), and this may be observed when using slow freezing rates [40]. The rate of nucleation is proportional to the surface area for heterogeneous nucleation. Hence, the added solute accelerates the nucleation process [158]. That is why B' is not as low as B. C' is lower than C because solutes cause a freezing point depression according to Raoult's law, which relates the solution's vapor pressure to the pure solvent's one based on solute concentration. Hence, the solute causes a decrease in the supercooling degree by promoting faster nucleation and lowered freezing point. In the pure water curve, C to D is the ice crystal growth interval. [40].

The freezing time (t_f) is defined as the time from nucleation onset (C) to the complete removal of latent heat (D). The temperature then drops from D to

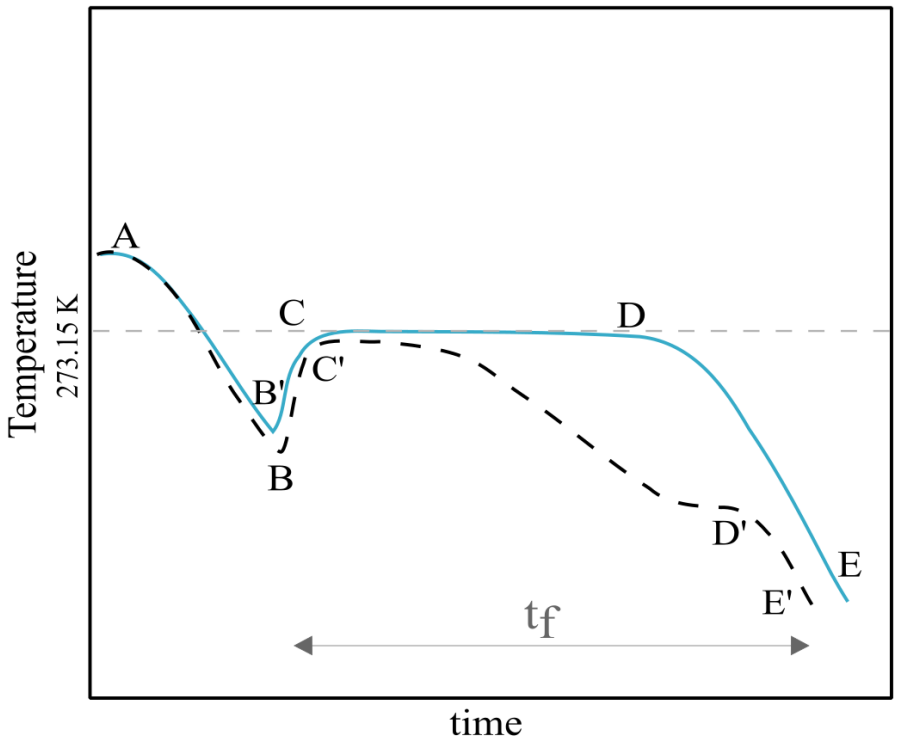

Figure 5.2: Freezing curves for water (-) and a hypothetical solution (- -).
Adapted from [40]

E as sensible heat is removed after crystallization is completed. During freezing of aqueous solutions, water freezes out of solution in the form of pure ice crystals (D'), leading to a freeze-concentration process. Still, some water remains in the liquid state even at temperatures considerably below the freezing point. An increase in the viscosity of this remaining liquid phase takes place, decreasing the system's diffusion properties and obstructing further crystallization. At D', one of the solutes may become supersaturated and release its latent heat of crystallization, causing a slight jump in temperature. These points are known as eutectic (T_{eu}) point for crystalline solutes and glass transition temperature for amorphous ones (T_g) [148]. After E', continued crystallization of the solvent and possibly of the solute may take place until the system is completely crystallized or solidified at very low temperatures. It is difficult to assign a precise freezing time to the freezing process of solutions based on the temperature. Nonetheless, it is usually assumed to be the time required to reach some predetermined temperature below the initial freezing point [40]. Although, the solidification end-point could be observed reflected in the inflection of the real-part capacitance measured at high frequency using through-vial impedance spectroscopy (TVIS) [159].

5.1.1 Freezing in vials

When freezing solutions in vials, the product is first in its liquid form and then cooled. The solution typically cools down below its freezing equilibrium temperature, staying in a supercooled state. Then, nucleation stochastically happens, which is visible since the solution immediately turns opaque. Subsequently, the shelf temperature is further lowered, and ice crystal growth takes place. Solutions being frozen are usually cooled until a point below their eutectic point or the glass transition temperature, according to the nature of the solute. Figure 5.3 portrays this process with pictures from experiments to evidence the freezing process in vials.

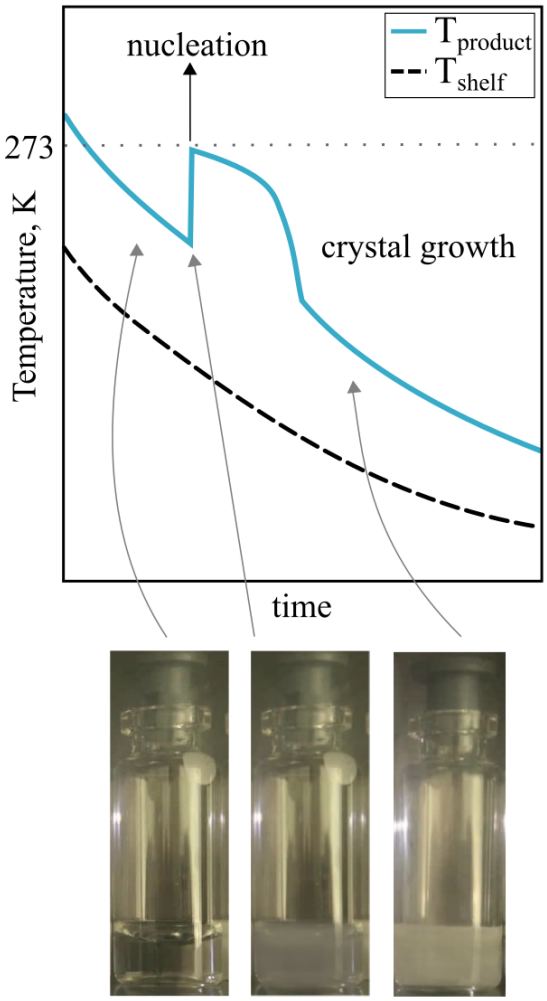

Figure 5.3: Typical freezing process of solutions in vials with pictures.

The freezing step for solutions in vials has been closely studied as it was proven to have a substantial influence on the drug residual activity [34, 39] and

on the product structure [32, 38]. In fact, the T_n is the main parameter affecting product morphology [57]. As described above, the supercooling degree determines the critical nuclei dimensions. Larger supercooling degrees require smaller critical diameters. In turn, the probability of the appearance of a stable nucleus in the solution increases ([160–163]. Therefore, the dimension and number of the ice crystals depend strongly on the nucleation temperature (T_n).

Moreover, slow freezing rates provide more time for the ice nuclei to form around the surfaces present (particles) at higher temperatures. Meanwhile, the diffusion of water molecules to the ice front is enhanced at higher temperatures facilitating crystal growth. This results in larger crystals. On the other hand, fast freezing promotes nucleation at lower temperatures. The mobility of water molecules under lower temperatures is lessened and so is the ice growth rate. This results is smaller ice crystals [159].

The ice crystals formed create the initial template for the porous structure of the freeze-dried cake of the resulting product. When low nucleation temperatures are used, a considerable number of small nuclei are generated. On the other hand, when higher nucleation temperature are used, fewer crystals but of greater size are generated [14]. Moreover, the porous structure is correlated with the vapor mass transport (J_w) (or the resistance thereof, R_p) during sublimation. In this stage, the water vapor being released moves from the frozen interface through the already dried fraction of the product and then to the chamber. The R_p influences the required time for ice removal and the product temperature during the primary drying stage [47].

Nucleation is often regarded as a series of phenomena, including a primary and secondary nucleation phenomenon. The difference between primary and secondary nucleation is that the first occurs in the absence of crystalline surfaces. Secondary nucleation occurs with pre-existing breeding crystals, surfaces, or interactions with walls, or impellers, amongst others. The primary one is highly stochastic. Hence, the induction times t_{ind}, i.e., the time interval between the point in which the solution reached its saturation and the moment when the first ice nuclei are formed, may largely vary. The product is cooled using the same rate for all vials in a batch to promote nucleation and crystal growth. Because of this, the random behavior of the induction times yields a stochastic distribution of the nucleation temperature across a batch. This non-uniform nucleation temperature distribution is one of the primary causes of batch heterogeneity. This condition leads to significant variability in the resistances to mass transport and thus, large range of the in-batch drying time [51]. One could interpret the stochastic behavior of nucleation as a probability distribution, in which the probability of homogeneous nucleation at 273.15 K would be close to zero while it would be 1 at 233.15 K. This would be an ideal scenario of *pure* water, not a practical one.

Nucleation can be manipulated to control the nucleation temperature directly and, therefore, reduce in-batch variability. After the nucleation process

starts, ice is formed rapidly, and the whole vial can change its optical properties, due to the appearance and growth of the nuclei, in a couple of seconds [19].

5.1.2 Controlled freezing methods

Because freezing is stochastic, using conventional freezing methods for freeze-drying applications results in vials nucleating at different temperatures. Because the nucleation temperature drives the size of the ice crystals formed, freezing is responsible for a lot of the heterogeneity present in a batch. Hence, controlled freezing techniques have recently gained popularity in the freeze-drying field to increase batch homogeneity, and better control product quality [51]. This way, a better understanding of the freezing phenomena and its implications for product morphology is of critical importance.

In an attempt to make the pore distributions more uniform or reduce batch heterogeneity, different controlled freezing techniques have been proposed. These techniques include annealing [164], pre-cooled shelves [38], ice-fog [59], electric field-induced nucleation [165] and VISF [11, 166] to list some. The cooling rate, the type of vials, and the filling height also play a role in affecting freezing since they influence the heat exchange during freezing and may affect the supercooling degree [38].

Annealing is a technique that only requires shelf temperature control. It does not control the nucleation temperature *per se*, but it is used to obtain a more homogeneous product structure across a batch. It consists of performing a ramp freezing without necessarily reaching a very low temperature. Then, after nucleation and partial freezing of the solution, the shelf temperature is increased and kept above the product's glass transition (and/or) temperature to induce a slender thawing of the frozen fraction [55]. This annealing temperature should be below the ice melting temperature and above the glass transition temperature of the freeze-concentrate (T'_g). The product may be kept at this temperature for a few hours [54]. This step takes place in a more homogeneous fashion for all vials in a batch, decreasing the intra-vial variability and rendering larger pores. More uniform drying cycles were reported after an annealing step was performed [54, 167].

Loading the vials onto the pre-cooled shelves (between 230-240 K) induces nucleation at higher T_n values. A possible explanation for this lays in the nucleation probability according to the solution's temperature. The probability of nucleation taking place is larger the lower the temperature. When vials are placed onto pre-cooled shelves, there is a large temperature gradient between the shelves and the vial. This promotes heat exchange between the two, which causes a fast cooling of the bottom surface of the vial. This surface in turn will promote a fast cooling of the solution in contact with it. This portion of solution at an extremely low temperature will have a higher probability of nucleating, inducing nucleation in the remaining of the solution which is still at a higher temperature. Thus, nucleating at higher

temperatures aims to cause a fast heat-removal due to the large temperature gradient between the product and the shelf and induce nucleation at higher temperatures. It does work well, and nucleation seems to be very sensitive to the shelf temperature chosen. However, despite achieving nucleation at higher temperatures, a wide range is observed between the nucleation temperatures between vials. Thus, batch homogeneity is not increased [14].

Nitrogen gas is passed through refrigerated coils (usually immersed in liquid nitrogen) and then introduced into the freeze-dryer chamber to perform the ice-fog technique. Ice fog is forced into the vials as the cold nitrogen gas enters the chamber, inducing nucleation at the desired temperature. This technique can be done in combination with reduced chamber pressure to improve the process. This technique, however, requires more GMO controls since the fog introduction could contaminate the product [15].

Electrically induced nucleation can be applied to any desired number of samples at the same time. However, to do so, electrodes or cannulas in contact with the solution are needed. Again, this creates a new possible contamination point that required proper Hazard Analysis and Critical Control Points (HACCP) and cGMP controls [165].

VISF is a convenient method because the required elements are commonly present in most freeze-drying equipment. All it needs is an ISO valve between the condenser and drying chamber (as shown in Figure 1.2) and manual or semi-automatic control over the vacuum pump and condenser [19]. In this technique, the chamber pressure is reduced as fast as possible to a product-specific value (approximately 0.1 to 0.2 kPa) and held until nucleation occurs in all the vials. After nucleation occurs, the chamber pressure is restored to atmospheric pressure. During the VISF a fast cooling of the upper layer of the solution is caused by the evaporation prompted by the vacuum. If the procedure is performed fast enough, the solution's surface cools so much that spontaneous nucleation occurs at the solution's surface. This surface nucleation instantly induces ice nucleation in the rest of the solution at the predefined T_n. Applying VISF in a process promotes a uniform nucleation temperature through the whole batch [53].

5.2 Experimental investigation: can IR monitoring help understand the freezing phenomenon?

Commonly, the temperature measurements are done using thermocouples in the research and development scale or TEMPRIS on a large scale. However, these sensors can only give point estimations, not temperature distributions. Moreover, they are invasive probes, strongly interfering with the monitored system, i.e., increasing the nucleation temperature. Additionally, since they only offer punctual temperature information, the acquired data must be extrapolated to the neighboring

vials, assuming similarities in the conditions, which do not always correspond to reality.

It is possible to use different technologies to monitor the freezing process [80]. Freezing was experimentally studied using simple image analysis to obtain the freezing progression in a solution [70, 168]. An infrared camera was previously applied to monitor the freezing step, but the data extraction algorithm used had many noise-reducing filters that impacted the data resolution [143]. Nonetheless, infrared monitoring of the freezing stage is incredibly promising. First, because it does not interfere with the process itself, and second, it can provide temperature distributions. This ability to provide a full product temperature profile provides an almost complete knowledge of the system without introducing additional heat transfer models. Therefore, applying infrared monitoring to the freezing stage with the new data processing algorithm seemed promising. Additionally, the application of IR thermography to the freezing step using controlled nucleation had not yet been investigated.

This section presents new experimental observations of the freezing phenomenon in vials using an infrared camera. These observations methodically evaluate different aspects of freezing. Moreover, the effects of spontaneous nucleation versus induced nucleation using the VISF technique are investigated[1].

Additionally, the effects of the different heat transfer mechanisms - using different vial setups - occurring during freezing are compared. This is included in this thesis research because the suspended vial configuration was proposed as an alternative for a continuous freeze-drying process and may result in more homogeneous temperature distributions in a batch [19]. Figure 5.4 illustrates the differences in the heat transfer between the two tested vial configurations.

Using the ON-shelf vial configuration, most of heat transfer takes place between the bottom of the vial an the shelf during freezing. The vial's bottom is not perfectly flat, it has a small gap where gas gets trapped. This way, the heat-exchange mechanism between the shelf and vial's bottom is conduction through the vial's contact points and though the trapped gas. Additionally, heat is exchanged through gas conduction and convection on the vial sides, besides radiation. It was estimated that gas conduction is the main heat-transfer mechanism using this configuration, accounting for 90% of the heat-exchange [19]. During drying, heat transfer is highly affected by the pressure in the drying chamber, with higher pressures resulting in more conduction. Most of the heat removal takes place between the vial bottom and the shelf and the heat exchange. This creates a large temperature gradient in the vial while radial and azimuthal effects can be neglected. Thus, for this vial setup, the thermal gradients can be approximated as unidirectional.

For the OFF-shelf configuration, natural convection is predominant and,

[1]Part of the results presented in this Chapter have been previously published in [169]

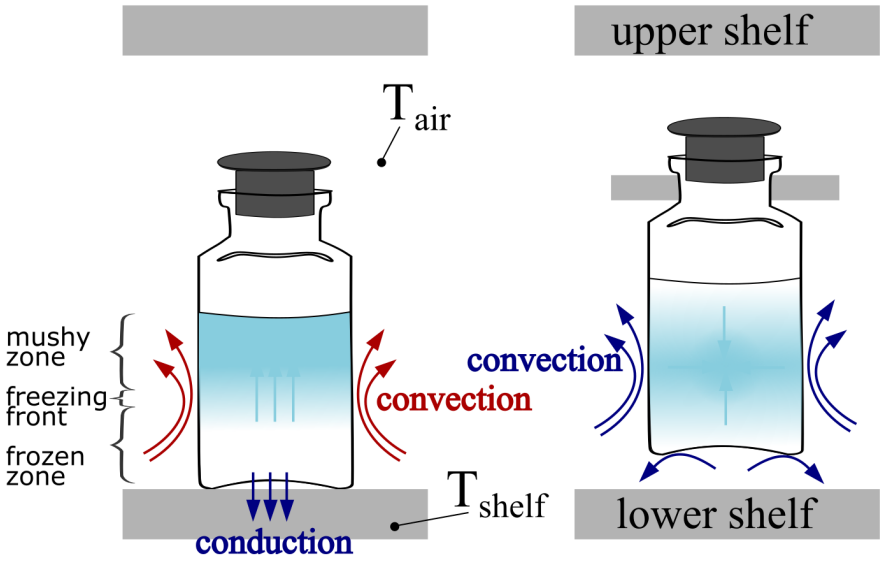

Figure 5.4: Schematic of the heat transfer during freezing of solutions in vials cooled by the shelf using the ON-shelf and the OFF-shelf configuration. The arrows represent possible freezing front profiles according to the configuration used.

heat is transferred through the bottom and the side of the vials almost uniformly. In this case, heat is supplied by radiation from the temperature-controlled surfaces, gas conduction, and convection. The contribution of gas conduction has been estimated to be around 62% with a 10 *mm* clearance, whereas radiation accounted for 38% [19]. In this scenario, it is reasonable to assume that freezing would proceed at the same rate along the vertical and the radial directions creating a frozen shell growing towards the center of the vial. Unfortunately, if this is the case, the solution in contact with the vial's wall would freeze first, and no advancement of the freezing front would be visible anymore with an IR camera.

The IR camera only monitors what happens on the outside of the vials within the field of view of the camera. IR monitoring depends a lot on the solution being in equilibrium with the vial wall and representing the product. That is true for ON-shelf vials that have negligible azimuthal and radial gradients [138]. However, the IR camera is not able to give accurate information about the inside of the product cake if there are radial gradients of any kind in the solution. Because of natural convection, it would be plausible to observe an almost homogeneous temperature profile from the outside of the vial with the two minima at the bottom and the top. Thus, the most considerable effect of this modification is that, in the suspended configuration, freezing cannot be considered unidirectional anymore and the experimental observation of the phenomenon itself can be more challenging.

The idea was to check if IR infrared monitoring could bring new insights

into the freezing phenomenon, experimental temperature profiles, heat transfer, and their impacts on the resulting dried product structure. These new observations will be thoroughly discussed ahead in this section. It is expected that they may also be helpful in the development of future models or adjustments to the current ones.

5.2.1 Experimental approach

For all the experiments, a total of 10 4R vials are used with a 1 mL fill volume of 5% sucrose, 5% mannitol, or 10% dextran, resulting in a 10 mm cake height (further descriptions of the materials in Appendix A). To test the effect of different heat transfer scenarios, two different configurations are used, as described in Figure 5.5.

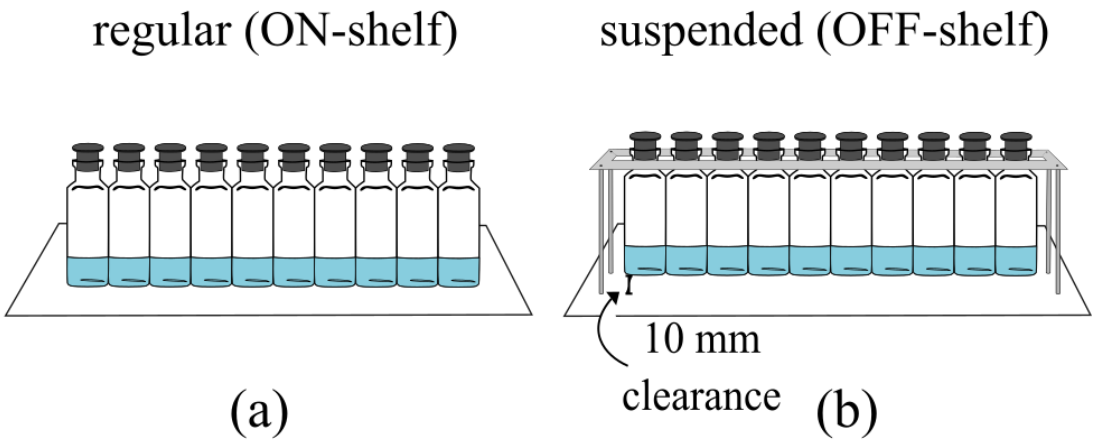

Figure 5.5: Experimental setup representations (not to scale). (a) ON-shelf and (b) OFF-shelf vial configurations used.

In the first configuration in Figure 5.5, the vials are placed in direct contact with the shelf. This way, heat is mainly transferred to the product by conduction between the shelf and the gas trapped in the vial bottom. This configuration will be called ON-shelf throughout the paper. In the second one, the vials are suspended by a Plexiglass track, as presented by Capozzi et al. [19], having a 10 $mm \pm 1$ mm clearance. This way, heat is transferred only through natural convection and radiation. This later configuration will be called OFF-shelf throughout the paper.

The Lyobeta 25 was the freeze-drying equipment used with an additional stainless steel box to reduce the radiation effect from the non-thermally controlled freeze-dryer walls. This is a 260 x 280 x 205 mm (width, depth and height) stainless steel box (Figure 5.6). The metal box was carefully designed. It had holes strategically placed to allow observing the vials with the IR sensor from outside at an approximate distance of 25 cm while guaranteeing uniform vacuum conditions. Moreover, it was placed in direct contact with two adjacent shelves, up and down,

to ensure thermal uniformity between the shelves and the walls of the box. This way, the box walls had a temperature profile at least 10 K lower than the chamber walls during most of the process. The IR sensor was placed between the back wall of the freeze-dryer and the metal box. Figure 5.6 shows a picture of the system.

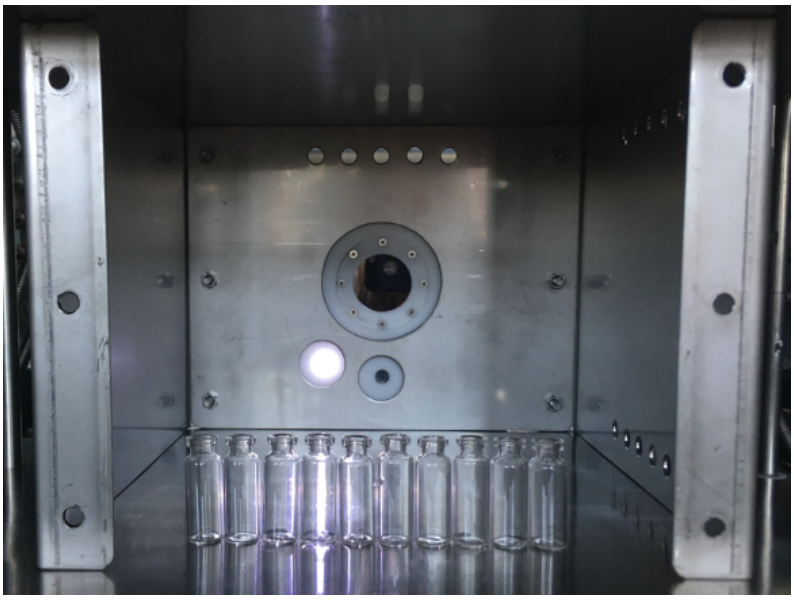

Figure 5.6: Picture of the box used with the IR sensor behind it and 10 vials placed ∼25 cm from the sensor, as set for the experiments. The front wall of the box was removed for the picture.

All temperature profiles were monitored using the infrared camera. The data acquisition was done as explained in Chapter 3, Subsection 3.3.3. The relevant variables discussed in this chapter are the T_{bottom}, T_{prof}, T_{max}, H_{max}. The first one, T_{bottom}, was just used as a standardized comparison variable across different vials in a test. The T_{prof} was important to observe the axial temperature profile and evaluate differences from the batch configurations used. Finally, T_{max} and H_{max} were crucial because, since freezing is an exothermic process, these variables may help to observe the freezing front temperature and position experimentally. Hence, the validity of this assumption is tested using these variables.

In all the controlled nucleation experiments, the vials were first equilibrated at the selected nucleation temperature T_n for ∼1 h. Then nucleation was induced by subjecting the samples to low pressure, using the VISF technique (Figure 5.7), as better explained in the previous Subsection 5.1.2 [53, 170].

In sum, the experiments in this section investigate freezing using three different solutions, sucrose, dextran, and mannitol testing two types of nucleation, spontaneous and controlled by VISF, using two different T_ns. A summary of the tested conditions is given in table 5.1.

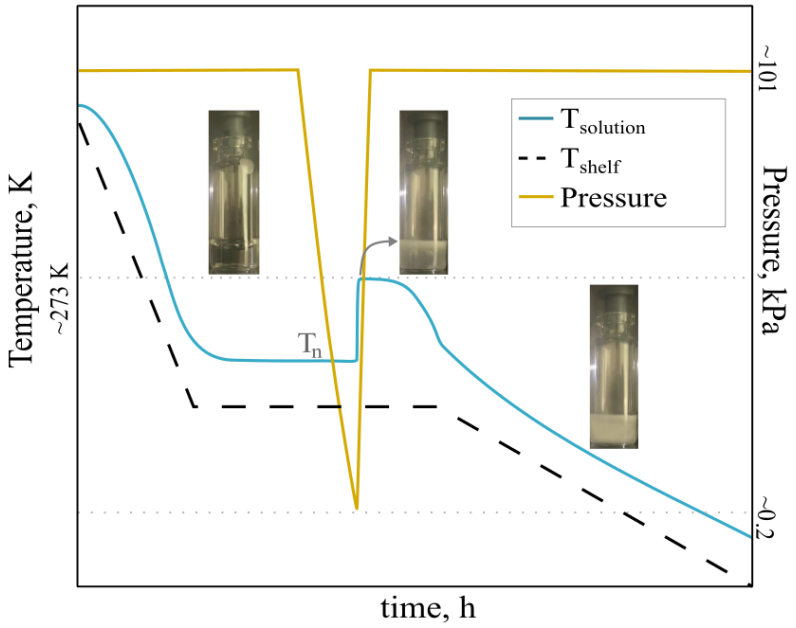

Figure 5.7: Schematic of the VISF technique. First, the shelf temperature is reduced to promote cooling until de desired T_n. After a couple of hours of stability at the desired T_n, the chamber pressure is reduced until approximately 0.1-0.2 kPa (1-2mbar). As soon as all vials are nucleated, the chamber pressure is restored to the atmospheric one using a nitrogen stream. Pictures represent the observed visual changes for the solutions inside the vials during the process.

Applying VISF in a process promotes a uniform nucleation temperature for the vials in a batch. As presented in Table 5.1, two values of T_n were used to test the effect of different nucleation temperatures on the ice crystal structure. The first, 271 K, close to the equilibrium temperature and the second, 263 K, on the limit of observing spontaneous nucleation for the solutions used. The shelf temperature (T_{shelf}) used when implementing VISF was set according to the loading configuration used (Figure 5.5) to obtain the same product temperature using different setups. This way, the shelf temperature for ON-shelf vials was 268 K to achieve a 271 K T_n and 258 K for a 263 K T_n. Using the OFF-shelf setup, the shelf temperature used was 262 K to achieve a 271 K T_n and 248 K for a 263 K T_n.

After nucleation, the shelf temperature was kept at the holding temperature (T_h) for 1 hour to ensure complete freezing. The shelf temperature to achieve the chosen T_h also depended on the batch configuration used and was the same T_{shelf} used to obtain a 263 K T_n, i.e., 258 K for ON-shelf setup and 248 K for OFF-shelf one. This way, the degrees of freedom of the freezing operating conditions are reduced.

After the holding time, shelf temperature was lowered to 223 K at a 0.5

Table 5.1: Solution, nucleation temperature and batch configurations used in the tests.

Type	Test code	Solution		Nucleation
ON shelf	Sp-ON	5%	sucrose	Spontaneous
	1-S	5%	sucrose	VISF ~271 K
	1-M	5%	mannitol	
	1-D	10%	dextran	
	2-S	5%	sucrose	VISF ~263 K
	2-M	5%	mannitol	
	2-D	10%	dextran	
OFF shelf	Sp-OFF	5%	sucrose	Spontaneous
	3-S	5%	sucrose	VISF ~271 K
	3-M	5%	mannitol	
	3-D	10%	dextran	
	4-S	5%	sucrose	VISF ~263 K
	4-M	5%	mannitol	
	4-D	10%	dextran	

K/min rate and held for two hours at 223 K. For spontaneous nucleation experiments, the product was held at the lower T_n, i.e., the shelf temperature required to obtain a 263 K product temperature for several hours. After that, the shelf temperature was lowered to 223 K at a 0.5 K/min rate and held for two hours. Visual inspection was used to verify when nucleation took place in all vials, i.e., observing when all vials turned opaque.

After freezing, the primary drying conditions were the same for all the tests. Chamber pressure was first lowered to 5 Pa, then, the shelf temperature was increased from 223 K to 253 K as fast as possible. The shelf temperature was kept at 253 K for 15 hours to complete primary drying. The shelf temperature was then raised from 253 K to 293 K in a 4-hour-ramp and then maintained at 293 K for two hours to complete secondary drying. At the end of the process, the vacuum was broken with a stream of nitrogen. Then, the vials were stoppered, sealed with aluminum caps, and stored in a freezer at 253 K for further evaluation.

SEM analysis

The dimension of the pores was analyzed using a Desktop SEM Phenom XL (Phenom-World B.V., Netherlands) at an accelerating voltage of $15kV$. The samples were extracted from the vials by carefully breaking the vial glass. This was done under a stream of nitrogen gas to prevent moiture from the environment

to be absorbed by the sample. The dried cake was then cut vertically, having a thickness of approximately 1 mm. The slice was then fixed on an aluminium circular stub and metallized with platinum using a sputter coater (Balzer AG, type 120B, Balzers, Liechtenstein). SEM pictures of the product were taken along five levels on the vertical axis to represent well the porous cake structure. In this Chapter, only the first, third, and fifth cake levels (bottom, middle and top) are examined. In Chapter 6, all five levels are analyzed in detail. The SEM images of the porous product structure obtained were 1088 × 1024 pixels.

These images were segmented using image processing techniques to extract the pore size distribution coupled with Multivariate Image Analysis [171] as described in [142].

Multivariate Image Analysis (MIA) techniques [171] were used to delimit the areas of the images that corresponded to pores. Some SEM images can present regions with a lighter hue than others on average due to a charging effect. The luminosity of the pictures was equilibrated using a moving average filter with 128 pixels x 128 pixels dimension [172]. Information was created for each image as the "Bharati matrix" [173], a data matrix that computes the intensities of the single pixels and the relative intensity compared to neighboring pixels. A Principal component analysis (PCA) model [174, 175] was retrieved from the resulting data matrix. The PCA performed a bi-linear decomposition of the $X_{img}(v_1 \times h_1)$ matrix as shown in Equation 5.1:

$$X_{img} = S_c L_d^T + Res \tag{5.1}$$

The $L_d(h_1 \times h_2)$ is the matrix of the loadings, $S_c(v_1 \times h_2)$ is the matrix of the scores, and $Res(v_1 \times h_1)$ is the matrix of the residuals. The later has the same number of rows and columns as the data matrix X_{img}. The variable h_2 corresponds to the extracted latent variables, v_1 is the number of pixels of the picture used to build the *Bharati* matrix and, h_1 is the number of columns, i.e., one for each variable of the *Bharati* matrix. Because a 3×3 moving window was used and each variable corresponds to the intensity of one of the pixels in the moving mask, h_1 equals nine. Each of the entrances of the X_{img} matrix reports a pixel intensity, thus, no additional data pre-treatments were conducted.

The first latent variable regards the mean intensity of each pixel, ignoring the gradients that are usually present in the edges, cracks, and other texture-type information. The pores were delimited by selecting all the pixels that had a higher score than the manually chosen limit. This protocol resulted in a intermediate image in which the segmented pores were highlighted as areas numerically described as *ones* while all the remaining pixels, which did not correspond to a segmented pore, were computed as *zeros*.

A second filter was applied to segment the brighter areas of the image and the areas having pronounced pixel intensity gradients. The objective was to

identify and remove the borders between two conterminous pores to ensure they were detected as different ones and not overestimated their area. This second filter was the *Canny* algorithm for edge detection [176]. The resulting masks are logical matrices that were combined as a logical *or* to further delimit the identified pores in an image.

Finally, all areas formed by less than 50 pixels or by more than 105 pixels were removed using a dimensional filter. Image noise cane be easily mistaken for tiny pores. At the same time, areas that are larger than the second established threshold value usually corresponded to fractures or micro-collapses of the cake. Including either of these values to the calculated pore size distribution would have negatively affected its characterization. A qualitative result of this image segmentation process is shown in Figure 5.8. Different colors have been applied to each different pore for better visualization. The cake structure from the source SEM image has not been edited. The number, area and equivalent diameter of the pores computed using the *regionprop* function [177–179]. For the variability evaluation, the 25th, 50th, and 75th percentiles were calculated from the histogram of the pore diameters obtained for each sample.

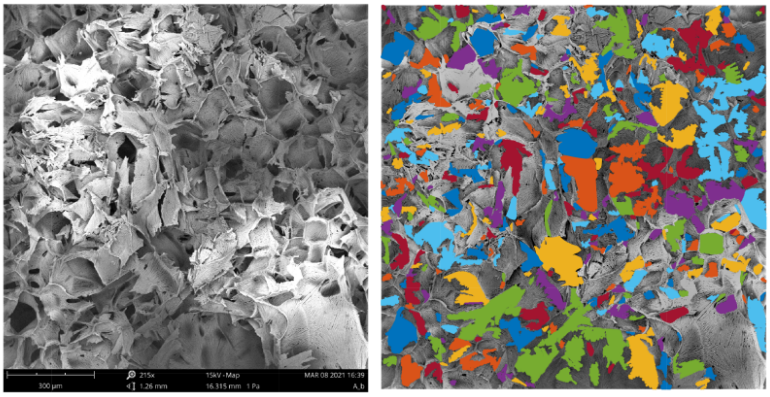

Figure 5.8: SEM image (left) and the extracted pores (right) through the image segmentation tool, highlighted in different colors for better visualization.

Statistical analysis

The pore size distribution within the freeze-dried samples was previously found to follow a beta distribution with the distribution parameters $\beta_1 = 1.2$ and $\beta_2 = 15$ [29]. A beta distribution follows the Equation 5.2 below, where N_k is a normalization constant to ensure that the total probability is 1.

$$f(\psi; \beta_1, \beta_2) = \frac{1}{N_k(\beta_1, \beta_2)} \psi^{\beta_1 - 1}(1 - \psi)^{\beta_2 - 1} \tag{5.2}$$

here, ψ is a realization, i.e., an observed value that actually occurred of a random process Ψ.

This assumption was tested for all VISF tests using a Q-Q plot. Based on the pore size distribution data, a variance and interquartile range analysis were done to compare between tests the statistical dispersion of the pore size distributions found. Variance is a measure of dispersion, meaning how far a set of numbers is spread out from their average value. The interquartile range finds where the middle half of the data values are; it evaluates where the bulk of the values lie. That is why it is preferred over many other measures of spread when reporting spread data, such as pore size distributions. The interquartile range was calculated by subtracting the first quartile from the third (Q3-Q1).

5.2.2 Results and discussion

VISF application

When applying VISF, the surface of the solution is dramatically cooled. The increase in the supercooling degree of the top surface of the solution increases the probability of nucleation. This way, the applied vacuum induces nucleation at the solution top, which in turn induces nucleation in the rest of the vial, held at the chosen T_n. Because this cooling happens on the top, nucleation is induced from the top to the bottom of the vial. Figure 5.9 shows a sequence of images extracted from a three-second video, depicting the induced nucleation using VISF.

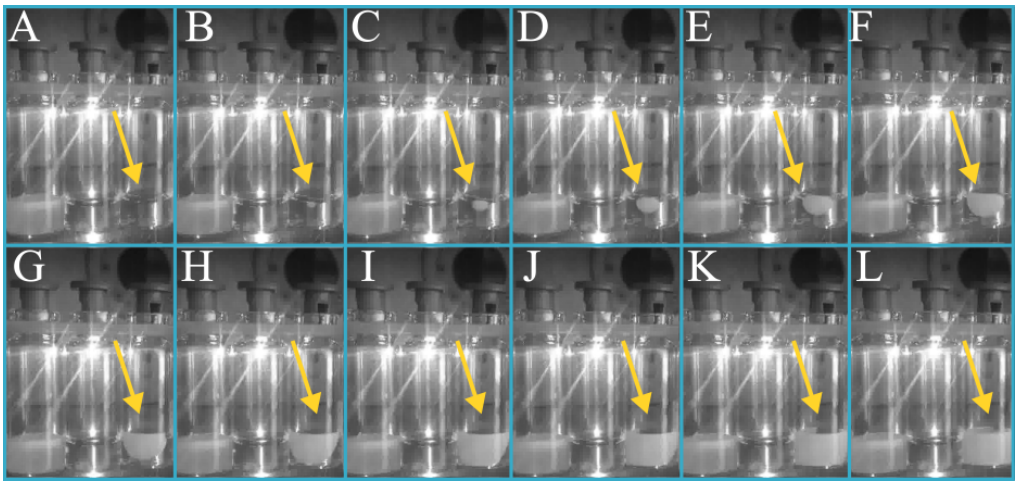

Figure 5.9: Frames from a three-second video depicting nucleation being induced in one vial (signalized with a yellow arrow), from top to bottom, using the VISF method.

After all vials nucleated, care should be taken to restore the chamber pressure; otherwise, cake suction may happen, affecting the appearance and quality

of the final product. Figure 5.10 shows a picture when all vials had just nucleated after applying the VISF technique, which typically took ∼100 seconds between the first vial to nucleate until the last under the tested conditions. In a shelf-ramp freezing process also using 10 vials, this interval was to be close to 1000 seconds [29].

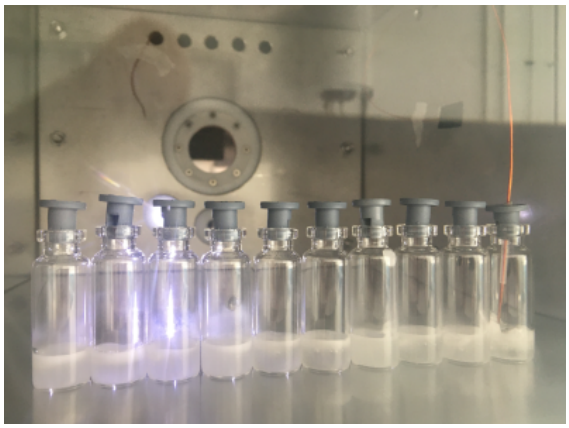

Figure 5.10: Vials on the ON-shelf configuration just after VISF was applied.

When the vacuum is applied, degassing of the solution happens before nucleation takes place. Degassing is usually not an issue. However, for large fill volumes and the vial containing the thermocouple, this affected product quality [58]. Larger fill volumes have a smaller frozen fraction (nuclei) and thus are more liquid. Under the low pressure used in VISF, they acquire a more solid structure while bubbling, conferring them an irregular frozen cake shape. Hence, irregular frozen cakes, such as the one observed for the vial containing the thermocouple in Figure 5.10 were often seen. Thus, VISF coupled with infrared monitoring, a non-invasive monitoring tool, showed a particularly positive synergy.

Heat of nucleation

As explained in Section 5.1, the nucleation phenomenon is exothermic; thus, it releases heat. Many freezing experiments keep vials apart from each other to prevent the heat of nucleation from a vial to retard the nucleation process in a neighboring vial since it would transfer some heat to it. In this present study, the vials were kept in contact to be as close as possible to the freezing process in vials *as is* in the industry. Nonetheless, two additional experiments - not accounted for in the experimental design - were conducted, keeping the vials apart from each other to verify if there were observable differences between them and if IR thermography could capture the effect of the heat of nucleation if present. To this end, Figure 5.11 shows the IR thermal profiles using the ON-shelf configuration with vials in

contact with each other and separated by a 16 *mm* space which corresponds to the diameter of a 4R vial that was used as a reference distance.

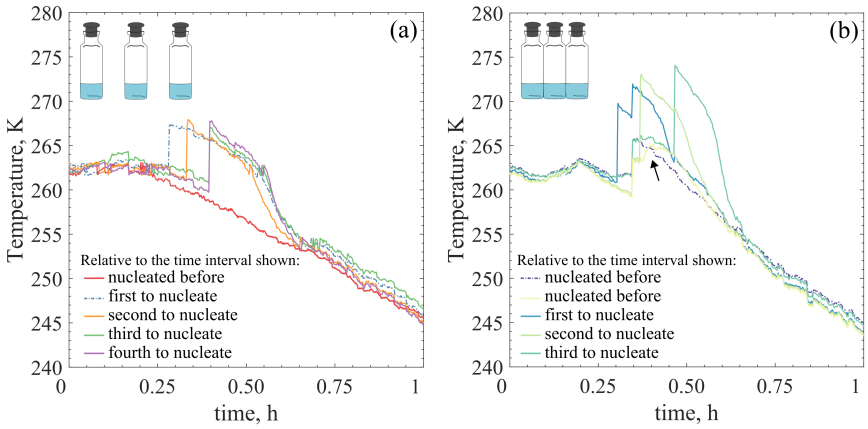

Figure 5.11: T_{bottom} of vials during nucleation using spontaneous nucleation that were (a) apart by a 16 *mm* distance or (b) in contact with each other. The time interval was chosen to focus on the influence of of the nucleation event on neighboring vials. The arrow points to the heat hump observed.

As it can be seen, when vials are apart from each other, not exchanging heat by conduction (5.11 graph (a), there is no substantial evidence of a nucleation heat effect. On the other hand, when vials are in contact (Figure 5.11 graph (b)), a heat hump can be seen in other surrounding vials from the thermal profile.

Figure 5.12 shows the thermal profiles of vials in contact with each other using the ON-shelf configuration during nucleation and apart by 16 *mm*.

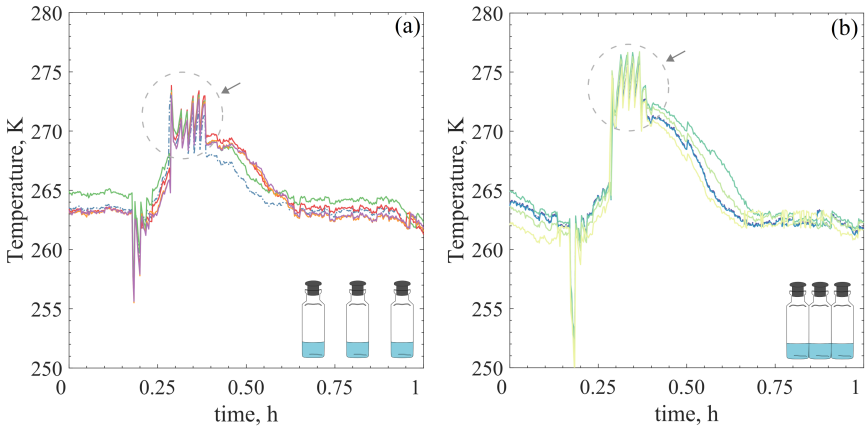

Figure 5.12: T_{bottom} of vials during nucleation using VISF that were (a) apart by a 16 *mm* distance or (b) in contact with each other. The arrow points to the heat hump observed, circled.

Since the vials nucleate together in a short period when using controlled nucleation, it was interesting to verify if these heat effects could also be noticed. As it can be seen in Figure 5.12. there is a particular hump, in this case a series of spikes after the nucleation ascending step, on the profile whether they are apart or in contact. This profile suggests that the vials themselves are absorbing the heat of nucleation being released. The hump looks marginally higher when they were in contact. This event could mean more heat is being absorbed because of the contact between the vials.

Thermal imaging could register the heat of nucleation being released to neighboring vials during the nucleation process. This way, the infrared sensor showed one of its advantages of giving a large amount of thermal data that can be used to gain better process understanding.

Freezing profiles: spontaneous versus controlled

First, the differences observed between spontaneous and controlled freezing should be discussed. Figure 5.13 presents the T_{bottom} profiles of all vials using the OFF-shelf configuration. The shelf temperature and chamber pressure profiles throughout the test are also shown. From this figure, the first immediate observation is the stochastic nature of freezing when uncontrolled freezing is used in contrast to when controlled freezing is applied. Additionally, nucleation heat effects can also be seen for the OFF-shelf vials, evidenced as humps in neighboring vials' thermal profiles as some nucleate.

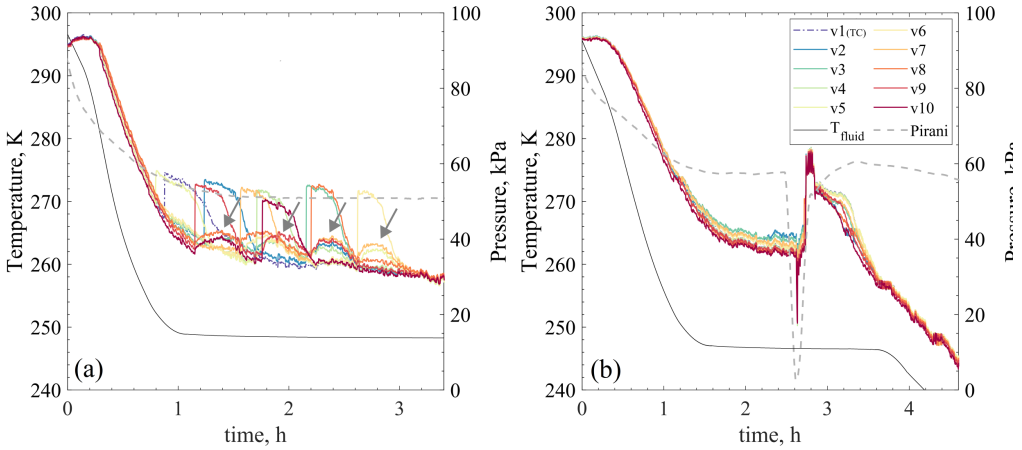

Figure 5.13: Freezing profiles of spontaneous nucleation (Sp-OFF) (a) and VISF at 263 K (b) (4-S)

Figure 5.14 shows the axial temperature profiles observed for all tests, using both controlled and uncontrolled nucleation and the ON and OFF shelf batch

configurations. Each line represents the temperature profile for a given pixel height and consequently a corresponding cake layer; i.e., diving the $10mm$ cake height into 8 layers corresponding to each of the 8 used pixels in the vertical data acquisition line. These profiles allow observing the vertical temperature gradients in the vials during freezing. Thus, changes in the temperature gradient direction can be observed if present.

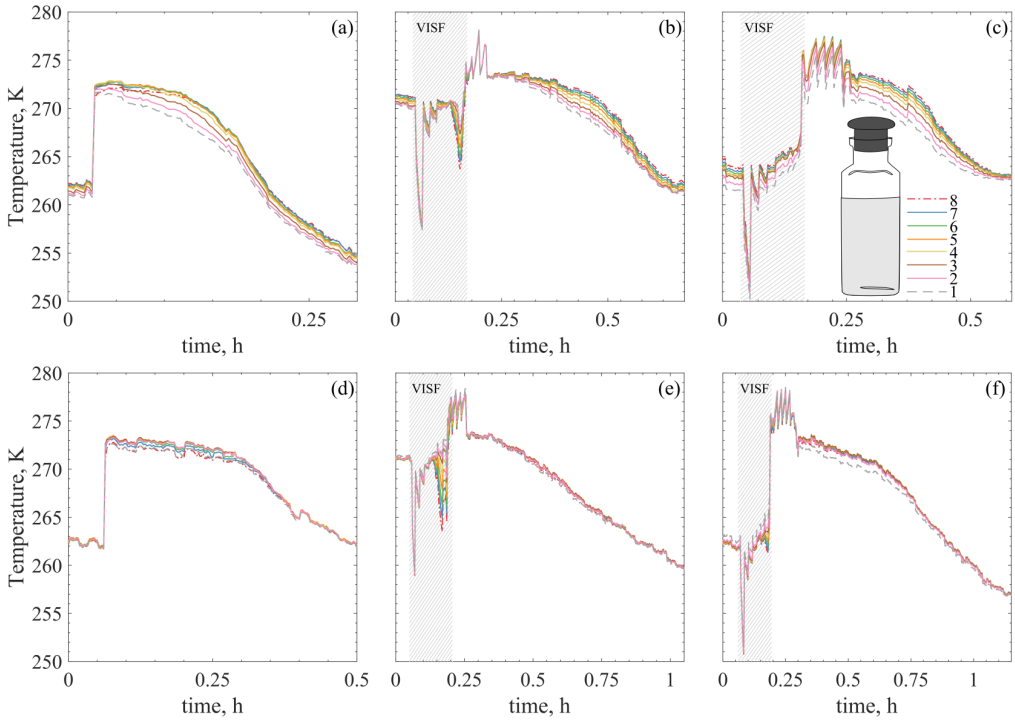

Figure 5.14: Vertical axial temperature profiles during the freezing interval. Graphs (a), (b), (c), (d), (e) and (f) are tests Sp-ON, 1-S, 2-S, Sp-OFF, 3-S and 4-S respectively (see Table 5.1).

In practice, when in solution, water never freezes completely. After nucleation, pure ice forms, and the solution cryo-concentrates. Once the system reaches a specific concentration characteristic of each excipient, the cryo-concentrated solution remains in a supercooled single-phase amorphous state. Water molecules get trapped into the excipient solidified matrix and are unable to diffuse and crystallize further [180, 181]. For this reason, freezing is usually regarded as complete when the solution reaches the eutectic point (T_{eu}) for crystalline solutes or the glass transition temperature (T_g) for amorphous ones. The T_g for 5% sucrose is 241 K, the one for 10% dextran is 264 K, and the T_{eu} for 5% mannitol is 295 K [148].

In this study, the interval between nucleation and the product reaching nearly 263 K was the only one closely examined. During this interval, temperature gradients could be observed in the vial. However, after reaching around 263 K,

for all tests, these gradients seemed less evident. The impact of the latent heat of solidification was less and less pronounced, and the product temperature tended to homogenize. Moreover, the IR sensor may lack the sensitivity to detect any temperature gradients after that moment accurately. Thus, freezing is presented and discussed in-depth, only covering the interval mentioned above (until 263 K). Following this definition, freezing takes approximately 20 minutes for ON-shelf vials and approximately 45 min for OFF-shelf ones.

As discussed, ice nucleation and freezing temperature directly affect the size distribution of the ice crystal formed. If a product has pronounced temperature gradients, differences in the crystal size distributions may be observed. Since VISF cools down the top surface of the solution, it seemed interesting to investigate if this surface cooling could affect the product's temperature gradient and if that could affect intra-vial homogeneity of ice crystal mythologies.

For ON-shelf vials, since most of the heat transfer was estimated to take place between the vial bottom and the cooling shelf, the bottom temperature is expected to be the lowest during cooling. Thus, depending on the severity of the surface cooling promoted by VISF, the lowest temperature point could change. For OFF-shelf vials, in turn, the lowest temperature point is not clear. It could be in the bottom, top or even be almost uniformly distributed around the cake's perimeter. In this case, the surface cooling caused by VISF could create a temperature gradient if the cooling effects are strong enough. IR thermography may help observing these temperature profiles and gradients during freezing if the camera's resolution permits.

A change in the temperature gradient direction is sometimes observed, and further exploratory information is needed. Hence, Table 5.2 lists whether the temperature profiles extracted from the bottom pixels are the lowest or highest temperatures observed for all tests.

Table 5.2 aims to help better analyze if there is an inversion on the vertical temperature gradients for any tested conditions and if this follows any pattern. Additionally, an alternative graph representation of the gradient profiles is represented in Figure 5.15 to help better visualize the data. In this figure, after the temperature depression during VISF (blue square), the temperature profile presents an increase with two marked inclinations: a first one not very steep (between the blue and the black square) and a second one, almost vertical (between the black square and the blue triangle). Between the two, a second depression in the temperature profile can be observed when T_n 271 K is used (see Figure 5.12 (b) and (e)). Thus, only the second interval of this ascending profile is assumed to effectively correspond to the nucleation event. From Figure 5.15 the difference in the temperature gradient in the pre-VISF point (red squares) appears to be only marginally greater for the ON-shelf vials when compared to the OFF-shelf ones. The point that the temperature gradients seem to differ more is the pre-nuc one (black square). Even so, the gradients are rather small, ranging form 1.5 to 4 K for ON-shelf vials and 1 to 2 K for OFF-shelf vials.

Table 5.2: Thermal profile before and after vacuum induced surface freezing for all tests.

Test code	Tbottom before nucleation	Tbottom after nucleation	VISF inversion observed?
Sp-ON	Lowest	Lowest	-
1-S	Lowest		Yes
1-M	Lowest	Lowest	Yes
1-D	Lowest		Yes
2-S	Lowest		Unclear
2-M	Lowest	Lowest	Unclear
2-D	Lowest		Unclear
Sp-OFF	Highest	Lowest	-
3-S	Highest		Unclear
3-M	Highest	Lowest	Unclear
3-D	Highest		Unclear
4-S	Highest		Unclear
4-M	Highest	Lowest	Unclear
4-D	Highest		Unclear

In the uncontrolled nucleation graph of Figure 5.14, some humps in the temperature profile are seen. Those humps are due to the energy released during the nucleation of neighboring vials since they were in contact with each other. This energy release may slightly increase vial temperature or simply affect the IR measured values. After nucleation, warmer temperature traces may remain in the vial glass wall until equilibrium between the vial wall and the product is reached. When VISF is applied, since all vials nucleate around the same time (∼100 s range), these interference is not observed. However, there is a very pronounced initial peak on the temperature profile just as nucleation happens. This peak in the temperature readings is also attributed to this energy release during nucleation. In fact, in both Figure 5.14 and Figure 5.13, the nucleation heat-release hump is present for VISF batches. This same hump was not markedly present when spontaneous nucleation was used because neighboring vials absorbed the released energy, as explained in the previous subsection.

From the axial temperature profiles plotted in Figure 5.14, differences in the vertical temperature gradient can be observed between the different tested setups. As expected, ON-shelf vials have a broader vertical axial temperature gradient than OFF-shelf vials. For the ON-shelf vials, the bottom temperature, as supposed, is the coldest. Then, VISF is applied, and an inversion is observed for the tests using

$T_n = 271K$, which means: the bottom temperature becomes the warmest. To help the visualization of the inversion profiles, when observed, Figure 5.15 portrays the axial temperature gradients before, during, and after freezing.

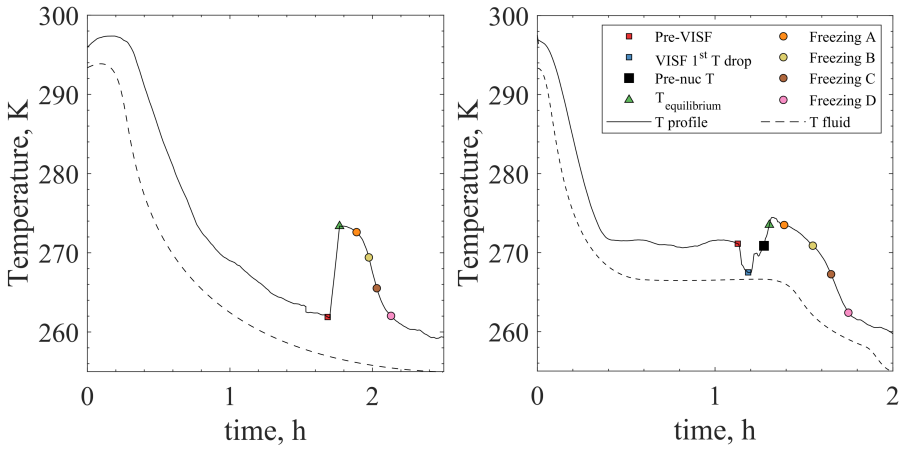

(I) Points of interest for spontaneous nucleation (left) and VISF tests (right).

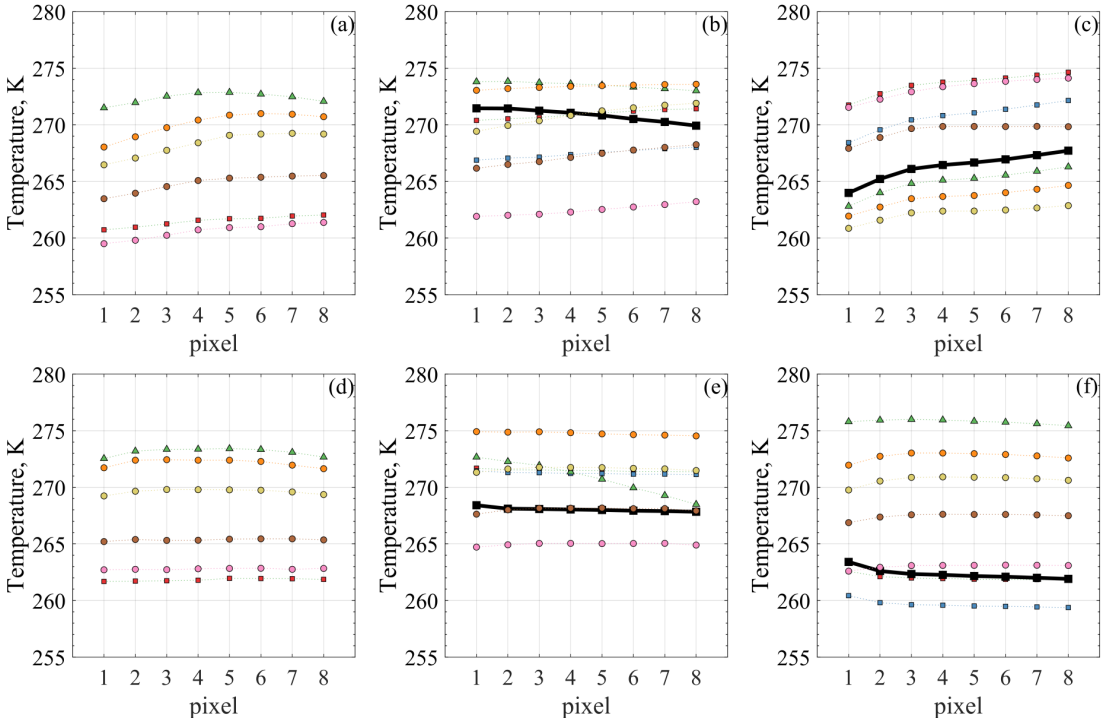

(II) Vertical temperature gradients and possible profile inversions for 5% sucrose.

Figure 5.15: Vertical (in the axial direction) temperature gradients during freezing for 5% sucrose. Graphs (a), (b), (c), (d), (e) and (f) are tests Sp-ON, 1-S, 2-S, Sp-OFF, 3-S and 4-S respectively.

The lower top temperature is expected since VISF is based on the fast cooling caused by the evaporation of the surface layer of the solution when the vacuum is applied. For the ON-shelf tests at $T_n = 271K$, this was observed. For all other tests, however, whether this happens or not was unclear for different reasons. For the experiments at $T_n = 263K$, the solution was already at a temperature close to its spontaneous nucleation limit and, therefore, nucleation probably occurred before any significant gradient could develop and be detected by the IR camera.

For the OFF-shelf vials, the T_{top} (pixel 8) was already the lowest temperature before VISF, and no inversion in the profile was observed. After nucleation, however, the T_{bottom} becomes the lowest temperature. The top layer many times followed the T_{bottom} having the next lowest temperature, whether VISF was applied or not. From this information, it seems that the top and bottom layers of the product are the coldest ones. In contrast, the center of the product is warmer during freezing of suspended vials, independently from the application of VISF. This observation was somewhat expected considering the different heat transfer mechanisms occurring for the different loading configurations. The thermal sensitivity of the IR sensor is 0.05 K which seems sufficient to observe the temperature gradients present in the vials. However, the noise typically present in IR profiles could affect this evaluation. Nonetheless, this is precisely why the thermal profiles presented in this chapter are unfiltered/ not smoothed, in an attempt to have the least interference possible from post-processing.

With the sensor's resolution, 8 pixels were enough to cover the cake height of 10 mm. However, this resolution does not seem sufficient to accurately identify the fast cooling of the solution surface while the vacuum is applied. Additionally, under the tested conditions, the IR sensor monitors the temperature of the external wall of the vial, which is in equilibrium with the product inside. Of course, calculations and corrections are made to account for the temperature gradient between the external wall and the product, but this also affects the ability to adequately account for this fast cooling of the product surface during VISF. Finally, the acquisition rate of 0.1 frames per second (fps), the highest rate available with the current sensor, leaves room for improvement. The nucleation phenomenon happens within a time scale of milliseconds, while freezing takes several minutes. Thus, the acquisition rate is not enough to capture the nucleation phenomenon accurately and with the deserved precision. However, it seems suitable for freezing, although faster rates in the future may grant better insights.

Freezing front temperature and position

Because freezing is an exothermic phenomenon, if the heat exchange follows a vertical gradient, i.e., in the ON-shelf experiments, the freezing front position could be inferred by tracking the maximum temperature within the product cake height. Once this profile is obtained, an evaluation can be done to determine whether this may be representative of the freezing front profile or not. As described in Figure 3.7, the position of the T_{max} was tracked and is plotted in Figure 5.16.

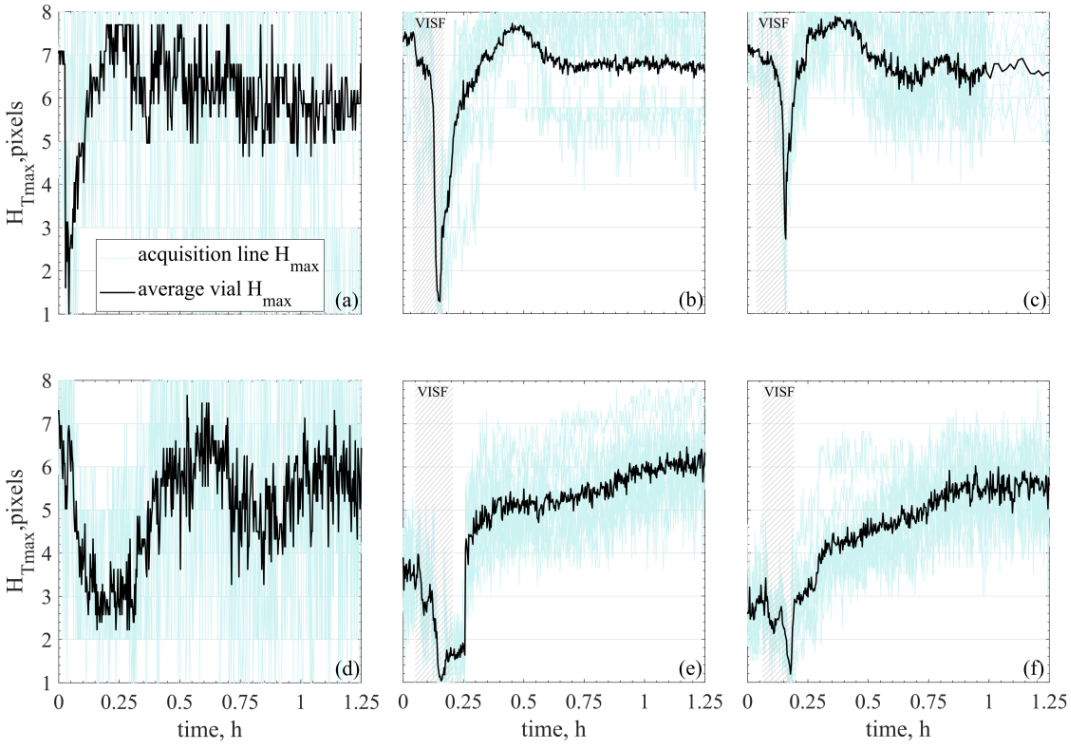

Figure 5.16: T_{max} axial position (H_{max}) during the freezing interval. Graphs (a), (b), (c), (d), (e) and (f) are tests Sp-ON, 1-S, 2-S, Sp-OFF, 3-S and 4-S respectively. For VISF (b, c, e and f).

For the VISF tests in Figure 5.16 (b, c, e and f), H_{max} is the batch average calculated from the vial average profiles of all ten vials (shadows plotted in light green). For the spontaneous tests (a and d), $H_{T_{max}}$ is the average profile obtained from the six acquisition lines of a single vial (shadows plotted in light green).

In practical terms, an H_{max} profile moving from bottom to top is observed when tracking the maximum temperature position, which agrees with what is expected from the freezing front (Figure 5.16). Still, since these are new observations, the observed profiles must be carefully evaluated to determine if the approximation H_{max} profile$\cong$ freezing front profile is valid.

As mentioned, these H_{max} profiles were obtained by averaging the observed profile of each of the six acquisition lines per vial. To understand if this averaging represents what is observed, Figure 5.17 shows the amplitude (ΔH_{max}) of the profiles differences during freezing.

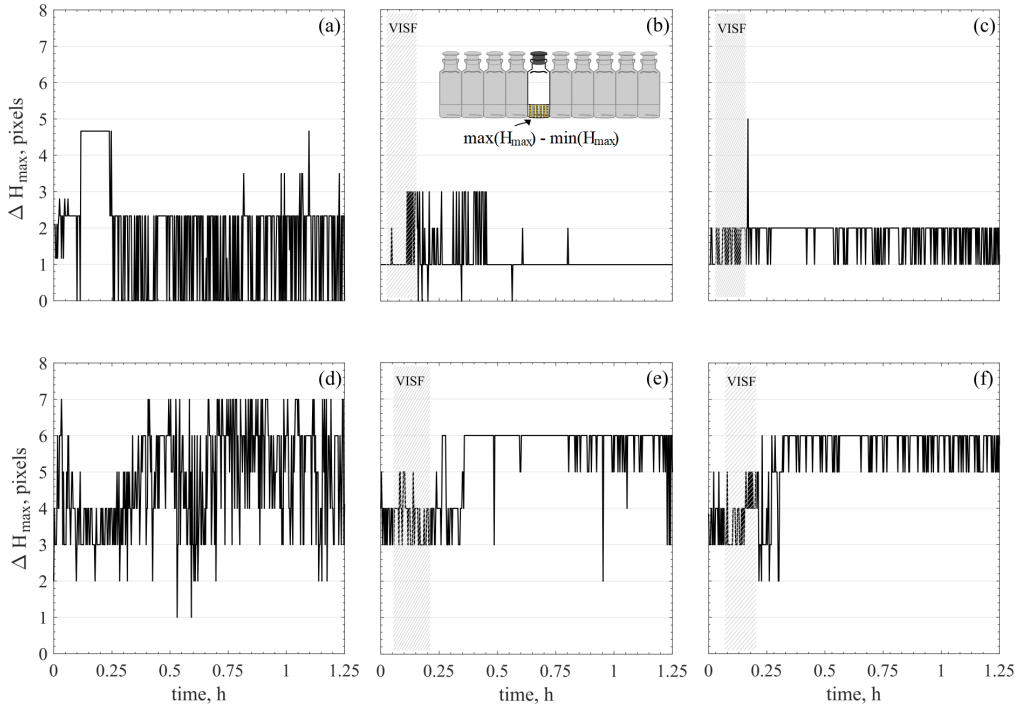

Figure 5.17: Range of measured H_{max} profile values for a single vial. Graphs (a), (b), (c), (d), (e) and (f) are tests Sp-ON, 1-S, 2-S, Sp-OFF, 3-S and 4-S respectively.

From Figure 5.17, it is clear that ON-shelf vials present much lower divergence between the observed H_{max} profiles compared to the OFF-shelf ones. These profiles imply that the tracking of H_{max} may represent a freezing front profile evolution that is clear enough only in the first case when the unidirectional heat exchange approach is valid.

If the position of the freezing front can be inferred, the same can be done for the temperature gradient of the frozen layer. For uncontrolled nucleated ON-shelf vials, the T_{min} will be the T_{bottom} after nucleation. The T_{top} will be the T_{max} for most of the freezing. However, that is not necessarily the case during the first minutes of freezing (∼6-12 min) after controlled nucleation takes place. This time-scale is in agreement with what was previously modeled for the freezing front of 10% mannitol using a T_n of 266 K with a cake high of 10 mm as well [31]. Experimentally, in this time-interval, the T_{max} seems to move upwards, from bottom to top for ON-shelf vials. A much less evident profile is observed for OFF-shelf vials, where the maximum temperature seems to fluctuate around the central height of the vial's

pixels. Nonetheless, for ON-shelf vials, to use the T_{max} position and temperature to infer the freezing front profile seems valid. In this case, the temperature gradient between the freezing front and the vial bottom can be inferred and is plotted in Figure 5.18.

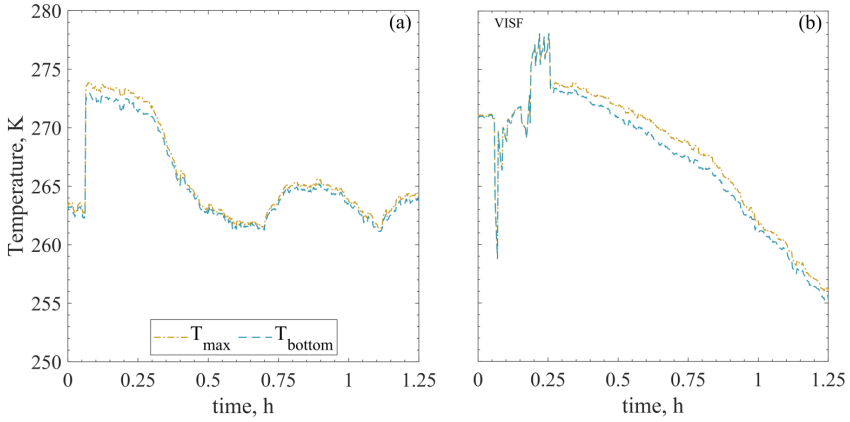

Figure 5.18: T_{max} and T_{bottom} (a) during spontaneous nucleation (Sp-ON) and (b) VISF (3-S)

A small fraction of the water in solution forms the first nuclei during nucleation, this state of solution is called *slush*. For the T_n values used, approximately only 3% of the bulk liquid freezes initially at 271 K and nearly 14% when 263 K T_n is used [14]. After this initial stage, the fraction of water being frozen advances slowly. The freezing progression after this point depends - among other factors such as the solution characteristics - on the cooling rate used. A slight temperature jump may be observed after one of the solutes becomes supersaturated and releases latent heat of crystallization [40]. In many cases, freezing is assumed to be complete when the glass transition temperature (for amorphous solutes) or the eutectic point (for crystalline solutes) is reached [90, 181]. However, the solution may continue its freezing process until very low temperatures [40]; thus, the determination of the end of freezing is arguable.

As mentioned, the freezing interval being observed in detail with the IR sensor is shorter than the required one to achieve the product's glass transition or eutectic point. In fact, intervals between 20-45 minutes after ice nucleation are the ones being investigated. The temperature profiles obtained in these time intervals allow tracking the position of the maximum axial temperature (H_{max}) of ON-shelf experiments. The H_{max} position, assumed to be equivalent to the freezing front position, seems to show an apparent upwards movement, which is consistent with the expected movement of the freezing front.

On the other hand, suspended vials tended to have the maximum temperature positioned around the middle of the product height. This T_{max} position indicates that during freezing, heat is being removed from the bottom and top of

the vial faster than from the sides, the vial walls. Maybe this is the case due to radiation effects on the vial walls. In any case, this heat removal on the bottom and top seems to prevent the observation of an upwards profile of the T_{max} and in this case, the T_{max} cannot be used to infer the position of the freezing front.

An important point from these experimental observations is the freezing front behavior. If indeed the approximation H_{max} profile $\cong$ freezing front position is adequate for ON-shelf vials, the progression of this front may be a bit different than previously modeled. In Figure 5.16, the H_{max} profiles of ON-shelf vials (a, b, and c) advance from bottom to top in a linear way in the first half of the ascending interval, i.e., with a constant progression rate. A deceleration is observed on the second half of this profile progression, and the freezing front seems to move much slower.

This behavior seen in Figure 5.18 could be attributed to an increment in the heat transfer resistance as the frozen layer increases. In our experiments, the shelf temperature and the freezing front temperature remained almost constant during freezing (excluding the cryo-concentration effects). However, as freezing advanced, the thickness of the ice layer increased, decreasing the thermal gradient in the ice, which is the heat transfer driving force of the system. Ice actually has a higher thermal conductivity than water (2.14 $Wm^{-1}K^{-1}$ at 273.15 K and 2.3 $Wm^{-1}K^{-1}$ for ice at 263.15 K while water has $0.6Wm^{-1}K^{-1}$ at 293.15 K) [182]. For sucrose solutions, on the other hand, the conductivity decreases the higher the sucrose concentration [183] with the effective thermal conductivity at 263 K being as low as ~ 0.45 $Wm^{-1}K^{-1}$ for 31.3% sucrose, for example. It is important to note that what is being called the "frozen layer" in this study has more ice particles formed than the initial ice-water slush produced by nucleation. However, this matrix is not completely solidified, so other factors that could pose some resistance to heat transfer may be in place. One possibility could be that the heterogeneous nature of the slush matrix could be adding increased resistance points to thermal flow. Alternatively - and more likely - more heat transfer evens between the shelf and the freezing front are taking place. Plus, the layer between the bottom and the top of the vial increases, and the *slush* in between is gradually freezing. In any case, this new observations and insights regarding the freezing front behavior for ON-shelf vials may be further analyzed together with uni-dimensional freezing models [31, 43, 44, 166] for a better application based on experimental data.

One-dimensional freezing models such as proposed by Nakagawa et al. [31] and by Arsiccio et al. [43] require the freezing rate and the temperature gradient of the frozen layer to estimate the dimension of the ice crystals formed. To use experimental data instead of simulated or assumed ones, the T_{max} profile tracking is assumed as descriptive of the freezing front, both for spontaneous nucleation and VISF tests. For ON-shelf vials, that assumption seems adequate for spontaneous nucleation and VISF; thus, the difference between the T_{bottom} and T_{max} can give the temperature gradient of the frozen layer while the H_{max} profile evolution can give

the freezing rate.

Resulting product cake structures

In 1991, Bald et al. proposed the concept of crystal size being proportional to the rate of temperature change in the system [44]. Following this, the velocity of a solidification (freezing) front together with the temperature gradient in the frozen product were defined as driving factors determining the ice crystal sizes obtained [31, 166]. Published works using ice crystal prediction models based on these concepts assumed a one-dimensional freezing front evolution, moving from bottom to top [31, 166, 184, 185]. Later, a mechanistic model to predict ice crystal size distribution was proposed by Arsiccio et al., also based on this one-dimensional assumption for the freezing front evolution ([43]. These models were developed and implemented using punctual temperature measurements of vials and using suitable mathematical models to estimate the temperature profile in the rest of the product. With the use of IR thermography these models may be implemented in-line with direct experimental data. The application of such ice prediction models with more details can be found in Chapter 6.

Different solutions and freezing protocols were tested in this present research. Figure 5.19 shows some SEM image results for the resulting cake structure of 5% sucrose solutions while Figure 5.20 shows SEM image results for the resulting cake structure of 5% mannitol solutions while Figure 5.21 shows SEM results for the resulting cake structure of 10% dextran solutions.

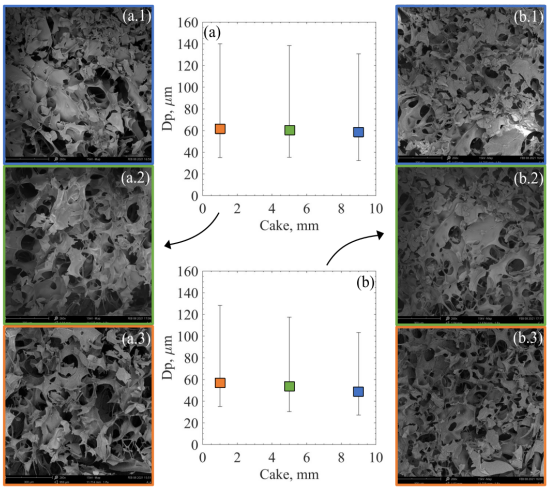

Figure 5.19: SEM images for the resulting 5% sucrose cake of tests (a) 1-S and (b) 3-S. The numbers after the test type letters (a and b) represent the cake section: (1) top, (2), middle and (3) bottom.

Figure 5.19, Figure 5.20 and Figure 5.21 were build using the pictures from

three of the five levels that were photographed. The detailed analysis and resulting pore sizes for each of the five layers is reported in Chapter 6. The results in this chapter concern only the bottom, middle and top of the vial, hence, three levels.

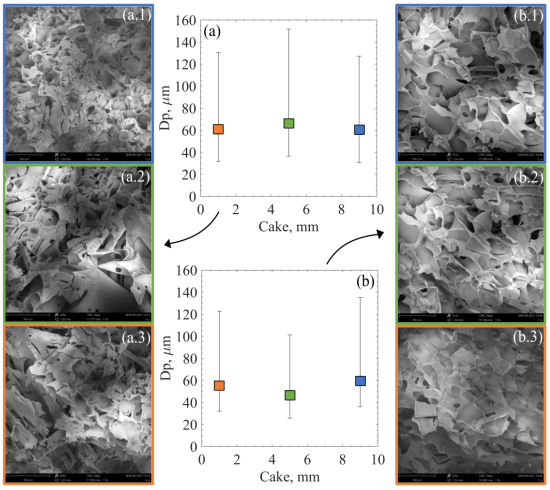

Figure 5.20: SEM images for the resulting 5% mannitol cake of tests (a) 1-M and (b) 3-M. The numbers after the test type letters (a and b) represent the cake section: (1) top, (2), middle and (3) bottom.

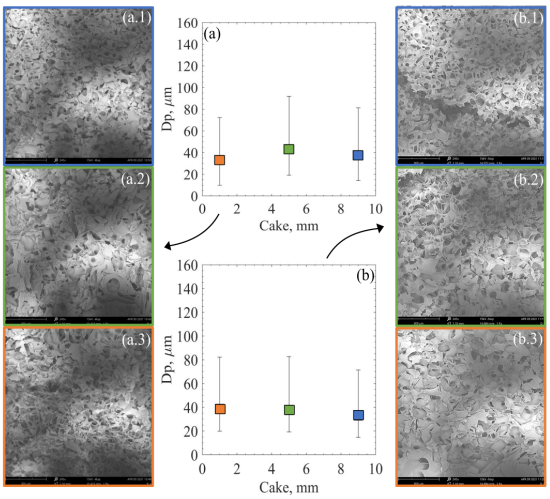

Figure 5.21: SEM images for the resulting 10% dextran cake of tests (a) 1-D and (b) 3-D. The numbers after the test type letters (a and b) represent the cake section: (1) top, (2), middle and (3) bottom.

From Figures 5.19, 5.20 and 5.21 the differences in the resulting average pore sizes between ON and OFF shelf configurations using VISF are modest, if any.

This suggests that the use of VISF has a stronger influence in the resulting pore sizes than the vial configuration.

The pore size distribution of lyophilized products was previously found to follow a beta distribution with $\beta_1 = 1.2$ and $\beta_2 = 15$ [29]. This assumption was tested using a Q-Q plot for all performed tests, based on the pore sizes obtained through the automated image segmentation software applied to the SEM images. The results are displayed in Figure 5.22, for sucrose (5.22a), mannitol (Figure 5.22b) and for dextran solutions (Figure 5.22c).

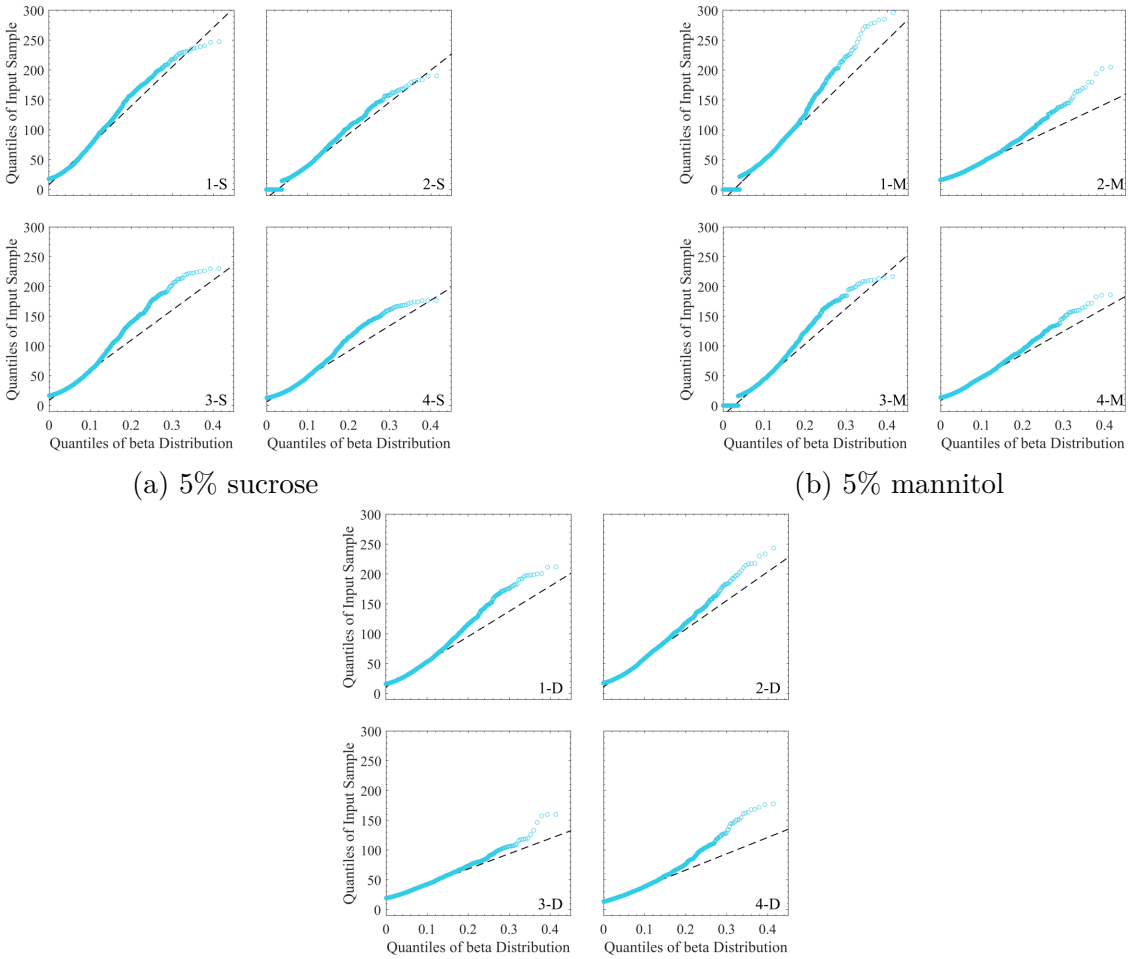

(a) 5% sucrose

(b) 5% mannitol

(c) 10% dextran

Figure 5.22: Q-Q plots for different solutions subjected to VISF at 263 K and 271 K, according to the test code plotted in each subfigure.

VISF was found to be able to produce product matrices with larger pores than the ones obtained using spontaneous nucleation when higher nucleation temperature were used [186]. OFF-shelf vials using uncontrolled nucleation were found

to render cakes with larger pores and higher batch homogeneity than ON-shelf vials. The resulting cakes of spontaneous nucleation were not evaluated using SEM in this study, thus a comparison between the results is not possible. Another pertinent question to be verified was whether VISF coupled with the suspended vial configuration would produce products with a more homogeneous cake structure, besides batch homogeneity.

Based on experimental observations and mathematical formulations for freezing models, the nucleation temperature and the temperature of the product during the freezing interval affect the resulting ice crystals formed. Thus, he thermal profiles observed create some expectations regarding the resulting cake structures. The OFF-shelf vials, which present narrower overall temperature gradients, should result in more homogeneous cakes. On the other hand, ON-shelf vials with broader vertical temperature gradients should have a less homogeneous cake structure.

The ice crystals formed during freezing strongly depend on the nucleation temperature and the cooling rate [187]. Based on the temperature gradients observed in Figure 5.14, more homogeneous cake structures would be expected for OFF-shelf vials because they presented smaller temperature gradients. Upon visual inspection of the SEM images of the resulting cake, it is hard to see any difference whatsoever. Both cakes appear very similar, and the high variability of the pore sizes makes any compassion difficult. Thus, to try to evaluate this, Figure 5.23 shows different statistical parameters to measure the statistical dispersion of samples in a group: the variance and the interquartile (Q3-Q1) range. As seen from this figure, although the differences are not very expressive, OFF-shelf vials have lower variability indicators consistently.

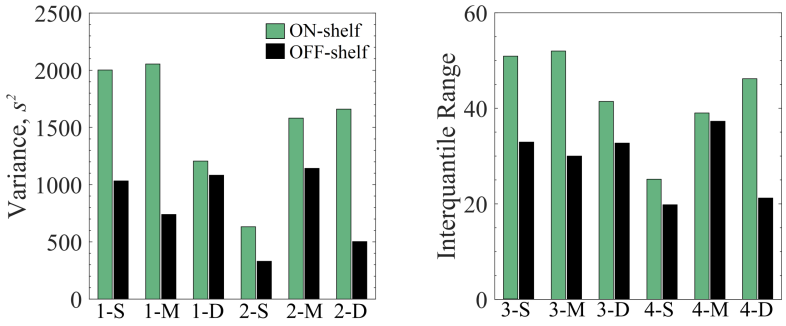

Figure 5.23: Variance (a) and interquartile range (b) of the resulting pore size distribution for all VISF tests.

Although the pore size distribution data is very spread, the variance and the interquartile range consistently showed lower values for OFF-shelf tests than ON-shelf. These results indicate, indeed, that the use of a suspended configuration does influence product homogeneity. However, the loading configuration has a modest effect, as expected. The nucleation temperature is the major player in

determining the resulting ice crystal sizes formed. To apply VISF, the vials were left for ∼1 h to reach the desired nucleation temperature and reach equilibrium. When VISF is applied, although the top surface of the vial cools down, the remaining of the solution is at a uniform temperature. This more uniform temperature may be the reason behind more homogeneous cakes using VISF. When shelf ramped freezing is used, and no type of freezing control is applied, the vials in direct contact with the shelf usually undergo a relatively fast-cooling ramp. Under these circumstances, the bottom of the vial tends to be colder than the rest of the solution, and when nucleation takes place, it may not happen at the same temperature across the product height. During nucleation, a temperature gradient could result in a less homogeneous cake, with smaller ice crystals (and consequent dried cake pores) in the bottom and larger crystals at the top. Fang et al. found that vials that nucleated at the same temperature (261 K) but had different freezing rates after nucleation also presented different resulting pore sizes in the resulting cake. The slowest freezing rate used (0.1 K / min) rendered larger pores (28-60 μm) while the fastest freezing rate used (2.5 K/min) rendered smaller pores (22-48 μm) [188]. According to these findings, the nucleation rate plays a role in the resulting ice crystal sizes and the freezing rate during freezing. In this case, some differences should be observed between the OFF-shelf and ON-shelf vials. OFF-shelf vials would have a slower freezing rate and, by this logic, should have a resulting cake structure with slightly larger pores. These large pores could not be observed in detail, however. The resulting pore sizes in this study have the nucleation temperature and conditions as the main driving force to determine the resulting cake pore size distribution.

5.3 Conclusions

In this chapter, the freezing of pharmaceutical solutions in vials using different loading configurations and process conditions was methodically observed using an IR camera. A deeper insight into the freezing phenomena was obtained from these experiments, and many notions were confirmed or deduced.

VISF worked very well to induce nucleation in a short time interval (∼100 s) and with a good intra-vial and inter-vial uniformity. The IR camera worked very well to monitor VISF tests in comparison to spontaneous nucleation ones. This was the case because the batch behavior was more homogeneous with the controlled freezing technique and the thermal profiles became clearer to be observed by infrared imaging, which typically shows noise in the acquired data. Assuming the T_{max} during the freezing interval to be the freezing front temperature and acquiring its axial position over time allowed inferring the freezing front position for ON-shelf vials.

Faster freezing rates (ON-shelf) reduce faster the diffusion of water molecules to the ice front for crystal growth. As a result, there is less time for the ice crystals

to grow and the stochastic nature of nucleation becomes more expressive in the resulting cake, having a wider distribution of crystal sizes. On the other hand, when the freezing rate is slower (OFF-shelf), more time is given for the water molecules to diffuse and promote crystal growth. With more time, the kinetics of crystal growth help uniform the heterogeneity deriving from nucleation.

Suspended (OFF-shelf) vials had a narrower overall temperature profile gradient than ON-shelf ones due to the different heat transfer mechanisms. These more narrow gradients were associated to the narrower variability observed in the pore sizes of the resulting cake. Using the OFF-shelf vial configuration applied to VISF, very homogeneous cakes can be obtained. The pore size distribution of cakes seemed to follow a beta distribution from the extracted pore sizes using the SEM images.

Chapter 6

Ice crystal size prediction

6.1 Introduction

Many different approaches have been made to model, predict and better understand the freezing phenomenon. There is a consensus regarding some aspects of freezing: its stochastic nature, the correlation between the supercooling degree and the number and size of the resulting crystals, and the fact that other solutes present in solution interfere with it since the freezing point is considered a colligative property [170, 189, 190].

In the literature, many papers about freezing are from meteorological studies where the environmental conditions during freezing may change dramatically [191–195]. Thus, many different ice crystal structures are investigated under those circumstances, as shown in Figure 5.1. For freezing under atmospheric pressure, ice type Ih is the relevant one. Additionally, in lab-scale or even industrial applications, heat removal during a freezing process is do under constant and controlled conditions. Nonetheless, modeling and simulating freezing has been a challenge due to difficulty determining which hydrogen bonds form. Still, some simulation approaches have been successfully implemented to better understand ice crystallization [162, 196–199].

Contemplating the common physiological (for biological matrices), laboratory and industrial conditions, nucleation is usually regarded to occur under constant temperature and pressure conditions. Under these conditions, the transfer of solute molecules from solution to aggregate the crystal is driven by the Gibbs free energy change [200]. The change in Gibbs free energy of crystallization, ΔG_{cryst}, at a constant temperature T, is the sum of the contributions of the enthalpy ΔH_{cryst} and entropy ΔS_{cryst}: $\Delta G_{cryst} = \Delta H_{cryst} - T\Delta S_{cryst}$. The associated crystallization equilibrium constant (K_{cryst}) is:

$$K_{cryst} \equiv exp\left(-\frac{\Delta G_{cryst}}{RT}\right) \tag{6.1}$$

J. W. Gibbs developed the thermodynamic part of the classical nucleation theory in two papers [201, 202]. An important contribution of classical nucleation theory is quantitatively relating the *nucleation rate* (J_0) to the *nucleation work* (ΔG_{cryst}) that is required to overcome the activation barrier for nucleation. The nucleation rate can be expressed as a product of a kinetic factor, which accounts for the frequency with which the system "attempts" to realize a nucleation event considering the concentration of potential nucleation sites (A_1), and a thermodynamic factor, which accounts for the probability that each such "attempt" results in actually overcoming this activation barrier. The kinetic factor focuses on the attachment frequency of monomer molecules to an incipient cluster, which reflects the mobility of the monomer molecules in a supercooled condition. The thermodynamic parameter expresses the probability of finding a system in a state that has a sufficient amount of free energy to overcome the activation barrier. The probability of such occurrence depends on the driving force for nucleation, which is the chemical potential differential between the thermodynamically stable (nuclei) phase and the metastable parent phase (supercooled solution) [157, 158]. These considerations lead to an equation which follows an Arrhenius model which results from the Boltzmann distribution of classical statistical physics. According to the classical nucleation theory, the ice nuclei formation rate can be described as:

$$J_0 = A_1 exp\left(-\frac{\Delta G_{cryst}}{k_{boltz} T_n}\right) \tag{6.2}$$

J_0 is the nucleation rate in terms of the number of ice crystals formed per second. The Gibbs free energy for the new phase formation is calculated assuming a spherical geometry of the nuclei (Equation 6.3). This assumption was verified by posterior *in silico* modelling [197]. J_0 is computed as the sum of a free energy variation caused by the formation of a new surface (the ice crystal surface being formed) and a variation caused by the bulk free energy from the volume of the newly created phase.

Volmer encountered a problem when observing the freezing behavior of different substances. Some could be undercooled a lot while others could not. To explain this, he started from the rationale that small particles are less stable than the bulk phase due to their surface tension. This would created a barrier for freezing, because small particles (nuclei) have to be formed for the phase change to take place. If the undercooled state is only metastable, it is not the lowest point of the free energy. Fluctuations of the free energy would occur in such a way that at some point they would be large enough to favor stability for particle formation. He assumed that the free energy change when a cluster of atoms formed into a new phase could be described by two contributions: one from the decrease in the free energy from the new phase formation and another related to the surface tension of the small cluster. Assuming that the cluster is a sphere with radius r_{ad}, the free energy change can be described by these two contributions as [203, 204]:

$$\Delta G = 4\pi r_{ad}^2 \gamma - \frac{4}{3}\pi r_{ad}^3 \Lambda_v \tag{6.3}$$

where γ is the surface tension and the first term corresponds to the interfacial free energy between the new phase and the old phase. Λ_v is the volumetric free energy of phase change, from the formation of a new cluster. The first term represents the increase in energy due to the surface tension (ΔG_s) and is proportional to the area of the newly formed surface, and thus proportional to the square of r_{ad}. The second term represents the decrease in the energy from the new phase formation proportional to the volume of the formed cluster (ΔG_v), and thus proportional to the cube of r_{ad}. Because of these power terms coupled to the fact that the first term is positive, while the second is negative, a maximum in the free energy will exist. This maximum will correspond to the energy barrier for nucleation to happen and it is associated with the cluster reaching a critical radius r_{cr}. The critical radius r_{cr} defines the required nucleus radius that renders them stable and non-dissolving. Once the system finds a way to overcome this energy barrier and form a cluster larger than this r_{cr}, the thermodynamically stable phase (nuclei cluster) can continue growing. Thus, the critical radius r_{cr} can be obtained as the maximum in the free energy function, by setting its derivative to zero (Figure 6.1).

$$r_{cr} = -\frac{2\gamma}{\Lambda_v} \tag{6.4}$$

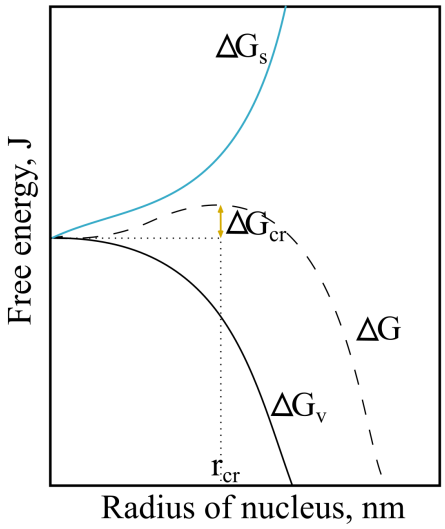

Figure 6.1: Free energy versus cluster radius. Assuming a constant temperature / pressure for which the prevailing phase is metastable.

It is noteworthy to discuss here that a cluster that is smaller than the r_{cr} and is in a supercooled state may have higher free energy than that of an ensemble

of monomers because the ΔG_s will be greater. Such clusters cannot exist in a thermodynamically stable system, but they may exist temporarily. These type of formations are thermodynamically unstable are are the heart of the nucleation theory and are possible because of the uncertainty principle of quantum mechanics. The lifetime of such clusters is very short but not zero. The probability of a monomer to attach to this unstable cluster increases with the increase of the clusters lifetime (more supercooling). This non-zero probability of a cluster forming and having an increase in size by the addition of a monomer during the cluster's lifetime confers the stochastic behavior of nucleation. The energy barrier for nucleation to take place may be overcome before reaching the required free energy state when monomers succeed in aggregating to these unstable clusters during they uncertain lifetime.

From molecular dynamics modeling studies, it was found that embryos containing hundreds or thousands of molecules are required for the system to crystallize [162]. A recent study using graphene oxide nanosheets found an experimental correlation between different r_{ad} and the nucleation temperature used. They found that below 8 nm, T_n is about 246 K and independent of graphene oxide size and concentration [156]. In the case of pure water, homogeneous nucleation theoretically occurs when the solution is supercooled at a temperature around 233 K. Under this ideal conditions, the critical radius can be calculated and it corresponds to 1.85 nm [205, 206].

If the growth rate from the nuclei is assumed to be determined by the Gibbs-Thompson equation, ΔG_{cr} can be described as:

$$\Delta G_{cr} = \frac{16\pi\gamma^3\Lambda^2}{3K_{boltz}^2 T^3 \ln(\sigma^2)} \tag{6.5}$$

where σ is the supersaturation, and Λ is the atomic volume of the species. High temperatures and supersaturation levels result in larger number of nuclei formed. High surface energies and atomic volumes result in smaller nucleation rates.

6.1.1 Modelling nucleation and ice crystal growth

Numerous mathematical models have been proposed to describe the evolution of the ice crystals during the freezing of solutions. In the mononuclear model, the notion is that more molecules will adhere to the nucleus and form, a whole layer at an arbitrarily speedy velocity. Then, the formation of a new nucleus will re-start the process over and over. Two-dimensional growth rate theories assume that the rate-controlling step is the incorporation of a new layer of molecules to an existing surface. The base concept is that nucleation can occur on a two-dimensional surface of an existing crystal the same way it can take place in three dimensions for homogeneous nucleation.

Volmer proposed the homogeneous nucleation theory, which is the base for several nucleation and crystal growth models although, homogeneous nucleation

rarely occurs in practice. Its underlying theories are quantum mechanics and statistical mechanics because they were able to help describe the energy fluctuations needed for the first clusters to be formed (as mentioned in the explanation of equation 6.3) and which result in the stochastic nature of freezing. Volmer's theory assumes that macroscopic thermodynamic properties pertain to the two phases, i.e., a supersaturated parent phase and tiny cluster of the daughter phase [203].

Vekilov explored a two-step mechanism for ice crystal nucleation [207], i.e., accounts for the secondary nucleation. A phenomenological theory was developed by Pan et al. (with Vekilov among the authors). That theory takes into account intermediate high-density metastable states in the nucleation process [208],i.e., the presence of a dense liquid intermediate in the nucleation reaction pathway. This could be interpreted as playing the role of unstable clusters smaller than the r_{cr} in the classical nucleation theory. The rate of nucleation of crystals within the dense liquid clusters was the rate determining step in the two-step nucleation mechanism, which supports the applicability of the Pan et al. model. Since cluster formation is fast, the clusters can be considered in equilibrium with the solution. Then the chemical potential of the solute in the clusters can be assumed to be equal to the chemical potential of the solute in the solution. In their research, the model allowed accurate predictions of the complex dependencies of the nucleation rate of the solute (lysozyme protein) crystals using a single adjustable kinetic parameter that was determined by experimental fit. Good correspondence between the model results and the experimental data supported some nucleation mechanism features. The intermediate is metastable concerning the dilute solution, and the rate-determining step in the nucleation mechanism is forming an ordered cluster within the dense liquid intermediate. Additionally, the viscosity within the metastable dense liquid droplet was found to be a crucial parameter in the kinetics of nucleation of ordered solid phases [208].

Fan et al. developed a phase-field model to describe the ice crystal growth and the freeze concentration dynamics at the mesoscale based on mean-field approximation of solute concentration and the underlying heat, mass, and momentum transport phenomena [69]. The model focused on the evolution of the interfaces between liquid solution and ice crystals and the degree of solute concentration due to partition, diffusive, and convective effects. The growth of crystals was driven by cooling of the bulk solution but suppressed by a higher solute concentration due to an increase of solution viscosity, a decrease of freezing point, and the release of latent heat. The results demonstrated the interplay of solute exclusion, space confinement, heat transfer, coalescence of crystals. Additionally, the dynamic formation of narrow gaps between crystals and plateau border areas along with correlations of thermophysical properties in the supercooled regime.

Vuist et al. modeled the ice growth and solute inclusion behavior during progressive freeze concentration of sucrose, soy protein, and whey protein [70]. Solute inclusion was estimated using an intrinsic distribution coefficient. For sucrose

solutions, the intrinsic distribution coefficient proposed was dependent on the initial and critical concentrations of the solute, where the last is related to the rapid increase in viscosity and decrease in diffusivity when the solution approaches the glass transition temperature. The predictions found were in agreement with experimental data, except when dendritic ice growth was observed. They tested solutions of whey and soy proteins, and they behaved differently due to their considerable difference in their solubility. In their study, these proteins showed different inclusion behavior than sucrose due to lower freezing point depression and lower concentrations far away from the glass transition temperature.

Shalaev et al. wanted to understand better two issues related to molecular mobility: unfrozen water in aqueous solutions at subzero temperatures and the role of water in the chemical stability of amorphous pharmaceuticals. They linked the unfrozen water in solution at subzero temperatures to the role of water for the chemical stability of amorphous pharmaceuticals via the concept of water clusters. In particular, freezing inhibition was associated with the water confinement in clusters in a solidified matrix of an amorphous solute. Nanoscaled water clusters were observed in aqueous glasses using wide-angle neutron scattering. The chemical instability was suggested to be directly related to the catalysis of proton transfer by water clusters, considering that proton transfer is the key elementary reaction in many chemical processes, including common reactions such as hydrolysis and deamidation. [181].

Freezing pharmaceutical solutions in vials

Some models were developed specifically for freezing solutions in vials. Once nucleation takes place, ice crystals start to grow. New water molecules become increasingly added to the existing initial ice crystal casts and the unfrozen solution cryo concentrates. This cryoconcentration, of course, depresses the freezing temperature equilibrium progressively in such a way that after a certain point, it becomes practically limiting to freeze the solution completely. Typically, vials are being frozen, exchanging heat in direct contact with the shelf. The shelf is removing energy from the solution, promoting freezing. This way, for solutions in vials in contact with the cooling shelf, a freezing front moving from bottom to top may be assumed as depicted in Figure 6.2. For vials in other configurations of using other freezing techniques, the freezing front position and behavior may change and thus must be further investigated.

Freezing defines the cake porous structure of freeze-dried products (Figure 6.2). The porous structure will determine the resistance to vapor flow (R_p) during sublimation. The R_p in turn will have an effect in the product temperature during sublimation. Large resistances will result in higher products temperatures during sublimation. As discussed in Chapter 1, product temperature is a critical parameter that must be kept bellow a threshold value to ensure product integrity. Because

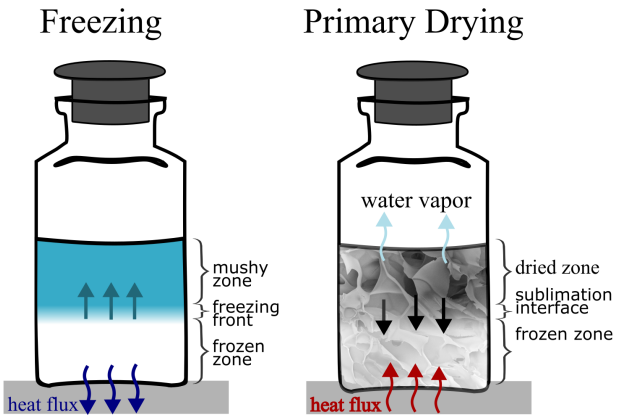

Figure 6.2: Freezing front for solutions in vials being cooled by a cooling shelf (left) and sublimation interface for the frozen product during primary drying receiving heat from the shelf (right).

of these, predicting the porous structure based on the freezing conditions becomes important and different models have been proposed.

The model proposed by Nakagawa et al. [31] is an empirical one. This model is influenced by Bald's proposition, in which the resulting ice crystal size would be inversely proportional to the rate of temperature change in the system. Hence, faster cooling rates would result in smaller crystal sizes [44]. Empirical models neglect the physics of the system and are developed from a practical perspective of application and adequate results. The model parameters have no physical meaning and are determined experimentally. Hence, they are only valid under the conditions tested, limiting the model's predictive reliability and accuracy. More details are given in Subsection 6.2.1.

Pisano et al. developed a mechanistic model to describe dynamics of an aqueous liquid solution during freezing and, thus, to predict the pore size distribution within the lyophilized product [166]. Their model simulations were experimentally validated using both crystallizing and amorphous solutes and varying freezing conditions such as nucleation temperature. That model could predict the larger ice crystal formation when VISF is used compared to those obtained using shelf-ramped freezing. Moreover, it could accurately describe the dependence of the average pore size on nucleation temperature. Through modeling, they found that higher nucleation temperatures produced lyophilized products with larger pores and narrow distribution of pore size along with the product height.

The model proposed by Arsiccio et al. [43] has a mechanistic approach. The basic idea underlying this approach is that exothermic processes both incorporate new water molecules into the existing crystals and create new interfaces. The cooling instrument and surrounding environment remove some of the energy released during freezing. This way, the energy balance in an infinitesimal slice of the material can

be related to the crystal growth dynamics. The nucleation kinetics are neglected, and the crystal growth rate is indirectly accounted.

Recently Colucci et al. [29] proposed a model based on the UNIQUAC model coupled with a one-dimensional Population Balance Model (PBM) to describe both the ice nucleation and the crystal growth. A stochastic model describes the nucleation kinetics. The ice crystal nuclei evolution over time is described by a 1D PBM. The crystal growth rate is modeled as a function of the supersaturation. An analytical solution of the proposed model is derived using the Method of Characteristics [209].

However, even though carefully validated with experimental campaigns, all these models to some extent still rely on heat and mass transfer models themselves to be applied.

6.2 Experimental investigation: can the theoretical models be applied with direct IR data?

In this Section, the objective is to test the validity of different freezing models applied to VISF using direct IR thermography data to predict the pore size distribution of the resulting product cake. The temperature acquisition will be made *in-line* by thermal imaging, obtaining each vial's axial temperature profile, thus allowing for a detailed prediction of the pore size distribution. The main advantage of this approach is that, by using direct experimental data describing the whole axial temperature profile and its gradients, no additional mathematical models are required to describe the pores along the cake. The resulting ice crystals and thus pore sizes may be predicted using *in line* IR thermal data and the models directly.

Moreover, to test the range of applicability of the models, the analysis will be done with the conventional vial configuration alongside vials suspended from the temperature-controlled shelf. In conventional freeze-drying, heat is transferred from the shelf to the vials or vice versa. This occurs mainly through direct contact between the glass and the stainless steel and conduction in the gas trapped in the concavity at the bottom of the vial. When vials are suspended, heat is transferred mainly due to natural convection and radiation. This difference in the heat transfer mechanism challenges the usual assumption of negligible radial and azimuthal thermal gradients and, therefore, the widespread one-dimensional freezing models may not be applicable anymore.

The validation of the predicted cake structures will then be done by comparing the pore sizes obtained through the models with the experimental ones obtained through SEM analysis. Additionally, primary drying temperature profiles and durations will be simulated based on the estimated pore sizes and compared to the experimental ones to validate the one-dimensional models further. The results will be discussed to evaluate if this direct temperature data brings new observations

alongside the proposed models.

6.2.1 Freezing models investigated

Different models have been proposed in the literature to describe the solidification process. Three freezing models were chosen to be further investigated applied to VISF using IR-based thermal data.

The first model, called model #1, is the empirical model proposed by Nakagawa et al. [31]. The second model used is the mechanistic approach proposed by Arsiccio et al. [43], called model #2 in this chapter. These first two models are based on the existence of a freezing front during the freezing process. They rely on parameters related to the rate of freezing as a moving interface that has a defined behavior. These parameters are the ν_H and the θ_H, as portrait in Figure 6.3. This is usually the cake having low fill volumes, although different behaviors of the freezing front were observed when using high fill volumes, such as having two freezing fronts, one moving from the bottom to the top and another from the top to the bottom [53].

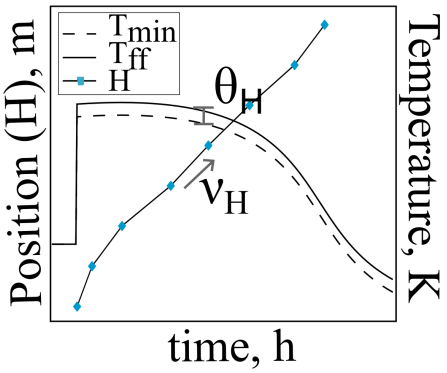

Figure 6.3: Representation of the parameters ν_H and the θ_H derived from the freezing front and the temperature profile of the frozen layer in the case of ON-shelf vials. Adapted from [31].

The ν_H is the freezing front rate $[m/s]$, i.e., how fast the freezing front advances from bottom to top. The parameter θ_H is the temperature gradient in the frozen layer $[K.m^{-1}]$, i.e., the temperature difference between the T_{bottom} and the temperature at the freezing front T_{ff}, relative to the frozen layer thickness. The subscript $_H$ refers to the value of these parameters relative to a segment of the cake height H.

The third ice crystal prediction model (model #3) presented is based on the supersaturation of the system. It accounts for the supersaturation as the drying force for ice crystal growth which depends on the solute and solution's activity coefficients. The ice nucleation rate is calculated coupled with a 1-D PBM model to

better describe the observed results in terms of pore size distribution as proposed by Colucci et al. [29]. Hence, this model does not depend on the existence of a distinguishable freezing front, only the solution's characteristics at the point being examined. Thus, only the product temperature of the investigated system is needed. With the IR thermal data, the whole cake profile can be described in terms of discrete layers, resulting from the 8 pixels that were needed to cover the product cake, as represented in Figure 6.4.

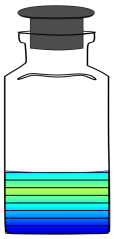

Figure 6.4: Representation of the 8 layers of the 10 mm cake that can be described using the IR axial profile temperature. Model #3 can be applied using the thermal data of each level to described the resulting pore size distribution of that cake layer.

The freezing front could be directly observed using IR data in the case of vials exchanging heat directly with the shelf as seen in Chapter 5. In this case, the heat removal occurs directly from the vial to the shelf, and the temperature at the bottom of the vial (T_{bottom}) is the lowest during the freezing step. Thus, the first two models (models #1 and #2) will only be applied to ON-shelf vials, to ensure the direct application of the experimental IR thermal data. The experimental data used for these two models was the H_{max} as correspondent of the freezing front evolution and the $T_{max} - T_{bottom}$, as correspondent of the temperature gradient in the frozen layer.

The supersaturation model, model #3, was tested using the whole axial temperature profile to obtain the freezing characteristics of each layer of cake. Since 8 pixels are used to describe the 10 mm cake height, eight layers of thermal profile yield the ice crystal predictions for the cake.

Model #1

The model presented by Nakagawa and Hottot (2012) [31] to predict the average ice crystal size (d_{p_H}) for solutions in vials will be called model #1 in this work and is presented below.

$$d_{p_H} = \alpha \nu_H^{\lambda 1} \theta_H^{\lambda 2} \tag{6.6}$$

In previous applications of this model, $\lambda 1 = \lambda 2 = 0.5$ were used while α was experimentally fitted to the resulting pore sizes and changed according to the solution and freezing protocol used [31, 184, 185]. Previously $\alpha = 4.59 \mu m s^{-0.5} K^{-0.5}$ was used for a 5% sucrose solution, while $\alpha = 1.7 \mu m s^{-0.5} K^{-0.5}$ was used for a 5% mannitol one [31, 142, 185]. For dextran 5%, the α used was the same as the one for sucrose. In the present study, the same α values were used for sucrose and mannitol. However, a value of $2 \mu m s^{-0.5} K^{-0.5}$ was chosen for 10% dextran based on the experimental results.

Model #2

The model #2 is the simplified mechanistic model proposed by Arsiccio (2017) [43] in which its parameters have more physical grounding than in previously proposed models for freezing in vials.

$$d_{p_H} = \frac{4\epsilon\gamma b\nu_H}{(\varepsilon\rho_{ice}\nu_H\Delta H_f - k_{frozen}\theta_H)\theta_H^{\frac{2}{3}}} \tag{6.7}$$

here, ϵ is the adimensional porosity of the dried product which can be approximated assuming that all water in solution is removed and only the solids constitute the dried cake. Although that is an approximation because not all the water will freeze. Some bound water will remain unfrozen, trapped in the frozen matrix of the solution and will be removed during secondary drying in a freeze-drying process. The k_{frozen} value used was 2.55 $Wm^{-1}K^{-1}$, corresponding to the ice conductivity at 238 K, ΔH_f is the latent heat of fusion for water, 33.5 $kJKg^{-1}$ and the ρ_{ice} used was 918 kgm^{-3} [182]. The parameter γ $[Jm^{-2}]$, is the interfacial tension from the newly formed surface and b $[K^{\frac{2}{3}}m^{\frac{-2}{3}}]$ is a constant coefficient of the model. γb, is fitted experimentally, according to the solution and freezing protocol similarly to the α value in model #1. Thus, the γb values used were 23000 $J.K^{\frac{2}{3}}m^{\frac{-8}{3}}$, 7000 $JK^{\frac{2}{3}}m^{\frac{-8}{3}}$, and 8000 $J.K^{\frac{2}{3}}m^{\frac{-8}{3}}$,for 5% sucrose, 5% mannitol and 10% dextran respectively. The first too are the same values previously used [43, 143] while for dextran the value was fitted based on the experimental results.

Model #3

Finally, the third model is driven by the supersaturation of the system (σ), similar to the approach presented by Colucci (2020) [29]. The supersaturation is described by the free Gibbs energy and calculated based on the activity coefficients of the solutes and solution using the UNIQUAC model.

This approach considers the phases of the different systems during freezing, the solution that cryoconcentrates, and the water that solidifies. The porous media approach used assumes that although a system might be heterogeneous at

the mesoscopic level, its effective properties (density, specific heat, conductivity, amongst others.) can be described by a linear combination of the properties of the single phases for a reasonably small part of the system (dV) during a given dt.

First, the initial nucleation rate (J_0) is calculated to determine the initial number of ice nuclei formed during the nucleation event [$m^{-3}s^{-1}$].

$$J_0 = k_n(T_f - T_n)^n \tag{6.8}$$

J_0 is driven by the difference between the equilibrium freezing temperature of a solution (T_f) and the actual nucleation temperature (T_n), i.e., the supercooling degree ($T_f - T_n$). The kinetic parameters k_n and n are based on the stochastic nature of freezing. In the previously proposed model [29], the nucleation kinetics is described by a stochastic model in a chemical Master equation. When the system reaches saturation is the moment from which ice crystals may start forming (t_{sat}). The nucleation kinetics parameters were fit to achieve the best agreement between simulated and experimental induction times for nucleation (t_{ind}). That fit was done based on the probability distribution function of the ice crystals formed, assuming the induction times would follow a series of Poisson distributions. This way, the kinetic parameters k_n and n were tied up by equation 6.9.

$$k_n = \frac{N}{V\sum_{i=1}^{N}\int_{t_{sat}}^{t_{ind}}[\Delta T(s)]^n ds} \tag{6.9}$$

In this present thesis, this model is only applied using VISF. A cGMP environment was established to avoid premature nucleation and, when the vacuum is applied, all vials nucleate in a brief time spam ($\sim$ 100s). By doing so, the VISF holding time would become the induction time. Thus, the stochastic nature of freezing is affected. This way, the assumption and previously made experimental fit to determine k_n and n are not representative anymore using controlled nucleation techniques. If the dt between saturation time and induction time was assumed to be zero, K_n would tend to infinity (equation 6.9). This assumption is linked to the idea that the supercooling degree would also be very high, leading to an incredibly high number of ice crystals. During VISF, the factor inducing nucleation is the fast cooling of the sample surface once vacuum is applied. Still, to have a rough idea of the K_n, some assumptions may be made.

In a hypothetical scenario, suppose $n = 1$, with a 2 K supercooling degree and $dt = 100s$ and $V \cong 2 \times 10^{-9}m^3$ (dV volume used for calculations in the monitored wall area, based on the pixel size of the IR temperature measurements

used. For 1 observation ($N = 1$, so, no distribution is to be considered. In that case, k_n would be in the order of 10^6.

Since only primary nucleation is accounted for, k_n and n are the only parameters determining the number of ice crystals formed in a given dV. The SEM images allow estimating the average number of crystals formed that grew to an observable size. This average crystal size number was estimated for tests using both T_{nuc}, 271 K and 263 K. This way, the kinetic parameters were defined fitting the simulated results to the experimental results using SEM and the pore extraction tool described in Chapter 5. Using this info, k_n and n were fitted to the experimental data, resulting in: $k_n = 1.3 \times 10^{10} m^{-1} s^{-1}$ and $n = 1.7$. A final check was done to verify if the fitted parameters were in agreement with the assumption of brief induction times for VISF. The Master Equation (Equation 6.10) [29] was used to obtain the probability distribution function for the induction times using the fitted k_n and n.

$$f(t_{ind}|k_n, n) = k_n[\Delta T(t_{ind})]^n V \exp\left\{-\int_{t_{sat}}^{t_{ind}} k_n[\Delta T(s)]^n V ds\right\} \tag{6.10}$$

This equation describes the induction time distribution, according to the k_n and n values used. s is the integration variable for $f(t_{ind}|k_b, b)$. By the induction time definition, the probability of having 1 nucleus formed during the t_{sat} and t_{ind} interval must be 100%, thus, $\int_{t_{sat}}^{t_{ind}} K(t)dt = 1$.

The probability distributions obtained always peaked at brief times using the estimated k_n and n values (Figure 6.5), showing that the fitted parameters agree with the short induction time assumption when performing VISF tests.

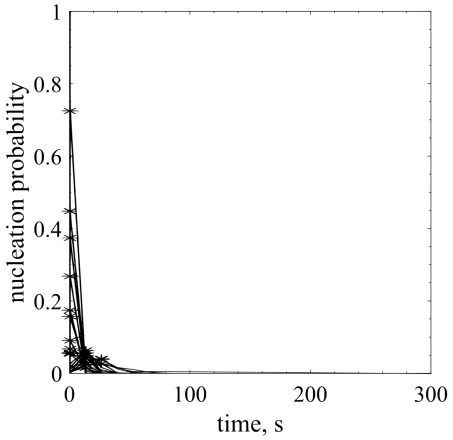

Figure 6.5: Induction time probabilities using the fitted k_n and n values.

The defined $k_n = 1.3 \times 10^{10} m^{-1} s^{-1} K^{-n}$ and $n = 1.7$ parameters were applied to all experimental data ahead, independently of the solute or the nucleation temperatures used. Previously used values for uncontrolled nucleation were $k_n = 10 \times m^{-1} s^{-1} K^{-n}$ and $n = 12$ [29]. These values are very different from the ones used in this present study, while the reported induction times were at least 10 times greater than the ones using VISF according to their reported values [29]. Based on the observed results using spontaneous nucleation in this study, the induction times were even more widely distributed. Some vials nucleated after a time interval in the order of 10^2 seconds after reaching a supercooled state while others took over 10^4 seconds. In any case, the parameters used in this series of experiments were fitted based on experimental data and check analyzing the nucleation probability distribution the best way possible to represent the observed freezing phenomena and induction times.

Ice crystal growth

The freezing rate ($\dot{I}$) is driven by the system's saturation. The saturation (S) is defined as the volume fraction of either water or ice over the volume of everything apart from the solute. This way, the liquid water saturation (S_{liquid}) plus the ice saturation (S_{frozen}) represent all the water in the system ($S_{liquid} + S_{frozen} = 1$) and follow the mass balance below.

$$\frac{\partial S_{frozen}}{\partial t} = -\frac{\partial S_{liquid}}{\partial t} = \frac{1}{(1-\phi)\rho_{ice}} \dot{I} \tag{6.11}$$

where ϕ is the volume fraction of the solute dissolved in the solution. The ice crystal growth rate (G, ms^{-1}) is driven by the supersaturation (σ) of the system, explained in detail ahead. G was calculated using the equations below, assuming cylindrical crystals and neglecting the surface of the top and bottom of the cylinders.

$$G(D_p, t) = k_g \sigma^g 2\pi \Delta z . D_{p_{t-1}} = G'(t) . D_{p_{t-1}} \tag{6.12}$$

$$D_p(t) = D_{p_{t-1}} \exp\left[\int_{t_0}^{t_{end}} G'(t) dt\right] \tag{6.13}$$

The parameters $2\pi\Delta z$ come from the assumption that the ice crystals are approximately cylindrical. In fact, hexagonal ice (Ih) represents the most common form in everyday application [46]. D_p is the distribution of the ice crystals, called with capital D to differentiate it from the average d_{p_H} from the first two models. Since the pore size distribution was found to follow a beta distribution with $\beta_1 = 1.2$ and $\beta_2 = 15$ [29], the first D_{pt0} values are defined during nucleation using a 1-dimensional population balance model PBM using these distribution parameters.

Thus, the first $D_{p_{t0}}$ is defined using this beta distribution, assigning initial radii from 0 to 0.5 μm. $D_{p_{t-1}}$ is the previous state of the pore size distribution (D_p). The average pore diameter (d_{p_H}) was obtained as the ratio between the distribution's first and zeroth order moments.

The kinetic parameters k_g and g are highly dependent on the time-step used for the integration interval. Previously, using time steps from 0.02 to 0.5 seconds in a completely simulated environment, $k_g 2\pi\Delta$ z was set as $10s^{-1}$ (meaning $k_g = 1592m^{-1}s^{-1}$) while g was set as 1. In this present study, using only experimental IR-based temperature data, $k_g 2\pi\Delta z = 1s^{-1}$ and $s^{-1} = 1$ were used with an integration time-step of 0.01 seconds.

The integration interval $t_0 - t_{end}$ is from nucleation to the end of freezing. Differently from models #1 and #2, model #3 calculates the evolution of the crystal growth over time. If the integration interval is too long, there will be no more free water in the system to freeze. To ground the calculation to a physical parameter, the end of freezing was based on the eutectic point (T_{eu}) for a 5% mannitol solutions (251.7 K) and on the glass transition temperature (T'_g) for the sucrose (240 K) and dextran solutions (264 K) [148]. It was expected that, if the model and the used parameters and assumptions correctly describe the freezing process, freezing will be over when T_{eu} or T'_g are reached and the final solid mass fraction is the one given by the systems characteristics.

Activity coefficients

- *Ice activity*

Using the UNIQUAC model, the supersaturation (σ) is given by the difference between the activity coefficients of the frozen (a_w^i) and liquid (a_w^l) fractions:

$$\sigma = \ln \frac{a_w^i}{a_w^l} \tag{6.14}$$

The ice activity is defined by its temperature [180].

$$\ln a_w^i = \frac{\Delta H_{fus}^0}{R}\left(\frac{1}{T_1^0} - \frac{1}{T}\right) - \frac{\Delta c_{p,l}^0}{R}\left(\ln\frac{T_1^0}{T} + 1 - \frac{T_1^0}{T}\right) \tag{6.15}$$

Where ΔH_{fus}^0 is the fusion latent heat at the standard condition, signalized with the "0" superscript. $\Delta c_{p,l}^0$ is the change in the liquid water specific heat capacity $[Jkg^{-1}K^{-1}]$, T_1^0 is the temperature $[K]$ at the standard condition, in this case, 273.15 K was used.

The liquid activity was calculated using different models for each solute, as described ahead.

- *liquid activity for sucrose solutions*

The liquid activity depends on the temperature and the solute concentration. For sucrose, it was calculated by the model described by Cattè et al. (1994) [210]. The liquid activity for sucrose is defined by the symmetric activity coefficient ($\ln \gamma_w^l$) and the molar fraction(x_i).

$$\ln a_w^l = \ln \gamma_w^l + \ln x_i \tag{6.16}$$

While the symmetric activity coefficient ($\ln \gamma_w^l$) is given by:

$$\ln \gamma_w^l = \ln \frac{w_i}{x_i} + 1 - \frac{w_i}{x_i} + q_i \left\{ 1 - \ln \left[\sum_j (\vartheta_{sj} \tau_{Bji}) - \sum_j \frac{\vartheta_{sj} \tau_{Bij}}{\sum_k \vartheta_{sk} \tau_{Bkj}} \right] \right\} \tag{6.17}$$

In which w_i is the ice volume fraction [-],x_i the molar fraction [-] (% sucrose or water/ice), q_i the ice molecular surface area parameter [-], ϑ_s the surface area fraction and τ_B the Boltzman factor for residual excess Gibbs energy, obtained from temperature-dependent interaction parameters a_{ij}, listed in the table below.

Table 6.1: UNIQUAC coeficients [210]

	r i	*q i*	*a ij1*	*a ij2*	*a ij3*
water	0.92	1.40	92.69	-0.55	0.59
sucrose	14.55	14.31	-69.68	0.56	-0.75

The reference temperature (T^0) used was 293 K and $\tau_{Bnn} = 1$ by definition. $\sum_j q_i x_i$ sums water-sucrose + sucrose-water, while the coefficients are calculated as follows:

$$a_{ij}(T) = -a_{ij,1} - a_{ij,2}(T - T^0) - a_{ij,3} \left[T \ln \frac{T^0}{T} + T - T^0 \right] \tag{6.18}$$

Surface area fraction of molecule i is calculated by:

$$\vartheta_{si} = \frac{q_i x_i}{\sum_j q_i x_i} \tag{6.19}$$

The Boltzman factor by:

$$\tau_{Bij} = \exp\left(\frac{a_{ij}}{T}\right) \tag{6.20}$$

And finally, the volume fraction of molecule i by:

$$w_i = \frac{x_i r_i^{\frac{2}{3}}}{\sum_j x_i r_j^{\frac{2}{3}}} \tag{6.21}$$

The letter j refers to the components of the system; in this case, 1 is water/ice and 2 is sucrose. The i (ice) position indicates the direction of the equilibrium. K = 1:2, to include the interactions $ij+jj$ in the lower summation for each j.

- *liquid activity for mannitol solutions*

The liquid activity for mannitol was calculated using the Norrish (1966) model, based on the mole fraction, x_i [211].

$$a_w^l = (1 - x_i)\exp(krx_i^2) \tag{6.22}$$

with $kr = -0.91$ [212].

- *liquid activity for dextran solutions*

For dextran, the liquid activity was calculated based on the model proposed by De Vito et al. (2015) [213] and checking the results based on the data presented by Fernandez et al. [190].

$$\ln a_w^l = -\frac{AV_wC^u}{R_gT}; \tag{6.23}$$

where $u = 2.1$, R_g is the universal gas law constant equal to 8315 $Jkmol^{-1}K^{-1}$, V_w is the partial molal volume of water ($18m^3mol^{-1}$) and A is a constant proportional to the excluded volume parameter estimated from Shimon Mizrahi (1997) data using the known resulting dextran a_w concentrations [214]:

$$A = 0.0479\exp(7.4628C) \tag{6.24}$$

where C is calculated based on the model for polymers [212]

$$C = \frac{ms}{\frac{mw}{\rho_{liquid}}} + \frac{ms}{\rho_{solid}} \tag{6.25}$$

in which mw is the water mass fraction, ms is the solid mass fraction, ρ_{liquid} and ρ_{solid} are the densities of the solid and liquid phase respectively $[kgm^{-3}]$.
Constants used

During cryo-concentration, the freezing point depression of the solutions was accounted for [215]. The solute conductivity value used was $0.293 W m^{-1} K^{-1}$ [183] and other parameters are listed in table 6.2.

Table 6.2: Thermodynamic parameters used (from [182, 183, 216–219]).

,

	k, W m^{-1} K^{-1}	**cp, J kg^{-1} K^{-1}**	**ρ, kg m^{-3}**
Ice	2.21 – 0.12·T	(2.12 + 0.008·T)·10^3	917 – 0.0137·T
Water*	0.75·δ$^{0.19}$	·55.5 (–19654.2 + 98.6·T– 0.14·T^2 + 2.3·10^8/T^2)	1007.9·exp(–T$_{critical}$ (3.97·10^{-4} + 1.68 10^{-3}·δ + 2·(–7.8·10^{-4})·δ$^{0.5}$))
Sucrose	0.29	1240.00	1587.90
Mannitol	0.70	1311.90	1489.00
Dextran	0.29	1106.20	400.00

δ = T/T$_{critical}$-1; T$_{critical}$ = 228 K.

6.2.2 Materials and methods

All test configurations, materials, and methods used are the same as described in Section 5.2. The only exception is the spontaneous nucleation tests that are not evaluated in this present section. Hence, only the VISF tests are further investigated through the application of mathematical freezing models to predict the resulting cake structure. Still, only the results pertinent to 5% mannitol and 5% sucrose will be graphically presented ahead in Subsection 6.2.3. The graphical results for 10% dextran will be made available in the near future, in a publication currently being elaborated.

Primary drying simulation

The primary drying *in silico* simulation was used as an additional validation method for the ice crystal models applied following the models presented in Section 4.1.1. The simulated temperature (T_i), R_p and drying duration (based on the sublimation flux, J_w) were the results used for the validation. Their calculation was based on one-dimensional heat-exchange models, explained in more detail in Subsection 4.1.1. The average K_v value obtained for ON-shelf batches was 33.0 ± 4.4 $W.m^2.K$ and was the value used for the simulations.

To tie the simulation to the estimated ice crystal sizes, Equation 6.31 was proposed [142]. It was formulated by assuming that the vapor flux in the dried cake occurs in Knudsen regime, and is therefore proportional to the effective diffusivity (di_e) and the difference between the water vapor concentration in the chamber ($c_{w,c}$) and at the sublimation interface ($c_{w,i}$) [220]:

$$J_w = di_e \frac{c_{w,i} - c_{w,c}}{L_{dried}} \tag{6.26}$$

By implementing the ideal gas law to describe the water vapor concentrations in terms of the partial pressures, we have:

$$J_w = \frac{M_w di_e}{R_g T} \frac{p_{w,i} - p_{w,c}}{L_{dried}} \tag{6.27}$$

where R_g is the universal gas law constant, M_w is the water molar mass (18 $kg\ kmol^{-1}$). Using this J_w definition into Equation 4.2 and assuming that the thermal gradient in the product is small, so that $T \cong T_i$, R_p can be described as:

$$R_p = \frac{R_g T_i}{M_w di_e} L_{dried} \tag{6.28}$$

The effective diffusivity can be described in terms of the Knudsen diffusivity (di_k):

$$di_e = \frac{\epsilon_p}{\tau} di_k \tag{6.29}$$

where ϵ is the dried product's porosity (assuming all water sublimated) and τ is the tortuousity of the dried cake. The tortuosity can be defined as the ratio of the actual vessel path length to the linear distance between its endpoints. The term di_k can be described as:

$$di_k = Kp \frac{d_{p_H}}{2} T_i^0.5 \tag{6.30}$$

where K_p is a constant parameter equal to 22.9 $ms^{-1}.K^{0.5}$ [142] and $\tau = 1$ was the tortuousity value used for all solutions. The physical meaning of this assumption is that the paths through which the vapor flows would be somewhat linear. Thus, the R_p could be calculated in terms of d_{p_H} using the equation below.

$$R_p = \frac{R_g T_i^{0.5}}{Kp\, \epsilon M_w \frac{d_{p_H}}{2\tau}} L_{dried} \tag{6.31}$$

6.2.3 Results and discussion

In practical terms, water in solution never completely freezes. After nucleation, pure ice is formed, and the solution cryo-concentrates. Once the system reaches a characteristic concentration, dependant on the excipient, the cryo-concentrated solution remains in a supercooled single-phase amorphous state. Water molecules get trapped into the excipient solidified matrix and are unable to diffuse and crystallize further [180, 181]. For this reason, freezing is usually regarded as "complete" when the solution reaches the glass transition temperature ($T_{g'}$) for amorphous solutions or the eutectic point (T_{eu}) for crystalline ones.

It was observed through the $T_{profile}$ that after the solutions reached nearly 260 K, the vertical temperature gradients became less evident. The release of the latent heat of solidification becomes less pronounced, and the product temperature tends to be more homogeneous. This way, the H_{max} and T_{max} tracking by the IR sensor detected a profile according to the expected freezing front one, moving from bottom to top, during the first 20 minutes of freezing for ON-shelf vials. This time scale is in agreement with what was previously reported for the same cake height[31]. Hence, this is the freezing interval that will be considered to obtain the freezing front rate (ν_H) and the temperature gradient in the frozen layer (θ_H) based on the T_{max} and H_{max} profiles.

Freezing front based models

Figures 6.6 and 6.7 (a) shows the T_{bottom} and T_{max} during freezing as well as the H_{max} for all tested solutions.

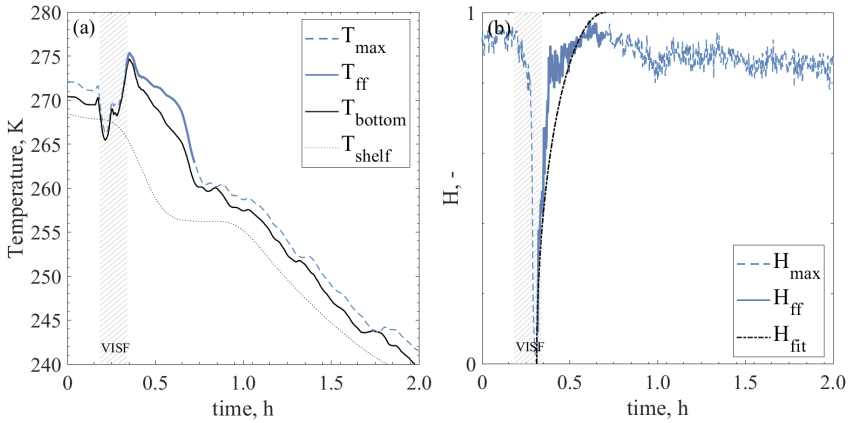

Figure 6.6: Maximum temperature profiles during freezing for test 1-M. (a) Temperature gradient between the bottom and the T_{max} measured. (b) H_{max} and fit used for the models along the vial adimensional axis, where 0 is the bottom and 1 the top.

In Figures 6.6 and 6.7, the T_{max} temperature and position in graphs (a) and (b) are plotted with a continuous line during the accounted freezing interval. Representing the freezing front temperature and position, respectively. The T_{max} and H_{max} intervals just after nucleation are marked more expressively with a thicker continuous line to stress the freezing interval considered for the application of models #1 and #2. These two temperatures during this interval are used in the model to calculate θ_H. The H_{max} profile was assumed to represent the freezing front profile. The regarded interval is based on the time-scale assumptions described in Subsection 5.2.2, i.e., for the first ∼15 min minutes of freezing, in agreement to what was previously modeled [221]. In Figure 6.6 and 6.7 graph B, the H_{max} is plotted together with a fit that was used in the d_{p_H} calculations to have a continuous progression of the H_{max} profile.

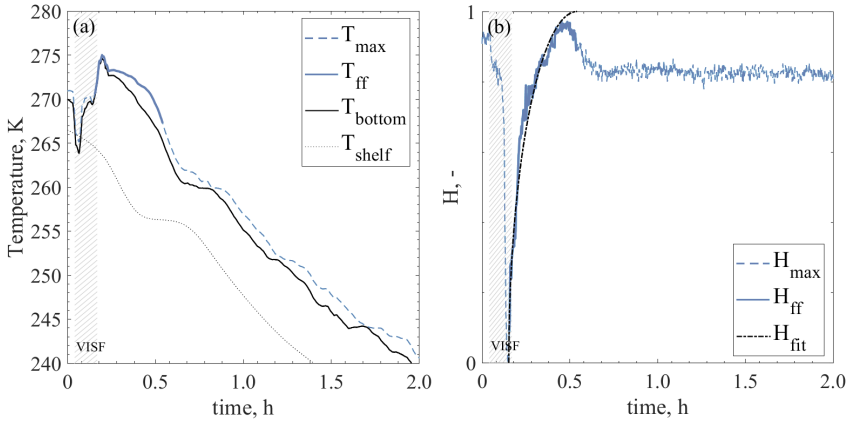

Figure 6.7: Maximum temperature profiles during freezing for test 1-S. (a) Temperature gradient between the bottom and the T_{max} measured. (b) H_{max} and fit used for the models along the vial adimensional axis where 0 is the bottom and 1 the top.

Supersaturation model

As explained, the supersaturation model depends not on the gradients but on the temperature at the point of interest. This way, the whole axial temperature profile was used in such a way that the thermal data of each pixel was used to estimate the ice crystal growth for the corresponding cake layer. Thus, the cake was divided into 8 levels, having the crystal size distribution calculated for each of the cake layers based on the average temperature of the corresponding pixel from all six acquisition lines used for each vial. Figure 6.8 shows an example of the axial temperature profile obtained for both ON-shelf and OFF-shelf vials for mannitol solutions. For the sucrose solution, the $T_{profile}$ data is plotted in Figure 6.9.

From Figure 6.8 and 6.9 it can be seen that the overall temperature gradient for OFF-shelf vials is narrower than for ON-shelf ones. Thus, based on the

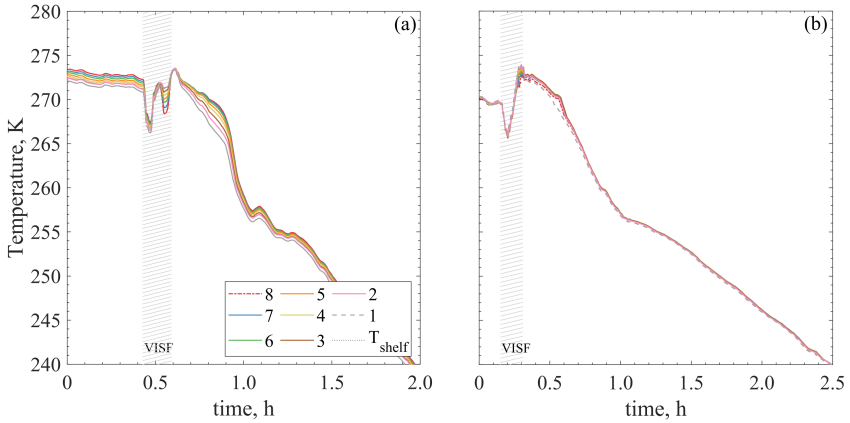

Figure 6.8: Axial temperature profile for for 5% mannitol (a) test 1-M, ON-shelf and test (b) 3-M, OFF-shelf. Lines 1 to 8 represent the pixels for data extraction for bottom to top, respectively.

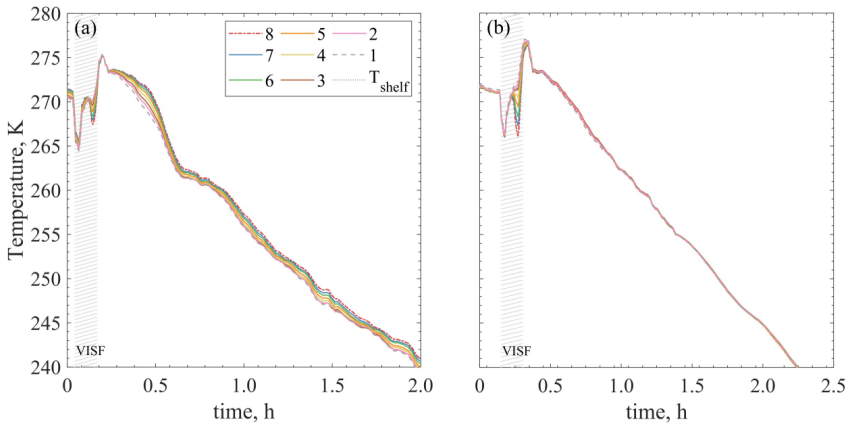

Figure 6.9: Axial temperature profile for for sucrose 5% (a) test 1-S, ON-shelf and test (b) 3-S, OFF-shelf. Lines 1 to 8 represent the pixels for data extraction for bottom to top, respectively.

supersaturation model, the resulting cake structures should be more homogeneous for suspended vials than ON-shelf vials. This higher homogeneity is consistent with what is expected since the heat transfer for OFF-shelf vials is less sharp than for ON-shelf vials, which exchange heat directly in contact with the cooling shelf.

Model validation through primary drying simulation

For the one-dimensional models, further validation was done besides confronting the SEM results. A simulation of the primary drying was performed with the estimated pore sizes and confronted with the experimental profiles observed during primary drying. Figure 6.10 shows the simulated T_{min}, R_p, L_{frozen} evolution

during primary drying for mannitol solutions plotted against the experimental corresponding data obtained after freezing. The same results for sucrose can be seen on Figure 6.11.

In Figures 6.10 and 6.11, T_{min} was obtained through IR thermography and the experimental R_p profile was calculated based on the IR-extracted T_{min}. The decrease of the L_{frozen} was used to estimate the end of freezing, thus is compared to the Pi/Ba signal. The time interval for the R_p plot is the estimate duration of each test, which was approximately 12 hours.

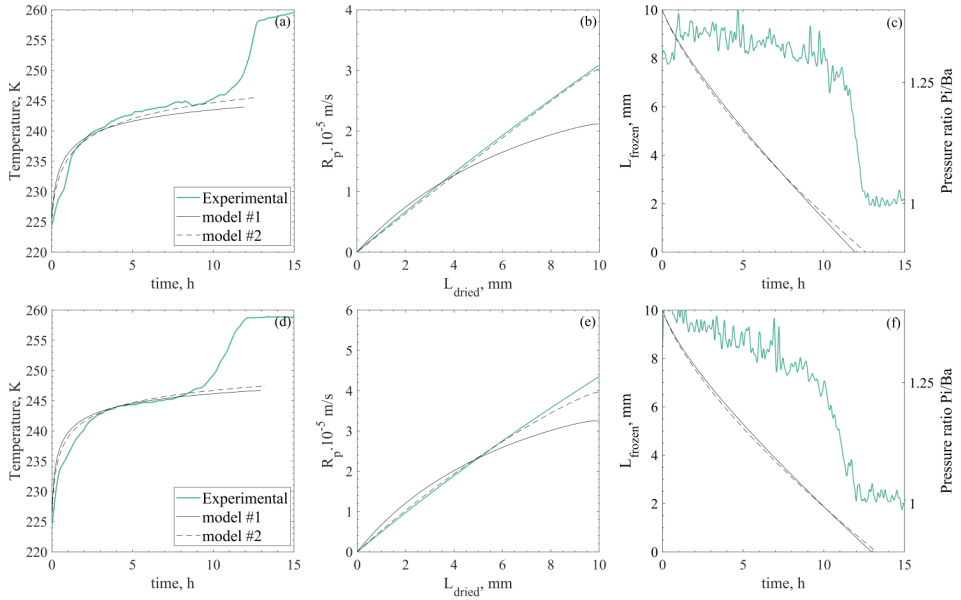

Figure 6.10: Linear models validation through primary drying simulation (temperature, R_p and end time) for ON-shelf tests. Top graphs are for test 1-M while bottom graphs for test 2-M.

From the results presented in Figures 6.10 and 6.11, a good correspondence between the simulated and experimentally obtained profiles can be observed. The temperature profile estimation based on the estimated pore sizes had a good fit and consequently, so did the cake resistance to vapor flow profiles. However, it can be observed that model #2 resulted in a better prediction of the R_p profile for all tests. The experimental duration will correspond to the simulated L_{frozen} progression if the simulated sublimation flux agrees with the experimental one. This agreement can be seen through the R_p profiles, which are in good agreement, belonging to the same order o magnitude.

Through primary drying simulation, models #1 and #2 showed a much more powerful result. The accuracy loss in the cake top and bottom did not affect the results because these deviations occur only for a small portion of the cake. Thus, these models could be successfully applied with IR-based data to simulate drying

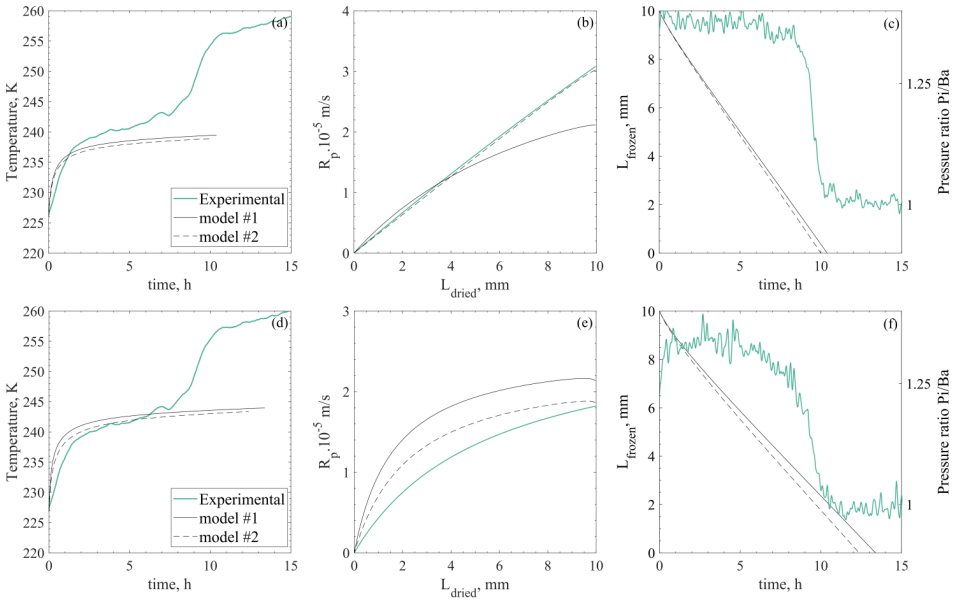

Figure 6.11: Linear models validation through primary drying simulation (temperature, R_p and end time) for ON-shelf tests. Top graphs are for test 1-s while bottom graphs for test 2-S.

and choose the best drying conditions to avoid collapse or damage to heat-sensitive active compounds.

Model validation through SEM

Figure 6.12 shows the predicted pore sizes based on the ice crystal growth models tested confronted with the experimental SEM results for the 5% mannitol solution. The results for the 5% sucrose solution are presented in Figure 6.13. Note that as explained in section 2, for ON-shelf vials, all models were applied while for OFF-shelf vials, only the model #3 was applied. Hence, this is the data represented in Figures 6.12 and 6.13 for the ON and OFF shelf configuration with the two tested nucleation temperatures.

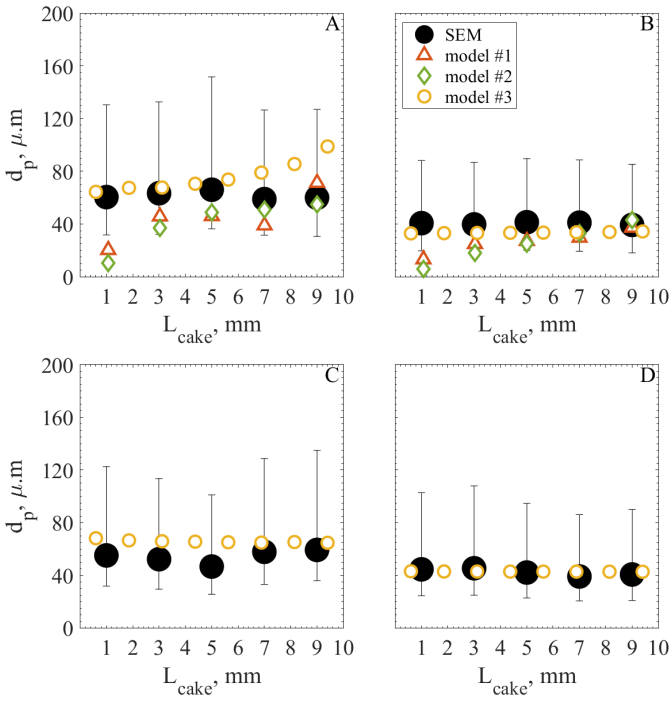

Figure 6.12: Cake pore sizes obtained experimentally and by all tested models for 5% mannitol. Top graphs, ON shelf, bottom graphs OFF-shelf. Tests (A) 1-M, (B) 2-M, (C) 3-M and (D) 4-M

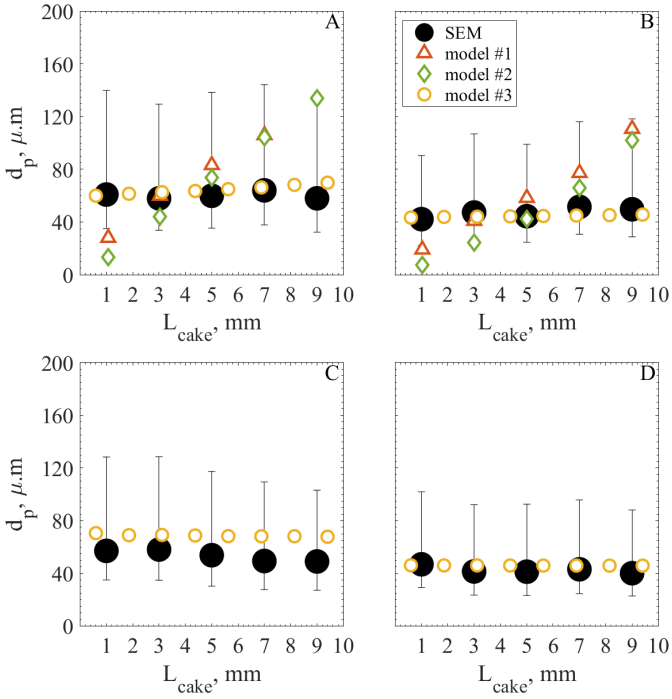

Figure 6.13: Cake pore sizes obtained experimentally and by all tested models for sucrose 5%. Top graphs, ON shelf, bottom graphs OFF-shelf. Tests (A) 1-S, (B) 2-S, (C) 3-S and (D) 4-S

From these results, model #1 and model #2 were able to predict the average pore size with sufficient accuracy. However, in Figure 6.13, graph A it can be observed that toward the edges of the cake (top and bottom), they became less accurate. For mannitol, Figure 6.12 this is also the case in graph B. This error might be because of the differences observed between the experimental IR-based freezing front profile and the modeled one used to derive the models. The simulated freezing front progression used for the development of the models presents a more constant progression of the frozen layer [31, 43, 166].

Regarding the cake structure in overall, from the temperature profiles, the resulting cake homogeneity could be accessed. Figure 6.14 shows a 3D representation of the predicted cake structure for 5% sucrose with a 271 K T_n for the ON-shelf and OFF-shelf configuration. As it can be seen, the using the model, the OFF-shelf cake also shows a more homogeneous cake, as observed in Subsection 5.2.2.

Regarding the system's state according to the calculations using model #3, the final solute solid fraction in the end of freezing was virtually the same for each solution. For the 5% mannitol it was 0.812 ± 0.004, for 5% sucrose it was 0.817 ± 0.003 and for 10% dextran it was 0.663 ± 0.005. Thus, the final solid mass fraction for the sucrose and mannitol solutions, having the same concentration, was practically the same. For dextran however, the final solute mass fraction was lower,

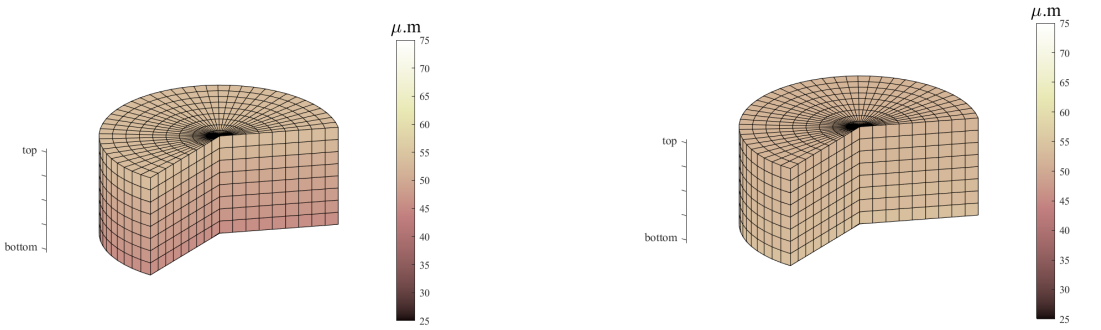

(a) ON-shelf. (b) OFF-shelf.

Figure 6.14: Predicted cake structure using model #3 for 5% sucrose using a 271 K T_n.

indication this this system has less free water to freeze under the tested conditions. This is expected considering that the dextran solute is a polymer of anhydroglucose one and a higher concentration was used.

In turn, the IR-based data presented a sharp trend at the beginning of freezing and then a deceleration towards the end when reaching the cake top. The profile of the freezing front directly influences the ν_H, and with the experimental data, ν_H diverged to very high values in the beginning and then very low ones towards the end. Ice has a higher K_v (2.22 $Wm^{-1}K^{-1}$) than water (0.6 $Wm^{-1}K^{-1}$) at 293 K, however, slightly melted snow has an even lower K_v (0.28 $Wm^{-1}K^{-1}$) than water. The characteristics of slightly melted snow are surely closer to the ones of a mushy ice-water region. This possible increase in the resistance to heat transfer by the growing mushy layer may be the reason for this deceleration on the presumed freezing front, based on the T_{max} profile. This way, using experimental data and the models #1 and #2 as is, the predictions are not reliable for the bottom and top of the cake. Alternatively, modifications of the existing models to better adjust to experimental IR-based profiles could be proposed in the future.

Regarding the results obtained for model #3, they were much more accurate throughout the whole cake height. From the calculations and tests done through this model, the nucleation conditions had the most expressive impact on the resulting crystal size. After nucleation, the temperature profile played more of a kinetic role driving the freezing duration than influencing the resulting crystal size. This observation from the mathematical perspective could be different if a secondary nucleation term were inserted in the model. It is a modification that could be examined in future studies.

6.3 Conclusions

IR allows application *in-line* with different freezing models to predict the resulting porous cake structure. The one-dimensional models were built based on a freezing front profile that was assumed to be more linear than it was previously assumed. The experimentally observed freezing front in terms of the H_{max} presented an initial steep trend at the beginning of freezing (cake bottom) and a slow-down towards the end (cake top), i.e., a less linear profile. This profile change affected the ν_H term for models #1 and #2, which in turn reflected is less accurate d_{p_H} estimations through these models for the bottom and top of the cake. Thus, the resulting estimated pores based on IR data do not always conform with the observed pore sizes using SEM. However, these disturbances only affected the predictions for the bottom and top of the cake, not affecting the the predictions for the rest of the cake. Thus, the primary drying simulation results were in very good agreement with the experimental results. This agreement shows that these models can still be be applied to experimental infrared thermal data and be used to predict the product morphology and batch behavior during primary drying.

The supersaturation model, model #3, was very stable and often resulted in better estimations of the resulting pore sizes. This model seems to be highly influenced by the nucleation temperature alone, having very little influence on temperature profiles after freezing. Because VISF was applied in all tests, cake variability based on the model would have come from the temperature gradients during ice nucleation.

Regarding the time required for the simulations and calculations: it was minimal. The freezing front based models required less than a minute to compute the parameters and estimate the resulting d_{p_H} values. The primary drying simulation also only required one to two minutes. The supersaturation model required more time, but still, using the experimental data, the calculation was done within five to ten minutes.

The main practical advantage that can be extracted from this chapter's results is the possibility to apply ice crystal size prediction models *in line*. They can be used to predict the resulting porous structure of the product and then select the best operating conditions for the primary drying step based on these estimations solemnly based on experimental IR data of the freezing stage.

Part IV

Infrared thermography applied to the primary drying step

Chapter 7

Process monitoring

7.1 Infrared monitoring of the primary drying stage

In freeze-drying processes, after the freezing stage comes the primary drying stage. During primary drying, the frozen solvent is removed by sublimation. As this frozen fraction is removed, a dried layer is left behind with residual amounts of solvent adhered to the dried cake [10]. The evolution of this dried layer can be representative of progression of primary drying. The sublimation interface position (H_i) starts at the top surface of the product's cake, where there is less resistance to the vapor flow (technically, it should be zero, unless there is a skin layer on top of the cake). Then, the sublimation interface moves towards the cake bottom. The closer to the bottom, the higher the resistance to vapor flow. This way, this sublimation interface profile should present a decelerating trend towards the end of sublimation. Assuming a unidirectional progression of the sublimation interface, when H_i reaches the bottom of the cake, it means all frozen layer has sublimated. After this point, additional heat can be supplied to the dried cake to remove the remaining adsorbed water during the secondary drying stage.

According to the nature of cake forming agents used, a critical melting temperature T_m will be defined.If the product reaches a higher temperature than its threshold one before the frozen layer is removed, ice melting takes place. This ice melting damages the product structure causing collapse of the cake.

Therefore, accurate temperature monitoring is critical to ensure product quality of freeze-dried pharmaceuticals. Additionally, the endpoint of primary drying must be accurately determined to: (i) prevent damage to the product in case it is done before all ice is removed; and (ii) to minimize operational costs due to unnecessarily long processing times [151].

According to the current recommendations given by the Guidance for Industry PAT, product quality must be ensured (i) by design or (ii) through

adequate process monitoring and control. To these end, an extensive array of sensors for freeze-drying process monitoring are available and have been described in Section 1.2.2. Some can be used to determine the end time, like the commonly used $\frac{Pi}{Ba}$ [26] curve. Other tools can be used for product temperature monitoring, however, they all present issues. The most commonly used sensors to monitor product temperature are invasive ones such as TCs and RTDs. These sensor present issues regarding:

i placement: it is difficult to place the sensor in the correct spot, i.e., in the center of the vial bottom. Even skilled operators equipped with thermocouple holders to facilitate the sensor's placement that have issues [74]. This becomes a major issue specially in large batches, where more sensors have to be place to properly monitor the whole batch.

ii reliability: this placement issue affects the reliability of this sensor. Additionally, the sensor may move during the process and the ice layer does not dry necessarily in a planar configuration. In these cases, the temperature profile will start to rise before primary drying is over. This rise happens because the sensor will monitor the temperature in a spot where sublimation is over; thus the heat being supplied is being used as sensible heat, increasing the local product temperature.

iii interference: the presence of the sensor has the potential to impact the ice crystal structure and thus the dry layer resistance and the drying time.

iv destructiveness: invasive monitoring is a destructive monitoring because the monitored vials are damaged by the sensor's placement and have to be discarded.

v sterility: last but not least, these sensors may introduce external contaminants to the batch when places and affect the batch sterility.

Infrared monitoring is a promising tool for freeze-drying process monitoring. It provides extensive thermal data on the process, which can be used to monitor the product temperature and to determine the end time without the inconvenience of thermocouples, whose profiles may rise inadvertently [23].

7.2 Experimental investigation: can IR thermography effectively monitor the primary drying stage?

In Chapter 4 the IR sensor's effect inside the drying chamber is deemed insubstantial. Additionally, infrared thermography is evaluated to have good accuracy for temperature monitoring during freeze-drying batches, comparable to

standard tools such as TCs. Still, IR thermography has a critical limitation which is its field of view: it can only monitor the product temperature of vials placed in front of the infrared camera. Additionally, other aspects of infrared thermography applied to the primary drying stage were not yet explored in this thesis: monitoring the minimum axial temperature (T_i) with the updated data acquisition algorithm. Since sublimation is an endothermic phenomenon, tracking the T_i could give the sublimation interface position and temperature throughout the process. Hence, this study aims are[1]:

1. To test and verify if batch representativeness could be improved through a geometrical approach, the use of a hexagonal array.

2. To further explore the T_i profile and its use for a reliable and consistent determination method of the primary drying end time.

7.2.1 Experimental setup

The experimental setup, process conditions, vials, and solutions used were the same as described in Chapter 4, Section 4.1.1. Anyhow, to improve the readability of this chapter, the setup by vial and the process conditions used are summarized in table 7.1 and table 7.2 below.

Table 7.1: Setup used by vial size

Vial size	Batch size	Edge vials	Fill volume	Solution	Gravimetric test durations
4R	157	52	1.5 mL	5% mannitol	260 min
6R	105	39	3 mL	5% sucrose	250 min
20R	30	12	5 mL	10% sucrose	180 min

Table 7.2: General process conditions used in all full cycle tests.

Step	Ramp	Hold
Freezing	from 293 K to 233 K in 1h (1 K / min)	at 233 K fo 2 h
Primary Drying (8 Pa)	from 233 K to 253 K in ~20 min (1 K/ min)	at 233 K until Pi/Ba has stabilized at ~1 for at least 2 h
Secondary drying (8 Pa)	from 253 K to 293 K in 4 h (0.17 K / min)	at 293 K for 2 h

[1]Part of the results presented in this Chapter have been previously published in [145]

Batch representativeness

The hexagonal array is used as a batch configuration in industrial applications because it allows fitting more vials per shelf. Nonetheless, this study evaluates the use of a hexagonal array also as a way to achieve better batch representativeness. Using this array, vials having six neighboring vials are formally considered *central*, whereas vials having less than that are considered *edge* vials.

Product temperature and the required primary drying time may change from vial to vial according to their position in a batch. Those that are more protected from radiating effects during sublimation will present lower temperature profiles and a more unidirectional sublimation progression [138]. Based on the K_v maps presented in Subsection 4.1.2 this was already observed. More exposed edge vials, having three neighboring vials, presented markedly higher K_v values than less exposed edge vials, having five neighboring vials. In Figure 7.1, the vials coloured in green represent those less exposed edge vials that show a closer behavior to central vials.

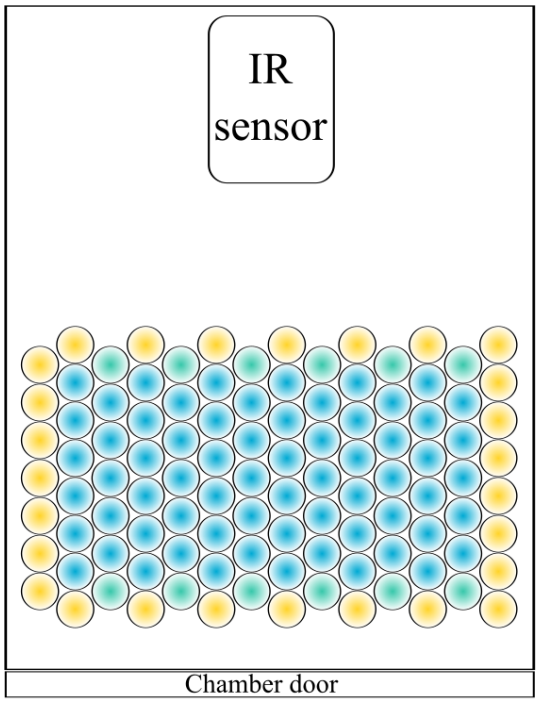

Figure 7.1: Graphical representation of the hexagonal array used in this study. The yellow vials were considered representative of edge vials ($\approx$*edge*) while the green colored vials were considered representative of central vials ($\approx$*central*), which, formally, should be the blue colored ones.

Because the infrared camera can only monitor the first row of vials an

approximation was done to try to enrich the IR acquired data. The infrared-based thermal data acquired from the more exposed edge vials (colored in yellow in Figure 7.1) will be called ≈*edge*. These profiles will be considered representative of the temperature profiles of formally edge vials when comparing IR thermal data to TC data. Meanwhile, IR data acquired from the less exposed edge vials (colored in green in Figure 7.1) will be called ≈*central*. These profiles will be considered representative of the temperature profiles of formally central vials when comparing IR data to TC-based data.

According to previous modeling, the behavior of the sublimation front is different between the ≈*central* and categorical central ones. Figure 7.2 shows the estimates sublimation front profiles highlighting the vial positions evaluated in the chapter.

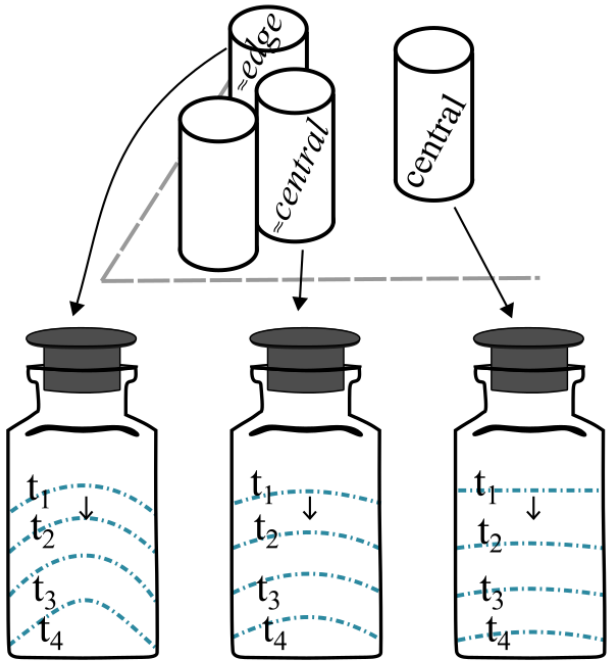

Figure 7.2: Graphical representation of the evolution of the sublimation interface from the beginning of primary drying (t_1) until close to the end (t_4) for vials according to their position in an hexagonal array. Adapted from [138].

From Figure 7.2 is evident that the profiles of ≈*central* are not equal to the profiles of categorical central vials, additionally, they are not necessarily planar [222]. Nonetheless, this is an extrapolation in an attempt to better monitor central vial temperature profiles using infrared thermography. This approximation was only used for the IR-based data. All TC thermal profiles and K_v results regard the formal classification for edge and central vials described above in Subsection f7.2.1.

Automatic end-time determination

The use of infrared-base data as a novel tool to determine the end time of primary drying was investigated. From the IR data, several variables with different physical meanings can be extracted, as described in Subsection 3.3.3. During primary drying, sublimation is the main phenomenon taking place, which is an endothermic process. This way, the tracking of the minima along the axial temperature profile during primary drying may yield information regarding the sublimation interface. The minimum axial temperature (T_{min}) and its position (H_{min}) can be inferred to be representative of the sublimation interface temperature (T_i) and position (H_i) during sublimation. This way, these two variables were tested to determine the end of primary drying.

When the sublimation interface temperature increases, it means that all ice was removed and the heat supplied by the shelf is being used as sensible heat, increasing product temperature. This way, by tracking the T_{min} profile, an increase in the temperature after the initial primary-drying plateau can be used to determine the end of primary drying. Using this ascending profile to determine the end of primary drying with a non-invasive sensor is more promising than doing the same using invasive sensors due to their issues, related to the probe's positioning and cake cracking as already listed.

Additionally, the position of this sublimation interface can also be used to determine the end of primary drying. When the sublimation interface reaches the bottom of the vial, it means that sublimation is over because the last frozen layer was removed. This way, by tracking H_{min}, when this profile reaches the bottom of the vial it would mean primary drying is over.

In order to determine the primary drying in an objective way using the proposed IR-based variables, T_{min} and H_{min}, a custom-made MATLAB (MATLAB R2019b 1994-2020 The MathWorks, Inc) code was developed. The idea was to remove subjective judgements of the used profiles to determine the end point. To automatically detect these points-of-interest using derivatives, the curves had to be first smoothed to remove interference from data noise.

To estimate the end time based on the H_{min}, the point of interest would be when H_{min} reaches the vial bottom. However, this profile will not necessarily reach this point because of the way the variable is acquired. The H_{min} profile is built by the average H_{min} position of six lines per vial. The pixel resolution used corresponds to approximately 4 pixels per 5 mm of cake. The minimum value that H_{min} can reach is the first pixel, corresponding to the bottom of the vial. However, very rarely all six H_{min} values per vial will reach the minimum due to data noise, and this is even more relevant when using the batch average. Observing the raw H_{min} data, after this profile reached a minimum value, the profile would rise. This rise can be indicative of the shelf heating the bottom of the vial because all frozen layer was removed. Using the fitted data for all tests, however, the best way to

delimit a corresponding point was by fitting H_{min} to an exponential function and defining the endpoint using a threshold value. This value worked for all tested vial sizes and was equal to 0.005 (no dimension as it is relative to the adimensional cake high, H). A graphical representation of this algorithm can be seen in Figure 7.3.

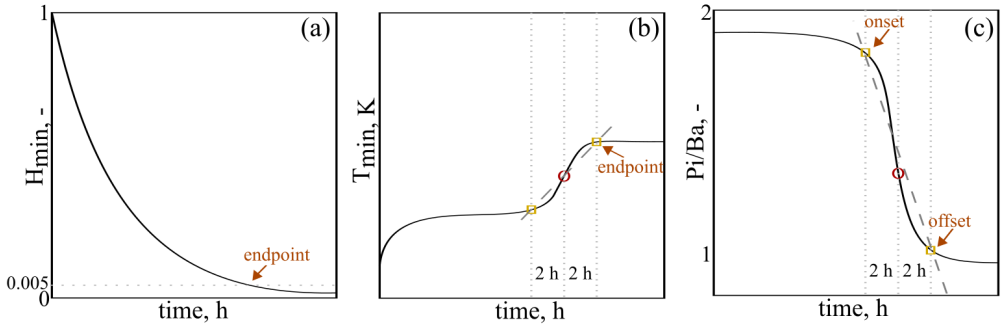

Figure 7.3: Representation of the algorithm used to automatically determine the end time based on the fitted/smoothed (a) H_{min}, (b) T_{min} and (c) $\frac{Pi}{Ba}$ profiles. The circle represents the inflection point detected by the (b) maximum or (c) minimum of the first derivative. The squares represent the points defined to build the tangent line, plotted in dashed light gray.

The *smoothingspline* is a build-in MATLAB function that smooths the data by fitting a set of intersecting polynomials to the curve while the smoothness can be controlled by a smoothing parameter. The T_{min} profile was smotheed using the *smoothingspline* with the default parameter set [223]. The fit was calculated using The T_{min}-based endpoint was determined by first identifying maximum value for the first derivative of the smoothed curve. This point reflects the inflection point after primary drying. This inflexion point occurs because, while there is ice in the cake, the heat being supplied by the shelf is used as latent heat for sublimation. Thus, the temperature remains almost constant, forming the first plateau. Once all the ice sublimated, the heat being supplied is used as sensible heat, increasing the product temperature until around shelf temperature, where it reaches an equilibrium and observed by the second plateau. Then, a tangent line was constructed based on two points: one 2 hours before the inflection point and one 2 hours after the inflection point. Using a tangent based on inflection points to determine points-of-interest is an often used methodology [224]. The end time using the T_{min} profile was defined as the intersection point between this tangent line and the upper temperature plateau of the profile.

To verify the validity of using these two IR-based proposed methods using the T_{min} and the H_{min}, the $\frac{Pi}{Ba}$ curve was used as a reference method. Additionally, the primary-drying duration according the the average batch K_v was included in the evaluation. This method calculates the required drying time to sublimate all water in the product. This is calculated based on the one-dimensional models presented

in Subsection 4.1.1. All heat exchange and mass transfer equations pertinent were described in Subsection 4.1.1 are further described in Subsection 7.2.1.

The $\frac{Pi}{Ba}$ curve was smoothed using the same function used for T_{min}. The method was also the same: identifying the inflection point and constructing a tangent line based on two points 2 hours before and after this inflection point. The difference is that for the $\frac{Pi}{Ba}$ curve, the inflection point of interest in the point with the minimum value for the first derivative. Then, the intersection of the tangent with the first plateau was defined as the onset time and the intersection with the second plateau, after a few hours of primary drying, was defined as the offset time. In previous studies, the cake presented collapse when stopping the cycle after the onset and after midpoint. The product only had a good appearance, without evident collapse, after the offset point using the Pirani sensor profile [26].

Heat and mass transfer models

The primary drying process of vials exchanging heat directly with the heating/cooling shelf can be adequately described by one-dimensional models [149]. Using the equations and assumptions presented in Subsection 4.1.1, K_v, R_p, J_q and J_w can be determined.

The heat exchange coefficient varies with the geometry and size of the used vial and on the chamber pressure. The shelf temperature setting and the solution used has an insignificant effect over this parameter [225]. This way, K_v can be described as a function of the chamber pressure for a given vial setup as illustrated in Equation 7.1 [87]:

$$K_v = a_{K_v} + \frac{b_{K_v} P_c}{1 + c_{K_v} P_c} \tag{7.1}$$

The K_v fit coefficients b_{Kv}, c_{Kv} provide the conditional relation between K_v and P_c while and the influence of the equipment on these coefficients can be ignored. The a_{Kv} coefficient describes the dependence of K_v on the equipment used and on the vial position [149].

Once K_v is known, J_q can be calculated using 4.1. Knowing J_q and ΔH_s, J_w can be calculated through Equation 4.1. Assuming chamber pressure to be uniform, $p_{w,c}$ is equal to the capacitance gauge chamber pressure measured value and calculating $p_{w,i}$ by Equation 4.2, R_p can then be calculated.

R_p has a dependence on the dried cake thickness (L_{dried}) and can be described using Equation 4.8, as described in Subsection 4.1.1.

Statistical analysis

The comparisons made always confronted mean values from two groups at a time as presented in Chapter 4. This way, the data was evaluated using the same statistical method and considerations described in Subsection 4.1.1.

7.2.2 Results and discussion

Batch representativeness

In Chapter 4 the camera was found to have an insignificant impact on batch dynamics and the accuracy of the infrared-based data based on the average bottom temperature profiles was verified. In this experimental investigation section, the infrared thermal profiles are further investigated to evaluate the batch representativeness of this monitoring tool. Figure 7.4 displays the average bottom temperature measured per vial for the 4R vials as described in Subsection 4.1.2. The first point to be noted is the consistently lower temperature measured for the less exposed vials (≈*central*) compared to the more exposed ones (≈*edge*). This overall lower temperature was the first indicator that the hexagonal array approach might help improve batch representativeness by assuming:

$$\text{IR}\, T_{\approx central} \cong \text{TC}\, T_{central} \tag{7.2}$$

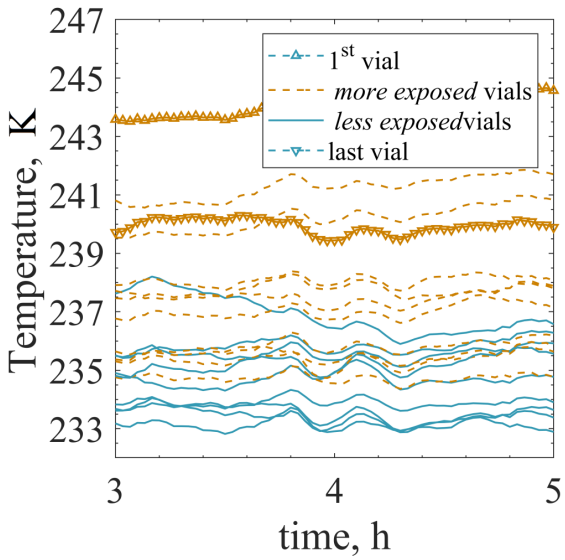

Figure 7.4: IR bottom temperature profile per vial. The first vial is the leftmost one and the last vial, the rightmost one from the camera's perspective.

Based on the profiles presented in Figure 7.4, the ≈*central* infrared-based profiles were used as representative of the thermal profiles of central vials in a batch.

In Chapter 4 the batch averages were compared, in this chapter the mean ≈*central* IR profiles are confronted to the mean central TC profiles and the mean (≈*edge*) IR profiles are confronted to the mean edge TC ones. These comparisons can be found plotted in Figures 7.5a, 7.5b and 7.5c.

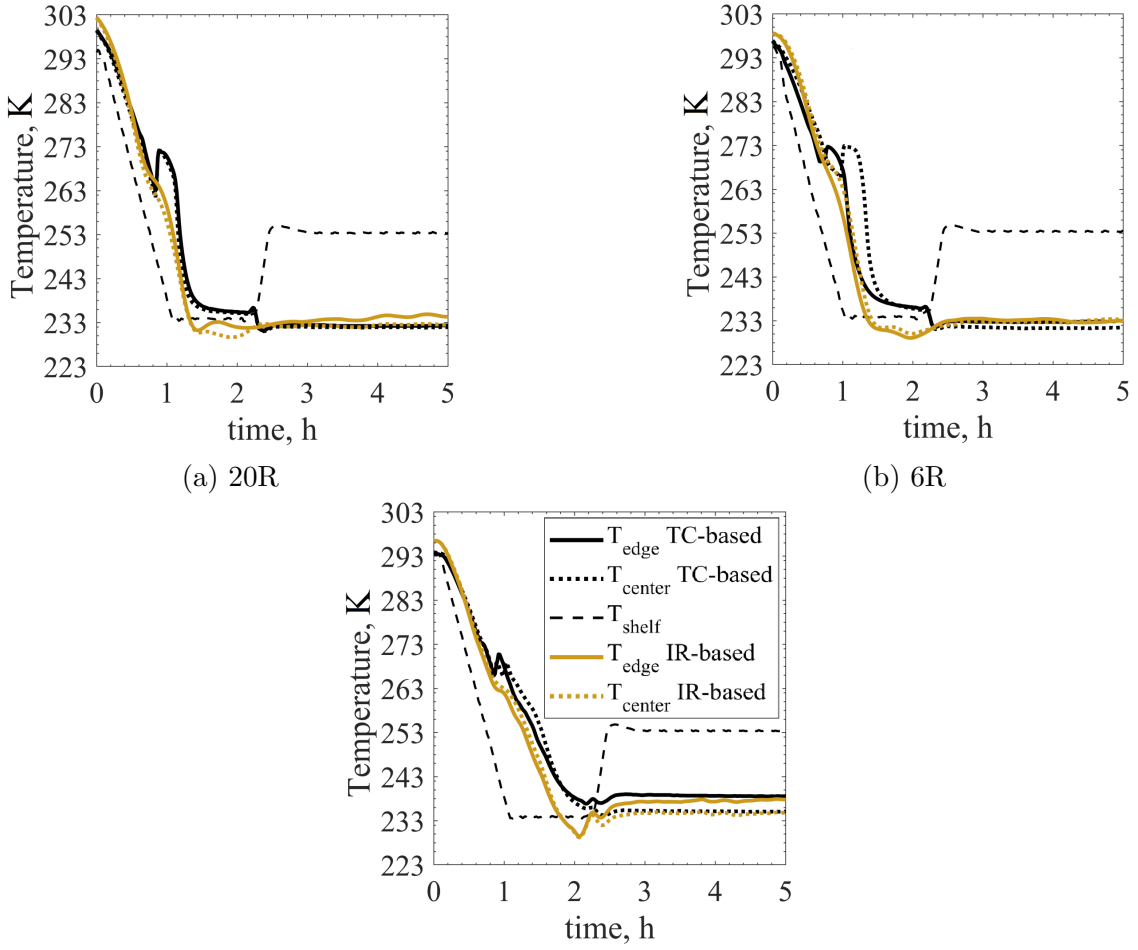

(a) 20R

(b) 6R

(c) 4R

Figure 7.5: TC edge and central T_{bottom} profiles confronted with the IR ≈*edge* and ≈*central* T_{bottom} profiles.

As mentioned in Chapter 3, the IR sensor cannot accurately monitor temperatures during the lowest temperature interval of freezing. Disregarding the profiles below 243 K, the ≈*central* average temperature profiles were in very good agreement with the thermocouple-based central vial profiles. The deviations on the measurements were within the ± 1 K accuracy of the sensors. The average ≈*edge* profile however presented differences reaching up to 5 K in the very beginning of primary drying which then became 3 K for 4R vials. After this initial interval, the differences were minimal. For the 20R vials some discrepancies were also observed,

but in the order of 2 K while these profiles for the 6R vials presented an extremely good agreement.

K_v model parameter

The precision of the infrared thermal profile will affect the K_v precision. Figure 7.6 shows the edge and central K_v values calculated using the ≈*edge* and ≈*central* IR-based thermal profiles in the calculation. These values were all in extremely good agreement to the thermocouple-based calculated values for all vial sized tested. The biggest discrepancy was observed for the edge vials of the 20R batch, presenting a deviation from the thermocouple-based value of 9.6%.

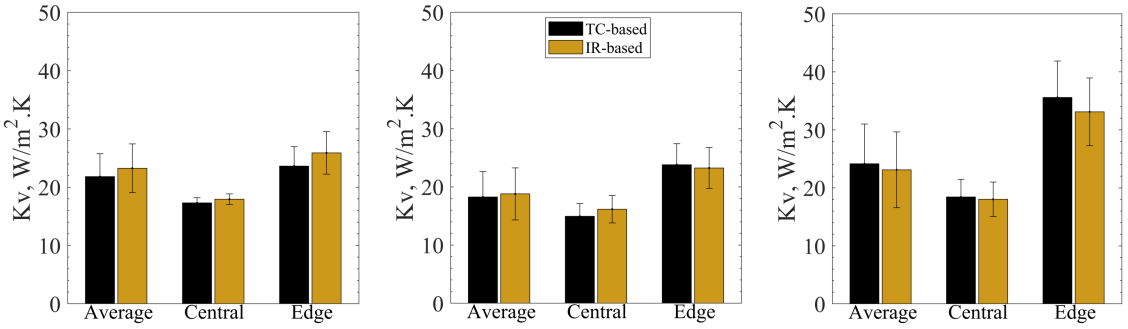

(a) 20R (b) 6R (c) 4R

Figure 7.6: IR-based average ≈*central* and ≈*edge* K_v values compared to TC-based ones.

Figure 7.7 shows the distribution map of the K_v values calculated for each vial in a batch. The map presented in this chapter has one particularity on the first row K_v values. Because the infrared camera allows the easy and non-destructive collection of the thermal profile of all front-row vials, the K_v of each vial in this row was calculated using the individual thermal profile acquired with the IR sensor. The other vials formally regarded as edge vials had their K_v calculated using the ≈*edge* IR profile while the central vials were calculated using the ≈*central* infrared thermal profiles.

Comparing Figure 7.7 to Figure 4.5 (K_v map of the same batch but based on thermocouple profiles) the advantages of the additional thermal data from the infrared sensor become clear. The pronounced higher temperature profiles observed for the leftmost vials (possibly due to the equipment's electric panel) reflected in even higher K_v for those vials. This helped make clear that the batch in this equipment may be skewed towards that vial position. This knowledge is important for process design to be able to develop conservative cycles to preserve product quality for the while batch. Or, to know by default that the thermal profiles of vials in a certain position are not representative of the rest of the batch and those vials

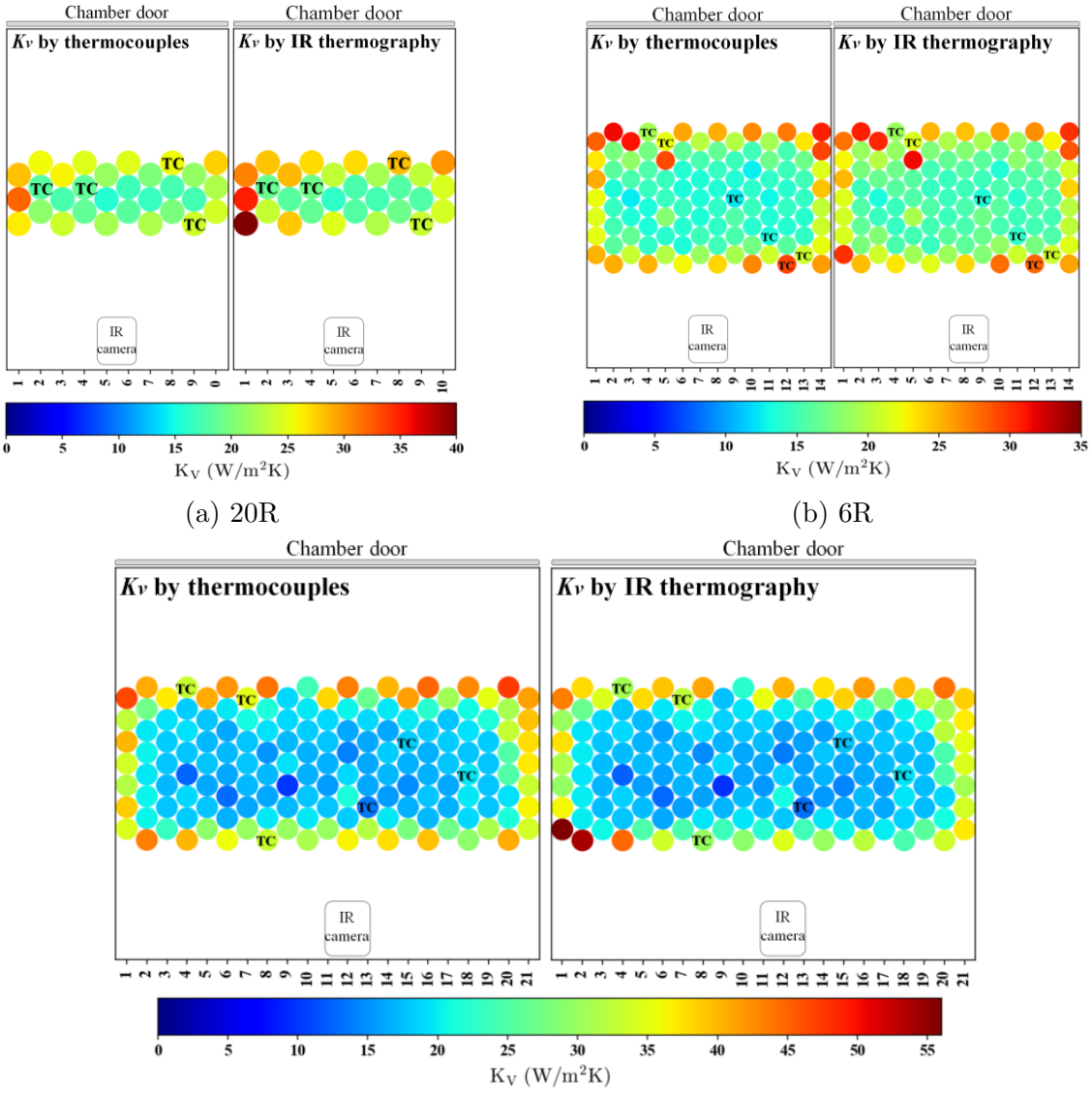

(a) 20R

(b) 6R

(c) 4R

Figure 7.7: IR-based K_v map. The K_v values of the front row vials were calculated using the individual vial thermal profile. For all edge vials the ≈*edge* IR-based T_{bottom} profiles were used while for central vials, the profiles used were the ≈*central* IR-based T_{bottom} ones.

must be discarded if aggressive cycle conditions are preferred to reduce processing costs.

Automatic drying endpoint determination

Freeze-drying is a costly process and, to reduce costs, process optimization becomes very important [226]. Several tools are available to determine the end-time, but they all present their own limitations or can only partially determine the end-time, presenting wide variability ranges.

IR thermography, as a non-invasive method, presents many advantages regarding temperature monitoring until the end of primary drying. Invasive sensors typically present issues as previously discussed. The IR-based profiles show a more consistent behavior in terms of the rise time interval than thermocouples, as can be seen in Figure 7.8. The interval between the first TC shows a profile rise until the last reaches the final temperature plateau is from 16 hours until 28 hours. The same interval for the IR thermal profile data ranges from 20 hours to 28 hours. This consistency motivated the use of IR temperature profiles to estimate the end time more effectively. If IR thermography, differently from TCs, exhibits a rising temperature profile towards the end of primary drying in a consistent way, it could be used as a reliable primary drying end time determination method. That means, if the IR measurements are less affected by small interference factors like positioning of the sensor, cake breakage amongst others. However, the limitation of monitor the vial glass, which in in contact with the external cake layer also poses its limitations. The outer cake also tends to have its ice removed faster than the inner core of the cake, which cannot be monitored by the IR sensor. This is particularly expressive precisely in edge vials, the ones monitored by the infrared camera.

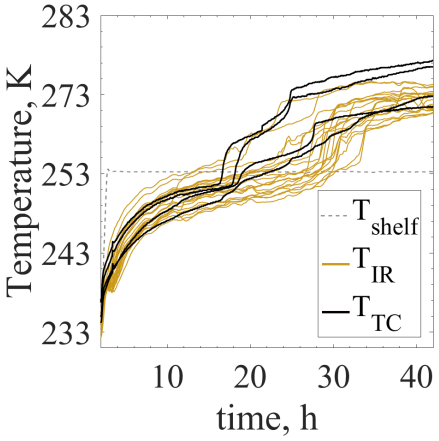

Figure 7.8: Product temperature profile rise of IR-based and TC-based profiles.

This way, Figures 7.9, 7.10 and 7.11 show the H_{min}, the T_{min} and the $\frac{Pi}{Ba}$ signals. These figures also show the resulting fitted or smoothed curve and the potential end-times based in each signal using the automated code developed to this end.

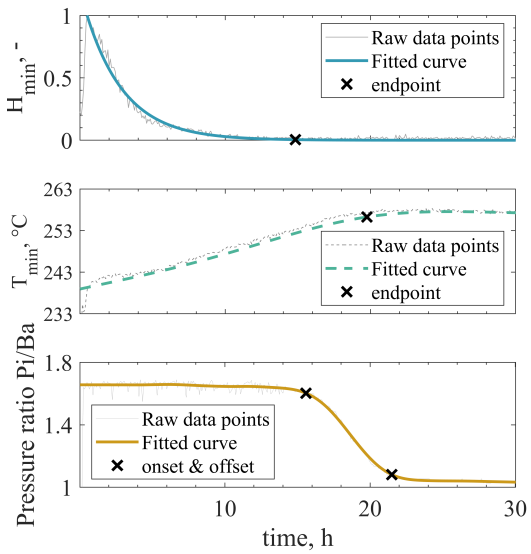

Figure 7.9: Different signals to identify primary end-time for 20R vials. The "x" markers indicate potential end-time points for primary drying for each signal.

The H_{min} profile remained close to its minimum value until the end for the 20R batch (Figure 7.9). However, the H_{min} profile reaches its minimum after approximately 21 hours for the 6R vials (In Figure 7.10). After this, H_{min} remained between this minimum and approximately a 0.5 value until the end. This behavior was also observed for the 4R vial batch (Figure 7.11.

As expected, the H_{min} raw data profile presents an increase or noisy behavior after it reaches its minimum. This trend can be used for a subjective evaluation of the end-time based on this profile. However, the main idea is to propose an automatic method. This way, the curve fit plus the threshold value seemed to work best as the H_{min} estimated durations were very close to the ones estimated by the onset time using the $\frac{Pi}{Ba}$ method. The closest one was for the 20R vials, representing a 5% difference relative to the $\frac{Pi}{Ba}$. The estimation for the 6R vials diverged the most, representing a 18% difference relative to the $\frac{Pi}{Ba}$ method. The use of the fit and threshold value allowed a standardized application of this method.

Table 7.3 shows the estimated drying times using all proposed methods. Additionally a K_v-based end time estimation was included. This estimation was done using the one-dimensional heat exchange models presented in Subsection 4.1.1. These models are used to determine how much time would be needed to sublimate all water based on the shelf temperature, an estimated product temperature and K_v.

To examine the results presented in this subsection, a discussion regarding what is practically being monitored by the infrared camera is required. As described

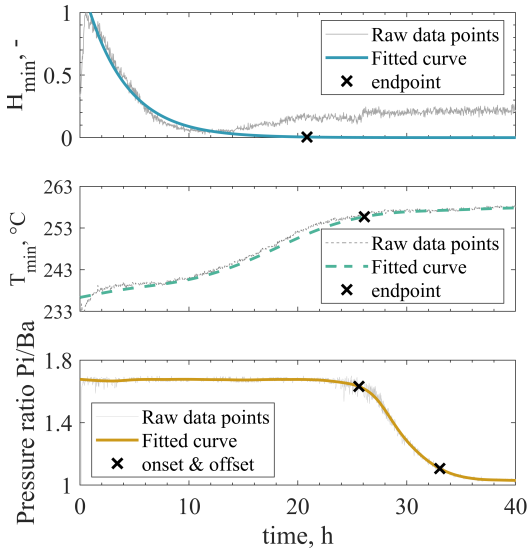

Figure 7.10: Different signals to identify primary end-time for 6R vials. The "x" markers indicate potential end-time points for primary drying for each signal.

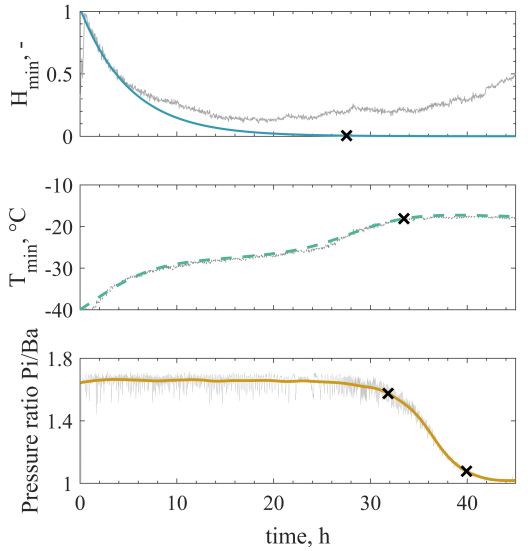

Figure 7.11: Different signals to identify primary end-time for 4R vials. The "x" markers indicate potential end-time points for primary drying for each signal.

in Chapter 4, the camera monitors the outer vial wall, in thermal equilibrium with the product immediately inside. Assuming the sublimation interface to move unidirectionally works well for most of the cake, however, it is not a good approximation towards the end of drying. Figure 7.2 shows the modeled evolution of the

Table 7.3: Estimated primary drying end-times in hours, based on different signal indicators.

	H	*Ti ≈edge*	*Ti average*	*Ti ≈central*	*Pi/Ba onset*	*Pi/Ba offset*	*Kv*
4R	27.5	32.6	33.5	34.2	31.8	39.9	31.5
6R	20.9	24.1	26.1	27.4	25.6	33.1	24.9
20R	14.8	18.9	19.7	20.7	15.6	21.5	24.7

sublimation interface as presented by Gan et al. [138] where this can be seen in detail.

This way, when the H_{min} reaches the minimum using the infrared camera, it means that the frozen fraction was sublimated for the outer cake layer. The last frozen fraction is in the core of the cake and cannot be practically observed by the infrared sensor. That is why the H_{min} estimated drying times are shorter than the drying times estimated by the other methods. Comparing the H_{min} to the reference methods, K_v and $\frac{Pi}{Ba}$ the discrepancies reached up to 40% for 20R vials. The H_{min} presented smaller differences for the smaller vial size, 4R, because when sublimation is over for the outer cake layer, it is also close to be over for the inner cake core. This way, the differences for the 4R vials were 12.7% relative to the K_v-based value and 13.6% relative to the $\frac{Pi}{Ba}$ onset time.

Still, the radial temperature gradients in the vial towards the end on primary drying are small for the fill volumes used. This way, the T_{min} profiles were still representative of the product temperature. The primary drying durations estimated by this method were in great agreement to the reference method, $\frac{Pi}{Ba}$. The T_{min} end-times always seemed to lay between $\frac{Pi}{Ba}$ onset and offset times and were very close to the K_v estimated durations. These differences between the end times estimated using the average T_{min} profiles compared to the K_v estimations ranged from 4% (for the 6R vials) to 20% for the 4R vials. Using the average vial temperature would probably not yield such good results because the difference in time for the rising profile of different parts of the cake would cause noise. Practically, when this was done, many times the inflection between the two plateaus was not clearly defined, instead, the whole temperature profile showed a gradual consistent rise during the whole batch. It could be attempted nonetheless.

To take advantage of the hexagonal array for better batch representation, $\approx$*edge* and $\approx$*central* T_{min} profiles were presented separately to estimate the end of primary drying for central and edge vials. It can be observed that the $\approx$*central* T_{min} estimated duration was very close to the $\frac{Pi}{Ba}$ offset signal. The best agreement was for the 4R vials, representing only a 4% difference relative to the $\frac{Pi}{Ba}$ offset signal. The worst correspondence was for the 6R vials, representing a 17% difference. This correspondence demonstrates the potential of this method as an consistent

alternative tool for primary drying end-time estimation. Additionally, even after ≈*central* vials have completed sublimated, the actual central vials behind them may have a cooling effect over the front row vials until they also finish sublimating. This may also be an explanation to why using this approach resulted in good estimations of the end point of primary drying.

7.3 Conclusions

This chapter evaluated the IR camera's batch representativeness for temperature monitoring, heat exchange coefficient estimation primary end-time determination. The assumption made considering less exposed edge vials as representative of central vials worked well to improve the batch representativeness based on infrared thermal profiles. It is not perfect and it cannot truly represent central vials, but it is an approximation that worked well. The heat exchange parameter K_v for central and edge batch conditions was adequately calculated using these ≈*central* and ≈*edge* IR-based profiles.

The end time determination method based on the H_{min} did not work very well. The times determined by this profile were always shorter than the required time and this discrepancy increased with the increase of the vial radius. The T_{min} profile, on the other hand, offered a great alternative to accurately determine the end of primary drying using the developed automated tool.

Chapter 8

Design space determination

8.1 Introduction

A key concept in the Quality by Design paradigm is the design space (DS). The DS is a multi-dimensional space which includes different combinations of processing variables that will guarantee product quality and production efficiency. The design space is outlined as a combined analysis of, product temperature, sublimation rate, shelf temperature, and drying chamber pressure. The limits of the DS describe the conditions that would process the formulation under aggressive cycle conditions, on the edge of optimization but on the limit of affecting product quality (if any parameter moves out of the control charts during processing). Other DS limits are determined by the equipment, including the cooling, heating, and condenser capacity or the limitation to remove the water vapor flow within the system. The definition of this design space ensures a complete understanding of the product and process.

The Food and Drug Administration's Quality by Design initiative is a new regulatory philosophy based on predefined quality goals and a deep understanding of the interplay of formulations and processes to influence critical quality characteristics of pharmaceuticals. This understanding is based on prior knowledge of device operations used in manufacturing a product, experimental data from development work, and published literature. Many presentations are based on the empirical determination of performance criteria from the analysis of experimental data.

During primary drying, product temperature should be kept below the formulation's critical temperature. This critical temperature usually is the glass transition temperature (T_g') for amorphous systems or the eutectic point (T_{eu}) for crystalline ones. Suppose this threshold is surpassed, changes in the porous cake structure may affect product solubility, drug activity, and overall product quality [26]. In some cases, such as nanoparticle suspensions [227], highly concentrated proteins [228] or the combined use of crystalline and amorphous bulking agents, surpassing the critical temperature may present macro collapse, while not necessarily

affecting product quality [229]. Nonetheless, it is crucial to determine and employ the operating conditions that will ensure product quality is preserved.

The DS is made by the set of operating conditions that ensure product temperature to be below its threshold value (Example in Figure 8.1. These conditions change according to the batch configuration and equipment characteristics. These operating conditions are the chamber pressure (P_c) and the shelf temperature (T_{shelf}). The P_c defines the vapor pressure that must be achieved for sublimation to occur, and the T_{shelf} provides the heat for sublimation.

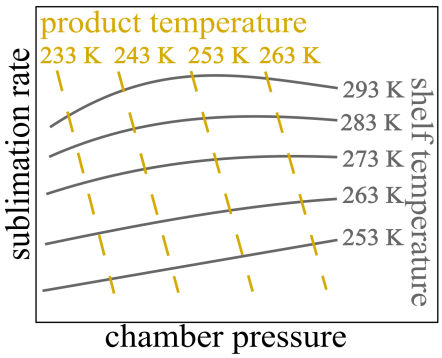

Figure 8.1: Example of a design space that shows the resulting product temperature that will be obtained according to the operating conditions.

The chamber pressure has a complex effect on the product temperature and sublimation rate. On the one hand, higher chamber pressure reduces the driving force of water vapor transfer from the product ice interface to the chamber. This driving force is defined as the difference between the pressure at the ice interface within the product and the chamber's pressure. On the other hand, this higher pressure also increases the heat transfer rate by increasing the thermal conductivity of the gas in the narrow space between the shelf surface and the bottom of the vial. This effect increases the temperature of the product, which in turn increases the vapor pressure of the ice inside the product that increases the water vapor pressure at the ice interface. This condition increases the driving force for the flow of this water vapor from the product into the chamber. Within the chamber pressure range used for drugs, the net effect of higher chamber pressure is usually to increase product temperature and product sublimation speed. This net effect tends to be the case because the improved thermal conductivity provided by the higher pressure outweighs the negative effect on the sublimation speed to reduce the driving force of water vapor flow from the product to the chamber. Therefore, for the most efficient processing, it is desirable to operate at the highest possible processing temperature and the lowest chamber pressure that will maintain the product's target temperature during initial drying.

It is essential to see the development of products and processes as an

integrated procedure and not as independent activities. When working in the cycle design for product, the developer needs to know what equipment will be used to process the product and the requirements for development.

To minimize the time-to-market for a given product, it is, therefore, necessary to quickly identify a suitable couple of values of P_c and T_{shelf} that allow obtaining the desired quality for the final product. Additionally, it must be remarked that primary drying alone was found to represent about 70% of the operational costs using an industrial freeze-dryer. Still, the operational costs represent less than 15% of the total expenses, which includes capital ones. Reducing the required processing time increases productivity which in turn reduces the capital costs per cycle [28].

Thus, the operating conditions that maximize the sublimation rate are preferred because they speed up the cycle duration [230]. The sublimation flow is typically measured via gravimetric tests, weighting the vials before and after sublimation to determine the mass of water that sublimated during a time interval, as described in Appendix B. Other tools such as TDLAS or methods such as the pressure rise test may be used. Obviously, the solvent flow rate must be compatible with the freeze-dryer condenser capacity. The characteristics of the duct connecting the chamber to the condenser must be considered as well to avoid choked flow [26, 94, 231]. Thus, these optimal operation settings must be carefully selected within the design space.

8.1.1 Design Space determination approaches

The operating settings for a given product are generally determined through extensive experimental work and, unfortunately, sometimes simply by trial and error [79]. The correct understanding of the heat and mass transfer mechanisms during freeze-drying allows determining the optimal operating conditions with just a few runs. In-line process design is also possible if appropriate monitoring tools are available. These tools should allow reliable product temperature monitoring and determination of the residual moisture present in the product. These tools help characterize the heat-flux from the shelf to the product and the mass flux from the sublimation interface to the chamber [232].

Empirical and mechanistic approaches can be used to obtain the design space. A non-expert practitioner can perform an empirical study. However, such an approach requires many time-consuming experiments to determine the relationship between the operating conditions and the resulting process. Besides, this approach is only valid *in situ*, which limits the scalability of the results found at lab-scale, where these experiments are typically carried out [22, 233]. On the other hand, mechanistic approaches allow scale up. This approach requires mathematical modeling of the product temperature, water vapor flow, and drying time throughout a process as a function of the chamber pressure and shelf temperature [234–237]. Such models are based on heat and mass transfer balances. They can be used once parameters

like the global heat transfer coefficient (K_v) and the cake resistance to vapor flow (R_p) are known. When this latter approach is used, fewer experiments are needed to obtain a comprehensive design space for a product, compared to the empirical approach. Nonetheless, even when using a mechanistic approach, the design space determination for a formulation is a time-consuming task.

The gravimetric method [235, 238, 239] is regarded as the standard method to obtain K_v. However, many alternative methods have been proposed. In fact, if reliable product temperature monitoring and primary drying endpoint determination tools are in place, non-gravimetric K_v estimations can be obtained. Many of the alternative methods are based on the pressure rise test (PRT) using different algorithms varying in complexity. Some of this methods are the Pressure Rise Analysis (PRA) [85]), the Manometric Temperature Measurement ([86], Dynamic Parameters Estimation Methods (DPE) [240] and DPE+ [87]. Other approaches presented were based on a heat flux sensor [81] and Tuneable Diode Laser Absorption Spectroscopy (TDLAS) [82, 83, 241] to cite a few. Some advantages can be obtained with these tools, for instance, the determination of K_v at different pressures in the same run using a heat-flux sensor. The main drawback is that a mean value of K_v is obtained for the batch without differentiating between the central vials (heated just through the shelf) and the edge vials (also heated through other mechanisms, e.g., radiation from chamber walls and door) [239]. In contrast, gravimetric tests provide a very detailed picture of the system. As far as R_p is concerned, it may be estimated as well as by means of PRT-based algorithms [87, 236], through TDLAS [242], or using the product temperature measurement in a run [243].

8.1.2 Mechanistic DS determination methods

To employ a mechanistic approach for design space determination, some process parameters must be first estimated. The model parameter K_v must be determined as a function of chamber pressure, as presented in Equation 7.1. Hence, at least three gravimetric tests must be carried out at different pressures as described in Fissore et al. [22]. These gravimetric tests can be performed with water to save formulation material and preparation time as the solution composition does not affect the resulting K_v [235].

For R_p estimation, at least one complete primary drying cycle should be performed for the target formulation. It is vital to ensure that product temperature is kept below the threshold value for that product during this test. Otherwise, cake collapse takes place, leading to misestimation of the R_p profile. If this happens, product temperature during primary drying will also be misestimated, and the resulting design space will not ensure product quality [233].

Primary drying simulation

To simulate *in silico* the process as it progresses and calculate T_{bottom} according to how much frozen cake is still left, Equation 8.1, i.e. the steady-state heat balance for the frozen product layer [142], can be used:

$$T_{bottom} = T_{shelf} - \frac{1}{K_v}\left(\frac{1}{K_v} - \frac{L_{frozen}}{k_{frozen}}\right)^{-1}(T_{shelf} - T_i) \tag{8.1}$$

The sublimation interface temperature, T_i, is calculated recursively together with $p_{w,i}$ and R_p, using Equations 4.1, 4.2 and 4.3 and Equations 4.8 and 8.1 for each integration interval. Twenty-second intervals were used in the simulations dome for this thesis. Once T_i is found, T_{bottom} can be calculated for any stage of freeze-drying, i.e., for any given percentage of frozen cake left.

Defining the design space

The T_{shelf} and P_c combinations that will ensure product T_{bottom} to be below the formulation critical formulation value can be calculated once these parameters are properly computed. Equations 4.2, 4.3 and 4.4 can be used to this end, determining the possible T_{shelf} and P_c combinations for each and any point of the primary drying progression, defined by the residual L_{frozen}. This way, for each pressure value being considered in the design space, the product T_{bottom} for the regarded L_{frozen} is calculated by testing different T_{shelf} values. Thus, the T_{shelf} values that ensure product T_{bottom} to be below its threshold limit comprise the design space for that pressure and considered L_{frozen} value. The threshold limit, i.e., the maximum allowed temperature for the case-study formulation, is usually the T_g' or T_{eu}. Additionally, once the T_{shelf} and resulting in T_{bottom} values for each pressure are known, J_w for any desired L_{frozen} can be calculated for the whole design space. Knowing J_w can be used to further optimize the process duration by choosing the conditions within the design space that will maximize the sublimation flux.

It is important to point out that, since R_p has a dependence in L_{dried} the predicted T_{bottom} values for different T_{shelf} and P_c combinations will also vary according to the L_{dried} portion considered. Since R_p reaches its maximum value towards the end of drying, so does T_{bottom}. Fissore et al. [244] proposed the estimation of a design space including the L_{dried} as a third coordinate to account for this dynamic behavior. In this study, a static environment is considered, i.e., one single T_{shelf} for the whole primary drying stage. To this end, all calculations are based on a critical T_{bottom} value using as a reference the moment when only 10% of frozen cake remains.

The use of a dynamic parameter estimation algorithm [51], manometric temperature measurement [245] and the use of a combined statistical and mechanistic

approach [246] were proposed for design space estimation. However, using a pilot-scale or lab-scale freeze-dryer equipped with thermocouples to monitor product temperature is still the most common tool used for the mechanistic approach. Typically, three gravimetric tests are performed for K_v estimation and one for R_p, as described above. If done in a research and development environment, one extra experiment on the industrial freeze-drying equipment is required to scale up the process. However, such experiments can be time-consuming, which increases operational costs. A sampling plan may be implemented to reduce the effort of performing gravimetric tests considering that these batches typically have a few hundred vials. However, the vial-weighting steps required for the gravimetric tests are still laborious even with such sampling plans. Additionally, inadequate thermocouple placement many times compromises batch monitoring if a non-expert performs this task [74].

8.2 Experimental investigation: Can IR be implemented as a novel PAT for Design Space determination

The main objectives of this chapter are to evaluate if the infrared camera can be used to determine the parameters K_v and R_p in a easier, less laborious way. If these parameters can be properly determined, a mechanistic approach for the design space determination can be built and verified.

Alongside with the IR sensor, another novel tool was included in the investigation: a MicroFD. The MicroFD was included to enrich the discussion regarding novel approaches for design space determination, proposing, evaluating and comparing novel alternative tools. Its main advantage is the tiny bath size. More details about this device can be found in Appendix A. In any case, this equipment hold a very small number of vials and its main advantage is that is has a temperature-controlled ring surrounding the batch, that can be used to simulate central or edge batch conditions of larger batches. Thus, it emulates larger batches and allows further investigating them while requiring much less time and effort.

Hence, two new methods for design space determination are presented ahead, based on the following devices:

1. An Infrared camera for monitoring a lab-scale freeze-dryer to (i) obtain R_p, and (ii) a non-gravimetric K_v estimation using the non-invasive monitoring tool.

2. A micro freeze-dryer, to obtain the model parameters R_p and K_v using fewer vials than usual.

As a base for comparison, the standard method used for mechanistic approaches is also presented. Which consists of using a research and development scale freeze-dryer, equipped with thermocouples for temperature monitoring. This way, the model parameters and the resulting design spaces obtained through the innovative methods are compared to those obtained using the standard methods. This comparison aims to verify their applicability.

Central vials correspond to more than 90% of the vials in industrial batch processes. Thus, this study does not present the design spaces for edge vials with five or fewer neighboring vials. Instead, the design spaces obtained targeted central batch conditions. Additionally, two different systems are evaluated, an amorphous and a crystalline one. Central batch conditions are those applicable to central vials in a batch, i.e., those with at least six neighboring vials. The advantages and limitations of each novel approach will be discussed ahead in the Chapter[1].

8.2.1 Methodology

Proposed Methods

Three methods of which two are novel approaches were investigated. The idea was to compare them when obtaining the design space for central batch conditions using 6R vials. These DS were obtained in a research and development level and would require one extra test in an industrial scale freeze-dryer to be scaled up, using any of the three methods presented ahead.

Reference method Design space estimation for central vial conditions using a lab-scale freeze-dryer (REVO) was performed. Each batch had 210 vials in a hexagonal array (14 rows with 15 vials each, 156 central vials). Six thermocouples were placed in central vials for temperature monitoring. Figure 8.2 illustrates the batch configurations used for each of the tested methods.

IR-based method In Chapter 7, the use of an infrared sensor to monitor batches with up to 157 vials in the REVO freeze-dryer was verified. An hexagonal array, exploiting the approximation IR-based $\approx$*central* vials $\cong$ TC-based central vials thermal profiles was implemented. This approximation should allow the estimation of model parameters, K_v, and R_p, for central batch conditions with reasonable accuracy. Additionally, through monitoring of the sublimation interface temperature (T_i) during primary drying, a consistent determination of the endpoint was achieved in Chapter 7.

Based on Chapter 7 results, the whole design space can be obtained without gravimetric tests by monitoring three complete cycles using the desired formulation. The K_v and R_p values are obtained based on the T_i profiles of these

[1]Part of the results presented in this Chapter have been previously published in [247].

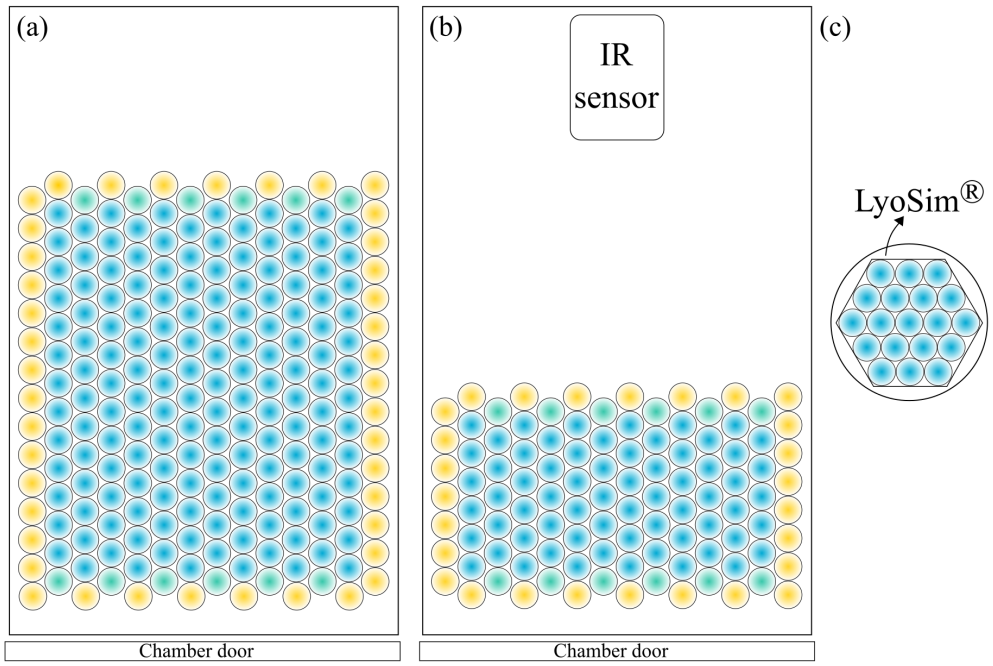

Figure 8.2: Illustration showing the setup used for each of the proposed methods: (a) the reference method, (b) the IR-based method (both in the REVO freeze-dryer), and (c) the MicroFD method.

vials, regarded as representative of central batch ones. Equation 4.5 and Equation 4.6 can be used to calculate K_v. Hence, assuming complete sublimation of the water present in the monitored vial and determining the primary drying duration by the T_i infrared-based method. R_p is directly obtained based on the T_i profiles of the monitored vials as previously discussed.

Using the same equipment and settings, no significant differences were reported for the central K_v values between these smaller IR-monitored batches and large thermocouple-monitored ones. One hundred five vials were used (14 rows with 7 or 8 vials each, 66 central vials) because some space is required to place the infrared sensor inside the chamber. Since the front row has 14 vials, this estimation is based on the profiles of the six more shielded vials in this row. This low number of samples could be a limitation to this method. However, the results for all tested conditions were satisfactory as reported ahead.

MicroFD method As mentioned, the MicroFD has a temperature-controlled ring surrounding its tiny batch called LyoSim (see Figure A.3 in the Appendix A). A LyoSim offset temperature 5 K lower than the monitored product temperature resulted in good batch homogeneity [95]. Moreover, this offset

setting was found to be a good emulator of central batch conditions in the REVO freeze-dryer [150]. This -5 K setting was also found to represent well the temperature profiles, and K_v values of central batch vials in another freeze-drying equipment of similar scale, the LyoStar III lyophilizer (SP Scientific, Warminster, PA, USA) [243]. The traditional three gravimetric tests (for K_v estimation) and a complete primary drying cycle (for R_p estimation) should be performed to determine the design space using the micro freeze-dryer. However, since the batch has a minimal number of vials (19 in this case using 6R vials), the task becomes much easier, less time-consuming, and requires less formulation material than normally. The MicroFD may also be equipped with a heat flux sensor (AccuFlux), allowing direct measurement of the heat flux to the product in the vials. With such a tool, vial weighing may be avoided, thus further simplifying the experiments. This tool, however, was not used because of operational issues. Thus, K_v was estimated gravimetrically and R_p based on Equation 4.1 and Equation 4.2.

Design of experiments

For all methods, the K_v estimation as a function of pressure was performed at 8, 13, and 26 Pa. The R_p profile for sucrose solution was obtained using a 253.15 K shelf temperature and 8 Pa chamber pressure setting, while for mannitol, it was obtained using 273 K and 13 Pa.

As mentioned, the critical temperature depends on the nature of the formulation. Additionally, the tolerable final product quality must be considered. For 5% sucrose, Horn and Friess reported a T_g' of 239.45 K [229]. If small micro collapses are allowed, a maximum product temperature value of up to 241.15 K could be accepted for sucrose solutions [149]. In this study, the threshold temperature for sucrose was defined as 240.15 K.

Mannitol formulations usually form stable cake structures, resulting in elegant final products with no noticeable shrinkage. Nonetheless, mannitol systems may present different polymorphs together with an amorphous phase [147]. A 10% crystalline mannitol formulation presenting α-mannitol and β-mannitol polymorphs, with the former as the most abundant one, was found to have a melting temperature of 251.65 K [148]. For pure amorphous mannitol, i.e., not in solution, a 286.15 K collapse temperature was reported [147].

Through Differential Scanning Calorimetry (DSC) analysis, a 10% amorphous mannitol formulation was found to have two T_g' points, one at 238.15 K and one 248.15 K [187]. This formulation also showed a subsequent crystallization exothermic peak. This trend shows the strong tendency of mannitol towards crystallization which makes it a stable cake forming agent [187, 248]. Melting for this formulation was observed near 273.15 K, which was attributed to ice melting. Since lyophilization operates below the water triple point, this melting transition

should not affect freeze-dried formulations. Still, lyophilization is generally used for heat-sensitive molecules. For this reason, a threshold value of 258 K was chosen for the design space calculation of the 5% mannitol solution.

Statistical Analysis

Statistical analysis was used to compare the K_v values obtained through the proposed tools to the reference method (gravimetric tests in the REVO freeze-dryer, using thermocouple measurements). The evaluations always compared the values in pairs. This way, they were analysed as described in Subsection 4.1.1: testing the normality of the values and subsequently comparing the group values using two-tailed, two-sample t-tests, assuming an unknown variance with a 99% confidence interval.

8.2.2 Results and discussion

Model Parameters for design space calculation

The ability of the proposed tools to accurately obtain the model parameters must be verified to evaluate their applicability for design space estimation. These critical model parameters are the K_v values at different pressures and R_p values for each tested solution. The resulting design spaces should be satisfactory if the key parameters found using the proposed devices are comparable to those obtained through the reference method.

The average K_v values found in each system under the tested pressures were all comparable, as illustrated in Figure 8.3. Compared to the reference method, the most pronounced differences were observed when using the IR-based method. These differences were 6.3%, 8.4%, and 8.1% for 8, 13, and 26 Pa, respectively. The micro freeze-dryer's differences were minimal for 13 and 26 Pa, representing respectively a 1.3% and 2.4% difference. For 8 Pa, however, it reached a 6.5% difference when compared to the reference method. Nonetheless, using the statistical analysis via t-tests, the global heat exchange coefficients found using the MicroFD and the IR-based method were not statistically different from the values obtained in the REVO freeze-dryer using the gravimetric test ($p > 0.01$).

Once the K_v determination obtained through the novel tools was evaluated and found to be in good agreement with the values found using the reference method, the accuracy in R_p determination for each tested formulation was examined. As investigated by Scutellà et al. [154], the product temperature during drying is affected by the cake resistance to vapor flow. The whole purpose of calculating the design space is to ensure product temperature stays below its threshold value. Thus, correct R_p determination is of crucial importance. Since the R_p calculation is based on product temperature, the resulting profiles using the different proposed tools will be similar if the product temperature profiles are comparable. One of the

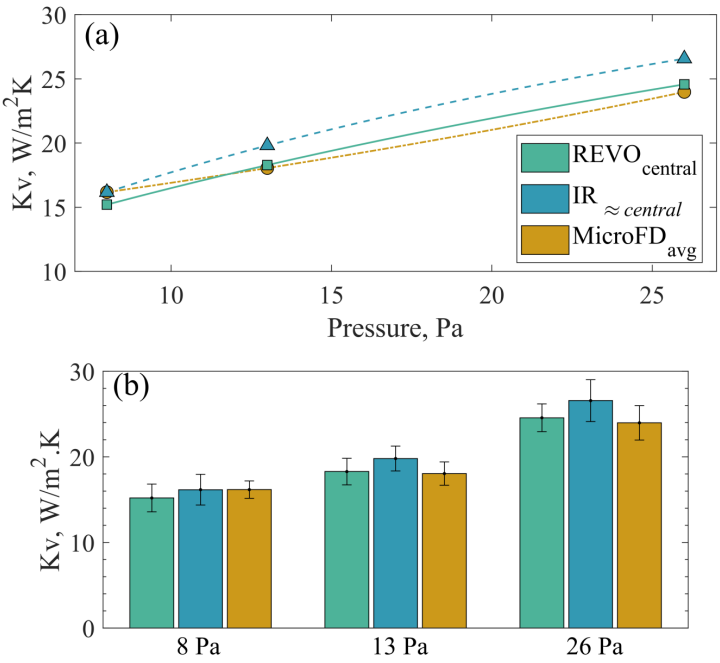

Figure 8.3: (a) K_v values with curve fit using Equation 7.1. (b) Bar chart for K_v values to evidence the standard deviation represented by the error bars.

most critical aspects of the observed R_p profiles is the maximum value it reaches. This maximum will also determine when the maximum product temperature will be observed, thus representing a critical control point for a given formulation.

Figure 8.4 presents the R_p results found for each solution. For all tested tools, the R_p profiles were comparable, i.e., they are within the same order of magnitude, and the values are quite correspondent. The observed R_p profiles are also in agreement to previously found values for 5% sucrose and 5% mannitol [48]. The difference in the profile behavior observed for sucrose and mannitol is due to the presence of micro-collapses. Sucrose typically presents micro-collapses in the dried cake and exhibits an asymptotic behavior after reaching a certain resistance. Mannitol, on the other hand, does not typically present micro-collapses and the behavior is more linear. This means that when using the R_p fit (Equation 4.8), the B_{rp} term for sucrose will be large while it will be very low and even zero for mannitol. These observations and results regarding the R_p profile are in agreement with previously reported results [242]. The thermocouple-based temperature profiles are unreliable towards the end of primary drying as discussed in Subsection 7.2.2. The raw R_p profiles observed in Figure 8.4 rise before the completion of sublimation for all tested tools. That is why the fitted curves (Equation 7.1) are very handy in process calculations to estimate the effective R_p profiles and resulting product temperatures during a process.

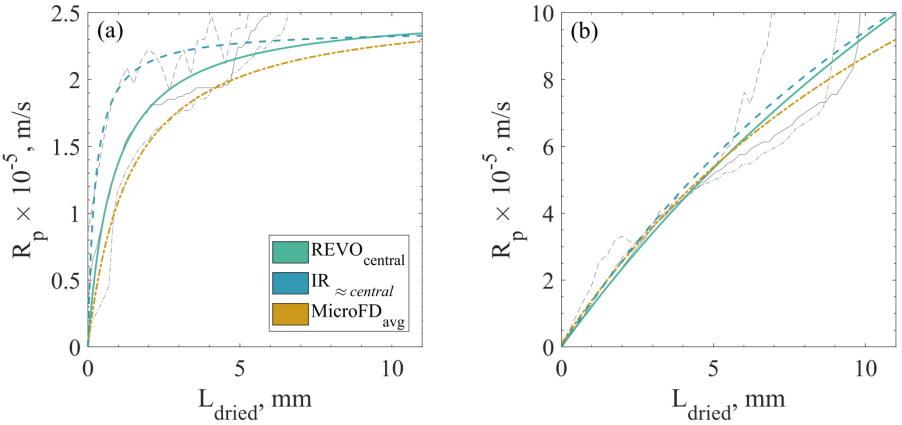

Figure 8.4: Calculated and fitted R_p profiles for (a) 5% sucrose using 8 Pa and 253 K shelf temperature and for (b) 5% mannitol using 13 Pa and 273 K shelf temperature. The light grey lines represent the raw data (Equation 4.7) and colored thicker lines represent the fitted values (Equation 4.8).

The duration of the process using each tested method does not impact directly the design space calculation but it can give a good indication regarding the equivalence between the tested systems. Suppose the global heat exchange coefficient and cake resistance to vapor flow are similar between systems, then, so should the overall process duration be. As seen in Table 8.1, based on the $\frac{Pi}{Ba}$ curve onset and offset points, the primary drying durations were all in good agreement. The onset time represents when drying is complete for several vials in the batch, but not yet for all of them. By the offset point, drying should be complete for all vials in a batch. It is essential to compare the onset and offset times together due to the large variability intrinsic to this end time determination method. These points vary according to batch size, drying conditions, and equipment characteristics [23]. Thus, they are not the same as the chamber volume and vacuum pump are different between the REVO and MicroFD.

Additionally, when the IR sensor was used, the batch size, and consequently the total solvent volume, was half the size of the full REVO batch. The time difference between the onset and offset signals comes from the batch heterogeneity and it also increases with batch size. Additionally, the $\frac{Pi}{Ba}$ signal was found to start decreasing when the sublimation rate becomes smaller than a threshold value of $2.10^{-6} kg.s^{-1}$, which may vary according to the equipment and its design [23]. This way, considering the intrinsic variability of the $\frac{Pi}{Ba}$ onset and offset signals, the primary drying duration observed using all tested methods may be presumed in good agreement.

Table 8.1: Primary drying estimated duration in hours based on the $\frac{Pi}{Ba}$ onset and offset values.

	Sucrose 5%		Mannitol 5%	
	Pi/Ba onset	*Pi/Ba* offset	*Pi/Ba* onset	*Pi/Ba* offset
MicroFD®	24.7	29.2	15.3	19.1
REVO-IR	25.6	33.1	15	16.8
REVO	28.2	33.2	16.9	20.1

Calculation of the design space

The design space calculation depends heavily on the K_v and R_p values found for a given product, vials used, and batch configuration. Since these parameters presented a good equivalence across the systems, a similar behavior is expected for the resulting design spaces. Figure 8.5 presents the upper limit of shelf temperature and chamber pressure settings for 10% remaining frozen cake, obtained through all the tested methods. As it can be seen, the resulting design spaces for sucrose are practically the same whether they were calculated based on the proposed tools or the reference method. For mannitol, some minor differences were observed in the design spaces. In the case of the MicroFD, the lower R_p profile for mannitol compared to the reference method resulted in slightly higher usable T_{shelf} settings, which was more evident for higher pressures, where the MicroFD K_v was smaller than the reference one.

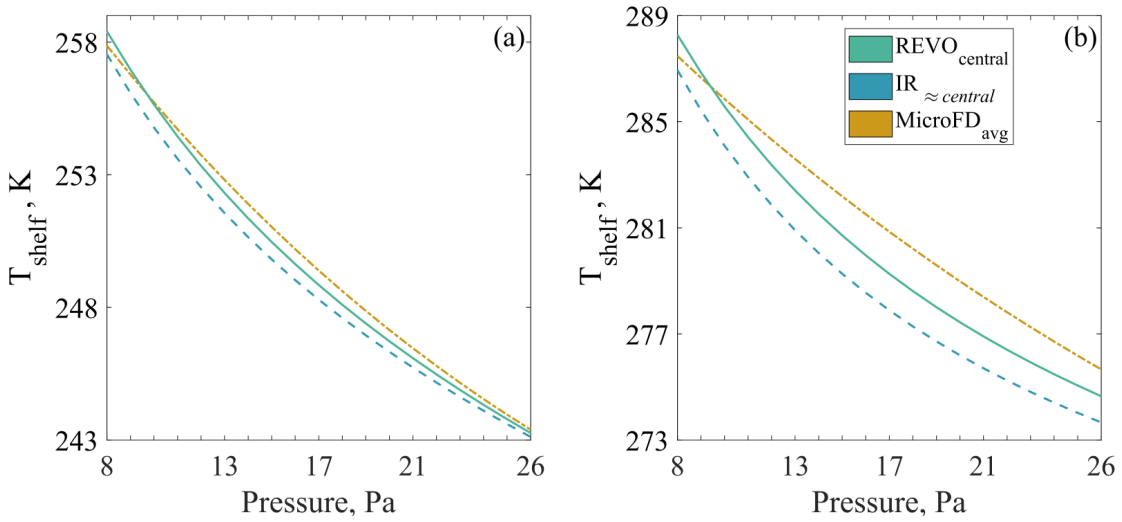

Figure 8.5: Obtained design space considering 10% of remaining frozen cake. Results for (a) 5% sucrose and (b) for 5% mannitol.

Simulating *in silico* the freeze-drying process until the last 10% of cake,

as described in materials and methods, the product bottom temperatures (T_{bottom}) were calculated. With this T_{bottom} and Equation 4.1 and Equation 4.4, J_w curves for different T_{shelf} and P_c values (since it will change the K_v) were calculated. This information, coupled with the design space, allows further optimization towards reducing the required primary drying time when higher sublimation rates are chosen.

As presented in Figure 8.6, the direction towards higher sublimation rates for sucrose is along with the lower pressures, which is in agreement with previously reported results [22, 149]. When lower pressures are used, K_v also decreases, allowing higher shelf temperatures. This increased shelf temperature setting provides heat for sublimation without compromising the cake structure. According to these results, the optimal direction concerning the operating conditions is towards the left and the top. However, in Figure 8.7, the sublimation flux curve behavior was different, more convex, shifting the optimization direction towards higher pressures. This trend means that the increase in K_v when operating at higher pressures contributes more to the sublimation rate than the decrease in vapor pressure when operating at low chamber pressure settings. At first glance, this may seem different from previously reported sublimation flux contour plots; however, it is not quite the case. Previously published J_w contour plots have a concave profile at lower T_{shelf} values which increasingly becomes less concave with higher T_{shelf} values until it finally becomes convex [22, 149]. This matter did not affect the optimization direction of those design spaces because the change in the profile only occurred around the T_{shelf} upper limit. The same can be observed in Figure 8.6. However, for mannitol, the T_{shelf} upper limit in Figure 8.7 is roughly 15 K higher than previously calculated [149] due to the higher threshold temperature is chosen in this present study. These higher operational temperatures explain the differences observed in the obtained J_w contour plots, which have a convex profile.

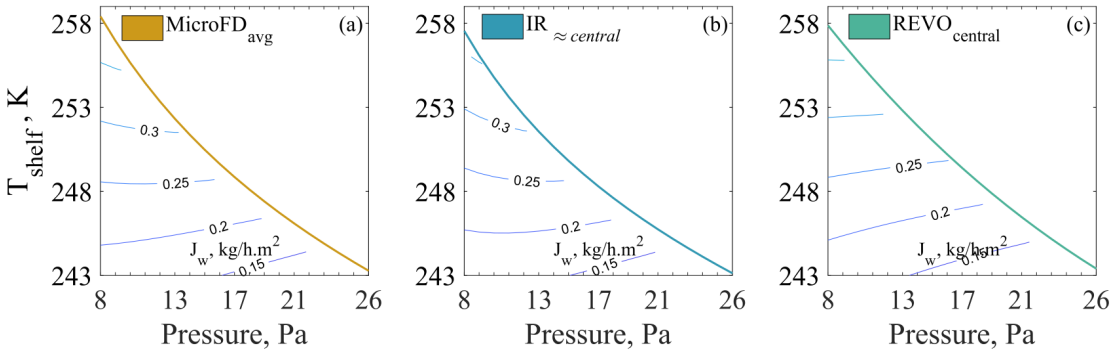

Figure 8.6: Design space for 5% sucrose coupled with the respective J_w contour plots using the (a) MicroFD, (b) the IR-based method and (c) the reference method.

However, it is essential to remember that the design spaces presented here are built for central batch conditions. Since edge vials would heat up more due to

less shielding, in this case, it is advisable to operate within a safety margin. In fact, it is always advisable to operate under a safety margin to ensure product quality [50]. For central batch conditions, a safety margin of 2 K was proposed, considering only the variability in vial dimensions, which affects the vial K_v. Moreover, the authors suggested that the safety margin for vials subjected to edge effects could be in that same order of magnitude [236].

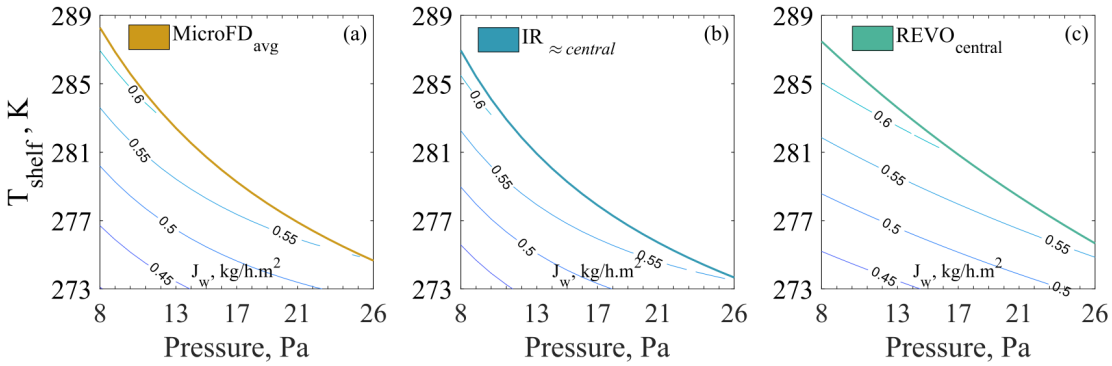

Figure 8.7: Design space for 5% mannitol coupled with the respective J_w contour plots obtained using the (a) MicroFD, (b) the IR-based method and (c) the reference method.

Another alternative is to use the proposed tools to determine the design space considering edge vials. The proposed tools in this study can be used to determine the design space based on edge vials simply by changing the settings used for K_v determination. This means that the MicroFD would have to emulate the batch conditions of edge vials being radiated. For this, the ring surrounding the vials has to be set at higher offset temperatures. For the infrared camera, to establish the design space for edge vials would mean using the more exposed vials as representative of edge vials, as explored in Chapter 7. However, choosing operating conditions aiming to preserve product quality in edge vials is not practical in industrial applications. In such cases, batches are huge, and edge vials comprise a small percentage of the whole batch. Since edge vials receive much more heating from the chamber walls than central vials, substantially lower shelf temperatures should be used.

As seen from the J_w results, this would increase considerably the required total drying time, representing a big increase in processing costs to preserve a tiny percentage of the batch. Longer cycles with lower shelf temperatures can ensure product quality for the whole batch and mean fewer batches produced per year, increasing capital costs per cycle. The final decision on designing a cycle will be based on what delivers a quality product at the fairest price to the patients.

Comparing the behaviors of the T_{shelf} and P_c upper limit line together with the J_w, it can be appreciated that the MicroFD tended to have a more linear

behavior than the observed ones for the IR-based method and the reference approach (both in the REVO). This trend is simply a direct reflection of the behavior of the fitted curve to K_v, also more linear, and it does not have any relevant physical meaning. The variation between the resulting design spaces using the novel tools compared to the reference method is irrelevant from the practical point of view. It is advisable to operate with a safety margin, as mentioned above.

Final considerations regarding the Design Spaces obtained

Product temperature must stay below the threshold value when operating under the DS conditions for a REVO full batch, with 210 vials. Considering all previous similarities in K_v and R_p between the different methods, this is expected to happen. As follows, Figure 8.8 shows the temperature profiles and pressure ratio ($\frac{Pi}{Ba}$) observed through a complete primary drying cycle for both tested solutions. The tests presented were the same ones used to determine the R_p profiles for the reference method. For both products, the conditions chosen are below the T_{shelf} and P_c pairs upper limit by a margin and, so do the resulting temperature profiles.

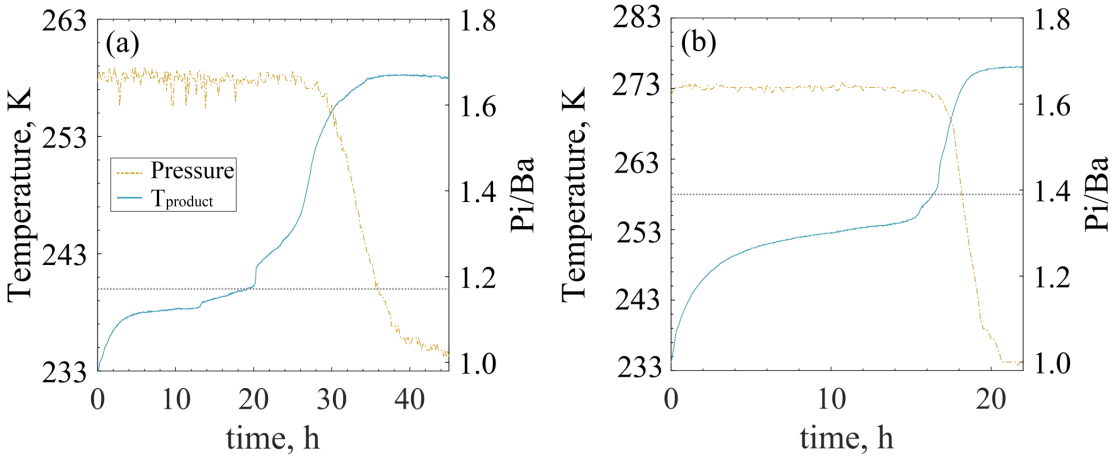

Figure 8.8: Product temperature and pressure ratio signal during primary drying for full REVO batch using (a) 5% sucrose at 253 K and 8 Pa; (b) 5% mannitol at 273 K and 13 Pa. The horizontal (..) grey lines show the threshold temperature for each solution.

As can be seen, product temperature was kept well below the defined threshold values. As explained above, thermocouple measurements are not reliable towards the end of primary drying. Thus, if the temperature profiles are above the threshold value by the end of the primary stage, that may not represent product jeopardy. In freeze-drying, as in multiple other processes, several factors influence the final product quality. This way, a holistic analysis of the results is preferred

over a reductionist one, which relies on just one sensor or attributes to evaluate and develop a cycle.

The heat and mass transfer coefficient results are in agreement with the reported values in Chapter 7. In that Chapter, K_v was gravimetrically estimated using IR-based temperature profiles. The resulting K_v found using 8 Pa, and 253.15 K shelf temperature was $16.7 \pm 2.3\ Wm^{-2}K^{-1}$. In this Chapter, the non-gravimetric K_v estimation resulted in $16.2 \pm 1.8\ Wm^{-2}K^{-1}$. For the MicroFD, using the -5 K offset setting for the LyoSim, K_v values in the MicroFD were found correspondent to REVO central batch ones [22]. The observed R_p values found in this study were also in good agreement with previously reported values [149, 154].

It can be noted that the resulting design spaces obtained through the different tested tools and approaches are all in good agreement. It is important to remember, however, that these results consider a static design space. Thus, only one shelf temperature setting was used, considering the last 10% of frozen cake as a critical control point in this process. Still, the design space is a result of the process parameters K_v and R_p. Since there was an excellent equivalence between the proposed tools and the reference method, the results suggest these tools could be used considering different percentages of remaining frozen cake. This additional consideration would allow the development of a dynamic design space, taking advantage of the lower R_p values at the beginning of drying to use higher T_{shelf} values and decrease the required drying time.

Furthermore, to scale the design space obtained using the reference method up to an industrial freeze-dryer, only one additional gravimetric test may be sufficient as described in Fissore et al. [149]. One test is enough to determine the a_{Kv} coefficient from Equation 7.1, the only one with a relevant dependence on the equipment, given that the fit was already done in a lab-scale or pilot-scale freeze-dryer. The R_p should also be obtained for the industrial equipment, but just one test would be sufficient for a given formulation. This scale-up method can also be analogously used for the proposed novel tools since such a good correspondence was found between the tested methods. Regarding choked flow, in lab-scale, this is typically less usual due to the equipment design [149]. Still, it can be an issue when high sublimation rates are used for industrial-scale freeze-dryers. To address this, the industrial equipment should be tested at full capacity and different pressures as described in Patel et al. [27]. This test should be done just once and can be used for all processes in that equipment.

8.3 Conclusions

Both proposed tools in this chapter present advantages and limitations. The non-gravimetric K_v determination obtained using the IR camera offers a great alternative removing the need for vial weighing, a step required by gravimetric tests.

Moreover, with simply one complete run, K_v and R_p profiles could be obtained with good accuracy. However, each run using the IR-based method requires using the actual formulation. This way, this method is recommended only when the tested product is not very expensive.

The MicroFD allowed obtaining the K_v gravimetrically without much hassle because only 19 6R vials are required. Additionally, only a tiny amount of actual product is needed to obtain the R_p profile. This method is recommended when working with expensive formulations or very new unstudied ones.

Conclusions

Conclusions and final remarks

This work presented an in-depth investigation on the use of an infrared sensor to monitor vacuum freeze-drying processes of pharmaceuticals. The aim was to fully evaluate all possible applications and test them using larger batch sizes, targeting practical applications. To do so, the work was divided into three parts: (I) an initial investigation to validate the sensor's initial use with larger batches, (II) its application to the freezing step, and (III) its application to the primary drying step. The sensor was not applied particularly to the secondary drying step because no additional valuable information could be gathered. Valuable information would be a particular gradient of profile that could be only observed through IR monitoring. Regarding freezing and primary drying, however, IR thermography proved worthy. With that in mind, a coupled application of IR and NIR could bring benefits since the latter can monitor the residual moisture in the product towards the end of primary drying and during the secondary drying stage [88]

In this final chapter summary of the main results obtained in the thesis and conclusions reached will be provided to highlight the thread that runs through the entire work. This summary will be achieved by addressing the relevant points listed in Chapter 2 which summarize the core objectives of this work.

I Sensor validation:

As discussed, there are many instruments and methods available to monitor freeze-drying processes. However, they all present their own set of limitations which push forward research into developing and validating new tools. Ideally, robust monitoring systems would not include just one single device or approach, but at least two that can complement each other. IR thermography was found to offer some noteworthy advantages. First, the temperature monitoring accuracy was verified and found to be in agreement with the standard tools, such as thermocouples and RTDs, which lays within $\pm 1K$. Second, the camera placement inside the drying chamber did not impose any relevant changes to the batch dynamics. There was a concern that the sensor placement inside the chamber could interfere in the batch for many reasons. The issue is that the sensor prototype used is not small and occupies a considerable space on the drying shelf. Because of this, the sensor's case

could have some shielding or radiative effects on the vials, for instance. However, this was found insignificant. Once these two starting aspects, accuracy and potential effects, were evaluated correctly and clarified, further sensor applications were closer investigated.

II Monitoring the freezing stage:

Upon applying IR monitoring to the freezing stage, new experimental observations of the freezing phenomenon in vials were obtained. Different batch configurations, using vials in the traditional configuration, exchanging heat in direct contact with the shelf (ON-shelf), and suspended vials (OFF-shelf) were studied. IR monitoring, with an improved data processing algorithm, offered new experimental evidence of the freezing process of solutions in vials. As a non-invasive sensor that provides a full thermogram of the vial axial profile, some observations could be made. First, the residual heat released during nucleation was observed as "humps" in the thermal profiles of neighboring vials. It was a known fact that vials in contact with each other will have an effect when nucleation happens. Still, these measurements with IR thermography were useful: the advantages of being able to monitor multiple vials at the same time in a non-invasive way are undeniable.

Using infrared thermography during controlled freezing using VISF enabled us to understand how the temperature gradients may change using this technique. The monitoring of the whole axial profile having a resolution of 1 pixel per 1.2 mm of cake height permitted that. An explicit inversion on the temperature gradient is observed when VISF is applied using a T_n of 271 K for ON-shelf vials. For the other tested cases, this inversion is not as apparent. In the case of suspended vials, it was evident that the temperature gradients within the vial were not as expressive as the ones of ON-shelf vials. The heat exchange, being driven by convection and radiation, yielded a more homogeneous thermal profile for the vial, presenting its lower temperatures at the bottom and top of the product cake.

A significant event that was experimentally explored was the freezing front evolution during freezing. Many freezing models for solutions in ON-shelf vials are based on the assumption that the freezing front moves from the bottom to the top of the product cake. Since freezing is an exothermic process, by tracking the position of the T_{max} after nucleation, this assumption could be checked. In all tests monitored using the infrared sensor, a clear trend was observed immediately after nucleation with the T_{max} moving from bottom to top, as predicted. An unequivocal definition of what is a freezing front in such conditions is arguable for many reasons. First, the definition of "complete" freezing on its own can be interpreted in different ways. For solutions with crystalline or amorphous solutes, usually, their T_g' or T_{eu} is used as a threshold to delineate freezing. When modeling freezing in vials, a mushy zone is often considered as a transition zone between the unfrozen and frozen portion of the solution. With this in mind, the tracking of the freezing front in terms of H_{max}

probably represents the upwards movement of a mushy zone from bottom to top. In the case of suspended vials, this trend could not be observed. This result was also expected since the temperature gradients of suspended vials a much less marked and present lower temperature at the bottom and top of the cake simultaneously during freezing. The H_{max} profile for such vials presented some rising trend only until about 30% of the cake height. This trend suggests that the heat removal from the bottom of the vial was enough to promote freezing in a somewhat unidirectional fashion only to a certain extent. Then, freezing advanced, not exhibiting strong temperature gradients.

The success full tracking of the T_{prof}, the T_{max} and the H_{max} allowed the application *in line* of different ice crystal prediction models. The T_{prof} was successfully used to predict the resulting cake structure after freezing, giving more detailed information for 8 different cake layers. Additionally, by estimating the freezing front rate based on the H_{max} profile and the temperature gradient of the freezing front based on the T_{bottom} and T_{max}, freezing front-based models could also be applied. However, the experimental H_{max} profiles resulted in inferred freezing fronts that behaved slightly differently from what was previously modeled. Meanwhile, the freezing front-based models were developed using these modeled profiles as input data. This way, these models did not work very well to predict the pore sizes at the bottom and at the top of the cake, where these differences in the freezing front rate were more pronounced. Future modifications to the existing models can be proposed to better predict the pore sizes based on experimental IR data taking this nonlinear profile of the freezing front rate into consideration.

These results show that IR thermography may be successfully used *in line* to predict in great detail the resulting product cakes, just with the freezing data. This information can then be used in *in silico* primary drying models to determine the best-operating conditions to be used for a given product.

III Monitoring the primary drying stage:

The first constraint of infrared monitoring is its field of view. To overcome this and achieve thermal monitoring that is representative of the thermal profile of the batch, an approximation was made. Using the hexagonal array, less exposed edge vials were regarded as central vials since their thermal profiles are more similar to the central vials than the more exposed edge vials. This approximation allowed to improve the batch representativeness. Nonetheless, for robustness, the use of more than one sensor simultaneously would be preferred in practical applications.

Since it is a non-invasive sensor, the thermal profiles of the monitored vials sing IR showed a much more consistent rise in their profile at the end of primary drying than thermocouples typically due. Also, since it can monitor many vials simultaneously, it offers a unique advantage point as a tool for primary drying end time determination. Because sublimation is an endothermic process, by tracking

the T_{min}, the sublimation interface position, H_{min}, could be inferred. However, the infrared sensor monitors only the product in thermal equilibrium with the glass vial, and this depth limitation makes this H_{min} to reach the vial bottom a couple of hours earlier than sublimation is complete in the vial. Still, the consistent rise of the T_{min} profile allowed the implementation of a standardized tool to determine primary drying duration objectively, unequivocally defining a primary drying duration.

By determining the primary drying duration, a non-gravimetric K_v estimation was possible. This end-time determination permitted the development of a new design space determination approach through IR. This new approach enables the determination of the K_vs as a function of the chamber pressure without weighting a single vial. This approach may represent a great advantage to accelerate and reduce labor needs in process development and optimization, representing lower production costs.

General overview

In sum, infrared monitoring proved to be a powerful tool to monitor freeze-drying processes. It offered new observations and insights on the freezing process by allowing new observations of the thermal profiles during freezing. Furthermore, ice crystal size prediction models could be directly applied to the infrared thermal data and predict the resulting cake structure. During primary drying, infrared thermography worked as a reliable non-invasive monitoring tool for product temperature and end-time determination. Additionally, it could be used as a novel tool to estimate heat-transfer coefficients in a less laborious way and this way, offer a new novel methodology for design space determination. However, IR also has its limitations that may be addressed in future works.

Closing remarks and future perspectives

Infrared monitoring offers many advantages for monitoring the freeze-drying process. However, the main disadvantage of IR thermography poses is the field of view limitation. The prototype used indeed offers an additional limitation: the space it requires inside the chamber. However, this limitation will be disregarded since modifications can be quickly done in future sensor versions to overcome this issue. The simplest one is reducing its size and changing the focal point of the camera. Designing the freeze-drying equipment to account for a specific chamber outside the drying chamber, containing the camera protected by a quartz glass, is also a solution, although practically challenging. It is feasible at a research and development level, but it is not realistic to think industries could make these adjustments anytime soon.

Another challenge to be addressed in practical applications is adjusting

the sensor to cGMP conditions. The sensor must allow CIP procedures to take place, for instance. These changes may be achievable since data transfer is already wireless. The challenge would be the energy supply, the only cable currently used. To provide energy to the sensor during the process, a battery should be used. Batteries are used in satellites, for instance. However, they are kept at room temperature and are considered to not operate well at low temperatures. Two fixes should be implemented to address this: first, the camera should be thermally isolated from the lyophilizer conditions; second, a small heater should be incorporated to ensure the batteries would not operate below their tolerable conditions. It is needless to say that new tests to assess the potential effects of the camera inside the chamber will be needed with such modifications. Still, infrared monitoring proved to offer many advantages for freeze-drying monitoring that would be worth its development.

Appendix

Appendix A

Materials and equipment used

Equipment

Three freeze-drying equipment were used:

LyoBeta 25 (Telstar, Terrassa, Spain)

This is a pilot-scale equipment with a 0.2 m^3 chamber. The equipment has an external condenser which operates at approximately -80°C with a maximum ice capacity of 40 kg. The system is equipped with T-type thermocouples (Tersid, Milano, Italy) and a capacitance gauge (Baratron type 626A, MKS Instruments, Andover, MA, USA) for pressure monitoring.

Figure A.1: Lyobeta 25 by Telstar.

REVO (Millrock Technology, Kingston, USA)

This is a pilot-scale freeze-dryer with roughly 1 m^2 of shelf area. It is provided with an external condenser with maximum condensing capacity of 30 kg operated at approximately 193 K. It is also equipped with a thermocouple

acquisition system in which T-type thermocouples (Tersid, Milano, Italy) were used. The freeze-dryer is supplied with a thermal conductivity gauge (Pirani type PSG- 101-S, Inficon, Bad Ragaz, Switzerland) and a capacitance gauge (Baratron type 626 A, MKS Instruments, Andover, MA, USA) for pressure monitoring.

Figure A.2: Revo by Millroch Technologies.

MicroFD (Millrock Technology, Kingston, USA)

This is a very small freeze-dryer, proposed for fast cycle and product development with minimal material consumption. Figure A.3 shows the tiny loading tray of the MicroFD with 19 6R vials.

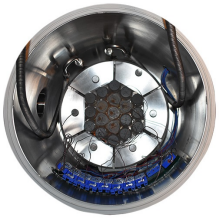

Figure A.3: Inside the MicroFD:loading tray and LyoSim surrounding the vials.

It has a chamber with a 15-cm-diameter circular shelf onto which the vials are loaded, encircled by removable thermal conductors. These conductors ensure the contact between the external vials of the batch and the temperature-controlled aluminium ring, LyoSim. The LyoSim is used to emulate the desired heating conditions observed in a larger batch, whether for edge or central batch conditions. To this end, the ring temperature can be set to range from -15°C to +15°C offset with respect to the average product temperature. The shelf temperature may range from -60°C to +60°C.

The MicroFD is provided with an external condenser with maximum condensing capacity of 0.5 kg operated at approximately 203 K. An additional system was available in the micro freeze-dryer for process monitoring, namely AccuFlux®. It consists in a thin film differential thermopile, placed in contact

Figure A.4: MicriFD by Millroch Technologies.

with the shelf and the bottom of the vials, that provides a direct measurement of the heat flux from the shelf to the vials. This tool was not used in the present thesis, however.

Solutions and vials

All solutions are made whether with water filtered using a Millipore water system (Milli-Q RG, Millipore, Billerica, MA) or with Water for injection (WFI) (Fresenius Kabi, Verona, Italy). The later is used specifically for the experiments investigating freezing in depth (Chapter 3). The solutes used are sucrose, mannitol (Sigma Aldrich, Milano, Italy) and dextran 40 (PanReac AppliChem, Chicago, USA).

The vial sizes used are 4R, 6R and 20R (Schott Pharmaceutical Packaging, Inc., Lebanon, USA) as illustrated in Figure A.5, partially stoppered with NovaPure Chlorobutyl Igloo Stoppers (West Pharma, Exton, USA) after filled. The solutions are then filtered with 0.22 μ m PVDF sterile filters (Merk Millipore, Cork, Ireland).

Figure A.5: Illustration of the 4R, 6R and 20R vial sizes used.

Vials monitored by thermocouples use holders (VTH-M-0020, Millrock Technology Inc. Kingston, NY, USA) to enable careful control and correct placement of the thermocouples used, touching the bottom of the vial [95].

Appendix B

Methods

$(\frac{Pi}{Ba})$ primary drying end time estimation

The ratio between the thermal conductivity and capacitance gauges signals $(\frac{Pi}{Ba})$ is used to assess a representative value for primary drying duration. The thermal conductivity gauge signal profile exhibits a sharp decreasing trend as the drying process is close to be completed. The onset and the offset of this decreasing interval may be used to define the variability range of the drying time [26]. This is an extensively used method, although it may sometimes present wide ranges between the onset and offset times. Which is unsurprising considering that drying conditions, and thus drying duration, are non-uniform in the batch [23].

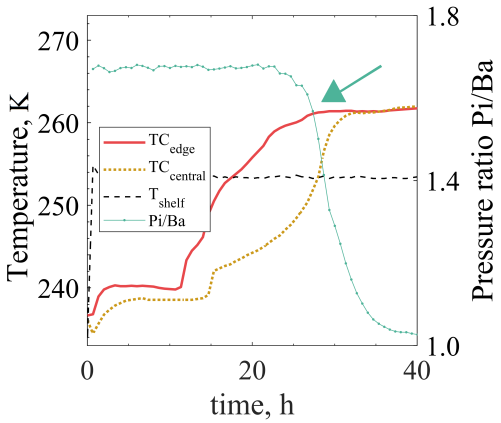

Figure B.1: Example of signals showing the sharp decrease trend presented by the $\frac{Pi}{Ba}$ sigal.

As previously reported, ending the cycle based on the onset point resulted in a product with 9% residual moisture and presenting cake collapse. Ending the cycle at the midpoint resulted in 5% residual moisture and cake collapse. Ending

the process at the offset resulted in a product with 4% residual moisture and no apparent collapse [26].

Gravimetric tests

For the gravimetric tests, vials are filled with water with the corresponding chosen fill volume for each vial size and weighted. A digital scale, set at four-decimal-point precis on, is used (Mettler Toledo, MS204S/01). The vials are then partially stoppered and loaded onto the shelf to be frozen. Once the freezing step is completed, primary drying is carried out for approximately 3-5 hours. After this, the cycle is stopped, the vials are closed with the stoppers and removed from the chamber to be weighed again and compute the mass change for the K_v calculation.

Appendix C

IR system characteristics

Table C.1 shows the characteristics of the IR camera used. The resolution refers to the pixel resolution. The thermal sensitivity or Noise Equivalent Temperature Difference (NETD), is a measure of how well a thermal imaging detector is able to distinguish between very small differences in thermal radiation in the image. In this camera is 0.05 K which is higher than the manufacture's default value (5 K or 5%) because of the built-in corrections such as the reflected apparent temperature. The focal length is the distance of a focus from the surface of a lens or curved mirror, in this case it is not very large. Hence, the images have a fish eye effect. The F-number for IR cameras is related to the contrast and the clarity of the image. The image frequency is how fast the camera can acquire thermal data. However, at least five frames are needed to generate one reliable frame. On top of that, the software configuration was set up to acquire thermal images in a 0.1 Hz frequency (6 frames per minute). The focus is fixed and was set for vials at around 20 to 30 *cm* away from the camera. Although fixed, this can be changed while setting up the camera.

Table C.1: FLIR A35 configurations and characteristics from Colucci 2019 [143]

Imaging optical data IR	
IR resolution	320 x 256 pixels
Thermal sensitivity	<0.05°C/50mK @ +30°C
Field of view	63° x 50°
Focal length	7.5 mm
F-number	1.4
Image frequency	60 Hz
Focus	Fixed
Detector data	
Detector type	Focal plane array, uncooled VOX microbolometer
Spectral range	7.5 – 13 µm
Detector time constant	12 ms
Object temperature range	-40 – 550 °C
Measurement analysis Atmospheric	
Atmospheric correction	Automatic provided distance, temperature and humidity
Optics transmission correction	Automatic, based on signals from internal sensors
Reflected temperature correction	Automatic based on input of reflected temperature
External optics/window correction	Automatic, based on input of optics transmission and temperature
Environmental data	
Operating temperature range	-40 / +70 °C
Humidity	24h @ 95% relative humidity and temperature in the range +25 to +40°C
Encapsulation	IP 40
Camera size (L x W x H)	106 x 40 x 40 mm
Housing material	Magnesium and aluminum 27

Nomenclature

Greek letters

α experimentally fitted parameter, $ms^{-0.5}K^{-0.5}$

β_1 first distribution parameter of a beta distribution, -

β_2 second distribution parameter of a beta distribution, -

ΔG free energy of the system, J

ΔG_s free energy associated with the formation of a new surface, J

ΔG_v free energy associated with the volume change from the formation of a new cluster, J

ΔH_f water's latent heat of fusion, $J.kg^{-1}$

ΔH_{fus} latent heat of fusion, $J.kg^{-1}$

ΔH_{max} maximum H_{max} pixel position − minimum H_{max} pixel position, pixels

ΔH_s latent heat of sublimation, $J.kg^{-1}$

Δ finite difference, -

ϵ Porosity of the dried cake, -

γ solid-solid interfacial tension ,$J.m^{-2}$

γ_w symmetric activity coefficient, -

$\lambda 1$ experimentally fitted parameter, -

$\lambda 2$ experimentally fitted parameter, -

Λ_v free energy associated with the volume change from the formation of a new cluster, $J.m^{-3}$

ν_H freezing front rate, $m.s^{-1}$

ω relative humidity, -

Ψ random process with ψ events, -

ψ observed value that took place, -

ρ density, $kg.m^{-3}$

σ supersaturation, -

σ_B Stefan–Boltzmann constant, $5.67037441910^{-8}.W.m^{-2}.K^{-4}$

τ tortuosity, -

τ_a transmittance of the atmosphere, -

τ_B Boltzman factor for residual excess Gibbs energy, -

θ_H temperature gradient at the frozen layer, $K.m^{-1}$

ε_{obj} Object's emissivity, K

ϑ_s Surface area fraction, -

Symbols

$\dot{I}$ freezing rate, $kg.m^{-3}.s^{-1}$

$\frac{Pi}{Ba}$ thermal conductivity and capacitance gauges pressure ratio, -

A parameter for dextran activity, -

a interaction coefficients in the UNIQUAC model, K

A_v vial's bottom area, m^2

a_w activity coefficient, -

a_{K_v} coefficients for $K_v(P_c)$ calculation, $W.m^{-1}.K^{-1}$

A_{rp} parameter used to model the dependence of R_p on L_{dried}, s^{-1}

b_{K_v} coefficients for $K_v(P_c)$ calculation, $W.m^{-1}.K^{-1}.Pa^{-1}$

B_{rp} parameter used to model the dependence of R_p on L_{dried}, m^{-1}

Ba capacitance gauge pressure signal, Pa

C parameter calculated based on polymers model, $m^3.kg^{-1}$

c_p	specific heat capacity, $J.Kg^{-1}.K^{-1}$
c_{K_v}	coefficients for $K_v(P_c)$ calculation, $W.m^{-1}.K^{-1}.Pa^{-1}$
$c_{w,c}$	water concentration in the drying chamber, $mol.m^{-3}$
$c_{w,c}$	water concentration in the drying chamber, -
$c_{w,i}$	water concentration in the in the ice sublimation interface, $mol.m^{-3}$
d	distance between the object and the sensor, m
D_p	ice crystals or pore size distribution, m
d_{p_H}	ice crystals or pore diameter, m
di_e	effective diffusivity, $m^2.s^{-1}$
di_k	Knudsen diffusivity, $m^2.s^{-1}$
G	growth rate, $m.s^{-1}$
g	growth rate order, -
G_{cryst}	Free energy of crystallization, J
H_i	sublimation interface position, -
H_{cryst}	Entalpy of crystallization, J
H_{max}	position of the maximum axial temperature, -
H_{min}	position of the minimum axial temperature, -
J	Nucleation rate, $m^{-3}.s^{-1}$
J_q	heat flux, $J.s^{-1}.ms{-}2$
J_w	mass flux, $kg.s^{-1}.ms{-}2$
K	nucleation rate, s
k	conductivity, $W.m^{-1}.K^{-1}$
k_g	kinetic parameter for crystal growth, $m.s^{-1}$
k_n	kinetic parameter for crystal nucleation, $m^{-3}.s^{-1}.K^{-n}$
K_v	global heat transfer coefficient, $W.m^{-1}.K^{-1}$

K_{cryst} Crystallization constant, -

Kp parameter for R_p calculation, $m.s^{-1}.K^{-0.5}$

kr parameter for mannitol activity, -

L_d matrix of the loading, -

L_{dried} dried cake thickness, m

L_{frozen} frozen cake thickness, m

m mass, kg

M_W water molar mass, $kg.kmol^{-1}$

ms solid mass fraction, -

mw water mass fraction, -

N number of observations for nucleation parameters optimization, -

n crystal nucleation order, -

N_c normalization parameter of a beta distribution, -

P_c chamber pressure, Pa

$p_{w,c}$ water partial pressure in the drying chamber, -

$p_{w,i}$ ice partial pressure in the sublimation interface, -

Pi Pirani gauge pressure signal, Pa

Q total heat, J

q molecular surface area parameter, -

Q_{atm} heat emitted by the atmosphere detected by the infrared sensor, J

Q_{obj} target object's heat detected by the infrared sensor, J

Q_{ref} reflected heat detected by the infrared sensor, J

Q_{tot} total heat detected by the infrared sensor, J

r parameters of the UNIQUAC model, -

R_g ideal gas constant, $J.mol^{-1}.K^{-1}$

R_p cake resistance to vapor flow, $m.s^{-1}$

$R_{(p,0)}$ parameter used to model the dependence of R_p on L_{dried}, $m.s^{-1}$

r_{ad} radius of a given cluster, m

r_{cr} critical radius, m

Res matrix of the residuals, -

S Saturation, -

s integration variable, -

S_c matrix of the scores, -

S_{cryst} Entropy of crystallization constant, $J.K^{-1}$

T temperature, K

t time, s

t_d duration of the sublimation step, s

T_f equilibrium freezing temperature, K

t_f freezing time, s

T_g glass transition temperature,K

T_h Holding temperature used after nucleation using VISF, K

T_i sublimation interface temperature, K

T_n nucleation temperature, K

T_{amb} ambient temperature of surroundings, K

T_{atm} atmospheric temperature, K

T_{bottom} bottom product temperature, K

T_{eu} eutectic temperature point, K

t_{ind} induction time, s

T_{max} maximum axial temperature, K

T_{min} minimum axial temperature, K

T_{obj} Object temperature, K

T_{prof} average axial temperature profile, K

t_{sat} saturation time, s

T_{shelf} Shelf temperature setting, K

T_{top} top product temperature, K

u potency parameter for dextran activity, -

V volume, m^3

v_1, h_1, h_2 lines and columns of the SEM image segmentation matrices

V_w partial molal volume of water, $m^3.mol^{-1}$

w volume fraction, -

W_{tot} total radiation emitted from an object, $W.m^{-2}$

x molar fraction, -

X_{img} data matrix for the SEM image segmentation tool, -

z axial coordinate, m

Subscripts and superscripts

0 initial

$frozen$ relative to the frozen fraction

H relative to the cake position H

ice relative to frozen water

ijk referent to different components i, j and k

$liquid$ relative to the liquid fraction

n relative to the nature of a given part of a system

$solid$ relative to the solute fraction

List of acronyms

FD freeze-drying

cGMP current Good Manufacturing Practices

VISF Vacuum Induced Surface Freezing

CAGR Compound Annual Growth Rate

PAT Pocess Analytical Technology

TDLAS Tuneable Diode Laser

NIR Near Infrared Spectroscopy

IR Infrared

RTD Resistance Thermal Detectors

TEMPRIS Temperature Remote Interrogation Systems

TFTC Thin-film thermocouples

OFS Optical Fiber Sensor

MTM Manometric Temperature Measurement

PRT Pressure Rise Test

DPE Dynamic Parameters Estimation Method

PRA Pressure Rise Analysis

RTRT Real Time Release Testing

PQS Performance, Quality and Safety

QbD Quality by Design

TC Thermocouples

SIP Sterilization in Place

CIP Cleaning in Place

APIs Active Pharmaceutical Ingredients

WFI Water for injection

HACCP Hazard Analysis and Critical Control Points

UNIQUAC Universal quasichemical

PBM Population Balance Model

SEM Scanning Electron Microscope

DS design space

DSC Differential Scanning Calorimetry

ISO valve Isolation valve

MIA Multivariate Image Analysis

VOx Vanadium oxide

a-Si Amorphous silicon

PCA Principal component analysis

FDA Food and Drug Administration

FRCNN Faster Region Convolutional Neural Network

KCF Kernelized Correlation Filter

TVIS through-vial impedance spectroscopy

NETD Noise Equivalent Temperature Difference

Bibliography

1. Market and Markets. Freeze-Drying/ Lyophilization Market by Type (Tray, Shell, Manifold), Scale of operation (Industrial, Lab, Pilot), Application (Food, Pharma & Biotech), Accessories (Loading & Unloading, Monitoring, Vacuum Systems) - Global Forecast to 2025. *B2B Reports PH2704* (2021).
2. Langford, A., Bhatnagar, B., Walters, R. & Tchessalov, S. Drying technologies for biopharmaceutical applications: Recent developments and future direction. *Drying Technology* **36,** 677–684. ISSN: 0737-3937. https://doi.org/10.1080/07373937.2017.1355318 (2018).
3. Abdul-Fattah, A. M., Kalonia, D. S. & Pikal, M. J. The Challenge of Drying Method Selection for Protein Pharmaceuticals: Product Quality Implications. *Journal of pharmaceutical sciences* **101,** 2271–2280 (2012).
4. Sharma, A., Khamar, D., Cullen, S., Hayden, A. & Hughes, H. Innovative Drying Technologies for Biopharmaceuticals. *International Journal of Pharmaceutics* **609,** 121115. ISSN: 18733476. https://doi.org/10.1016/j.ijpharm.2021.121115 (2021).
5. Velardi, S. A., Rasetto, V. & Barresi, A. A. Dynamic parameters estimation method: Advanced manometric temperature measurement approach for freeze-drying monitoring of pharmaceutical solutions. *Industrial and Engineering Chemistry Research* **47,** 8445–8457 (2008).
6. Oetjen, G.-W. & Haseley, P. *Freeze-drying* 2nd editio. ISBN: 9783527306206 (Wiley, Weinheim, 2004).
7. Reh, G. 2020 Global life sciences outlook. *Deloitte Insights* (2020).
8. Aschenbrenner, M. & Kulozik, U. Freezing of Probiotic Bacteria. *Advances in Probiotic Technology,* 187–220 (2015).
9. Barresi, A. A. & Fissore, D. in *Operations in Food refrigeration* 353–368 (Taylor & Francis Group, Boca Raton, 2012). ISBN: 9781420055511.
10. Fissore, D. in *Encyclopedia of Pharmaceutical Science and Technology* 4th. August, 1723–1737 (Taylor and Francis, New York, NY, 2013). ISBN: 978-1-84569-746-4.

11. Arsiccio, A. *et al.* Vacuum Induced Surface Freezing as an effective method for improved inter- and intra-vial product homogeneity. *European Journal of Pharmaceutics and Biopharmaceutics* **128,** 210–219. ISSN: 18733441. https://doi.org/10.1016/j.ejpb.2018.04.002 (2018).
12. Adali, M. B., Barresi, A. A., Boccardo, G. & Pisano, R. Spray Freeze-Drying as a Solution to Continuous Manufacturing of Pharmaceutical Products in Bulk. *Processes* **8,** 21–27 (2020).
13. Van Bockstal, P. J., De Meyer, L., Corver, J., Vervaet, C. & De Beer, T. Non-contact Infrared-Mediated Heat Transfer During Continuous Freeze-Drying of Unit Doses. *Journal of Pharmaceutical Sciences* **106,** 71–82. ISSN: 15206017. http://dx.doi.org/10.1016/j.xphs.2016.05.003 (2017).
14. Searles, J. A., Carpenter, J. F. & Randolph, T. W. The ice nucleation temperature determines the primary drying rate of lyophilization for samples frozen on a temperature controlled shelf. *Journal of Pharmaceutical Sciences* **90,** 860–871 (2001).
15. Patel, S. M., Bhugra, C. & Pikal, M. J. Reduced pressure ice fog technique for controlled ice nucleation during freeze-drying. *AAPS PharmSciTech* **10,** 1406–1411. ISSN: 15309932 (2009).
16. Nakagawa, K., Hottot, A., Vessot, S. & Andrieu, J. Influence of controlled nucleation by ultrasounds on ice morphology of frozen formulations for pharmaceutical proteins freeze-drying. *Chemical Engineering and Processing: Process Intensification* **45,** 783–791. ISSN: 02552701 (2006).
17. Colucci, D., Fissore, D., Rossello, C. & Carcel, J. A. On the effect of ultrasound-assisted atmospheric freeze-drying on the antioxidant properties of eggplant. *Food Research International* **106,** 580–588. ISSN: 09639969 (2018).
18. Nema, S. & Ludwig, J. D. *Pharmaceutical dosage forms: Parenteral medications: Third Edition* 1–312. ISBN: 9781420086485 (2016).
19. Capozzi, L. C. Continuous Freeze-Drying of Pharmaceuticals (2018).
20. Montgomery, D. *Introduction to statistical quality control* 6th, 754. ISBN: 9780470169926 (John Wiley & Sons, Inc., Jefferson City, 2009).
21. Food and Drug Administration. Guidance for Industry, PAT-A Framework for Innovative Pharmaceutical Development, Manufacturing and Quality Assurance. http://www.fda.gov/downloads/Drugs/GuidanceComplianceRegulatoryInformatio Guidances/ucm070305.pdf (2004).
22. Fissore, D., Pisano, R. & Barresi, A. A. Advanced Approach to Build the Design Space for the Primary Drying of a Pharmaceutical Freeze-Drying Process. *Journal of pharmaceutical sciences* **100,** 4923–4933 (2011).

23. Pisano, R. Automatic control of a freeze-drying process: Detection of the end point of primary drying. *Drying Technology,* 1–18. ISSN: 0737-3937. https://doi.org/10.1080/07373937.2020.1774891 (2020).

24. Sheehan, P. & Liapis, A. I. Modeling of the primary and secondary drying stages of the freeze drying of pharmaceutical products in vials: Numerical results obtained from the solution of a dynamic and spatially multi-dimensional lyophilization model for different operational policies. *Biotechnology and Bioengineering* **60,** 712–728. ISSN: 00063592 (1998).

25. Nakach, M. & Authelin, J.-R. Scale-Up and cGMP Manufacturing of Nanodrug Delivery Systems for Clinical Investigations. *Pharmaceutical Nanotechnology: Innovation and Production,* 295–330 (2016).

26. Patel, S. M., Doen, T. & Pikal, M. J. Determination of end point of primary drying in freeze-drying process control. *AAPS PharmSciTech* **11,** 73–84. ISSN: 1530-9932. http://www.springerlink.com/index/10.1208/s12249-009-9362-7 (2010).

27. Patel, S. M., Chaudhuri, S. & Pikal, M. J. Choked flow and importance of Mach I in freeze-drying process design. *Chemical Engineering Science* **65,** 5716–5727. ISSN: 00092509. http://dx.doi.org/10.1016/j.ces.2010.07.024 (2010).

28. Stratta, L., Capozzi, L. C., Franzino, S. & Pisano, R. Economic Analysis of a Freeze-Drying Cycle. *Processes* **8,** 1–17 (2020).

29. Colucci, D., Fissore, D., Barresi, A. A. & Braatz, R. D. A new mathematical model for monitoring the temporal evolution of the ice crystal size distribution during freezing in pharmaceutical solutions. *European Journal of Pharmaceutics and Biopharmaceutics* **148,** 148–159. ISSN: 18733441. https://doi.org/10.1016/j.ejpb.2020.01.004 (2020).

30. Arsiccio, A., Barresi, A. A. & Pisano, R. Prediction of Ice Crystal Size Distribution after Freezing of Pharmaceutical Solutions(supporting info). *Crystal Growth and Design* **17,** 4573–4581. ISSN: 15287505 (2017).

31. Nakagawa, K. & Hottot, A. Modeling of Freezing Step during Freeze-Drying of Drugs in Vials. *AIChE Journal* **53,** 1362–1372. ISSN: 12350621. arXiv: 0201037v1 [physics] (2007).

32. Kasper, J. C. & Friess, W. The freezing step in lyophilization: Physico-chemical fundamentals, freezing methods and consequences on process performance and quality attributes of biopharmaceuticals. *European Journal of Pharmaceutics and Biopharmaceutics* **78,** 248–263. ISSN: 09396411. http://dx.doi.org/10.1016/j.ejpb.2011.03.010 (2011).

33. Oddone, I. *Vacuum Induced Nucleation as a method for freeze drying optimization* PhD thesis (Politecnico di Torino, 2015).

34. Arsiccio, A., Giorsello, P., Marenco, L. & Pisano, R. Considerations on Protein Stability During Freezing and Its Impact on the Freeze-Drying Cycle: A Design Space Approach. *Journal of Pharmaceutical Sciences* **109,** 464–475. ISSN: 15206017. https://doi.org/10.1016/j.xphs.2019.10.022 (2020).

35. Schellekens, H., Aldosari, M., Talsma, H. & Mastrobattista, E. Making individualized drugs a reality. *Nature Biotechnology* **35,** 507–513. ISSN: 15461696 (2017).

36. Korpus, C. & Friess, W. Evaluation of Different Holder Devices for Freeze-Drying in Dual-Chamber Cartridges With a Focus on Energy Transfer. *Journal of Pharmaceutical Sciences* **106,** 1092–1101. ISSN: 15206017. http://dx.doi.org/10.1016/j.xphs.2016.12.016 (2017).

37. Ellenberg, S. S. Discussion: Is the FDA in need of a major change in the way it regulates? *Biostatistics* **18,** 414–416. ISSN: 14684357 (2017).

38. Hottot, A., Vessot, S. & Andrieu, J. Freeze drying of pharmaceuticals in vials: Influence of freezing protocol and sample configuration on ice morphology and freeze-dried cake texture. *Chemical Engineering and Processing: Process Intensification* **46,** 666–674. ISSN: 02552701 (July 2007).

39. Fang, R., Tanaka, K., Mudhivarthi, V., Bogner, R. H. & Pikal, M. J. Effect of Controlled Ice Nucleation on Stability of Lactate Dehydrogenase During Freeze-Drying. *Journal of Pharmaceutical Sciences* **107,** 824–830. ISSN: 00223549 (Mar. 2018).

40. Akyurt, M., Zaki, G. & Habeebullah, B. Freezing phenomena in ice – water systems. *Energy Conversion and Management 43* **43,** 1773–1789 (2002).

41. Kane, S. G., Evans, T. W., Brian, P. L. & Sarofim, A. F. Determination of the kinetics of secondary nucleation in batch crystallizers. *AIChE Journal* **20,** 855–862. ISSN: 15475905 (1974).

42. Colucci, D., Morra, L., Zhang, X., Fissore, D. & Lamberti, F. An automatic computer vision pipeline for the in-line monitoring of freeze-drying processes. *Computers in Industry* **115,** 103184. ISSN: 01663615. https://doi.org/10.1016/j.compind.2019.103184 (2020).

43. Arsiccio, A., Barresi, A. A. & Pisano, R. Prediction of Ice Crystal Size Distribution after Freezing of Pharmaceutical Solutions. *Crystal Growth and Design* **17,** 4573–4581. ISSN: 15287505 (2017).

44. Bald, W. *Food Freezing: Today and Tomorrow* 206. ISBN: 978-1-4471-3448-0. http://link.springer.com/10.1007/978-1-4471-3446-6 (1991).

45. Arsiccio, A., McCarty, J., Pisano, R. & Shea, J. E. Heightened Cold-Denaturation of Proteins at the Ice-Water Interface. *Journal of the American Chemical Society* **142,** 5722–5730. ISSN: 15205126 (2020).

46. Arsiccio, A. & Pisano, R. The Ice-Water Interface and Protein Stability: A Review. *Journal of Pharmaceutical Sciences* **109,** 2116–2130. ISSN: 00223549 (July 2020).

47. Patapoff, T. W. & Overcashier, D. E. The importance of freezing on lyophilization cycle development. *BioPharm* **15,** 16–21. ISSN: 10408304 (2002).

48. Konstantinidis, A. K., Kuu, W. Y., Otten, L., Nail, S. L. & Sever, R. R. Controlled nucleation in freeze-drying: effects on pore Size in the dried product layer, mass transfer resistance, and Primary drying rate. *Journal of pharmaceutical sciences* **100,** 3453–3470 (2011).

49. Passot, S. *et al.* Effect of controlled ice nucleation on primary drying stage and protein recovery in vials cooled in a modified freeze-dryer. *Journal of Biomechanical Engineering* **131,** 1–5. ISSN: 01480731 (2009).

50. Tang, X. & Pikal, M. J. Design of Freeze-Drying Processes for Pharmaceuticals: Practical Advice. *Pharmaceutical Research* **21,** 191–200. ISSN: 07248741 (2004).

51. Giordano, A., Barresi, A. A. & Fissore, D. On the use of mathematical models to build the design space for the primary drying phase of a pharmaceutical lyophilization process. *Journal of Pharmaceutical Sciences* **100,** 311–324. ISSN: 15206017. http://dx.doi.org/10.1002/jps.22264 (2011).

52. Geidobler, R. & Winter, G. Controlled ice nucleation in the field of freeze-drying: Fundamentals and technology review. *European Journal of Pharmaceutics and Biopharmaceutics* **85,** 214–222. ISSN: 18733441. http://dx.doi.org/10.1016/j.ejpb.2013.04.014 (2013).

53. Oddone, I., Pisano, R., Bullich, R. & Stewart, P. Vacuum-Induced Nucleation as a Method for Freeze-Drying Cycle Optimization. *Industrial & Engineering Chemistry Research* **53,** 18236–18244. ISSN: 0888-5885 (Nov. 2014).

54. Searles, J. A., Carpenter, J. F. & Randolph, T. W. Annealing to optimize the primary drying rate, reduce freezing-induced drying rate heterogeneity, and determine Tg pharmaceutical lyophilization. *Journal of Pharmaceutical Sciences* **90,** 872–887. ISSN: 00223549 (2001).

55. Lu, X. & Pikal, M. J. Freeze-Drying of Mannitol-Trehalose-Sodium Chloride-Based Formulations: The Impact of Annealing on Dry Layer Resistance to Mass Transfer and Cake Structure. *Pharmaceutical Development and Technology* **9,** 85–95. ISSN: 10837450 (2004).

56. Kuu, W. Y., Doty, M. J., Rebbeck, C. L., Hurst, W. S. & Cho, Y. K. Gap-freezing approach for shortening the lyophilization cycle time of pharmaceutical formulations-demonstration of the concept. *Journal of Pharmaceutical Sciences* **102,** 2572–2588. ISSN: 15206017. http://dx.doi.org/10.1002/jps.23610 (2013).

57. Assegehegn, G., Brito-de la Fuente, E., Franco, J. M. & Gallegos, C. The Importance of Understanding the Freezing Step and Its Impact on Freeze-Drying Process Performance. *Journal of Pharmaceutical Sciences* **108,** 1378–1395. ISSN: 15206017 (2019).

58. Wenzel, T., Gieseler, M. & Gieseler, H. Design of Vacuum-Induced Freezing Protocols for High Fill Volume Formulations in Freeze-Drying: A Strategic Approach. *Journal of Pharmaceutical Sciences* (2020).

59. Chakravarty, P., Lee, R., Demarco, F. & Renzi, E. Ice fog as a means to induce uniform ice nucleation during lyophilization. *BioPharm International* **25,** 33–38. ISSN: 1542166X (2012).

60. Ling, W. *Controlled Nucleation During Freezing Step of Freeze-Drying Cycle Using Pressure Differential Ice Crystals Distribution from Condensed Frost. Wo 2014/028119 Al* 2014.

61. Hottot, A., Nakagawa, K. & Andrieu, J. Effect of ultrasound-controlled nucleation on structural and morphological properties of freeze-dried mannitol solutions. *Chemical Engineering Research and Design* **86,** 1362–1372. ISSN: 02638762 (2008).

62. Shichiri, T. & Araki, Y. Nucleation mechanism of ice crystals under electrical effect. *Journal of Crystal Growth* **78,** 502–508. ISSN: 00220248 (1986).

63. Kurz; W. & Fisher, D. J. *Fundamentals of solidification* 3rd. ISBN: 9780878495221 (Aedermannsdorf, Switzerland, 1992).

64. Kochs, M., Körber, C., Nunner, B. & Heschel, I. The influence of the freezing process on vapour transport during sublimation in vacuum-freeze-drying. *International Journal of Heat and Mass Transfer* **34,** 2395–2408. ISSN: 00179310 (1991).

65. Bomben, J. L. & King, C. J. Heat and mass transport in the freezing of apple tissue. *International Journal of Food Science & Technology* **17,** 615–632. ISSN: 13652621 (1982).

66. Reid, D. S. Cryomicroscopic studies of the freezing of model solutions of cryobiological interest. *Cryobiology* **21,** 60–67. ISSN: 10902392 (1984).

67. Woinet, B., Andrieu, J., Laurent, M. & Min, S. G. Experimental and theoretical study of model food freezing. Part II. Characterization and modelling of the ice crystal size. *Journal of Food Engineering* **35,** 395–407. ISSN: 02608774 (1998).

68. Van Der Sman, R. G. Phase field simulations of ice crystal growth in sugar solutions. *International Journal of Heat and Mass Transfer* **95,** 153–161. ISSN: 00179310 (2016).

69. Fan, T. H. *et al.* Phase-field modeling of freeze concentration of protein solutions. *Polymers* **11,** 1–20. ISSN: 20734360 (2018).

70. Vuist, J. E., Linssen, R., Boom, R. M. & Schutyser, M. A. Modelling ice growth and inclusion behaviour of sucrose and proteins during progressive freeze concentration. *Journal of Food Engineering* **303,** 110592. ISSN: 02608774. http://creativecommons.org/licenses/by/4.0/%0Ahttps://linkinghub.elsevier.com/retrieve/pii/S0260877421001175 (2021).

71. Arsiccio, A. & Pisano, R. Application of the Quality by Design Approach to the Freezing Step of Freeze-Drying: Building the Design Space. *Journal of Pharmaceutical Sciences* **107,** 1586–1596. ISSN: 15206017. https://doi.org/10.1016/j.xphs.2018.02.003 (2018).

72. Fissore, D., Pisano, R. & Barresi, A. A. Process analytical technology for monitoring pharmaceuticals freeze-drying – a comprehensive review. *Drying Technology* **36,** 1–27. ISSN: 15322300 (2018).

73. Nail, S. *et al.* Recommended Best Practices for Process Monitoring Instrumentation in Pharmaceutical Freeze Drying—2017. *AAPS PharmSciTech* **18,** 2379–2393. ISSN: 15309932 (2017).

74. Demichela, M., Barresi, A. A. & Baldissone, G. The Effect of Human Error on the Temperature Monitoring and Control of Freeze Drying Processes by Means of Thermocouples. *Frontiers in Chemistry* **6,** 1–11. ISSN: 2296-2646 (2018).

75. Schneid, S. & Gieseler, H. Evaluation of a new wireless temperature remote interrogation system (TEMPRIS) to measure product temperature during freeze drying. *AAPS PharmSciTech* **9,** 729–739. ISSN: 15309932 (2008).

76. Kasper, J. C., Wiggenhorn, M., Resch, M. & Friess, W. Implementation and evaluation of an optical fiber system as novel process monitoring tool during lyophilization. *European Journal of Pharmaceutics and Biopharmaceutics* **83,** 449–459. ISSN: 09396411. http://dx.doi.org/10.1016/j.ejpb.2012.10.009 (2013).

77. Oddone, I., Fulginiti, D., Barresi, A. A., Grassini, S. & Pisano, R. Non-Invasive Temperature Monitoring in Freeze Drying: Control of Freezing as a Case Study. *Drying Technology* **33,** 1621–1630. ISSN: 15322300. http://dx.doi.org/10.1080/07373937.2015.1040026 (2015).

78. Fissore, D. Model-Based PAT for quality management in pharmaceuticals freeze-drying: state of the art. *Frontiers in Bioengineering and Biotechnology* **5,** 1–15. ISSN: 2296-4185 (2017).

79. Pisano, R., Fissore, D., Velardi, S. A. & Barresi, A. A. In-Line Optimization and Control of an Industrial Freeze-Drying Process for Pharmaceuticals. *Journal of pharmaceutical sciences* **99,** 4691–4709 (2010).

80. Moino, C., Bourlés, E., Pisano, R. & Scutellà, B. In-Line Monitoring of the Freeze-Drying Process by Means of Heat Flux Sensors. *Industrial & Engineering Chemistry Research.* ISSN: 0888-5885 (2021).

81. Carfagna, M., Rosa, M., Lucke, M., Hawe, A. & Friess, W. Heat flux sensor to create a design space for freeze-drying development. *European Journal of Pharmaceutics and Biopharmaceutics* **153,** 84–94. ISSN: 18733441. https://doi.org/10.1016/j.ejpb.2020.05.028 (2020).

82. Gieseler, H. *et al.* Evaluation of Tunable Diode Laser Absorption Spectroscopy for In-Process Water Vapor Mass Flux Measurements During Freeze Drying. *Journal of Pharmaceutical Sciences* **96,** 1776–1793 (2007).

83. Kuu, W. Y. & Nail, S. L. Rapid freeze-drying cycle optimization using computer programs developed based on heat and mass transfer models and facilitated by tunable diode laser absorption spectroscopy (TDLAS). *Journal of Pharmaceutical Sciences* **98,** 3469–3482. ISSN: 15206017. http://dx.doi.org/10.1002/jps.21813 (2009).

84. Mayeresse, Y., Veillon, R., Sibille, P. & Nomine, C. Freeze-drying process monitoring using a cold plasma ionization device. *PDA Journal of Pharmaceutical Science and Technology* **61,** 160–174. ISSN: 10797440 (2007).

85. Chouvenc, P., Vessot, S., Andrieu, J. & Vacus, P. Optimization of the freeze-drying cycle: A new model for pressure rise analysis. *Drying Technology* **22,** 1577–1601. ISSN: 07373937 (2004).

86. Tang, X. C., Nail, S. L. & Pikal, M. J. Evaluation of manometric temperature measurement (MTM), a process analytical technology tool in freeze drying, part III: Heat and mass transfer measurement. *AAPS PharmSciTech* **7.** ISSN: 15309932 (2006).

87. Fissore, D., Pisano, R. & Barresi, A. A. On the methods based on the pressure rise test for monitoring a freeze-drying process. *Drying Technology* **29,** 73–90. ISSN: 07373937 (2011).

88. Bobba, S., Zinfollino, N. & Fissore, D. Application of Near-Infrared Spectroscopy to statistical control in freeze-drying processes. *European Journal of Pharmaceutics and Biopharmaceutics* **168,** 26–37. ISSN: 09396411. https://doi.org/10.1016/j.ejpb.2021.08.009 (2021).

89. Davies, A. M. C. & Norris, K. H. *An Introduction To Near Infrared (Nir) Spectroscopy* 2015.

90. De Beer, T. *et al.* In-line and real-time process monitoring of a freeze drying process using Raman and NIR spectroscopy as complementary process analytical technology (PAT) tools. *Journal of Pharmaceutical Sciences* **98,** 3430–3446. ISSN: 15206017. http://dx.doi.org/10.1002/jps.21633 (2009).

91. Emteborg, H. *et al.* Infrared thermography for monitoring of freeze-drying processes: Instrumental developments and preliminary results. *Journal of Pharmaceutical Sciences* **103,** 2088–2097. ISSN: 15206017 (2014).

92. Lietta, E., Colucci, D., Distefano, G. & Fissore, D. On the use of infrared thermography for monitoring a vial freeze-drying process. *Journal of Pharmaceutical Sciences* **108,** 391–398. ISSN: 15206017 (2018).

93. Colucci, D., Prats-Montalbán, J. M., Fissore, D. & Ferrer, A. Application of multivariate image analysis for on-line monitoring of a freeze-drying process for pharmaceutical products in vials. *Chemometrics and Intelligent Laboratory Systems* **187,** 19–27. ISSN: 18733239 (2019).

94. Patel, S. M. & Pikal, M. J. Lyophilization process design space. *Journal of Pharmaceutical Sciences* **102,** 3883–3887. ISSN: 15206017 (2013).

95. Fissore, D., Gallo, G., Ruggiero, A. E. & Thompson, T. N. On the use of a micro freeze-dryer for the investigation of the primary drying stage of a freeze-drying process. *European Journal of Pharmaceutics and Biopharmaceutics* **141,** 121–129. ISSN: 18733441. https://doi.org/10.1016/j.ejpb.2019.05.019 (2019).

96. Astarita, T. & Carlomagno, G. M. *Infrared Thermography for Thermo-Fluid-Dynamics* (eds Merzkirch, W., Rockwell, D. & Tropea, C.) 1–224. ISBN: 9783642295089 (2013).

97. Vollmer, M. & Möllmann, K.-P. *Infrared Thermal Imaging. Fundamentals, Research and Applications* 2nd. ISBN: 978-3-527-69332-0 (Wiley-VCH, Weinheim, Germany, 2006).

98. Henini, M. & Razeghi, M. *Handbook of Infrared Detection Technologies* 1st. ISBN: 1856173887 (Elsevier Ltd., Kidlington, Oxford, 2002).

99. Bagavathiappan, S., Lahiri, B. B., Saravanan, T., Philip, J. & Jayakumar, T. Infrared thermography for condition monitoring - A review. *Infrared Physics and Technology* **60,** 35–55. ISSN: 13504495. http://dx.doi.org/10.1016/j.infrared.2013.03.006 (2013).

100. FLIR LLC. *Uncooled detectors for thermal imaging cameras Uncooled detectors: a brief history* 2021.

101. Kaplan, H. *Practical Applications of Infrared Thermal Sensing and Imaging Equipment, Third Edition* 3rd. ISBN: 9780819467232 (SpiePress, Bellingham, Washington, 2009).

102. Minkina, W. & Dudzik, S. *Infrared Thermography errors and uncertainties* 1st. ISBN: 978-0-470-74718-6 (John Wiley & Sons, Ltd Registered, Chippenham, Wiltshire, 2009).

103. ISO 18434-1. Conditions of monitoring and diagnostics of machines - Thermography. *International Standard* **03/01.** ISSN: 1545-0279 (2008).

104. Fishbune, R. J. Infrared Thermography for Electronic Assembly Design Verification. *IBM® Power Technology and Qualification* (2000).

105. Lahiri, B., Bagavathiappan, S., Jayakumar, T. & Philip, J. Medical applications of infrared thermography: A review. *Infrared Physics and Technology* **55,** 221–235. ISSN: 13504495. http://dx.doi.org/10.1016/j.infrared.2012.03.007 (2012).

106. Astasio-Picado, A., Escamilla Martínez, E., Martínez Nova, A., Sánchez Rodríguez, R. & Gómez-Martín, B. Thermal map of the diabetic foot using infrared thermography. *Infrared Physics and Technology* **93,** 59–62. ISSN: 13504495. https://doi.org/10.1016/j.infrared.2018.07.008 (2018).

107. Côrte, A. C. *et al.* Infrared thermography study as a complementary method of screening and prevention of muscle injuries: Pilot study. *BMJ Open Sport and Exercise Medicine* **5,** 1–5. ISSN: 20557647 (2019).

108. Akafuah, N. K., Salazar, A. J. & Saito, K. Infrared thermography-based visualization of droplet transport in liquid sprays. *Infrared Physics and Technology* **53,** 218–226. ISSN: 13504495. http://dx.doi.org/10.1016/j.infrared.2009.12.002 (2010).

109. Ranilović, B., Cukrov, A., Boras, I., Švaić, S. & Zovko, M. Infrared Thermography as a Prediction Tool for the Irrigation Requirement in Agriculture. *Transactions of Famena* **45,** 367074. ISSN: 18491391 (2021).

110. Liu, L., Wang, Z., Li, J., Zhang, X. & Wang, R. A non-invasive analysis of seed vigor by infrared thermography. *Plants* **9,** 1–12. ISSN: 22237747 (2020).

111. Ceccardi, T. L., Heath, R. L. & Ting, I. P. Low-temperature exotherm measurement using infrared thermography. *HortScience* **30,** 140–142. ISSN: 00185345 (1995).

112. Livingston, D. P. *et al.* High-definition infrared thermography of ice nucleation and propagation in wheat under natural frost conditions and controlled freezing. *Planta* **247,** 791–806. ISSN: 14322048. https://doi.org/10.1007/s00425-017-2823-4 (2018).

113. Travain, T. *et al.* How good is this food? A study on dogs' emotional responses to a potentially pleasant event using infrared thermography. *Physiology and Behavior* **159,** 80–87. ISSN: 1873507X. http://dx.doi.org/10.1016/j.physbeh.2016.03.019 (2016).

114. Gowen, A. A., Tiwari, B. K., Cullen, P. J., McDonnell, K. & O'Donnell, C. P. Applications of thermal imaging in food quality and safety assessment. *Trends in Food Science and Technology* **21,** 190–200. ISSN: 09242244. http://dx.doi.org/10.1016/j.tifs.2009.12.002 (2010).

115. Meinlschmidt, P. & Maergner, V. Detection of foreign substances in food using thermography. *Thermosense XXIV* **4710,** 565–571 (2002).

116. Senni, L. *et al.* On-line automatic detection of foreign bodies in biscuits by infrared thermography and image processing. *Journal of Food Engineering* **128,** 146–156. ISSN: 02608774. http://dx.doi.org/10.1016/j.jfoodeng.2013.12.016 (2014).

117. D'Huys, K., Saeys, W. & De Ketelaere, B. Active infrared thermography for seal contamination detection in heat-sealed food packaging. *Journal of Imaging* **2.** ISSN: 2313433X (2016).

118. Ghosh, P., Rana, S. S., Nayak, A. & Pradhan, R. C. Quality evaluation of food by thermal imaging. *International Journal of Processing and Post Harvest Technology* **7,** 126–133. ISSN: 09765638 (2016).

119. Yanmaz, B. Use of infrared thermography in determining meat quality. *Eurasian Journal of Food Science and Technology,* 54–58. https://dergipark.org.tr/en/pub/ejfst/issue/58124/789134 (2020).

120. Torrecilla, J. S., Cancilla, J. C., Pradana-Lopez, S. & Perez-Calabuig, A. M. Detection of adulterations of extra-virgin olive oil by means of infrared thermography. *Olives and Olive Oil in Health and Disease Prevention,* 79–84 (2021).

121. Harguindeguy, M., Bobba, S., Colucci, D. & Fissore, D. Effect of vacuum freeze-drying on the antioxidant properties of eggplants (Solanum melongena L.) *Drying Technology* **39,** 3–18. ISSN: 15322300. https://doi.org/10.1080/07373937.2019.1699834 (2019).

122. Pereira, C. G., Ramaswamy, H. S., Giarola, T. M. d. O. & de Resende, J. V. Infrared thermography as a complementary tool for the evaluation of heat transfer in the freezing of fruit juice model solutions. *International Journal of Thermal Sciences* **120,** 386–399. ISSN: 12900729 (2017).

123. Veras, A. O., Béttega, R., Freire, F. B., Barrozo, M. A. & Freire, J. T. Drying kinetics, structural characteristics and vitamin c retention of dedo-de-moça pepper (capsicum baccatum) during convective and freeze drying. *Brazilian Journal of Chemical Engineering* **29,** 741–750. ISSN: 01046632 (2012).

124. Cuibus, L., Castro-Giráldez, M., Fito, P. J. & Fabbri, A. Application of infrared thermography and dielectric spectroscopy for controlling freezing process of raw potato. *Innovative Food Science and Emerging Technologies* **24,** 80–87. ISSN: 14668564. http://dx.doi.org/10.1016/j.ifset.2013.11.007 (2014).

125. Arocas, A., Sanz, T., Hernando, M. I. & Fiszman, S. M. Comparing microwave- and water bath-thawed starch-based sauces: Infrared thermography, rheology and microstructure. *Food Hydrocolloids* **25,** 1554–1562. ISSN: 0268005X. http://dx.doi.org/10.1016/j.foodhyd.2011.01.013 (2011).

126. Berry, B. Use of Infrared Thermography To Assess Temperature Variability in Beef Patties Cooked From the Frozen and Thawed States. *Foodservice Research International* **12,** 255–262. ISSN: 1524-8275 (2000).

127. Fito, P. *et al.* Vacuum impregnation for development of new dehydrated products. *Journal of Food Engineering* **49,** 297–302 (2001).

128. Tomas-Egea, J. A., Castro-Giraldez, M. & Fito, P. J. Thermodynamic model of freeze-drying of poultry breast using infrared thermography. *IDS'2018 – 21st International Drying Symposium,* 11–14 (2019).

129. Sun, Y., Zhang, M., Mujumdar, A. S. & Yu, D. Pulse-spouted microwave freeze drying of raspberry: Control of moisture using ANN model aided by LF-NMR. *Journal of Food Engineering* **292,** 110354. ISSN: 02608774. https://doi.org/10.1016/j.jfoodeng.2020.110354 (2021).

130. Jiang, H., Zhang, M., Mujumdar, A. S. & Lim, R. X. Drying uniformity analysis of pulse-spouted microwave–freeze drying of banana cubes. *Drying Technology* **34,** 539–546. ISSN: 15322300. http://dx.doi.org/10.1080/07373937.2015.1061000 (2016).

131. Wang, Y., Zhang, M., Mujumdar, A. S. & Mothibe, K. J. Microwave-assisted pulse-spouted bed freeze-drying of stem lettuce slices-effect on product quality. *Food and Bioprocess Technology* **6,** 3530–3543. ISSN: 19355130 (2013).

132. Bobba, S., Harguindeguy, M., Colucci, D. & Fissore, D. Diffuse interface model of the freeze-drying process of individually frozen products. *Drying Technology* **38,** 758–774. ISSN: 15322300. https://doi.org/10.1080/07373937.2019.1710711 (2020).

133. Gonçalves, B. J. *et al.* Infrared (IR) thermography applied in the freeze-drying of gelatin model solutions added with ethanol and carrier agents. *Journal of Food Engineering* **221,** 77–87. ISSN: 02608774 (2018).

134. Wiedey, R. & Kleinebudde, P. Infrared thermography — A new approach for in-line density measurement of ribbons produced from roll compaction. *Powder Technology* **337,** 17–24. ISSN: 1873328X. https://doi.org/10.1016/j.powtec.2017.01.052 (2018).

135. Lindner, J. A., Müller, M. G., Briesen, H. & Foerst, P. Monitoring temperature evolution and drying of coating on a single fluidized particle by infrared thermography. *Powder Technology* **382,** 331–338. ISSN: 1873328X (2021).

136. Kawakami, K. Parallel thermal analysis technology using an infrared camera for high-throughput evaluation of active pharmaceutical ingredients: A case study of melting point determination. *AAPS PharmSciTech* **11,** 1202–1205 (2010).

137. Kelen, Á., Ress, S., Nagy, T., Pallai, E. & Pintye-Hódi, K. Mapping of temperature distribution in pharmaceutical microwave vacuum drying. *Powder Technology* **162,** 133–137. ISSN: 00325910 (2006).

138. Gan, K. H., Bruttini, R., Crosser, O. K. & Liapis, A. I. Heating policies during the primary and secondary drying stages of the lyophilization process in vials: Effects of the arrangement of vials in clusters of square and hexagonal arrays on trays. *Drying Technology* **22,** 1539–1575. ISSN: 07373937 (2004).

139. Van Bockstal, P. J., Corver, J., De Meyer, L., Vervaet, C. & De Beer, T. Thermal Imaging as a Noncontact Inline Process Analytical Tool for Product Temperature Monitoring during Continuous Freeze-Drying of Unit Doses. *Analytical Chemistry* **90,** 13591–13599. ISSN: 15206882 (2018).

140. Colucci, D., Prats-Montalbán, J. M., Ferrer, A. & Fissore, D. On-line product quality and process failure monitoring in freeze-drying of pharmaceutical products. *Drying Technology* **39,** 134–147. ISSN: 15322300. https://doi.org/10.1080/07373937.2019.1614949 (2019).

141. Colucci, D., Prats-Montalbán, J. M., Ferrer, A. & Fissore, D. in *Freeze Drying of Pharmaceutical Products* 53–76 (2019). ISBN: 9780429022074.

142. Colucci, D., Maniaci, R. & Fissore, D. Monitoring of the freezing stage in a freeze-drying process using IR thermography. *International Journal of Pharmaceutics* **566,** 488–499. ISSN: 18733476. https://doi.org/10.1016/j.ijpharm.2019.06.005 (2019).

143. Colucci, D. *Infrared Imaging: a New Process Analytical Technology for Real Time Monitoring and Control of a Freeze-Drying Process* PhD thesis (Politecnico di Torino, 2019).

144. Shekhawat, R. S. Infrared Thermography - A Review. *International Journal of Engineering Trends and Technology* **35,** 287–290 (2016).

145. Harguindeguy, M. & Fissore, D. Temperature/end point monitoring and modelling of a batch freeze-drying process using an infrared camera. *European Journal of Pharmaceutics and Biopharmaceutics* **158,** 113–122. ISSN: 09396411 (2021).

146. Sritham, E. & Gunasekaran, S. Thermal evaluation of sucrose-maltodextrin-sodium citrate bioglass: Glass transition temperature. *Food Hydrocolloids* **60,** 589–597. ISSN: 0268005X. http://dx.doi.org/10.1016/j.foodhyd.2016.04.030 (2016).

147. Kim, A. I., Akers, M. J. & Nail, S. L. The physical state of mannitol after freeze-drying: Effects of mannitol concentration, freezing rate, and a noncrystallizing cosolute. *Journal of Pharmaceutical Sciences* **87,** 931–935. ISSN: 00223549 (1998).

148. Barresi, A., Ghio, S., Fissore, D. & Pisano, R. Freeze drying of pharmaceutical excipients close to collapse temperature: Influence of the process conditions on process time and product quality. *Drying Technology* **27,** 805–816. ISSN: 07373937 (2009).

149. Fissore, D., Pisano, R. & Barresi, A. A. *Using mathematical modeling and prior knowledge for QbD in freeze-drying processes* (ed Jameel, F.) 565–593. ISBN: 978-1-4939-2315-1 (Springer Science, New York, 2015).

150. Fissore, D., Harguindeguy, M., Ramirez, D. V. & Thompson, T. N. Development of freeze-drying cycles for pharmaceutical products using a micro freeze-dryer. *Journal of Pharmaceutical Sciences* **109,** 797–806. ISSN: 00223549. https://doi.org/10.1016/j.xphs.2019.10.053 (2020).

151. Bosca, S. & Fissore, D. Design and validation of an innovative soft-sensor for pharmaceuticals freeze-drying monitoring. *Chemical Engineering Science* **66,** 5127–5136. ISSN: 00092509 (2011).

152. Gan, K. H., Crosser, O. K., Liapis, A. I. & Bruttini, R. Lyophilization in vials on trays: Effects of tray side. *Drying Technology* **23,** 341–363. ISSN: 07373937 (2005).

153. Maity, A. & Sherman, M. The two-sample t test with one variance unknown. *American Statistician* **60,** 163–166. ISSN: 00031305 (2006).

154. Scutellà, B., Trelea, I. C., Bourlés, E., Fonseca, F. & Passot, S. Determination of the dried product resistance variability and its influence on the product temperature in pharmaceutical freeze-drying. *European Journal of Pharmaceutics and Biopharmaceutics* **128,** 379–388. ISSN: 18733441. https://doi.org/10.1016/j.ejpb.2018.05.004 (2018).

155. Cheftel, J. C., Lévy, J. & Dumay, E. Pressure-assisted freezing and thawing: Principles and potential applications. *Food Reviews International* **16,** 453–483. ISSN: 87559129 (2000).

156. Bai, G., Gao, D., Liu, Z., Zhou, X. & Wang, J. Probing the critical nucleus size for ice formation with graphene oxide nanosheets. *Nature* **576,** 437–441. ISSN: 14764687. http://dx.doi.org/10.1038/s41586-019-1827-6 (2019).

157. Kashchiev, D. *Nucleation, basic theory with applications* 1st. ISBN: 0750646829 (Butterworth Heinemann, Oxford, UK, 2000).

158. Maeda, N. Brief overview of ice nucleation. *Molecules* **26.** ISSN: 14203049 (2021).

159. Smith, G. & Jeeraruangrattana, Y. *Freeze Drying of Pharmaceutical Products* 1st (ed Davide Fissore Roberto Pisano, A. B.) ISBN: 9780367076801 (Taylor & Francis Group, Boca Raton, FL).

160. Heneghan, A. F., Wilson, P. W., Wang, G. & Haymet, A. D. J. Liquid-to-crystal nucleation: Automated lag-time apparatus to study supercooled liquids. *The Journal of Chemical Physics* **115,** 7599–7608. ISSN: 0021-9606 (Oct. 2001).

161. Heneghan, A. F. & Haymet, A. D. Liquid-to-crystal nucleation: A new generation lag-time apparatus. *Journal of Chemical Physics* **117,** 5319–5327. ISSN: 00219606 (Sept. 2002).

162. Pereyra, R. G., Szleifer, I. & Carignano, M. A. Temperature dependence of ice critical nucleus size. *Journal of Chemical Physics* **135.** ISSN: 00219606 (2011).

163. Wilson, P. W., Heneghan, A. F. & Haymet, A. D. Ice nucleation in nature: Supercooling point (SCP) measurements and the role of heterogeneous nucleation. *Cryobiology* **46,** 88–98. ISSN: 00112240 (2003).

164. Hottot, A., Vessot, S. & Andrieu, J. A direct characterization method of the ice morphology. Relationship between mean crystals size and primary drying times of freeze-drying processes. *Drying Technology* **22,** 2009–2021 (2004).

165. Petersen, A., Rau, G. & Glasmacher, B. Reduction of primary freeze-drying time by electric field induced ice nucleus formation. *Heat and Mass Transfer* **42,** 929–938 (2006).

166. Pisano, R. & Capozzi, L. C. Prediction of product morphology of lyophilized drugs in the case of Vacuum Induced Surface Freezing. *Chemical Engineering Research and Design* **125,** 119–129. ISSN: 02638762. http://dx.doi.org/10.1016/j.cherd.2017.07.004 (2017).

167. Jennings, T. *Lyophilization intro and basic principles* ISBN: 978-1-57491-081-0 (Informa Healthcare, New York, NY, 1999).

168. Becheleni, E. M., Rodriguez-Pascual, M., Lewis, A. E. & Rocha, S. D. Influence of Phenol on the Crystallization Kinetics and Quality of Ice and Sodium Sulfate Decahydrate during Eutectic Freeze Crystallization. *Industrial and Engineering Chemistry Research* **56,** 11926–11935. ISSN: 15205045 (2017).

169. Harguindeguy, M., Stratta, L., Fissore, D. & Pisano, R. Investigation of the Freezing Phenomenon in Vials Using an Infrared Camera. *Pharmaceutics* **13,** 1–22 (2021).

170. Kramer, M., Sennhenn, B. & Lee, G. Freeze-drying using vacuum-induced surface freezing. *Journal of Pharmaceutical Sciences* **91,** 433–443. ISSN: 00223549 (Feb. 2002).

171. Prats-Montalbán, J. M., de Juan, A. & Ferrer, A. Multivariate image analysis: A review with applications. *Chemometrics and Intelligent Laboratory Systems* **107,** 1–23. ISSN: 01697439. http://dx.doi.org/10.1016/j.chemolab.2011.03.002 (2011).

172. Grassini, S., Pisano, R., Barresi, A. A., Angelini, E. & Parvis, M. Frequency domain image analysis for the characterization of porous products. *Measurement: Journal of the International Measurement Confederation* **94,** 515–522. ISSN: 02632241. http://dx.doi.org/10.1016/j.measurement.2016.08.031 (2016).

173. Bharati, M. H. & MacGregor, J. F. Texture analysis of images using principal component analysis. *Process Imaging for Automatic Control* **4188,** 27. ISSN: 0277786X (2001).

174. Hotelling, H. Analysis of a complex of statistical variables into principal components. *Journal of Educational Psychology* **24,** 417–441. ISSN: 00220663 (1933).

175. Pearson, K. LIII. On lines and planes of closest fit to systems of points in space. *The London, Edinburgh, and Dublin Philosophical Magazine and Journal of Science* **2,** 559–572. ISSN: 1941-5982 (1901).

176. Canny, J. A Computational Approach to Edge Detection. *IEEE Transactions on Pattern Analysis and Machine Intelligence* **PAMI-8,** 679–698. ISSN: 01628828 (1986).

177. Gonzalez, R. C. & Woods, R. E. *Digital image processing* 2nd (ed George, D. A.) ISBN: 0201180758 (Prentice Hall, Upper Saddle River, New Jersey, 2002).

178. C.Gonzalez, R., E.Woods, R. & L.Eddins, S. *Understanding Digital Image Processing Using MATLAB* 1st. ISBN: 978-81-7758-898-9 (Pearson/Prentice Hall, Upper Saddle River, NJ, 2004).

179. González-Martínez, J. M., Camacho, J. & Ferrer, A. MVBatch: A matlab toolbox for batch process modeling and monitoring. *Chemometrics and Intelligent Laboratory Systems* **183,** 122–133. ISSN: 18733239 (2018).

180. Corti, H. R. *et al.* Empirical and theoretical models of equilibrium and non-equilibrium transition temperatures of supplemented phase diagrams in aqueous systems (IUPAC technical report). *Pure and Applied Chemistry* **82,** 1065–1097. ISSN: 00334545 (2010).

181. Shalaev, E. *et al.* Freezing of Aqueous Solutions and Chemical Stability of Amorphous Pharmaceuticals: Water Clusters Hypothesis. *Journal of Pharmaceutical Sciences* **108,** 36–49. ISSN: 15206017 (2019).

182. Lide, D. R. in *CRC Handbook of Chemistry and Physics* (ed Haynes, W. M.) 90th Editi, 6–12 (CRC Press, Taylor & Francis Group, Boca Raton, FL, 2010). http://www.ncbi.nlm.nih.gov/pubmed/3841419.

183. Pongsawatmanit, R., Miyawaki, O. & Yano, T. Measurement of the Thermal Conductivity of Unfrozen and Frozen Food Materials by a Steady State Method with Coaxial Dual-cylinder Apparatus. *Bioscience, Biotechnology, and Biochemistry* **57,** 1072–1076. ISSN: 13476947 (1993).

184. Bosca, S., Barresi, A. A. & Fissore, D. On the robustness of the soft sensors used to monitor a vial freeze-drying process. *Drying Technology* **35,** 1085–1097. ISSN: 15322300. https://doi.org/10.1080/07373937.2016.1243553 (2017).

185. Bosca, S., Fissore, D. & Demichela, M. Risk-based design of a freeze-drying cycle for pharmaceuticals. *Industrial and Engineering Chemistry Research* **54,** 12928–12936. ISSN: 15205045 (2015).

186. Capozzi, L. C., Trout, B. L. & Pisano, R. From Batch to Continuous: Freeze-Drying of Suspended Vials for Pharmaceuticals in Unit-Doses. *Industrial and Engineering Chemistry Research* **58,** 1635–1649. ISSN: 15205045 (2019).

187. Cavatur, R. K. *et al.* Crystallization behavior of mannitol in frozen aqueous solutions. *Pharmaceutical Research* **19,** 894–900. ISSN: 07248741 (2002).

188. Fang, R., Bogner, R. H., Nail, S. L. & Pikal, M. J. Stability of Freeze-Dried Protein Formulations: Contributions of Ice Nucleation Temperature and Residence Time in the Freeze-Concentrate. *Journal of Pharmaceutical Sciences* **109,** 1896–1904. ISSN: 15206017. https://doi.org/10.1016/j.xphs.2020.02.014 (2020).

189. Rasmussen, D. H. Thermodynamics and nucleation phenomena - A set of experimental observations. *Journal of Crystal Growth* **56,** 56–66. ISSN: 00220248 (1982).

190. Fernández, C., Fodeke, A. A. & Minton, A. P. Quantitative characterization of the concentration-dependent interaction between molecules of Dextran 70 in aqueous solution: Measurement and analysis in the context of thermodynamic and compressible sphere models. *Biopolymers* **110,** e23284. ISSN: 10970282 (2019).

191. Um, J. *et al.* Dimensions and aspect ratios of natural ice crystals. *Atmospheric Chemistry and Physics* **15,** 3933–3956. ISSN: 16807324 (2015).

192. Murphy, D. M. & Koop, T. Review of the vapour pressures of ice and supercooled water for atmospheric applications. *Quarterly Journal of the Royal Meteorological Society* **131,** 1539–1565. ISSN: 00359009 (2005).

193. Koop, T., Kapilashrami, A., Molina, L. T. & Molina, M. J. Phase transitions of sea-salt/water mixtures at low temperatures: Implications for ozone chemistry in the polar marine boundary layer. *Journal of Geophysical Research* **105,** 393–402 (2000).

194. Barrere, M. *et al.* Evaluating the performance of coupled snow-soil models in SURFEXv8 to simulate the permafrost thermal regime at a high Arctic site. *Geoscientific Model Development* **10,** 3461–3479. ISSN: 19919603 (2017).

195. Untersteiner, N. Calculations of Temperature Regime and Heat Budget of Sea Ice in the Central Arctic. *Journal of Geophysical Research* **69,** 4755–4766 (1964).

196. Matsumoto, M., Saito, S. & Ohmine, I. Molecular dynamics simulation of the ice nucleation and growth process leading to water freezing. *Nature* **416,** 409–413. ISSN: 00280836 (2002).

197. Zaragoza, A. *et al.* Competition between ices Ih and Ic in homogeneous water freezing. *Journal of Chemical Physics* **143.** ISSN: 00219606. http://dx.doi.org/10.1063/1.4931987 (2015).

198. Russo, J., Romano, F. & Tanaka, H. New metastable form of ice and its role in the homogeneous crystallization of water. *Nature Materials* **13,** 733–739. ISSN: 14764660 (2014).

199. Moore, E. B. & Molinero, V. Structural transformation in supercooled water controls the crystallization rate of ice. *Nature* **479,** 506–508. ISSN: 00280836. http://dx.doi.org/10.1038/nature10586 (2011).

200. Prausnitz, J. & Foose, L. Three frontiers in the thermodynamics of protein solutions. *Pure and Applied Chemistry* **79,** 1435–1444. ISSN: 00334545 (2007).

201. Gibbs, J. W. On the Equilibrium of Heterogeneous Substances I. *Transactions of the Connecticut Academy,* 108–248 (1876).

202. Gibbs, J. W. On the Equilibrium of Heterogeneous Substances II. *Transactions of the Connecticut Academy* **16,** 343–524 (1878).

203. Volmer, M. Kinetic der Phasenbildung. *Angewandte Chemie* **52,** 503–504. ISSN: 00448249 (1939).

204. Jackson, K. A. *Kinetic Processes: Crystal Growth, Diffusion, and Phase Transitions in Materials* 1st, 1–409. ISBN: 9783527603893 (Wiley-VCH, Weinheim, Germany, 2004).

205. Wu, W. & Nancollas, G. H. Interfacial free energies and crystallization in aqueous media. *Journal of Colloid and Interface Science* **182,** 365–373. ISSN: 00219797 (1996).

206. Franks, F. *Water: A Comprehensive Treatise: Volume 4: Aqueous solutions of amphiphiles and macromolecules* 1st. **9,** 862. ISBN: 978-1-4684-2960-2 (Plenum Press, New York, NY, 1975).

207. Vekilov, P. G. The two-step mechanism of nucleation of crystals in solution. *Nanoscale* **2,** 2346–2357. ISSN: 20403364 (2010).

208. Pan, W., Kolomeisky, A. B. & Vekilov, P. G. Nucleation of ordered solid phases of proteins via a disordered high-density state: Phenomenological approach. *Journal of Chemical Physics* **122.** ISSN: 00219606 (2005).

209. Marchal, P., David, R., Klein, J. P. & Villermaux, J. Crystallization and precipitation engineering-I. An efficient method for solving population balance in crystallization with agglomeration. *Chemical Engineering Science* **43,** 59–67. ISSN: 00092509 (1988).

210. Catté, M., Dussap, C. G., Achard, C. & Gros, J. B. Excess properties and solid-liquid equilibria for aqueous solutions of sugars using a UNIQUAC model. *Fluid Phase Equilibria* **96,** 33–50. ISSN: 03783812 (1994).

211. Norrish, R. Equation for the activity coefficients and equilibrium relative humidities. *JInternational Journal of Food Science & Technology* **1,** 25–39 (1966).

212. Lewicki, P. P. in *Food Properties Handbook* (ed Rahman, M. S.) (CRC Press, 2009). ISBN: 9781420003093.

213. De Vito, F., Veytsman, B., Painter, P. & Kokini, J. L. Simulation of the effect of hydrogen bonds on water activity of glucose and dextran using the Veytsman model. *Carbohydrate Polymers* **117,** 236–246. ISSN: 01448617. http://dx.doi.org/10.1016/j.carbpol.2014.09.024 (2015).

214. Mizrahi, S., Ramon, O., Silberberg-Bouhnik, M., Eichler, S. & Cohen, Y. Scaling approach to water sorption isotherms of hydrogels and foods. *International Journal of Food Science and Technology* **32,** 95–105. ISSN: 09505423 (1997).

215. LERICI, C. R., PIVA, M. & ROSA, M. D. Water Activity and Freezing Point Depression of Aqueous Solutions and Liquid Foods. *Journal of Food Science* **48,** 1667–1669. ISSN: 17503841 (1983).

216. Yu, J., Wang, H., Kong, L., Zhu, H. & Zhu, Q. Study on the Thermal Conductivity of Mannitol Enhanced by Graphene Nanoparticles for Thermoelectric Power Generation. *Journal of Nanomaterials* **2020.** ISSN: 16874129 (2020).

217. Benchikh, O., Fournier, D., Boccara, A. C. & Teixeira, J. Photothermal Measurement of the Thermal Conductivity of Supercooled Water. *Journal de physique Paris* **46,** 727–731. ISSN: 03020738 (1985).

218. Biddle, J. W., Holten, V., Sengers, J. V. & Anisimov, M. A. Thermal conductivity of supercooled water. *Physical Review E - Statistical, Nonlinear, and Soft Matter Physics* **87.** ISSN: 15393755 (2013).

219. Perry, R., Perry, S., Green, D. & Maloney, J. *Chemical Engineers' Handbook, 7th ed.* pp. 25–94. ISBN: 0070498415 (1997).

220. Ho, N. & Roseman, T. Lyophilization of Pharmaceutical Injections : Theoretical Physical Model. *American Pharmaceutical Association* **68,** 1170–1174 (1979).

221. Nakagawa, K., Hottot, A., Vessot, S. & Andrieu, J. Modeling of freezing step during freeze-drying of drugs in vials. *AIChE Journal* **53,** 1362–1372. ISSN: 00011541 (May 2007).

222. Pandya, B., Smith, G., Ermolina, I. & Polygalov, E. Observations on the changing shape of the ice mass and the determination of the sublimation end point in freeze-drying: An application for through-vial impedance spectroscopy (TVIS). *Pharmaceutics* **13.** ISSN: 19994923 (2021).

223. Aydin, D., Memmedli, M. & Omay, R. E. Smoothing Parameter Selection for Nonparametric Regression Using Smoothing Spline. *European Journal of Pure and Applied Mathematics* **6,** 222–238. ISSN: 1307-5543. www.ejpam.com (2013).

224. Gerald Farin. *Curves and Surfaces for CAGD: A Practical Guide* 5th (ed Barsky, B. A.) 1–476. ISBN: 9788578110796 (Morgan Kaufmann Publishers AN, San Francisco, 2002).

225. Pisano, R., Fissore, D. & Barresi, A. A. in *Developments in Heat Transfer* (ed Bernardes, D. M. A. D. S.) 1st ed., 91–114 (InTech, 2011). ISBN: 978-953-307-569-3. http://www.intechopen.com/books/developments-in-heat-transfer/heat-transfer-in-%20freeze-drying-apparatus.

226. Boss, E. A., Filho, R. M. & Vasco De Toledo, E. C. Freeze drying process: Real time model and optimization. *Chemical Engineering and Processing: Process Intensification* **43,** 1475–1485. ISSN: 02552701 (2004).

227. Beirowski, J., Inghelbrecht, S., Arien, A. & Gieseler, H. Freeze Drying of Nanosuspensions, 2: the Role of the Critical Formulation Temperature on Stability of Drug Nanosuspensions and Its Practical Implication on Process Design. *Journal of pharmaceutical sciences* **100,** 4471–4481 (2011).

228. Colandene, J. D. *et al.* Lyophilization Cycle Development for a High-Concentration Monoclonal Antibody Formulation Lacking a Crystalline Bulking Agent. *Journal of pharmaceutical sciences* **96,** 1598–1608 (2007).

229. Horn, J. & Friess, W. Detection of collapse and crystallization of saccharide, protein, and mannitol formulations by optical fibers in lyophilization. *Frontiers in Chemistry* **6,** 1–9. ISSN: 22962646 (2018).

230. Haeuser, C., Goldbach, P., Huwyler, J., Friess, W. & Allmendinger, A. Be aggressive! amorphous excipients enabling single-step freeze-drying of monoclonal antibody formulations. *Pharmaceutics* **11,** 1–16. ISSN: 19994923 (2019).

231. Nail, S. L. & Searles, J. A. Elements of quality by design in development and scale-up of freeze-dried parenterals. *BioPharm International* **21,** 44–52. ISSN: 1542166X (2008).

232. Bosca, S., Barresi, A. A. & Fissore, D. Fast freeze-drying cycle design and optimization using a PAT based on the measurement of product temperature. *European Journal of Pharmaceutics and Biopharmaceutics* **85,** 253–262. http://dx.doi.org/10.1016/j.ejpb.2013.04.008 (2013).

233. Bourlés, E. *et al.* in (eds K., W. & P., M.) 215–240 (Humana Press, New York, NY, 2019). ISBN: 9781493989287.

234. Fissore, D. & Pisano, R. Computer-aided framework for the design of freeze-drying cycles: optimization of the operating conditions of the primary drying stage. *Processes* **3,** 406–421. ISSN: 2227-9717. http://www.mdpi.com/2227-9717/3/2/406/ (2015).

235. Pikal, M. J., Roy, M. L. & Shah, S. Mass and heat transfer in vial freeze-drying of pharmaceuticals: Role of the vial. *Journal of Pharmaceutical Sciences* **73,** 1224–1237. ISSN: 15206017 (1984).

236. Scutellà, B., Passot, S., Bourlés, E., Fonseca, F. & Tréléa, I. C. How Vial Geometry Variability Influences Heat Transfer and Product Temperature During Freeze-Drying. *Journal of Pharmaceutical Sciences* **106,** 770–778. ISSN: 15206017 (2017).

237. Scutellà, B. & Erwan, B. Development of freeze-drying cycle via design space approach: a case study on vaccines. *Journal of Pharmaceutical Sciences.* https://ejournal3.undip.ac.id/index.php/jamt/article/view/5101 (2020).

238. Hibler, S., Wagner, C. & Gieseler, H. Vial Freeze-Drying, Part 1: New Insights into Heat Transfer Characteristics of Tubing and Molded Vials. *Journal of pharmaceutical sciences* **101,** 1189–1201 (2012).

239. Pisano, R., Fissore, D. & Barresi, A. A. Freeze-drying cycle optimization using model predictive control techniques. *Industrial and Engineering Chemistry Research* **50,** 7363–7379. ISSN: 0888-5885. http://www.scopus.com/inward/record.url?eid=2-s2.0-79958826980&partnerID=40&md5=b3d7f6c03b2345dcb8e4de114b1e53fe (2011).

240. Velardi, S. A. & Barresi, A. A. Development of simplified models for the freeze-drying process and investigation of the optimal operating conditions. *Chemical Engineering Research and Design* **86,** 9–22. ISSN: 02638762 (2008).

241. Korpus, C., Pikal, M. & Friess, W. Heat Transfer Analysis of an Optimized, Flexible Holder System for Freeze-Drying in Dual Chamber Cartridges Using Different State-of-the-Art PAT Tools. *Journal of Pharmaceutical Sciences* **105,** 3304–3313. ISSN: 15206017. http://dx.doi.org/10.1016/j.xphs.2016.07.005 (2016).

242. Kuu, W. Y., Obryan, K. R., Hardwick, L. M. & Paul, T. W. Product mass transfer resistance directly determined during freeze-drying cycle runs using tunable diode laser absorption spectroscopy (TDLAS) and pore diffusion model. *Pharmaceutical Development and Technology* **16,** 343–357. ISSN: 10837450 (2011).

243. Goldman, J. M. *et al.* Representative scale-down lyophilization cycle development using a seven vial freeze-dryer MicroFD. *Journal of Pharmaceutical Sciences* **108,** 1486–1495 (2019).

244. Fissore, D. & Barresi, A. A. Scale-up and process transfer of freeze-drying recipes. *Drying Technology* **29,** 1673–1684. ISSN: 07373937 (2011).

245. Tang, X., Nail, S. L. & Pikal, M. J. Freeze-drying process design by manometric temperature measurement: Design of a smart freeze-dryer. *Pharmaceutical Research* **22,** 685–700. ISSN: 07248741 (2005).

246. Sundaram, J., Shay, Y. H. M., Hsu, C. C. & Sane, S. U. Design space development for lyophilization using Doe and process modeling. *BioPharm International* **23,** 40–45. ISSN: 1542166X (2010).

247. Harguindeguy, M. & Fissore, D. Micro Freeze-Dryer and Infrared-Based PAT : Novel Tools for Primary Drying Design Space Determination of Freeze-Drying Processes. *Pharmaceutical Research* **38,** 707–719 (2021).

248. Pyne, A., Surana, R. & Suryanarayanan, R. Crystallization of mannitol below Tg during freeze-drying in binary and ternary aqueous systems. *Pharmaceutical Research* **19,** 901–908. ISSN: 07248741 (2002).

This Ph.D. thesis has been typeset by means of the TEX-system facilities. The typesetting engine was pdfLATEX. The document class was `toptesi`, by Claudio Beccari, with option `tipotesi=scudo`. This class is available in every up-to-date and complete TEX-system installation.